Data-driven and Deep Learning-based Equivalent Modelling of HRES Plant for System Transient Stability Studies

A thesis submitted to The University of Manchester for the degree of
Doctor of Philosophy
in the Faculty of Science and Engineering

2022

Miss Ana Radovanović, B.Sc., M.Sc.

School of Engineering

Department of Electrical and Electronic Engineering

Blank page

Contents

Word count: 72,459

List of Figures

List of Tables

List of Abbreviations

AC - Alternating Current

ADN - Active Distribution Network

AM - Aggregate Model

AMISE - Asymptotic Mean Integrated Squared Error

AMSE - Asymptotic Mean Squared Error

ANN - Artificial Neural Network

AR - Autoregressive

ARIMA - Autoregressive Integrating Moving Average

ARMA - Autoregressive Moving Average

AVR - Automatic Voltage Regulator

BESS - Battery Energy Storage System

BFV - Best Fit Value

BIRCH - Balanced Iterative Reducing and Clustering Using Hierarchies

BMU - Best Matching Unit

BPPT - Backpropagation through Time

CDF – cumulative distribution function

CDI - Clustering Dispersion Index

CLARA - Clustering Large Application

CLARANS - Clustering Large Applications based upon RANdomized Search

CS – Case study

CURE - Clustering using Representatives

CVaR - Conditional Value-at-Risk

DBSCAN - Density Based Spatial Clustering of Applications with Noise

DC - Direct Current

DEM - Dynamic Equivalent Model

DENCLUE - Density-based Clustering

DFIG - Doubly-fed Induction Generator

DN - Distribution Network

DSL - DIgSILENT Simulation Language

DTW - Dynamic Time Warping

EM - Equivalent Model

FC - Fully Connected

FCC - Full Converter Connected

GPU - Graphical Processing Unit

HC - Hierarchical Clustering

HMM - Hidden Markov Model

HPP - Hydro Power Plant

HRES - Hybrid Renewable Energy Source Plant

IEC - International Electrotechnical Commission

IEEE - Institute of Electrical and Electronic Engineers

KDE - Kernel Density Estimation

LCSS - Longest Common Subsequence

LG - Single-Line-To-Ground

LL - Line-To-Line

LLG - Double Line-To-Ground

LLL - Three-Phase

LSTM - Long Short Term Memory

MA - Moving Average

MC - Monte Carlo

MG - Microgrid

MIA - Mean Index Adequacy

MISE - Mean Integrated Squared Error

MSE - Mean Squared Error

N4SID – Numerical Algorithm for Subspace State Space System Identification

NARX - Nonlinear Autoregressive with Exogenous Inputs

NCPLM - Negative Constant Power Load Model

OPF - Optimal Power Flow

OPTICS - Ordering Points to Identify the Clustering Structure

PAM - Partitioning Around Medoids

PCC - Point of Common Coupling

PDF - probability density function

PI - Proportional-Integral

PSO - Particle Swarm Optimization

PV - Photovoltaic

RAM – Random Access Memory

RES - Renewable Energy Source

RMSE - Root Mean Squared Error

RNN - Recurrent Neural Network

RoCoF - Rate of Change of Frequency

SG - Synchronous Generator

SI - Silhouette Index

SOM – Self Organizing Map

TDL - Time-Delay-Line

TF - Transfer Function

TL - Tie-Line

TN - Transmission Network

TSI - Transient Stability Index

TSO - Transmission System Operator

VPP - Virtual Power Plant

WCBCR - Within Cluster Sum of Squares to between Cluster Variation Ratio

WECC - Western Electricity Coordinating Council

WF - Wind Farm

Abstract

Hybrid renewable energy source (HRES) plants, a combination of renewable generation and storage technologies with a common grid connection point, have been seen as a promising option for obtaining controllable RES production, and thus, contributing to system stability maintenance. Assessing the impact of HRES plants on system dynamic behaviour requires their adequate dynamic representation in system stability studies. Dynamic equivalent models (DEMs) of HRES plants as a part of the overall system dynamic model can provide a fast reliable system stability estimation without modelling individual HRES plant components. The main contribution of the research described in this thesis is in the area of dynamic equivalent modelling of HRES plants. The thesis also looks into the concept of geographically distributed HRES plant at transmission network (TN) level from the system stability perspective, as this concept is an expected extension of the existing concept of aggregators at distribution network level.

The thesis starts by discussing the techniques for dynamic equivalent modelling of plants and networks. It then provides a computationally efficient procedure for assessing the typical annual impact of HRES plant on power system stability. The outputs of this procedure are the basis for developing preliminary equivalents of HRES plant for small-disturbance, transient, frequency and long-term voltage stability studies. Two, data-driven and deep learning-based, methodologies for developing DEMs of HRES plant for transient stability studies using system-identification methods are developed. The first, data-driven, methodology is designed from the perspective of the overall transient stability assessment as the accuracy of the global transient stability status is what is of a critical importance when performing large transient stability studies. On the other hand, the deep learning-based methodology develops DEM in a conventional way, i.e., focusing on the shape of time domain HRES plant power responses. Both methodologies do not require the detailed dynamic data about physical devices in the HRES plant, provide a small set of DEMs capable of covering the most probable HRES plant dynamic behaviour in annual transient stability studies, and include a practical procedure (separate procedures were developed for each methodology) for selecting the adequate equivalent from the set of previously developed DEMs at any time of the year knowing HRES plant operating scenario only. Finally, the thesis presents an exploratory study on the potential challenges in the preservation of transient stability of the TN due to the integration of a geographically distributed HRES plant that has more than one TN connection point.

The main findings of the research confirm the ability of DEMs of HRES plant, that were not derived based on the shape of time domain HRES plant power responses, to provide reliable overall transient stability assessment, and the importance of taking into account TN dynamic performance when deciding on the deployment of individual RESs within the spatially distributed HRES plant.

Declaration

No portion of the work referred to in this thesis has been submitted in support of an application for another degree or qualification of this or any other university or other institute of learning.

Copyright statement

Acknowledgment

I would like to express my sincere gratitude to my supervisor Professor Jovica V. Milanović for his guidance, support, and encouragement throughout the period of my PhD study. His commitment to hard work and excellence have constantly inspired and motivated me to progress in my research.

A special acknowledgment must go to the EU Horizon 2020 CROSSBOW and EPSRC Supergen Energy Networks hub projects, which provided me with the opportunity to work on large collaborative projects between academia and industry, and obtain invaluable skills and professional experience. The work on these projects and support received from The University of Manchester enabled me to fund my PhD research.

My appreciation also goes to my colleagues from the Power Quality and Power Systems Dynamics group at The University of Manchester. I would like to thank them for their friendship, kind help and constructive discussions whenever I needed them.

Finally, I would like to express my deepest gratitude to my parents, Gordana and Pera, and my sister Ivana. Their unconditional love, understanding, and continuous support throughout this period have been invaluable. I cannot thank them enough for always being there for me, even when we are thousands of kilometres far away from each other.

In Manchester, June 29th 2022

To Gordana, Pera and Ivana

1 Introduction

1.1 Background

Over the past few decades, electric power systems around the world have experienced a significant increase in the installation capacity of renewable energy sources (RESs). By the end of 2021, RESs represented 38% of the total generation capacity in the world reaching around 3,064 GW [1]. During the last 2021 year, 257 GW of RESs was added to the system globally, with 133 GW (around a half of new RES capacity in 2021) and 93 GW coming from solar and wind energy, respectively [1]. It is expected that RES capacity will increase by more than 1,800 GW by 2026 [2].

Future grids will be dominated by RESs, which will then have the main responsibility in securing energy supply and maintaining the overall power system stability. This, in turn, implies that the typical mode of RES power plant operation based on producing as much electricity as possible and receiving the remuneration for it according to the fixed feed-in tariff or power purchase agreements will have to be modified [3]. A number of countries has already introduced feed-in premium schemes and balancing responsibilities (identical to the ones for conventional synchronous generators (SGs)) for RESs [4]. Under feed-in premium schemes, RES producers receive a payment that is a sum of electricity market price and a premium representing an incentive for RES integration [5]. In this way, RES producers are encouraged to adapt their production profiles to market conditions. However, these marked-based schemes provide limited opportunities for

RESs relying on weather conditions for producing electricity due to their intermittent and uncontrollable power production [3].

A full use of market-based schemes, and, eventually, becoming a regular player on markets, requires dispatchable power production from a RES power plant. In order to address the issue of stochastic production, and thus, "ensure profitability at an individual asset level" [3], the concept of grid-connected hybrid renewable energy source (HRES) plant has been proposed. HRES plant represents an aggregation of several technologies (non-dispatchable and dispatchable RES and storage systems) having the same point of connection to the grid (the same point of common coupling (PCC)), and operated and seen in a system as a single entity [3, 6]. (*Note*: The definition of hybrid power plant including non-renewable generation technologies as well, can be found in the literature [3]. In this thesis the focus is only on the mix of renewable generation and storage technologies.) The HRES plant concept is illustrated in Figure 1.1. The treatment of HRES plants as a single resource is what distinguishes them from co-located RES power plants (individual plants within a co-located power plant have the same PCC but independent operation/control) [6]. The HRES plant operation is based on complementary properties of different technologies, i.e., their ability to compensate each other's deficiencies (in terms of power production) to a certain extent, which in turn should reduce the stohasticity in power production at the PCC [7].

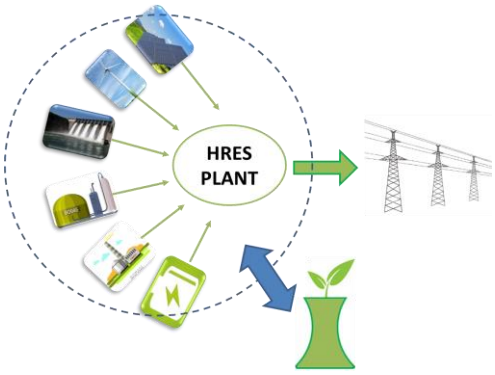

Figure 1.1 The illustration of the HRES plant concept (adapted from [8])

Combining technologies with different performance characteristics into a single plant provides various benefits compared to single technology-based RES power plants [3, 6, 9]:

- Reduction in the variability of power production during the year;

- Ability to participate in energy and ancillary service markets in a manner similar to traditional SGs;
- Flexibility in plant configuration;
- Reduction in the investment, operation and maintenance cost due to equipment sharing;
- Reduction in the cost associated with interconnection request due to a single grid connection point;
- Reduction in infrastructure costs for roads, maintenance buildings, etc.

Individual units within the HRES plant can be "ac-coupled" or "dc-coupled", with the former being more common approach [6, 9]. The "ac-coupled" topology requires all individual plants to be connected to the low-voltage side of the transformer used for connecting the whole HRES plant to the grid. On the other hand, in case of the "dc-coupled" design individual units of different technologies share the same converter. The converter sharing can increase its efficiency as converters usually perform better at higher loading, but may deteriorate the performance of individual units as they have to be located in close proximity to each other (e.g., shading of photovoltaic (PV) panels by wind turbine blades and tower in the case of "dc-coupled" PV and wind turbine units). Regardless of the way of coupling of individual resources, all plants in the HRES plant share the same substation and grid connection point.

HRES plants have an ability to easily modify their configuration by increasing the installation capacity of the already integrated technologies or adding new technologies in the existing HRES plant, while keeping the maximum HRES plant output below the approved grid-connection capacity (the HRES plant would have to repeat the grid code compliance process otherwise) [6]. This flexibility is of a particular importance to investors as it indicates that HRES plants can quickly adapt to changes in market requirements. Given that HRES plants could potentially even outperform conventional sources due to their flexible nature, the question of whether the existing market standards are capable of monetizing the HRES plant flexibility in an adequate manner has been raised [6]. Current pricing and payment schemes are based on operational constraints of conventional generators (start-up cost and time, no-load costs, minimum run time,

minimum downtime), and paying conventional generators for the aforementioned limitations could be seen as "an implicit subsidy for inflexibility" [6] in case of a high share of HRES plants in electricity markets.

The integration of HRES plants into power systems is at its early stages, but a constant increase in the number of installed HRES plants over the following years is expected [3, 9-18]. Vestas and General Electric have already made HRES plants a part of their business strategies [3]. Typical technology mix in HRES plants in operation and under development includes wind and solar energy, and storage systems, with hydro energy becoming attractive as well [10]. Vestas installed the first utility-scale HRES plant consisting of a wind farm (WF), PV plant and battery energy storage system (BESS), Kennedy Energy Park, in Australia in 2018, and the plant was put into operation in 2021 [17]. The plant contains a 43 MW WF, a 15 MW PV plant and a 2 MW BESS [9]. Another operational, large HRES plant in Australia is the Bulgana Green Power Hub (a 204 MW WF and a 20 MW BESS) [11]. The first utility-scale WF/PV/storage plant developed by Vattenfall is Haringvliet energy park in the Netherlands, which comprises a 22 MW WF, 38 MW PV plant and 12 MW storage system, while Vattenfal's first HRES plant integrating a WF and PV plant was installed in the UK by adding PV panels (with a total capacity of 4.95 MW) to an existing 3.6 MW WF [9]. Siemens Gamesa is also committed to HRES plant projects, with its first commercial HRES plant installed in India in 2018 – a combination of 29 MW solar plant and 50 MW WF [9]. When it comes to the USA, at the end of 2020, 34% (159 GW) of solar and 6% (13 GW) of wind plants in interconnection queues were registered as parts of hybrid systems (HRES plants and co-located RES power plants) [10].

1.2 Motivation

Combining various renewable generation and storage technologies into a single plant enables more stable and controllable power production at the grid connection point. However, dynamic characteristics of individual HRES plant components can be considerably dissimilar due to differences in their technology type and/or controller structure. Different dynamic responses of individual technologies together with their individual stochastic behaviour makes the prediction of the overall HRES plant dynamic performance at the PCC throughout the year much more complex than in the case of single technology-based RES power plants. In order to assess the dynamic response of

the whole HRES plant, and consequently, to what extent the HRES plant can contribute to the overall power system stability behaviour, numerous system-level stability studies, with the adequate HRES plant dynamic representation, have to be performed.

Given that system operators are progressively relying on RESs to provide services traditionally obtained from conventional generators, the control systems of RES power plants are becoming more complex. The complexity of controllers together with a large number of individual units within the plant results in detailed dynamic models of RES power plants, and in particular the models of HRES plants comprising several technologies, being high-order structures. In the presence of substantial number of RES and HRES plants in the system (which is the expected situation in the future), detailed dynamic representation of these plants would be impractical as it would result in considerable computational time required for carrying out large system-level analyses [19, 20]. On the other hand, there is a growing need for collaboration between all system actors in the operation and planning of future power systems, while data protection laws might not allow the exchange of full-scale dynamic models between different system operators [21].

In order to address the aforementioned issues with the detailed dynamic modelling of RESs, dynamic equivalent models (DEMs) have been recommended [22-27]. A DEM represents a simplified representation of the detailed dynamic model of the investigated plant that does not compromise the accuracy of system stability analyses. Smaller mathematical order of DEM compared to the full-scale model provides reduction in computational burden when conducting large system stability studies. More efficient system stability assessment provides system operator with more time to carry out additional studies in case a problem has been identified and/or perform actions to resolve the issue. Given that DEMs do not include detailed dynamic data, they can overcome confidentiality issues, and contribute to information sharing and cooperation between different system operators.

Due to technology mix present in the plant, developing the structure of an equivalent HRES plant model that will provide a reliable plant representation in system stability studies is more challenging compared to the equivalencing of RES power plants with a single type of generation technology. A lot of research has already been done in the area

of dynamic equivalent modelling of single technology-based RES plants (a detailed overview is given in the following sections), whereas the HRES plant concept is relatively new and lacks extensive analysis on plant design, dynamic modelling and control [3].

1.3 Review of the Past Work

1.3.1 The Concept of Hybrid Renewable Energy Source Plant

The research on HRES plants has been mainly devoted to the selection of the optimal technology mix, sizing of individual components and optimization algorithms for economic operation. The exact combination of technologies in the particular HRES plant is determined by RES potential at the given location, the complementarity of the sources (assessed on the basis of historical production data or a joint probability distribution of production of individual sources), expected plant functionalities and local market conditions [3, 9]. When it comes to the sizing of the individual plants within the HRES plant, optimal individual capacities are usually obtained as the outputs of the optimization procedure that maximizes the overall plant profit [7]. The total plant profit is commonly defined as a difference between the plant revenue due to selling the electricity to the grid, and the total plant cost including the investment, operational and maintenance costs for all individual components, and the cost of the electricity purchased from the grid. The total plant revenues and costs are calculated for the expected lifetime of the HRES plant, and net present value is then used as the objective function in the optimization problem [3, 28, 29]. In [28] potential equipment replacement during and equipment sale at the end of the plant lifetime were included in the calculation of the total plant profit as well. In order to avoid the dependence of the optimization results on electricity market price that can change drastically over a course of the study period, in [30] energy imported from and exported to the grid during the year were considered.

Optimization of the physical layout of individual components in the HRES plant has not been in the focus of the research work [3, 31]. This task inherits all difficulties of the physical layout determination for single technology-based RES power plants and incorporates additional ones due to the interactions between different technologies. In [31] the determination of the optimal rated capacities of individual components and the optimal locations of wind turbines and PV panels within a WF/PV/BESS hybrid plant

was carried out on the basis of maximizing the total annual HRES plant profit. The wind turbines were placed within a rectangular grid in the pre-defined HRES plant area, and their locations were defined by optimizing the row and column spacing in the grid, and the position of the grid within the whole HRES plant area. The locations of PV panels were defined as a function of wind turbine locations, PV plant capacity and the minimum allowed spacing between wind turbines and PV panels. When it comes to the BESS, it was assumed that the BESS size was not large, and thus the BESS could be installed anywhere within the HRES plant area boundaries. In [32] the optimization of the number and locations of PV panels added to an existing WF was based on the potential wind turbine towers' shadow on PV panels. For each wind turbine, the length and direction of tower's shadow were computed using the hourly data of azimuth and zenith of the sun, which provided a "heat map" of areas affected by the tower's shadow.

Given that the idea of HRES plant concept is to enable the integration of RESs in markets, the focus of the research on optimal operation of HRES plant is on the optimal bidding of HRES plants on markets from the perspective of plant revenue. The procedure for specifying the optimal economic HRES plant dispatch can include the total plant profit (the difference between the plant revenue obtained by participating in markets and total plant costs) only [33, 34] or the risk management can be taken into account as well [35-37]. The uncertainties in market prices and production of non-dispatchable individual HRES plant components can increase the risk of low plant revenues, and in order to avoid them, the risk is included using conditional value-at-risk (CVaR). CVaR is defined as a conditional expectation of economic loss above amount α, where α represents the minimum value among all loss values whose cumulative distribution function (CDF) value is equal to the chosen probability level [38]. The main inputs for the procedure are market price data, and generation forecast of individual HRES plant components, while various operational limits of individual HRES plants, power offer and imbalance limitations represent the procedure constraints. In [35] the ability to reduce plant power imbalances was stated as the main reason for the HRES plant (a WF and a reversible hydro power plant (HPP)) outperforming the co-located WF and HPP, as well as the separate WF and HPP, in terms of the revenue on the day-ahead market. The results obtained with the test systems in [33, 34] showed that relying on the participation on

energy market only can result in considerable reduction in the plant revenues compared to the provision of both energy and ancillary service products.

The analysis of the influence of HRES plant on power system dynamic performance has not received significant attention. In [39] the impact of an HRES plant comprising a PV plant, WF and small HPP on transient stability of the small test system was investigated. The critical clearing time was chosen for assessing transient stability performance for several operating scenarios and locations of three-phase short circuit-faults. The dynamic performance of a HRES plant consisting of a PV plant, WF and BESS in frequency stability studies was investigated in [40]. The focus was on fast frequency response provision. A frequency controller for the whole HRES plant with the deviation of frequency from the nominal value and the rate of change of frequency (RoCoF) value as input signals was proposed. In [41] a BESS provided synthetic inertia, and the WF output was reduced by 20% at normal operating conditions, so that it can provide frequency support in case of frequency drop. The test HRES plant had negligible effect on frequency nadir and RoCoF value as its size was considerably smaller compared to the total capacity of SGs in the system.

1.3.2 Dynamic Equivalent Models of Large Power Systems with Conventional Generators

Equivalent modelling of power systems with SGs as the only generation technology represents a mature research area as the first approaches appeared in the 1970's [42]. The strategies for DEM development can be divided into four main groups:

- Modal analysis-based;
- Coherency-based;
- Modal-coherency-based;
- System identification-based.

1.3.2.1 Modal Analysis-based Dynamic Equivalent Models

Modal analysis-based modelling requires the identification of the detailed state-space system model and elimination of the irrelevant/non-dominant modes from the detailed system in order to reduce the state-space model order. In [43] modes with high damping, not significantly excited by the inputs and not having a considerable effect on the

linearized state-space model outputs were neglected. However, the approach showed to be impractical for real power systems and the use of linearized state-space model without model order reduction was recommended in [44]. The application of the full-scale linearized state-space model was justified by significant reduction in computational time due to "computationally efficient structure of the dynamic equations" [44]. In [45] the moment-matching method was used for state-space model reduction, but the size of the reduced system has to be defined *a priori* and the methodology for selecting the optimal system model order was not provided. Equivalent modelling based on the non-linear detailed state-space model was proposed in [46]. Empirical controllability and observability covariance matrices capable of reflecting non-linear system behaviour were used for computing Hankel singular values, and then states corresponding to small Hankel singular values were removed from the model.

In [47] the expression for deviations of real and reactive power at the boundary buses (i.e., the buses connecting the study area represented in detail and the external area being equivalenced) from their pre-disturbance values due to small step changes in voltage angles of boundary buses were defined using the linearized state-space model of the external area. Modes producing modal components of small amplitude in the power deviations at all boundary buses were neglected. Unlike other modal analysis-based methods deriving the equivalent in the mathematical form, for each of the retained modes, a second-order non-linear generator (so-called, modal generator) was used for representing the whole external area. The parameters of the modal generator were estimated in such a way that the linearized power responses at the boundary buses for the particular mode of oscillations were preserved.

1.3.2.2 Coherency-based Dynamic Equivalent Models

Coherency-based modelling approaches rely on the identification of the coherent groups of SGs (i.e., SGs having similar dynamic behaviour) and development of an equivalent, aggregate SG for the whole group. The equivalent SG has to preserve the total mechanical and electrical power of individual generators from the coherent group. In the case of hydro and steam generators being in the same group, separate equivalents are designed for each of them [48]. The same approach is usually followed if coherent SGs are equipped with different types of controllers [49]. Coherent SGs in the external area

were defined in [48, 50-52] as generators with similar swing curves. In [50, 51] SG swing curves were obtained by simulating a short-circuit fault in the study area in a dedicated software package for system stability studies, whereas the numerical integration of linearized system dynamic equations was performed in [48, 52].

1.3.2.3 Modal-Coherency-based Dynamic Equivalent Models

In order to use the best characteristics of the modal analysis-based method (mathematical foundation, ability to preserve various modes of oscillation, independence of the selection of the disturbance used for model development) and coherency-based approach (model is in the form of a standard system model, which eliminates the need for software modifications), a modal-coherency approach was proposed. In this method, the identification of coherent generators is carried out using modal methods [42]. Slow coherency method was used for dividing SGs into coherent groups in [49]. The method assumes that coherent groups swing against each other with respect to slower frequencies, whereas generators within the same coherent group swing against each other with respect to higher frequency modes [53]. Weak-link coherency approach was presented in [54]. The state matrix of the linearized state-space model is transformed in such a way that the system is decomposed into subsystems that are weakly coherent, while generators within the same subsystem are strongly coherent. In [55] SGs were organized into a hierarchical tree structure according to their involvement in electromechanical modes defined for the whole system incorporating both the study and external area. Only modes involving any of the SGs from the study area were retained, which defined tree cut points for system division (i.e., grouping of SGs into coherent groups). Similarly, in [56] the rms coherency measure was computed for each pair of SGs in the external area using the linearized state-space model. The coherency measure of two SGs is based on the differences in their rotor angle responses to a set of random disturbances in mechanical power outputs of the SGs in the external area. The obtained values were sorted from the smallest to largest, and SGs were iteratively grouped starting from a pair of SGs with the lowest coherency measure. In [57] two SGs were considered coherent if the differences between their rotor angles in frequency domain (obtained from the linearized state-space system model) for a set of disturbances in the study area were below the pre-specified threshold value for the whole frequency spectrum of interest.

1.3.2.4 System Identification-based Dynamic Equivalent Models

System identification-based techniques use measured or simulated dynamic responses of the system in order to develop DEMs, i.e., DEM parameters are estimated by minimizing the difference between DEM and measured/simulated responses. Depending on the amount of the information about the system, they can be divided into black-box, grey-box and white-box methods, where black-box and white-box models require the smallest and largest amount of information about the system, respectively. White-box models are in fact full-scale system models comprising detailed representation of all system components, and thus characterized by high model order. Grey-box models are usually in the form of a combination of physical models of the most important system components. Unlike grey-box models that require certain amount of knowledge about the significant physical devices in the analysed system, black-box models are only focused on matching responses of the detailed model and DEM without taking into account system structure. Black-box model design can thus correspond to a linear or non-linear mathematical model, or an artificial intelligence structure. Given that white-box models do not correspond to a simplified system representation, only grey-box and black-box methods were used for equivalent modelling.

In [58] the parameters of the second-order equivalent SG were obtained through the least squares optimization process focused on minimizing the difference between the model response and recorded response for a single short-circuit fault. DEM parameters were obtained from measurements of voltage magnitude and angle, real and reactive power at the boundary buses in [59]. The DEM is in the form of an equivalent SG (stator transients and damper windings were neglected in the SG model) and an equivalent composite load in parallel. Parameter estimation was carried out for a single fault disturbance using the Levenberg-Marquardt algorithm. The DEM was tested for different fault locations, but the operating point corresponded to the one used in model development. In [60] two artificial neural networks (ANNs) were proposed for modelling a part of a power system. A feed-forward ANN was used for estimating system states, whereas a recurrent ANN was used for predicting real and reactive power at the boundary bus on the basis of the estimated state variables. The equivalent is robust to fault duration and variations in operating point. A combination of an ANN and a coherency-based equivalent was

proposed in [61]. The ANN-part of the DEM was introduced to increase the accuracy in voltage responses at the boundary buses compared to the case with the coherency-based equivalent only by injecting additional real and reactive power at the boundary buses. The coherency-based equivalent comprise the second-order equivalent SGs representing coherent groups defined using the weak-link coherency method.

1.3.3 Dynamic Equivalent Models of Renewable Energy Source Plants

The research on equivalent modelling of RES power plants has been devoted to plants consisting of a large number of same-technology units [62]. The focus of DEM development has been on deriving equivalents capable of producing dynamic plant responses with the highest possible accuracy. Equivalent modelling of a RES plant is commonly carried out by representing all units in the plant by a single- or multi-machine equivalent, which has the same structure as the model of individual units [63]. Single-machine equivalent is characterized by simple derivation, but its dynamic response might not be able to reflect different dynamic behaviour of individual generators with high accuracy. On the other hand, in the case of the multi-machine method, the main difficulty is a choice of adequate criteria for identifying coherent units that can be allocated to a single group and represented by a common DEM.

The parameters of DEM of a group of coherent units are usually obtained using the capacity equal weighted method [64]. The method assumes that all units in the group are characterized by the same model structure. The DEM is obtained by scaling-up the model of individual unit according to the number of units in the group. However, dynamic model data of individual units might not be available, and/or individual units may be characterized by different model structures/parameters [64]. In order to overcome the aforementioned issues, the measurement/simulation-based approach can be used for determining DEM parameters. The measurement/simulation-based method estimates DEM parameters through an optimization procedure that minimizes the deviation of DEM responses from the measured responses or the responses produced by the detailed model of the investigated group of individual units [64]. Regarding the equivalent modelling of the collector system in RES power plants, the impedance of a collector/cable connecting DEM to the PCC is commonly defined by preserving the total losses in or the weighted average voltage drop (the weights are power outputs of coherent units) across cables connecting coherent units to the PCC [63, 65-67].

The work in the area of equivalent modelling of RES plants has been mainly focused on developing equivalents for large WFs. The majority of papers use multi-machine representation of WFs as most wind turbines in large WFs operate at different wind speeds due to the wake effect and time lag in their wind profiles [63, 64]. In order to increase the accuracy of the single-machine WF equivalent, in [68] the mechanical torque of the equivalent generator was multiplied by a factor computed using the average wind speed of all wind turbines in the WF and the standard deviation of the wind speed values. However, introducing this factor resulted only in the improved model performance in terms of being able to follow wind speed variations, whereas there was no increase in the accuracy of model dynamic responses to grid disturbances compared to the standard single-machine DEM. In [69] the mechanical torques of individual wind turbines in the WF were used as inputs to the single-equivalent generator, but the approach is not suitable for commercially available software packages as it modifies the standard wind generator model [63].

When it comes to the multi-machine equivalents of WFs, the most common criteria for identifying coherent units are wind speed and real power output of individual units, and clustering algorithms, such as the k-means, fuzzy c-means, support vector machine, etc. are then used for grouping wind turbines according to the selected coherency criteria [63-65, 70]. However, coherent generators are typically defined for a single WF operating point [71]. In order to take into consideration constant changes in WF operation, probabilistic equivalents of WFs were developed in [65, 72] and [71]. For a range of the values of speed and direction of wind entering the WF, wind turbines were grouped using Support Vector Clustering applied to their input wind speeds (defined taking into account the wake effect) in [65, 72]. The probability of the occurrence of each clustering result was identified, and the DEM for the most probable clustering result was proposed as an adequate representation of the WF throughout the whole year. In [71] three equivalent wind turbines with parameters depending on WF operating condition were used for representing the WF during the year. The allocation of a wind turbine to one of the three coherent groups (each represented by an equivalent wind turbine) was determined by the value of its wind speed and impedance to the PCC.

The equivalent modelling of PV plants has received significantly less attention in comparison to WF equivalents [62]. As in the case of WF equivalent modelling, most of the reported PV plant equivalents are multi-machine equivalents [73]. Typical coherency criteria used for identifying PV systems with similar dynamic behaviour can be divided into four groups [73]:

- feature quantities (e.g., PV array type, inverter control mode, protection circuit switching actions);
- operating conditions (e.g., voltage and current at the DC and AC side of inverter, real and reactive power inverter output);
- controller parameters;
- dynamic responses (e.g., PV system current, real and reactive power responses following a disturbance).

In order to group PV units with similar dynamic characteristics, in [74] PV systems were clustered according to the Euclidean distance between their weighted inverter parameters (filter inductance, and proportional gain and constant of real power control loop). A weight corresponded to the sensitivity of the power output of a PV system to changes in a parameter value, and was computed for characteristic levels of PV system production. The approach requires the clustering to be performed whenever operating condition changes using the weights associated with the characteristic PV system production that is the most similar to the investigated PV system power output. Equivalent modelling of a PV plant with equivalent synchronous characteristics was presented in [75]. PV systems having converters with similar R/X ratio of equivalent impedance, and similar real and reactive power responses for step changes in the plant real power and voltage reference, were represented by a common model. The DEM has the same structure as the model of individual PV systems - a two-diode PV model and an inverter with a synchronous power controller. In [76] the DEM of a group of PV units was developed in the form of a deep ANN with irradiance intensity, voltage at the PCC, and reactive power reference for inverters as inputs, and the total real and reactive power output of the group as outputs. Coherent groups were defined using the clustering index based on the parameters of the inverter current controller, the angle of the phase locked loop and PV power production.

1.3.4 Dynamic Equivalent Models of Active Distribution Networks and Microgrids

Two main approaches for developing DEMs of active distribution networks (ADNs) and microgrids (MGs) are modal analysis- and system identification-based methods (grey-box and black-box models). Unlike in the case of equivalent modelling of large power systems with SGs as the only type of generation technology, system identification-based equivalents account for the largest number of proposed DEMs of ADNs and MGs.

1.3.4.1 Modal Analysis-based Dynamic Equivalent Models

As in the case of equivalent modelling of large power systems with conventional generators only, modal analysis-based models represent simplified detailed state-space system models. The DEM development requires the eigenvalue analysis of the full state-space system model linearized around an operating point, and the state-space model order reduction is achieved by selecting and preserving only the most dominant modes [77].

In [78] Hankel norm approximation was used for the model order reduction. The state-space model was simplified on the basis of the Hankel singular values that define the maximum amplitude of the difference between the transfer functions (TFs) of the original and equivalent system model. As voltage and current at the PCC are model input and output, respectively, the model can be integrated into software packages for system stability simulations in the form of a voltage controlled current source connected to the PCC. Modal truncation technique was applied in [79]. The simplification of a full state-space MG model was achieved by preserving the two slowest oscillatory modes and real modes smaller than 1% of the real part of the most damped mode. Singular perturbation approach that divides system states into fast and slow was used in [77]. The order of the detailed MG model was reduced by eliminating fast state variables. All techniques used for identifying the dominant modes in [77-79] require the specification of the threshold that determines which modes should be considered as the dominant ones, and the papers lack the methodology for defining this threshold value. The domain of validity of modal analysis-based equivalents is restricted to small deviations around the investigated operating point, meaning DEM has to be derived whenever operating condition changes [42].

1.3.4.2 System Identification-based Dynamic Equivalent Models

1.3.4.2.1 Grey-box Dynamic Equivalent Models

A grey-box model consisting of an inverter interfaced SG (the third-order model) in parallel with a composite load model (ZIP load model and an induction motor representing the static and dynamic load part, respectively) was proposed in [19, 20, 42] to model an ADN. Similarly, the DEM of ADN in [80] consists of a parallel combination of a SG, induction motor, converter and static constant power load. In order to estimate DEM parameters by minimizing the difference between detailed model and DEM responses, the equations for individual DEM components were organized into a non-linear state-space model with real and reactive power at the PCC as outputs. Voltage and frequency at the PCC represented state-space model inputs in [19, 20, 42], whereas only voltage at the PCC was used as an input signal in [80]. In [19, 20, 42] parameters were defined for several ADN compositions with the same total power production and load, and representative DEM parameter values were recommended for characteristic groups of analysed cases (identified by clustering of power responses according to similarity). On the other hand, cases with different directions of power flow at the PCC were considered in [80], but the model has to be redeveloped for every new operating point.

An iterative procedure for developing a grey-box equivalent for radial networks comprising several voltage levels was presented in [81, 82]. At each voltage level, RES plants characterized by the same technology and grid code requirements were aggregated and represented by a DEM corresponding to a scaled-up model of individual plants, whereas all loads were modelled by a single scaled-up model of individual loads. The model was tested for various voltage dips at the connection point to the transmission network (TN), but the operating point was the same as in the model development.

The use of grey-box models for dynamic equivalencing of MGs was reported in [83-86]. The detailed model of voltage source inverter, and a grey-box model of micro turbines and fuel cells was suggested as an equivalent MG model in [83, 84]. The grey-box model was derived assuming that the dynamic behaviour of micro turbines and fuel cells equipped with PQ inverters could be simulated by the model with the structure corresponding to a governor in a diesel generator. Model validation was carried out using several MG operating points and load following transients. In [86] the equivalent comprising a seventh-order SG model with governor and automatic voltage regulator

(AVR), and a voltage source converter was proposed as a DEM of SGs and converter-connected generators in a MG. The parallel combination of the equivalent SG and converter was connected to the PCC through a series impedance representing network losses. DEM parameters (including the resistance and reactance of the series impedance) were estimated using the responses of the detailed MG model to step changes in the reference values of real and reactive power output of generation sources. DEM demonstrated satisfactory accuracy for several combinations of operating points and step disturbances, as well as when tested on a three-phase short-circuit fault in the TN, but this testing was carried out for the operating condition used in DEM development. The parameter estimation procedure described in [86] was used for defining the parameters of a small-disturbance DEM of a MG containing SGs as only generation technology in [85]. The proposed model is a linearized third-order SG model with a governor and an AVR, and SG parameters have to be calculated for every new operating condition.

In [21] DEM of an ADN with converter-connected generators as the only sources was developed for large-disturbance stability simulations. DEM structure corresponds to the dynamic model of individual generators adjusted to take into consideration potential tripping of individual units. DEM parameters were estimated to match the average of ADN power responses produced by Monte Carlo (MC) procedure that takes into account uncertainty in the values of parameters of the individual generators' detailed models. The methodology was extended in [87] to include different operating points. The proposed approach requires producing dynamic MC responses using the detailed dynamic ADN model whenever operating scenario changes as well as assessing whether any of the already developed DEMs is sufficiently accurate for the new operating scenario (if this is not the case, new set of DEM parameters has to be estimated). Further improvement of the accuracy of the modelling procedure was proposed in [88]. The installation of a BESS at the PCC that would compensate for the differences between DEM power responses (obtained in simulations) and measurements at the PCC in case of large disturbances in the TN was recommended, which is supposed to reduce the frequency of DEM parameter updates (due to changes in ADN operating conditions).

1.3.4.2.2 Black-box Dynamic Equivalent Models

In [89] and [90] the measured real and reactive power responses to small disturbances in voltage at the PCC (within ±0.1 p.u. variations) were used for deriving ADN equivalent in the form of a combination of linear functions and TFs. In [89] the main assumption was that the responses associated with similar pre-disturbance, steady state voltage and power at the PCC could be described by the same set of TF poles. In order to enable quick estimation of DEM parameters in online applications, an ANN, capable of predicting model parameters based on pre-disturbance conditions at the PCC and generation and load mix in the network, was designed for each group of responses associated with a common TF poles. Unlike in [89], in [90] the decoupling of DEM performance from the initial, pre-disturbance ADN operating point was achieved by using the deviation of voltage and real/reactive power at the PCC from their pre-disturbance values as DEM input and output, respectively. Similarity in the dynamic performance of different ADN operating points was assessed by comparing their responses to the same disturbance. For that purpose, for each operating point, a TF was developed using the deviation of measured voltage and real/reactive power at the PCC from their pre-disturbance values as input and output, respectively, and clusters of the outputs of TFs excited by the same input signal defined groups of operating conditions represented by a common model.

Black-box DEM for ADN in the form of the linear state-space model was proposed in [91]. Voltage and frequency at the PCC were the model inputs, while real and reactive power at the PCC were used as the outputs. The state-space model order was determined by plotting the Hankel singular values against model order, and selecting the model order corresponding to the significant drop in the singular value diagram. However, model parameters were estimated on the basis of a single ADN response, and model performance is highly affected by the type and location of a disturbance used for parameter estimation.

The approaches involving identification of dominant modes in network responses and developing model in the form of a sum of damped sinusoids were described in [42, 92-94]. Black-box models for small-disturbance stability studies were derived based on the combination of Prony analysis and non-linear least squares optimization for model parameter estimation. In [42, 94] it was assumed that ADN responses to small

disturbances can be represented by the sum of an initial step and a damped sinusoid response. On the other hand, in [92, 93] initial model order was chosen using the numerical algorithm for subspace state space system identification (N4SID) and singular value decomposition, respectively, while the final order was defined by further trial-and-error in order to minimize the mismatch between the measured/simulated responses and the responses generated by the equivalent. In order to increase the robustness of Prony terms to changes in pre-disturbance operating point and disturbance amplitude, linear correction factors for the amplitudes of Prony terms were introduced in [92].

In [83, 95-97] and [98] a feed forward ANN with tapped time delays and feedback from outputs, and a recurrent ANN (an ANN with a feedback from hidden units), respectively, were proposed as network equivalents. For all ANNs, real and imaginary parts of current at the boundary buses were ANN outputs. When it comes to input signals, different combinations of real and imaginary part of voltage and frequency at the boundary buses at the current time step as well as several (four or five) previous time steps represented ANN inputs. In addition, all ANN inputs and outputs were normalized with respect to their pre-disturbance steady state values to increase model robustness to changes in operating condition. Long Short Term Memory (LSTM) network, an ANN with LSTM cells and regular neurons in hidden layers, was used for equivalent ADN modelling in [99] (more information on LSTM structure is provided in Section 2.4.1.3). Separate ANNs, with voltage at the boundary bus at the current time step and four previous time steps as inputs, were developed for real and reactive power responses. Only converter-connected technologies were considered as generation sources in the test systems in [83, 95, 96, 98], whereas only SGs were present in the test network in [99]. Furthermore, all ANNs were trained and tested using a few network responses.

A feed forward ANN with tapped time delays and feedback from outputs was proposed in [100] for dynamic equivalent modelling of BESSs spatially distributed across an ADN. In addition to frequency and voltage at the PCC, the ANN used the information about the total production of PV systems (the only generation sources in the test ADN) and the reference BESS power output specified by the central entity (all BESSs in the system were characterized by the same operating point) as input signals. The ANN training and testing was performed on seven and two responses, respectively.

A random forest-based model was suggested in [80] for the equivalent ADN modelling in an attempt to avoid the overfitting issue common in ANN applications. Still, as in the case of the previously described ANN-based equivalents, the proposed modelling approach was trained and tested using a small number of network responses, and the model was not evaluated for different operating points or compared with an ANN-based equivalent (the ANN overfitting issue was the main reason for adopting the random forest-based approach).

Equivalent model (EM) for long-term voltage stability studies in the form of Hammerstein-Wiener model, which represents nonlinear system dynamics using nonlinear static functions and a linear TF, was described in [101]. Model input and output are voltage and real/reactive power at the PCC, respectively. EM validation was carried out on only three case studies (CSs). In addition, model performance is highly influenced by the chosen types of training disturbances, and model parameters are valid only for the operating point for which they were derived.

1.3.5 Summary of Past Work

So far, the focus of the research on HRES plants has been on optimal HRES plant sizing and operation with respect to economic costs, while the HRES plant dynamic performance has been commonly neglected. When it comes to the dynamic equivalent modelling of power plants and networks, even though a lot of work has been done in this area, it is still very challenging to derive equivalents that are suitable for various combinations of generation and storage technologies, and can reflect constant changes in system operation. Modal analysis-based models are adequate for small variations around the operating point used for model development, and thus require model redevelopment whenever there is a change in system operating condition. On the other hand, coherency-based modelling techniques can be used for power plants/networks containing only SGs as generation sources, which makes them unsuitable for plants/networks with RESs. Furthermore, modelling approaches developed for RES power plants are focused on plants with a single type of generation technology, and thus cannot be used for equivalent modelling of HRES plants.

System identification-based methods relying on measured/simulated system responses have demonstrated promising capabilities for deriving robust EMs of plants/networks with renewable generation and storage technologies for both small and large disturbance

stability studies. ANNs with feedback from the outputs or hidden units represent a popular technique for addressing the issue of equivalent modelling of ADNs and MGs, and they have shown a potential to be robust to changes in operating conditions.

The reported equivalent modelling methodologies (in particular those for large disturbance stability analysis) lack a thorough assessment of EM performance. The EMs described in the literature were developed and evaluated using a single or limited number of system operating points and disturbances, which limits the confidence in their adequacy for practical application, i.e., their ability to reliably represent the plant/network in system stability studies throughout the whole year. Few methodologies ([19-21, 42, 80, 87, 88, 90]) recognized that DEM parameter values could be different for different operating scenarios, but they did not provide the procedure/guidelines for selecting DEM parameters for an arbitrary system operating condition or require DEM parameter estimation/redevelopment whenever operating point changes. In addition, developing of DEMs for large disturbance stability studies was mainly based on system responses to three-phase short-circuit faults with zero fault impedance ([19, 20, 42, 80, 95, 96, 98, 100]). However, this type of short-circuit fault has the lowest probability of occurrence in real power systems. As a result, the derived models are adequate for the extreme, worst-case scenario in the system, and thus not capable to represent the typical, most probable system dynamic behaviour during the year.

The accuracy of all reported DEMs was assessed by comparing DEM power responses in time domain with the responses produced by the detailed system model or measured system responses, i.e., the shape of time domain responses was adopted as a criterion for evaluating model performance. However, when conducting large system stability studies, the accuracy of the overall system stability status/results is what is ultimately of importance. Due to complex interactions between system elements, power responses of the plant/network being equivalenced that have different shape in time domain might be associated with similar global system stability performance, which then lessens the significance of obtaining highly accurate DEM power responses. The equivalent modelling approach based on the provision of reliable overall system stability results could potentially provide smaller mathematical order and/or number of models required

for representing the plant/network in annual system stability simulations compared to the procedure focusing on the shape of time domain power responses.

As can be seen from the review of the previous work, the concept of HRES plant has been concerned about the combination of different technologies having the same grid connection point. In light of the appearance of virtual power plants (VPPs), i.e., the aggregators at distribution network (DN) level, one would assume that similar concept of aggregators could be brought up to TN level (more information on the VPP concept is given in Chapter 6 of the thesis). In this case, an aggregator at TN level could own various RES power plants located in different areas of the TN, which can be seen as a concept of geographically/spatially distributed HRES plant connected to the TN at more than one bus. As in the case of HRES plant with a single PCC, geographically distributed HRES plant should be able to provide stable and controllable power production, and thus enable the aggregator to choose the plant dispatch that would provide the highest revenue on markets. However, given that geographically distributed HRES plant is connected to different buses in the TN, its impact on the overall system dynamic performance is complex, and deciding on the plant dispatch without taking into account system stability limits might have a detrimental effect on system stability. The contribution of optimal economic dispatch of geographically distributed HRES plant to system stability has basically not been addressed at all, as the research on the concept of aggregators was mainly devoted to VPPs at DN level, and even then the most emphasis was on VPP operation that provides financial benefits to the aggregator/owner while the influence of VPPs on system stability was not particularly, if at all, considered.

1.4 Aims and Objectives of the Research

This thesis focuses on overcoming the identified shortcomings of the past work presented in the previous section. There are three aims of the research presented in the thesis. The first one is the development of the methodology for dynamic equivalent modelling of HRES plant from the perspective of the accuracy of the overall system stability results, while the second one involves the procedure for developing DEM of HRES plant that focuses on the shape of HRES plant power responses in time domain. Both methodologies are focused on transient stability studies and should result in models capable of representing HRES plant behaviour in transient stability simulations during the whole year. Finally, the third aim of the research is an exploratory study of the

contribution of geographically widely distributed HRES plant to the transient stability performance of the TN.

In order to fulfil the aims of the research, the following objectives have been defined:

- To propose the procedure for identifying typical annual HRES plant operating conditions in order to eliminate the requirement for investigating all possible plant operating points;
- To propose the computationally efficient procedure for identifying the most probable HRES plant performance in annual power system stability studies;
- To develop the methodology for equivalent modelling of HRES plants for transient stability studies from the perspective of the accuracy of the overall transient stability assessment. A system identification-based approach should be used for that purpose;
- To develop the methodology for equivalent modelling of HRES plants for transient stability studies from the perspective of the accuracy of the shape of HRES plant power responses in time domain. A system identification-based approach should be used for that purpose;
- To develop for both previously mentioned methodologies a practical procedure for identifying the adequate equivalent HRES plant representation at any time of the year that does not require model redevelopment whenever operating condition changes and uses the information available to system operators;
- To integrate the developed DEMs into DIgSILENT/PowerFactory, a commercially available software package for power system studies;
- To validate both methodologies on a wide range of system operating points and disturbances in DIgSILENT/PowerFactory environment;
- To compare the performance of DEMs developed using the two methodologies in terms of the accuracy in the shape of HRES plant power responses in time domain and the global system stability results. The purpose of this analysis is to investigate whether focusing on the shape of plant power responses in equivalent

modelling procedure is needed for the reliable overall transient stability assessment in practice;

- To perform the exploratory, probabilistic analysis on the impact of spatially widely distributed HRES plant on the transient stability of the TN for different RES penetration levels in the system.

1.5 Main Contributions of the Research

The major contributions of the work presented in the thesis are in the area of dynamic equivalent modelling of HRES plants for transient stability studies of the system. The following points summarise the main contributions of the research, with the references given in brackets indicating the author's research publications where the contributions were initially made (the full list of author's publications is given in Appendix E and F):

- The development of the computationally efficient procedure for determining the most probable HRES plant behaviour in power system stability studies throughout the year. The procedure is based on characteristic annual HRES plant operating scenarios defined by applying the unsupervised data mining method to historical HRES plant production dataset, which in turn eliminates the need for investigating all possible HRES plant operating conditions during the year. (E1, E4)
- The development of preliminary EMs of HRES plant for small-disturbance, transient, frequency, and long-term voltage stability studies. All modelling procedures aim to derive EMs capable of representing typical annual HRES plant behaviour in the relevant system stability study. EM development is based on the results of the procedure for determining the most probable annual HRES plant performance in the relevant system stability study. (E5, E8, E9)
- The development of the data-driven methodology for dynamic equivalent modelling of HRES plants for transient stability studies from the perspective of the overall system transient stability performance. This represents a departure from the previous work on DEMs of power plants and networks focusing on highly accurate modelling of power responses in time domain. In this research, HRES plant power responses resulting in similar transient stability status are simulated by a common DEM, regardless of dissimilarity in their shape in time

domain. The methodology results in a few low-order TF-based models capable of providing reliable global transient stability assessment of the system during the whole year. As a part of this methodology, the procedure for selecting the adequate model (from the previously developed set of models) at any time of the year knowing HRES plant operating scenario only is provided. (E1, E10)

- The development of the deep learning-based methodology for dynamic equivalent modelling of HRES plants for annual system transient stability studies that focuses on the shape of HRES plant power responses in time domain. Similar typical time domain HRES plant power responses in annual transient stability simulations are clustered and a DEM in the form of a deep ANN (LSTM network) is developed for each group of responses. Unlike in the past work on ANN-based dynamic equivalents, the deep learning-based modelling procedure includes an efficient way of training the LSTM-based DEM structure on large datasets. The methodology also includes the procedure for selecting the most suitable DEM (from the set of previously developed models) at any time of the year based on the information about power outputs of individual plants within the HRES plant, which ensures the use of a small set of models for simulating HRES plant power responses in annual transient stability studies. (E3, E6, E7)
- Indication of potential challenges that geographically distributed HRES plant can pose to transient stability of the TN. The results of this exploratory, probabilistic study pave the way to more comprehensive assessment of the influence of the dispatch of spatially widely distributed HRES plant on the overall TN transient stability performance. (E11)

1.6 Thesis overview

The thesis consist of seven chapters. The overview of all chapters following this introductory chapter (Chapter 1) is provided below.

Chapter 2 Techniques for Dynamic Equivalent Modelling of Power Plants and Networks

The chapter presents an overview of three groups of methods for equivalent modelling of power plants and networks (modal analysis-, coherency- and system identification-based methods), indicating their main advantages and disadvantages. Given that developing EMs adequate for a wide range of system operating scenarios requires the analysis of large datasets, a comprehensive review of the unsupervised data mining methods, clustering algorithms, is provided as well. The major characteristics of the representatives of five categories of clustering methods are presented. Furthermore, the key stages in the clustering procedure and typical difficulties associated with the application of clustering algorithms are described.

Chapter 3 Probabilistic Analysis and Modelling of HRES Plant for System Stability Studies

This chapter presents the methodology for identifying the typical annual HRES plant performance in power system stability studies. The procedure relies on the identification of characteristic annual HRES plant operating scenarios using historical HRES plant production data and unsupervised clustering algorithm, and on a probabilistic MC approach for addressing the uncertainties in the power output and location of individual plants in the HRES plant. In addition, the preliminary structures of EMs of HRES plant for small-disturbance, transient, frequency and long-term voltage system stability studies (designed using the results of the aforementioned procedure) are proposed. A CS using the HRES plant comprising six renewable generation and storage technologies illustrates the application of the procedure and EM development for all four system stability studies.

Chapter 4 Data-driven Equivalent Modelling of HRES Plant for Power System Transient Stability Studies

The fourth chapter of the thesis introduces the methodology for development of DEM of HRES plants for transient stability studies from the perspective of the overall transient stability assessment. All stages in the proposed methodology, from the generation of the most probable annual HRES plant power responses to the identification of responses associated with similar transient stability status of the system and model development in the form of a low-order TF, are presented in detail. The selection of the adequate model

at any time of the year is described as well. The methodology is validated on two HRES plant configurations connected to the same IEEE 9-bus network model for a wide range of system operating conditions. The accuracy of the developed models is compared with the performance of a common representation of RESs in system stability simulations – a negative constant power load model (NCPLM). Furthermore, the sensitivity of the model performance to the historical production dataset features (the size, sampling rate and missing data for individual technology(ies)) is investigated. An approach for generating artificial historical production data in the case of data unavailability is proposed.

Chapter 5 Deep Learning-based Equivalent Modelling of HRES Plant for Power System Transient Stability Studies

The chapter describes the methodology for developing DEM of HRES plants for transient stability studies from the perspective of the similarity between HRES plant power responses at the PCC in time domain produced by DEM and the detailed model. The equivalent modelling procedure relies on the identification of the groups of similar most probable annual HRES plant power responses. The procedure for computationally efficient design of the deep ANN-based DEM structure using a large dataset, and a practical approach for selecting the adequate DEM at any time of the year knowing only HRES plant operating conditions (the power output of individual RESs) are presented. The methodology is evaluated on the test HRES plant with three renewable generation technologies integrated into the IEEE 9-bus network model. The performance of the deep learning-based DEMs is compared with the data-driven models developed in Chapter 4 (for the same test system) to investigate whether focusing on the shape of power responses in equivalent modelling is required for obtaining reliable overall transient stability assessment of the system.

Chapter 6 Limitations of the Reliance on Assessment of the Contribution of Spatially Distributed HRES Plant to Real System Operation

The focus of this chapter is on geographically distributed HRES plant, i.e., the plant with multiple connection buses to the TN. Typical principles of operation of VPPs at DN level, which can be applied to spatially distributed HRES plants at TN level, are discussed. The exploratory study on the potentially negative influence of optimal economic dispatch of

HRES plant on the transient stability of the TN is presented. The CS uses a simplified representation of the interconnected system of four real European TNs with an HRES plant containing PV plants and WFs spread across the whole test system.

Chapter 7 Conclusions and Further Work

The final chapter of the thesis presents the main conclusions of the research, and discusses suggestions for further improvement of the presented methodologies and exploratory studies.

2 Techniques for Dynamic Equivalent Modelling of Power Plants and Networks

2.1 Introduction

Following the growth in the installation capacity of RESs, electric power systems have increased in size and complexity. Representing whole plants/networks in detail in system stability studies is becoming highly impractical and in some cases even impossible due to the unavailability of necessary data and/or data protection policy that prohibits the exchange of full-scale models between different network operators. EMs of plants/networks have been seen as a promising solution to the above-mentioned issues. The basic principle of equivalent modelling is to simplify the detailed model of a plant/network in such a way that the desired level of accuracy in its behaviour at boundary buses (when compared to the detailed model responses) is preserved. EM development from the perspective of boundary buses is justified when only the responses of the plant/network at boundary buses are considered relevant for performing system studies. The chapter provides an overview of the techniques for equivalent modelling of power plants and networks. Methods for EM development can be divided into three major groups: modal analysis-, coherency- and system identification-based methods, with the first two dominantly used for equivalent modelling of plants and networks containing only SGs as generation sources.

A number of equivalent modelling approaches of RES power plants and networks containing RESs that were reported in the literature (a review of the work has been presented in Section 1.3.3 and 1.3.4) requires large datasets of measured or simulated responses of the considered system to develop EMs suitable for a large number of system conditions. In order to improve the efficiency of modelling and analysis of power systems, adequate data pre-processing should be carried out. Over the years, various data mining methods have been proposed in order to address the challenges of large database analysis. Clustering methods, as unsupervised data mining techniques, have gained popularity due to their ability to identify patterns/homogenous groups in datasets, and thus minimize the amount of data that have to be considered in a given analysis. This chapter revises the most widely used clustering algorithms, with a focus on the clustering methods suitable for analysing the responses of dynamic systems (i.e., time series data). In addition, the main stages in clustering process as well as common issues related to the practical application of data clustering methods are discussed.

2.2 Modal Analysis-based Equivalent Modelling Methods

The objective of most equivalent modelling techniques based on modal analysis is to reduce the order of linearized state-space model of the analysed system [42, 102] (*Note*: The modal-analysis based techniques described in this chapter assume that all system eigenvalues are distinct.):

$$\begin{aligned} \Delta\dot{x}(t) &= A\Delta x(t) + B\Delta u(t) \\ \Delta y(t) &= C\Delta x(t) + D\Delta u(t) \\ x(0) = x_0, u(0) &= u_0, y(0) = y_0 \end{aligned} \quad , \tag{2.1}$$

where $u(t)$ and $y(t)$ are the inputs and outputs of the system, respectively, $x(t)$ is the vector of state variables, Δ stands for a small deviation, x_0 are the initial conditions for state variables, u_0 and y_0 are the input and output of the system corresponding to x_0, A is the state matrix, B is the input matrix, C is the output matrix, D is the feedforward matrix.

The modes that are less damped, that is, those that persist longer, are the ones that determine the overall system performance. Therefore, the reduction of the order of the linearized full-scale model is achieved by neglecting modes that do not have a significant influence on system response. Different procedures for identifying non-dominant modes have resulted in different modal analysis-based techniques.

2.2.1 Modal Truncation

Modal truncation technique relies on the calculation of all eigenvalues of the system and elimination of the non-dominant modes by converting the system from (2.1) into the system with diagonal state matrix [43, 79]. The first step in reducing the order of the system given by (2.1) is the transformation of state variables *x* into modal variables *z* using the matrix *P* whose columns are the right eigenvectors of the state matrix *A*:

$$\Delta x(t) = P\Delta z(t). \tag{2.2}$$

Using the previous transformation, the system from (2.1) transforms to:

$$\begin{matrix} \dot{\Delta z}(t) = \Lambda\Delta z(t) + B'\Delta u(t) \\ \Delta y(t) = CP\Delta z(t) + D\Delta u(t) \end{matrix}, \tag{2.3}$$

where $\Lambda = P^{-1}AP$ and $B' = P^{-1}B$. The elements of the diagonal matrix Λ are the eigenvalues of the original state matrix of the system, *A*.

Given that the matrix Λ is a diagonal matrix, there is no coupling between modal variables (as it is the case with the original states) and the expression for modal variables from (2.3) becomes:

$$\Delta z(t) = (I - e^{\Lambda t})\Lambda^{-1}B'\Delta u(t). \tag{2.4}$$

The state-space model reduction is achieved by neglecting non-dominant modal variables, that is, modal variables assumed to reach steady state almost instantaneously and modal variables that can be assumed to be zero. After identifying the non-dominant modes, the set of differential equations from (2.3) can be rearranged as follows:

$$\begin{bmatrix} \dot{\Delta z}_r(t) \\ \dot{\Delta z}_{nr1}(t) \\ \dot{\Delta z}_{nr2}(t) \end{bmatrix} = \begin{bmatrix} \phi_r & 0 & 0 \\ 0 & \phi_{nr1} & 0 \\ 0 & 0 & \phi_{nr2} \end{bmatrix} \begin{bmatrix} \Delta z_r(t) \\ \Delta z_{nr1}(t) \\ \Delta z_{nr2}(t) \end{bmatrix} + \begin{bmatrix} B'_r \\ B'_{nr1} \\ B'_{nr2} \end{bmatrix} \Delta u(t), \tag{2.5}$$

where $z_r(t)$ are modal variables that are retained in the simplified system model, $z_{nr1}(t)$ are modal variables assumed to reach steady state instantaneously, $z_{nr2}(t)$ are modal variables assumed to be zero, ϕ_r, ϕ_{nr1} and ϕ_{nr2} are the submatrices of the diagonal matrix Λ, B'_r, B'_{nr1} and B'_{nr2} are the submatrices of the matrix B'.

Therefore, the reduced order of the set of differential equations from (2.3) has the following form:

$$\Delta \dot{z}_r(t) = \phi_r \Delta z_r(t) + B'_r \Delta u(t). \tag{2.6}$$

In order to derive the expression for the reduced order system output equation, the transformation from (2.2) can be written as follows:

$$\begin{bmatrix} \Delta x_r(t) \\ \Delta x_{nr1}(t) \\ \Delta x_{nr2}(t) \end{bmatrix} = \begin{bmatrix} \alpha_r & \alpha_{nr1} & \alpha_{nr2} \\ \beta_r & \beta_{nr1} & \beta_{nr2} \\ \gamma_r & \gamma_{nr1} & \gamma_{nr2} \end{bmatrix} \begin{bmatrix} \Delta z_r(t) \\ \Delta z_{nr1}(t) \\ \Delta z_{nr2}(t) \end{bmatrix}, \tag{2.7}$$

where $x_r(t)$ are original state variables that are retained in the simplified system model, $x_{nr1}(t)$ and $x_{nr2}(t)$ are original state variables that are neglected in the simplified system model, and α_r, α_{nr1}, α_{nr2}, β_r, β_{nr1}, β_{nr2}, γ_r, γ_{nr1}, γ_{nr2} are the submatrices of the transformation matrix *P*.

Taking into account $z_{nr2}(t) = 0$, and combining the expression for $x_r(t)$ from (2.7) and the expression for $\Delta z_{nr1}(t)$ obtained from (2.5) by adopting $\dot{z}_{nr1}(t) = 0$ for a step input, the system output equation in the reduced order system model becomes:

$$\Delta y(t) = C \Delta x_r(t) + D \Delta u(t), \tag{2.8}$$

$$\Delta y(t) = C[\alpha_r \Delta z_r(t) - \alpha_{nr1} \phi_{nr1}^{-1} B'_{nr1} \Delta u(t)] + D \Delta u(t), \tag{2.9}$$

$$\Delta y(t) = C' \Delta z_r(t) + D' \Delta u(t), \tag{2.10}$$

where $C' = C\alpha_r$ and $D' = D - C\alpha_{nr1}\phi_{nr1}^{-1} B'_{nr1}$.

Therefore, the reduced order model of the system is given by (2.6) and (2.10).

2.2.2 Balanced Realization

Balanced realization technique uses controllability and observability properties of the system to perform the state-space model reduction. The controllability of the system represents the ability of the system to change the system state from the initial one to any other by exciting the system by certain input signals [78]. In other words, it indicates the strength of coupling between input signals and state variables. The controllability gramian of the system determines the minimum input energy required for changing the

system state. On the other hand, the observability of the system is a measure of the state-to-output connection [78]. The observability gramian of the system defines the output energy produced by the state variables only (input signals are assumed to be zero). The expressions for the controllability and observability gramian are the solutions of the Lyapunov equations [42]:

$$\begin{aligned} AW_C + W_C A^T + BB^T = 0 \\ A^T W_O + W_O A + C^T C = 0 \end{aligned} \tag{2.11}$$

where W_C and W_O are the controllability and observability gramian of the system, respectively.

Applying linear coordinate transformation to system matrices and state variables (similar to the balanced truncation approach), while preserving inputs and outputs of the system, the state-space model can be converted into the model with equal observability and controllability gramians (so-called a balanced state representation) [78]:

$$\widetilde{W_C} = \widetilde{W_O} = \Sigma = diag(\sigma_1, \sigma_2, \dots, \sigma_n), \tag{2.12}$$

$$\sigma_i = \sqrt{\lambda_i(W_C W_O)}, \tag{2.13}$$

where $\widetilde{W_C}$ and $\widetilde{W_O}$ are the controllability and observability gramian calculated for the transformed state-space model, σ_i is the *i*-th Hankel singular value, $\lambda_i(W_C W_O)$ is the *i*-th eigenvalue of the product of two gramians W_C and W_O, and *n* is the number of the system states.

The computation of Hankel singular values provides the information about the controllability and observability of the states. Small Hankel singular values correspond to weakly controllable and observable state variables, and neglecting these states results in the reduced-order system model.

2.2.3 Optimal Hankel Norm

Similar to the balanced realization method, the optimal Hankel norm technique is based on the calculation of Hankel singular values [42, 78, 83]. The order of the reduced model is chosen using the key property of Hankel values. Namely, the maximum amplitude of

the difference between the transfer function of the detailed model and the *k*-th order reduced model, for all frequencies, is determined by the *k*+1-th Hankel singular value:

$$\|H(s) - H_k(s)\| \leq \sigma_{k+1}, \tag{2.14}$$

where $H(s)$ and $H_k(s)$ is the transfer function of the detailed model and the *k*-th order reduced model, respectively. Hence, the suitable model order can be selected on the basis of the known worst-case error.

2.2.4 Singular Perturbation Theory

The singular perturbation theory is based on the division of states into slow and fast state variables and their calculation in different time domains [103]. The main assumptions of the approach are:

- slow state variables are constant during fast transients;
- fast states have reached their quasi-steady state values by the time the change of slow states becomes significant.

The model with separated fast and slow state variables can be expressed in the following form [103]:

$$\begin{matrix} \frac{dx}{dt} = f(x,z,t),\ x(t_0) = x_0 \\ \frac{dz}{dt} = G(x,z,t),\ z(t_0) = z_0 \end{matrix}, \tag{2.15}$$

where *x*, *z*, x_0 and z_0 are slow states, fast states, and the initial values of slow and fast states, respectively.

The singular perturbation theory relies on two time scales: one time scale (t) is used for slow states, and the second one (τ) for fast state variables. The connection between two time scales is established through a small positive parameter ε:

$$\tau = \frac{t - t'}{\varepsilon}, \tag{2.16}$$

where t' in *t*-time scale corresponds to τ=0.

Smaller parameter ε results in longer time period τ for the same interval $(t - t')$, i.e., it provides fast states with more time to reach their quasi-steady state values, while the

assumption that the time interval $(t - t')$ is short enough to consider slow states constant remains valid. The transformation of (2.15) into the system suitable for two-time scale approach is carried out by assuming that the dynamics of fast states is 1/ε times faster than the dynamics of slow states. Consequently, the derivatives of fast states are 1/ε times larger than derivatives of slow states. Therefore, the model (2.15) can be transformed into the following form:

$$g = \varepsilon G, \tag{2.17}$$

$$\begin{matrix} \frac{dx}{dt} = f(x,z,t),\ x(t_0) = x_0 \\ \varepsilon\frac{dz}{dt} = g(x,z,t),\ z(t_0) = z_0 \end{matrix}, \tag{2.18}$$

where g and f are the functions of the same order of magnitude.

Assuming that $\varepsilon \to 0$, the model in t-time scale, that is, the quasi-steady state model, has the following form:

$$\begin{matrix} \frac{dx_s}{dt} = f(x_s,z_s,t),\ x_s(t_0) = x_0 \\ 0 = g(x_s,z_s,t) \end{matrix}, \tag{2.19}$$

where x_s and z_s are quasi-steady states of x and z variables, respectively.

The parts of state variables in τ-time domain can be obtained using the following model:

$$\begin{matrix} \frac{dx}{d\tau} = \varepsilon f(x,z,t' + \varepsilon\tau) \\ \frac{dz}{d\tau} = g(x,z,t' + \varepsilon\tau) \end{matrix}. \tag{2.20}$$

In the case of $\varepsilon \to 0$, states x are constant in τ-time domain. Adopting $t' = t_0$, the following equation for fast states in τ-time domain can be obtained:

$$\frac{dz_f}{d\tau} = g\big(x_0, z_s(t_0) + z_f(\tau), t_0\big),\ z_f(0) = z(t_0) - z_s(t_0), \tag{2.21}$$

where z_f is the part of z-variables in τ-domain.

Finally, the expressions for slow and fast state variables are as follows:

$$\begin{aligned} x(t) &\cong x_s(t) \\ z(t) &\cong z_s(t) + z_f\left(\frac{t-t_0}{\varepsilon}\right) \end{aligned} \quad (2.22)$$

2.2.5 Discussion

Modal analysis-based methods have a strong mathematical background and can provide the information about all types of oscillations in the system [91]. However, these techniques use linearized detailed model of the system, which makes them unsuitable for large disturbance system studies as well as for complex power systems with a number of renewable generation and storage technologies due to the problem of data availability and high computational burden associated with the development of the unreduced system model [91]. Furthermore, all four modal analysis-based methods require previous experience/knowledge about the dynamics of system variables (differentiation between dominant and non-dominant modes in the case of modal truncation, differentiation between small and large Hankel singular values in the case of balanced realization and optimal Hankel norm, decomposition of states into fast and slow in the case of singular perturbation theory), and are thus very application dependant [83, 91].

2.3 Coherency-based Equivalent Modelling Methods

Coherency-based methods represent a typical approach for equivalent modelling of a group of SGs. Unlike the modal analysis-based techniques, coherency-based EM is based on nonlinear, physical, machine model [42, 83, 104]. The application of coherency-based methods consists of three major steps [42, 83]:

1. Identification of coherent SGs
2. Development of an EM for a group of coherent SGs
3. Aggregation of generator buses.

2.3.1 Identification of Coherent Synchronous Generators

In order to simplify coherency analysis, the linearized system model, classical SG model and the decoupling between real and reactive power in network equations are commonly adopted [52]. The simplifications are justified by assuming that coherency between SGs is not affected by the size of the disturbance or SG model order (increasing the order of SG model does not have a significant impact on the natural frequency and mode shapes

of the swing curves), and that there is a high ratio of reactance/resistance of the lines of transmission systems [52].

For a particular disturbance, terminal buses of two generators are considered to be electrically coherent if the ratio of their complex bus voltages is constant [105]:

$$\frac{\underline{V_i}(t)}{\underline{V_j}(t)} = \frac{V_i(t)}{V_j(t)} e^{j\left(\theta_i(t)-\theta_j(t)\right)} = \frac{V_i(t_0)}{V_j(t_0)} e^{j\left(\theta_i(t_0)-\theta_j(t_0)\right)} = \underline{\vartheta_i} = const, \text{ for all } t \geq t_0, \quad (2.23)$$

where $\underline{V_i}(t)$ and $\underline{V_j}(t)$ are complex voltages at the terminal buses of the *i*-th and *j*-th SG, respectively, $V_i(t)$ and $V_j(t)$ are the magnitudes of voltages at the terminal buses of the *i*-th and *j*-th SG, respectively, $\theta_i(t)$ and $\theta_j(t)$ are the phase angles of voltages at the terminal buses of the *i*-th and *j*-th SG, respectively, t_0 is the time of the occurrence of the disturbance.

Given that the classical SG model (a constant generator electromotive force behind generator reactance) is used for representing SGs, coherency criterion (2.23) simplifies to (2.24) for the internal buses of two SGs [105]:

$$\delta_i(t) - \delta_j(t) = \delta_i(t_0) - \delta_j(t_0) = c, \text{ for all } t \geq t_0, \quad (2.24)$$

where $\delta_i(t)$ and $\delta_j(t)$ are the rotor angles of the *i*-th and *j*-th SG, and *c* is a constant. Expression (2.24) is known as the electromechanical coherency. The electromechanical coherency condition can also be given by (2.25):

$$\Delta\delta_i(t) = \Delta\delta_j(t), \text{ for all } t \geq t_0, \quad (2.25)$$

where $\Delta\delta_i(t) = \delta_i(t) - \delta_i(t_0)$ and $\Delta\delta_j(t) = \delta_j(t) - \delta_j(t_0)$.

In practice, (2.25) can never be satisfied, so a tolerance parameter has to be introduced [105]:

$$\left|\Delta\delta_i(t) - \Delta\delta_j(t)\right| \leq \varepsilon, \text{ for all } t \geq t_0, \quad (2.26)$$

where ε is the tolerance parameter corresponding to a small positive number (typical values are (5-10)° [106]). Thus, two SGs are electromechanically coherent if their rotor angle curves are similar in shape.

The three main techniques for assessing the coherency between SGs are [42, 83]:

- Time domain approach;
- Weak-link coherency identification;
- Slow coherency method.

Time domain approach creates the groups of coherent SGs by identifying similarity in time domain responses of their rotor angles or speeds after a given disturbance [52, 83]. The responses can be obtained in simulation environment or can correspond to real power system measurements [52, 83, 104, 107]. The other two methods, weak-link and slow coherency, are analytical methods, and can establish the groups of coherent SGs independently of the disturbance [83].

Weak-link coherency identification is based on reordering the linearized system state matrix in the following way [54]:

$$\frac{d}{dt}\begin{bmatrix}X_1\\X_2\end{bmatrix}=\begin{bmatrix}A_{11} & \varepsilon A_{12}\\ \varepsilon A_{21} & A_{22}\end{bmatrix}\begin{bmatrix}X_1\\X_2\end{bmatrix}+\begin{bmatrix}B_1 & 0\\ 0 & B_2\end{bmatrix}\begin{bmatrix}U_1\\U_2\end{bmatrix}, \tag{2.27}$$

where X_1 and X_2 are vectors of state variables of the machines in subsystem 1 and subsystem 2, respectively, and ε is a small positive parameter ($\varepsilon \approx 0$). For ε=0, the system is divided into two completely decoupled subsystems.

The aim of the method is to decompose the system in such a way that the obtained subsystems are as weakly electromechanically connected as possible, while each subsystem consists of strongly coherent machines. The measure of the strength of electromechanical connection between subsystems is assessed using the coupling factor, which is calculated as the ratio of the sum of the norms of submatrices in the off-diagonal area and the sum of the norms of submatrices in the diagonal area of the state matrix. The smaller the coupling factor is, the smaller electromechanical connection between the subsystems is. The coupling factor is calculated for all possible system decompositions into two subsystems, and the minimum coupling factor is defined for each structure of system decomposition (only one SG in subsystem 1 and the remaining machines in

subsystem 2; two SGs in subsystem 1 and the remaining machines in subsystem 2, etc.). The system decomposition resulting in the minimum factor for the current analysed structure of system decomposition represents a basis for identifying the best decomposition for the following structure, i.e., the difference between the group of machines in subsystem 1 for the following and current structure is in only one SG. The method produces the coupling graph by plotting the minimum coupling factor for each investigated structure of system decomposition against the number of the machine added to the first subsystem in that particular system decomposition. The local minima of the graph divide the system into weakly coupled subsystems.

The main assumption of the third coherency-based method, slow coherency identification, is that groups of coherent SGs are swinging against each other with respect to slower oscillatory modes, while generators within the same group are oscillating against each other with respect to higher frequency modes [53, 108]. The method computes eigenvalues of the linearized state-space system model with SGs represented using the classical model. A matrix of right eigenvectors for the *r* smallest eigenvalues in terms of magnitude is determined (the choice of *r* defines the number of coherent groups), and then it is reduced to the components of the right eigenvectors associated with SG rotor angles. The *r* most linearly independent rows in the matrix define reference SGs for *r* coherent groups. Given that SGs in the same coherent group have similar mode shapes with respect to slow modes, the remaining (non-reference) SGs are allocated to coherent groups according to the similarity between their mode shapes for the relevant *r* slow modes and the corresponding mode shapes of the referent machines.

2.3.2 Development of an Equivalent Model for a Group of Coherent Synchronous Generators

Following the identification of groups of coherent SGs, each group is represented by a single equivalent machine developed using a classical or a detailed aggregation approach. The former relies on the classical SG model for modelling the equivalent generator [105]. The mechanical and electrical power of the equivalent machine are equal to the sum of mechanical and electrical power of all SGs in the group, respectively, and all coherent SGs are characterized by the same rotor speed (as if they are on the same shaft). The swing equation of the equivalent SG is given by (2.28) and (2.29):

$$M_{eq}\frac{dw}{dt} = P_{m,eq} - P_{e,eq} - D_{eq}(w-1), \tag{2.28}$$

$$M_{eq} = (\sum_{i=1}^{n} M_i),\ P_{m,eq} = \left(\sum_{i=1}^{n} P_{m,i}\right),\ P_{e,eq} = \left(\sum_{i=1}^{n} P_{e,i}\right),\ D_{eq} = (\sum_{i=1}^{n} D_i), \tag{2.29}$$

where w is the rotor speed of the equivalent SG, M_{eq}, $P_{m,eq}$, $P_{e,eq}$ and D_{eq} are the inertia coefficient constant, mechanical power, electrical power and damping coefficient of the equivalent SG, respectively, M_i, $P_{m,i}$, $P_{e,i}$ and D_i are the inertia coefficient constant, mechanical power, electrical power and damping coefficient of the *i*-th SG, respectively, and *n* is the number of coherent generators in the group.

The transient reactance of the equivalent generator ($X'_{d,eq}$) is calculated as a parallel connection of reactances of individual SGs [83]:

$$X'_{d,eq} = \frac{1}{\sum_{i=1}^{n}\frac{1}{X'_{d,i}}}, \tag{2.30}$$

where $X'_{d,i}$is the transient reactance of the *i*-th generator in the group.

The detailed aggregation approach takes into consideration control systems of generators (turbine governors, excitation systems, power system stabilisers). If coherent generators are equipped with different types of control systems, the aggregate controller can be derived for each type separately or a simplified structure of a control device suitable for all types can be used [49, 109]. When it comes to the determination of the parameters of the equivalent controllers, iterative non-linear optimization techniques as well as ANNs are most commonly applied [83]. The estimated parameters should provide a satisfactory match between the responses (in time or frequency domain) produced by the reduced and detailed model of the coherent group of SGs.

2.3.3 Aggregation of Generator Buses

The final stage in the application of coherency–based equivalencing methods is the aggregation of generator buses, which is performed using Zhukov's method [105]. Zhukov's method eliminates the terminal buses of individual coherent generators and replaces them with a single equivalent bus (the illustration of the method is presented in Figure 2.1). The process of network reduction relies on two requirements [105]:

- the currents and voltages at the retained buses in the network have to remain the same as in the detailed network model, and

- the power injection at the equivalent bus has to be equal to the sum of individual power injections at the aggregated (eliminated) buses.

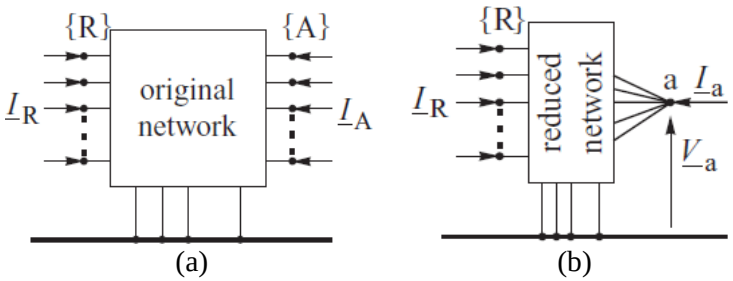

Figure 2.1 Network reduction using Zhukov's method: (a) the original detailed network ({A} and {R} refer to the aggregated/eliminated and retained buses, respectively); (b) the reduced network (adopted from [105])

The change in network structure can be described as follows:

$$\begin{bmatrix} \underline{I}_R \\ \underline{I}_A \end{bmatrix} = \begin{bmatrix} \underline{Y}_{RR} & \underline{Y}_{RA} \\ \underline{Y}_{AR} & \underline{Y}_{AA} \end{bmatrix} \begin{bmatrix} \underline{V}_R \\ \underline{V}_A \end{bmatrix}, \tag{2.31}$$

$$\begin{bmatrix} \underline{I}_R \\ \underline{I}_a \end{bmatrix} = \begin{bmatrix} \underline{Y}_{RR} & \underline{Y}_{Ra} \\ \underline{Y}_{aR} & \underline{Y}_{aa} \end{bmatrix} \begin{bmatrix} \underline{V}_R \\ \underline{V}_a \end{bmatrix} = \begin{bmatrix} \underline{Y}_{RR} & \underline{Y}_{RA}\underline{\vartheta} \\ \underline{\vartheta}^{*T}\underline{Y}_{AR} & \underline{\vartheta}^{*T}\underline{Y}_{AA}\underline{\vartheta} \end{bmatrix} \begin{bmatrix} \underline{V}_R \\ \underline{V}_a \end{bmatrix}, \tag{2.32}$$

where: $\underline{I}_R$ and $\underline{V}_R$ is the current injection and voltage at the retained buses, respectively;

$\underline{I}_A$ and $\underline{V}_A$ is the current injection and voltage at the eliminated buses, respectively;

$\underline{I}_a$ and $\underline{V}_a$ is the current injection and voltage at the equivalent bus, respectively;

$\underline{Y}_{RR}$ is the self-admittance matrix of the retained system calculated using the detailed network model;

$\underline{Y}_{RA}$ is the mutual-admittance matrix of the retained system calculated using the detailed network model;

$\underline{Y}_{AA}$ is the self-admittance matrix of the eliminated system calculated using the detailed network model;

$\underline{Y}_{AR}$ is the mutual-admittance matrix of the eliminated system calculated using the detailed network model;

$\underline{Y}_{Ra}$ is the mutual-admittance matrix of the retained system calculated using the reduced network model (a column matrix);

$\underline{Y}_{aR}$ is the mutual-admittance matrix of the equivalent bus calculated using the reduced network model (a row matrix);

$\underline{Y}_{aa}$ is the self-admittance of the equivalent bus calculated using the reduced network model;

$\underline{\vartheta}$ is the vector of voltage transformation ratios between the eliminated buses and equivalent bus, $\underline{\vartheta} = \underline{V}_a^{-1}\underline{V}_A$.

The expressions for the submatrices in the reduced network model can be obtained on the basis of the mathematical formulation of the two requirements for the network reduction process:

$$\underline{Y}_{RR}\underline{V}_R + \underline{Y}_{RA}\underline{V}_A = \underline{Y}_{RR}\underline{V}_R + \underline{Y}_{Ra}\underline{V}_a, \tag{2.33}$$

$$\underline{V}_a\underline{I}_a^* = \underline{V}_A^T\underline{I}_A^*. \tag{2.34}$$

The vector $\underline{\vartheta}$ is determined by the voltage angle at the equivalent bus, which can be calculated as follows [105]:

$$\theta_a = \frac{\sum_{i\in\{A\}} S_i\theta_i}{\sum_{i\in\{A\}} S_i}, \tag{2.35}$$

where θ_a is the voltage angle at the equivalent bus, S_i is the apparent power injection at the *i*-th bus, θ_i is the voltage angle at the *i*-th bus, and $\{A\}$ is a set of buses eliminated in the process (terminal buses of individual generators).

Given that the admittances of the reduced network model depend on the transformation ratio $\underline{\vartheta}$, and thus on network operating condition, the reduced network model is valid for another operating point if the transformation ratios are the same for both conditions [105].

2.3.4 Discussion

Above-described coherency-based techniques rely on the swing curves of generators, and thus cannot be applied to converter-connected renewable generation and storage

technologies. Over the years, various coherency-based approaches adapted to converter-connected units have been used for equivalent modelling of RES power plants consisting of a single generation technology type [63]. Namely, as coherency cannot be established on the basis of rotor angle trajectories, similarity between generators in RES plants is assessed according to their real power production, the parameters of primary energy source (e.g., wind speed in the case of wind generators, solar irradiance in the case of PV systems), structure and parameters of control systems, etc. So far, there has been no agreement on the most suitable coherency criteria for each of the types of converter-connected technologies. Following the identification of coherent units, groups of coherent generators are replaced by a single EM, as in the case of conventional coherency-based methods. EM parameters can be determined by scaling-up the model of individual units (in this case it is assumed that individual units are represented by the same model) or estimated in an optimization procedure that minimizes the difference between the responses produced by the detailed model and EM of the plant.

2.4 System Identification-based Equivalent Modelling Methods

System identification-based approach develops EMs of power plants and networks using measured or simulated responses at their boundary buses. These methods are not limited to a particular generation technology (unlike the coherency-based techniques) and require less information about the analysed system compared to modal analysis-based approaches, which makes them suitable for modern systems containing a large number of converter-interfaced units. The equivalent modelling procedure consists of three stages:

1. Selection of EM structure
2. Estimation of EM parameters
3. Validation of EM.

2.4.1 Selection of Equivalent Model Structure

Depending on the amount of knowledge about the analysed system, EM representation can be in the form of [42, 83, 91, 110]:

- a white-box model,
- a grey-box model, or
- a black-box model.

The white-box model is in fact a detailed mathematical model of the system that includes the models of and relationships between all system components, and thus can be developed only when all data about the system are available. As in the case of the white-box modelling, the grey-box method requires a physical insight into the investigated system, but the amount of data needed is much smaller compared to the white-box approach. In the case of power system modelling, the main network/plant characteristics in terms of topology and major devices usually have to be known and the structure of the grey-box model then corresponds to the combination of physical models of the most important devices in the system. Given that grey-box models are physically intuitive, this type of equivalents is often considered to be practical for the implementation in standard power system software packages [26].

In the case of black-box approach, model structure has no resemblance to physical properties of the system. The focus is only on obtaining high match between the responses of the detailed and equivalent model at the boundary buses, without taking into account the physical structure of the system. Given that measured/simulated responses at the boundary buses of the system are the only prerequisite for the application of the method, this type of equivalent modelling can be used when there is a lack of data about the system. The detailed model of the system is replaced by an adequate mathematical model (e.g., autoregressive-moving-average model with exogenous input, autoregressive model with exogenous inputs, transfer function, state-space model) with suitably chosen input and output signals [91, 110]. In case the analysed system cannot be represented by any mathematical form, ANNs, as a proven powerful tool for time series forecasting, are usually used to model the system. ANNs can learn from experience and thus are capable of predicting system outputs for the unknown input signals. Power plants are dynamic systems, and their response at the current time step is influenced by the current input signals as well as the past behaviour of the plant [98]. Therefore, classical feed-forward ANNs are not adequate for modelling dynamic systems as their outputs are determined by the input signals at the current time step only. On the other hand, recurrent ANNs with feedback from hidden units or output signals can use the information from the past to

predict the current system output. Still, ANNs are prone to overfitting, there is no formal methodology for defining their architecture and they require large amount of the training data [111]. The following sections discuss typical ANNs used for dynamic equivalent modelling of power plants and networks.

2.4.1.1 Nonlinear Autoregressive with Exogenous Inputs Neural Network

A nonlinear autoregressive with exogenous inputs (NARX) network is one of the simplest ANNs for development of EMs of dynamic systems. The operation of the NARX network corresponds to the discrete-time nonlinear NARX model [100, 112]:

$$y_t = G\begin{pmatrix} x_t, x_{t-1}, \dots, x_{t-n_x} \\ y_{t-1}, \dots, y_{t-n_y} \end{pmatrix}, \tag{2.36}$$

where x_t and y_t are the network input and output at time step *t*, respectively, n_x and n_y are the input and output time delays, respectively, and *G* is the nonlinear ANN mapping function.

The NARX network architecture is based on several hidden layers of neurons (a feed-forward ANN) and a feedback loop from the output. The first hidden layer is fed by the exogenous input (signals originating outside the network) at the current time step, and two time-delay-line (TDL) memories containing past values of network input and output signals (see Figure 2.2 (a)). Two TDL memories store the information about the past behaviour of the system, and thus make NARX networks suitable for modelling dynamic systems. In case the feedback from the output is removed, the obtained ANN topology (having only the current and past exogenous inputs as inputs to the multilayer structure) is known as a time-delay ANN.

A neuron in a hidden layer is connected to all neurons in the next layer, with weights indicating the "strength" of the connection between two neurons. The neuron calculates the weighted sum of its input signals, assigns a bias to the sum, and then forwards the modified sum to the nonlinear activation function [113]:

$$v_{j,t} = \sum_{k=1}^{m} w_{j,k} x_{k,t} + b_j, \tag{2.37}$$

$$y_{j,t} = \varphi_j\left(v_{j,t}\right), \tag{2.38}$$

where m is the number of inputs of the j-th neuron, $x_{k,t}$, $v_{j,t}$ and $y_{j,t}$ are the k-th input, induced local field, and output of the j-the neuron at time step t, respectively, $w_{j,k}$ is the weight of the connection between the j-th and k-th neuron, b_j is bias of the j-th neuron, φ_j is the nonlinear activation function of the j-th neuron (the most common functions are sigmoid and hyperbolic tangent function). The operation of the neuron is illustrated in Figure 2.2 (b).

The main disadvantage of NARX networks is their low efficiency as both the number of network parameters and computational burden grow by the same factor – the number of time delays [114]. Furthermore, it can be difficult to train these networks for long-term dependencies, i.e., when the current network output depends on the input and output values from the distant past [112, 115] (more details on the network learning algorithm are provided in Section 2.4.2).

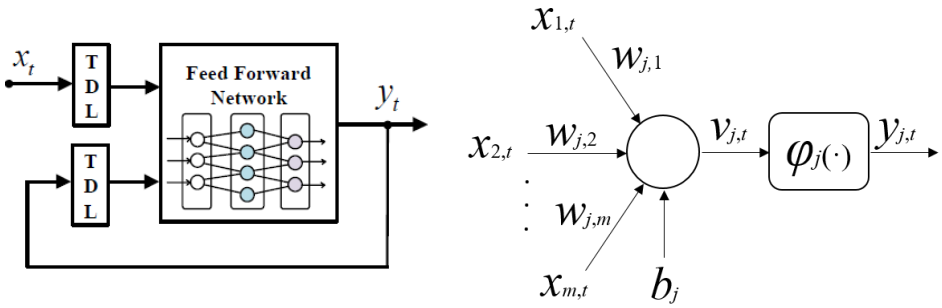

(a) (b)

Figure 2.2 (a): The NARX network architecture (adapted from [100]); (b): The illustration of neuron operation (adapted from [113])

2.4.1.2 Recurrent Artificial Neural Network

The architecture of the recurrent neural network (RNN) is similar to the standard, static, feed-forward ANN, except its hidden units/neurons are characterized by recurrent connections (see Figure 2.3) [116]. The recurrent connections provide RNN with a memory of previous inputs (so-called hidden state), and consequently enable the input presented at an earlier time to influence the current network output [117-119]. At each time step, the hidden state is determined by the current input vector and hidden state from the previous time step. RNN with a single hidden layer of recurrent neurons operates as follows [118, 120]:

$$h_t = \sigma_h(W_{xh}x_t + W_{hh}h_{t-1} + b_h), \tag{2.39}$$

$$y_t = \sigma_y\left(W_{yh}h_t + b_y\right), \tag{2.40}$$

where x_t and y_t is the input and output vector of the network, respectively, h_t is the hidden state of the hidden layer, all at time step *t*; W_{xh} is the correlation weight matrix between the input *x* and hidden layer, W_{hh} is the matrix of recurrent weights between the two consecutive hidden states, W_{yh} is the correlation weight matrix between the hidden state and output *y*, b_h and b_y is the bias matrix of the hidden and output layer, respectively, σ_h and σ_y is the activation function of the hidden (sigmoid or hyperbolic tangent function) and output layer, respectively.

One of the main issues associated with the application of RNNs is the occurrence of the vanishing or exploding gradient during the network training (they are even more prone to this issue than NARX networks [115]). Namely, the partial derivatives of the cost function with respect to weights/biases may experience a large exponential decrease or increase if network outputs depend on network inputs from temporally distant time intervals [113, 117, 119] (more detailed description of the network learning algorithm is given in Section 2.4.2). As a result, RNNs are not adequate for modelling dynamic systems characterized by long-term dependencies (delays of more than 10 time steps make the training of RNNs almost impossible [117]).

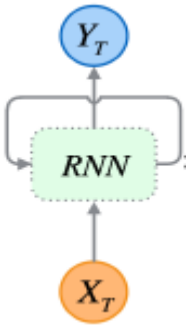

Figure 2.3 The architecture of the RNN (adopted from [121])

2.4.1.3 Long Short-Term Memory Artificial Neural Network

In order to solve the issue with the vanishing gradient problem, long short-term memory (LSTM) networks were proposed [122]. The name of this type of ANNs stems from their property to store the information about previous inputs (short-term memory, as opposed to long-term memory in the network that refers to slowly changing weights of connections between network elements) through feedback connections for long time periods [122]. Unlike RNNs that have ordinary neurons in hidden layers, LSTM

networks contain LSTM blocks in hidden layers. Each LSTM block consists of at least one recurrently connected LSTM memory cell with four multiplicative gates (the input, input modulation, forget and output gate) [117, 122]. The gates control the information stored in and exported from the LSTM cell. It was shown in [122] that this minimizes the possibility of the occurrence of the vanishing gradient problem. The structure of a single LSTM cell is illustrated in Figure 2.4, while the operation of LSTM cell can be mathematically described as follows [120]:

$$f_t = \sigma\left(W_{xf}x_t + W_{hf}h_{t-1} + b_f\right), \tag{2.41}$$

$$i_t = \sigma(W_{xi}x_t + W_{hi}h_{t-1} + b_i), \tag{2.42}$$

$$g_t = \phi(W_{xc}x_t + W_{hc}h_{t-1} + b_c), \tag{2.43}$$

$$c_t = f_t \circ c_{t-1} + i_t \circ g_t, \tag{2.44}$$

$$o_t = \sigma(W_{xo}x_t + W_{ho}h_{t-1} + b_o), \tag{2.45}$$

$$h_t = o_t \circ \phi(c_t), \tag{2.46}$$

where x_t and h_t are the inputs and outputs (hidden state) of the LSTM cell, respectively, f_t, i_t, g_t, and o_t are the forget, input, input modulation and output gate, respectively, c_t is the internal memory cell state, all at time step *t*, W_{xf}, W_{xi}, W_{xc} and W_{xo} are the weight matrices between the input *x* and the forget, input, input modulation and output gate, respectively, W_{hf}, W_{hi}, W_{hc} and W_{ho} are the weight matrices between the last time step of the hidden state *h* and the forget, input, input modulation and output gate, respectively, b_f, b_i, b_c and b_o are the biases of the forget, input, input modulation and output gate, respectively, $\sigma()$ is sigmoid activation function, $\phi()$ is hyperbolic tangent activation function, and $\circ$ stands for the element-wise multiplication. The elements of the weight matrices and bias vectors are estimated as a part of the ANN training procedure. The combination of sigmoid and hyperbolic tangent activation functions is used in LSTM network structure in this research, as it was adopted in many previous studies [99, 112, 123-128].

The input gate controls the information that is transferred to the memory cell and consequently protects the content of the LSTM cell from irrelevant inputs, whereas the input modulation gate modifies the information that is going to be stored in the cell by

adding non-linearity to the information [118, 122]. The input and the input modulation gate differ in the type of the activation function – the input gate uses the sigmoid function, whereas the input modulation gate relies on the hyperbolic tangent function. One of the principle differences between the two is that the output of the sigmoid activation function is within the range (0, 1), while the output of the hyperbolic tangent function lies between -1 and 1. The output gate decides on the LSTM cell output, and thus prevents the perturbation of other network elements by currently irrelevant information stored in the cell [122]. The forget gate provides LSTM network with the ability to reset the cell state by controlling the value of the self-loop weight of the memory cell. In this way, the information that is no longer needed can be selected and removed from the content of the memory cell [120]. Otherwise, continuous flow of input data could result in the unbounded growth of the cell state [129].

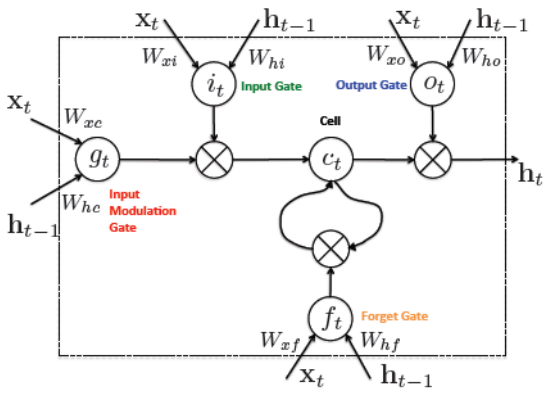

Figure 2.4 The architecture of an LSTM block with a single LSTM cell (adopted from [120])

2.4.2 Estimation of Equivalent Model Parameters

Once EM structure has been selected, model parameters have to be estimated. Optimization procedures used for parameter tuning minimize the difference between the responses produced by the EM and the measured/simulated responses of the system [42]:

$$\min_{\theta} \sum_{t=1}^{N} \varepsilon^2 = \sum_{t=1}^{N} \|y(t) - y_M(\theta, t)\|^2, \tag{2.47}$$

where N is the number of time steps in the responses, θ is a set of EM parameters, ε is EM error, $y(t)$ and $y_M(\theta, t)$ is the measured/simulated output of the actual system and EM output, respectively. The Quasi-Newton and Levenberg-Marquardt method as well as heuristic optimization algorithms represent the most commonly used optimization

techniques [91]. The EM parameter estimation stage is shown in Figure 2.5 (the signal r_s in Figure 2.5 denotes possible noise in the measured system responses).

In the case of black-box EMs in the form of ANNs, EM parameter estimation process includes the application of the network learning algorithm in combination with the selected optimization technique [117]. The values of network trainable parameters (weights and biases) are iteratively updated in the network training process starting from the initial, randomly chosen values, with the aim of identifying those that result in the best ANN cost function value.

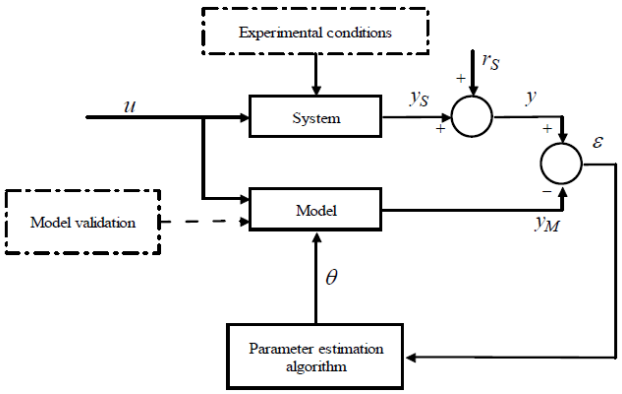

Figure 2.5 The estimation of system identification-based model parameters (adopted from [42])

In the case of NARX and time-delay ANNs, the static backpropagation can be used for the network learning process [112]. In order to perform the static backpropagation, NARX network has to be transformed into the open-loop architecture (i.e., traditional feed-forward ANN) first (see Figure 2.6). Given that the target output values from the training dataset are known, the feedback from the output can be eliminated and delayed target outputs can be used as inputs to the multilayer structure together with the current and past exogenous inputs. Following the network training, the feedback from the output is re-introduced and the network performs time series prediction in the closed-loop architecture (i.e., the original NARX topology).

The backpropagation includes two phases: the forward and backward pass. The forward pass represents the computation of the outputs of all neurons in the network starting from the input layer, while the backward pass involves the calculation of the partial derivatives of the ANN cost function with respect to weights and biases. For each time step in the trained time series, the whole backpropagation process is carried out. The partial derivative of the ANN cost function with respect to a weight is defined by (2.48) [113]:

$$\frac{\partial O}{\partial w_{j,i}} = \sum_{t=1}^{T} \frac{\partial O_t}{\partial w_{j,i}} = \sum_{t=1}^{T} \frac{\partial O_t}{\partial y_{j,t}} \frac{\partial y_{j,t}}{\partial v_{j,t}} \frac{\partial v_{j,t}}{\partial w_{j,i}}, \tag{2.48}$$

where T is the total number of time steps in the input data, O is the ANN cost function, which can be split into T time steps, $O = \sum_{t=1}^{T} O_t$, and w_{ji} is the weight between the j-th and i-th neuron. The partial derivative of the cost function with respect to a bias can be derived in a similar manner.

In case the j-th neuron is in the output layer, the calculation of $\frac{\partial O_t}{\partial y_{j,t}}$ is straightforward as the ANN cost function is defined on the basis of the difference between the target and actual response of the output neurons. However, in case the j-th neuron is located in a hidden layer, the following recursive formula has to be used:

$$\frac{\partial O_t}{\partial y_{j,t}} = \sum_{k \in K} \frac{\partial O_t}{\partial y_{k,t}} \frac{\partial y_{k,t}}{\partial v_{k,t}} \frac{\partial v_{k,t}}{\partial y_{j,t}}, \tag{2.49}$$

where K is a set of neurons in the next layer that are connected to the j-th neuron.

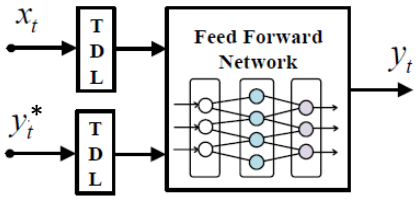

Figure 2.6 The illustration of the open-loop architecture for NARX network training, with y_t^* representing the target outputs (adapted from [100])

On the other hand, the backpropagation through time (BPPT) is a typical choice for the learning algorithm of RNNs and LSTM networks [118, 124]. The BPPT algorithm represents an extension of the static backpropagation [113]. The principle of the BPPT algorithm lies in unfolding/unrolling RNN into a multi-layered feed-forward network, with each layer corresponding to a single time step. An example of an unrolled RNN is shown in Figure 2.7. Each layer in the RNN unfolded in time is a copy of the whole RNN structure, meaning weights and biases are the same in each layer. As in the case of the static backpropagation, the BPPT consists of two stages: the forward and backward pass. The former represents a forward calculation applied to the input data from the first until the last time step (the set of equations describing ANN operation given in Section 2.4.1.2 and Section 2.4.1.3). The goal of the second stage of the BPPT is the computation of the

partial derivatives of ANN cost function with respect to network parameters (weights and biases) using the unrolled RNN structure. The calculation of the partial derivatives relies on the following equation [113]:

$$dv_{j,t} = \frac{\partial O}{\partial v_{j,t}} = \begin{cases} \varphi_j'(v_{j,t})\left[\frac{\partial O}{\partial y_{j,t}} + \sum_{k\in S} w_{j,k} dv_{k,t+1}\right], t < T \\ \varphi_j'(v_{j,t})\frac{\partial O}{\partial y_{j,t}}, t = T \end{cases}, \tag{2.50}$$

where $w_{j,k}$ is the weight of the connection between the *j*-th and *k*-th neuron, and *S* is the set of indices of neurons for which the target response is defined.

In the case of the RNNs, the backward error propagation involves the computation of $\frac{\partial h_t}{\partial h_k}$ across many time steps [116]:

$$\frac{\partial h_t}{\partial h_k} = \prod_{k<i\leq t} \frac{\partial h_i}{\partial h_{i-1}} = \prod_{k<i\leq t} W_{hh} diag\left(\sigma'_h(W_{xh}x_i + W_{hh}h_{i-1} + b_h)\right). \tag{2.51}$$

As seen in (2.51), the error backpropagation relies on the multiplications of the recurrent weight matrix, which can, depending on the values of the weights and the number of time steps considered in the backward pass, cause a large increase or decrease of the gradient [116]. When it comes to LSTM networks, the partial derivative of c_t with respect to c_{t-1} does not necessarily reduce to zero as the number of time steps increases, as LSTM networks can control the forget gate and reduce the rate of the gradient decay [130]:

$$\frac{\partial c_t}{\partial c_{t-1}} = \frac{\partial c_t}{\partial f_t}\frac{\partial f_t}{\partial h_{t-1}}\frac{\partial h_{t-1}}{\partial c_{t-1}} + \frac{\partial c_t}{\partial c_{t-1}} + \frac{\partial c_t}{\partial i_t}\frac{\partial i_t}{\partial h_{t-1}}\frac{\partial h_{t-1}}{\partial c_{t-1}} + \frac{\partial c_t}{\partial g_t}\frac{\partial g_t}{\partial h_{t-1}}\frac{\partial h_{t-1}}{\partial c_{t-1}}, \tag{2.52}$$

$$\begin{aligned} \frac{\partial c_t}{\partial c_{t-1}} = {} & diag(f'_t) W_{hf} diag\left(o_{t-1} \circ \phi'(c_{t-1})\right) \circ (c_{t-1} I) + \\ & + diag(f_t) + \\ & + diag(i'_t) W_{hi} diag\left(o_{t-1} \circ \phi'(c_{t-1})\right) \circ (g_t I) + \\ & + diag(g'_t) W_{hc} diag\left(o_{t-1} \circ \phi'(c_{t-1})\right) \circ (i_t I) \end{aligned} \tag{2.53}$$

where *I* is the identity matrix.

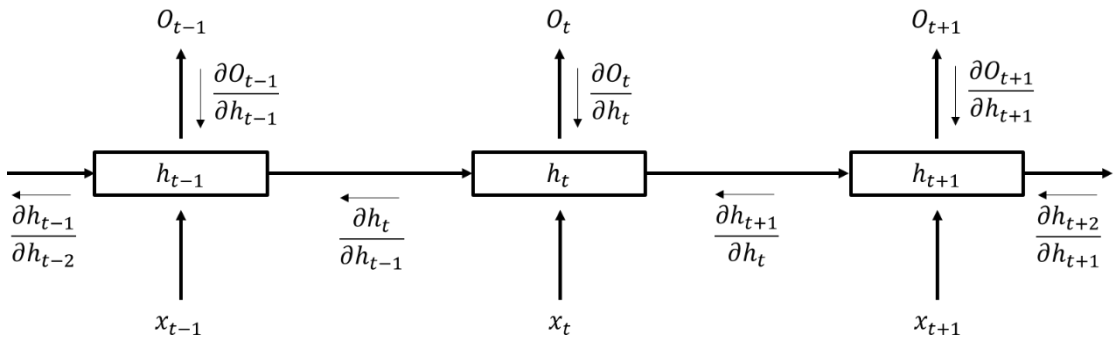

Figure 2.7 The graph of the RNN unrolled in time (adapted from [116])

Following the computation of the required partial derivatives of the cost function with respect to network parameters, the weights and biases are adjusted according to the chosen optimization technique (e.g., steepest descent, gradient descent with momentum, Levenberg-Marquardt, Adam optimizer, Adagrad optimizer, RMSProp optimizer, evolutionary algorithms) [113, 117]. The backpropagation and adjustment of network parameters are repeated until the best/optimal ANN cost function value is identified.

2.4.3 Validation of Equivalent Model

Assessing the suitability of the developed EM for representing the given system is the final step in system identification-based equivalent modelling. The EM accuracy is usually analysed using the objective function from EM parameter estimation process. If the parameters of EM structure have a physical meaning, the estimated values of parameters should be compared "with what is reasonable from prior knowledge" as well [42].

2.5 Unsupervised Data Mining Methods – Clustering Algorithms

Clustering process represents unsupervised grouping of unlabeled data according to their similarity [131, 132]. The objective is to achieve high similarity between objects within the same group/cluster and high dissimilarity between objects from different clusters. Clustering results can provide a useful insight into the natural patterns in the analysed dataset and serve as a pre-processing step in more complex data mining tasks [133].

Most of the work in this area has been focused on the clustering of static data (i.e., data whose features remain unchanged or change negligibly over time), meaning the majority

of the existing clustering algorithms was originally developed for static data [133, 134]. However, due to the increasing capacity for data storage, data from various areas ranging from sales data and stock prices to biomedical and electrical power system measurements can be recorded and stored as time series data for a long period. A need to analyse/process these datasets efficiently has resulted in an increasing interest in time series clustering. Even though the characteristics of time series data are considerably different from the ones of static data, clustering of both data types is usually carried out using the same clustering methods [134]. As times series are characterized by high dimensionality in space, clustering algorithms designed for static data are usually slightly modified in order to be used for time series clustering. So far, three techniques have been used for addressing the issue [134]: raw data-, feature- and model-based approach. Raw data-based method combines traditional clustering algorithms with distance measures more suitable for finding similarity in temporal sequences. On the other hand, the other two approaches attempt to reduce the dimensionality of clustering data by representing time series by a set of its most important features (feature-based clustering) or assuming that it is produced by a certain model (model-based clustering). Standard clustering methods with distance measures suitable for static data are then applied to transformed time series. However, the selection of relevant features is highly application dependent, while the model-based approach requires setting up model structure and/or parameters and is not efficient for large datasets [133].

Typical stages in clustering analysis of both static and time series data include the selection of distance metric, selection and application of clustering algorithm, and validation of clustering results [133]. These steps are described in the following sections.

2.5.1 Distance Measures

Distance measure has a high influence on clustering results as it determines how the similarity between clustering objects is calculated. There is no universal distance metric suitable for all datasets, meaning distance measure should be chosen according to data type and specific properties of the considered clustering dataset [134]. In the case of time series clustering, it also has to be taken into account whether the similarity in time, shape or structural similarity is analysed [133]. Two time series are similar in time if they are characterized by similar patterns occurring at the same time, whereas time misalignment between patterns is allowed in the clustering on the basis of similarity in shape. Structural

similarity is assessed according to the parameters of models representing the analysed time series (model-based clustering).

The most widely used distance measure is the traditional Euclidean distance [131]:

$$d_E = \sqrt{\sum_{k=1}^{d}(x_k - y_k)^2}, \tag{2.54}$$

where *x* and *y* are the clustering objects, and *d* is the dimensionality of the objects.

Another commonly utilised distance measure is the Mahalanobis distance, which takes into consideration the correlation between the clustering objects as it is calculated on the basis of variance-covariance matrix, *C* [131]:

$$d_M = \sqrt{(x-y)C^{-1}(x-y)^T}. \tag{2.55}$$

Both the Euclidean and Mahalanobis distance are suitable for static data as well as time series of equal length [134].

When it comes to the clustering of time series based on the similarity in shape, Dynamic Time Warping (DTW) and Longest Common Subsequence (LCSS) distance measures can be used as well [134-136]. Both measures are capable of assessing similarity between the sequences of different lengths.

The calculation of similarity between two time series using the DTW is based on a cost matrix that contains distances (usually Euclidean distances) between each pair of data points from the considered two time series [135]. The aim is to find a sequence of matrix elements (so-called a warping path) that corresponds to the minimum distance between the time series. The elements of the warping path have to satisfy three conditions:

- The warping path has to start with a pair of the first data points of the time series and ends with a pair of the last data points;
- The elements of the warping path have to be adjacent matrix elements;
- The indices of paired elements have to be non-monotonically decreasing.

Given that the main disadvantage of the DTW is its high computational burden ($O(nm)$, where n and m are the lengths of the analysed time series), several techniques that limit the part of the cost matrix being investigated have been proposed [135]. The most popular approaches are the Sakoe-Chiba Band and the Itakura Parallelogram (see Figure 2.8) [137].

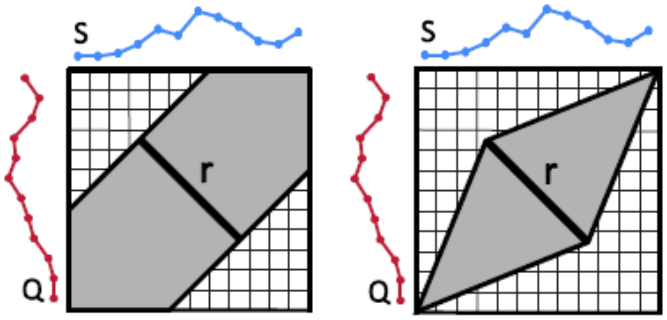

(a) (b)

Figure 2.8 The Sakoe-Chiba Band (a) and the Itakura Parallelogram (b) constraints (grey areas are considered in the DTW calculation) (adopted from [138])

The LCSS measure determines similarity between two time series by identifying the longest common subsequence [136]. The spatial and temporal distances between the data points that can be matched into a common subsequence have to be below user-defined thresholds. Unlike the other three described distance measures, the LCSS allows for a certain number of data points in time series to be unmatched. Consequently, the measure is robust to noise, as it does not "consider the most dissimilar part of the objects" [136]. The computational complexity is $O(\delta(n+m))$, where δ is the maximum allowed number of time steps between the instances of the data points being matched [136].

2.5.2 Clustering Algorithms

Clustering algorithms can be divided into five main categories: partitioning, hierarchical, model-based, density-based and grid-based, with the last two types rarely used for time series clustering [134]. Even though various clustering algorithms have emerged due to a growing need for solving different clustering tasks, the basic clustering algorithms, partitioning and hierarchical algorithms, have been most commonly utilized [134]. The simplicity and availability in software packages are the major reasons for their widespread application [131, 139]. The following sections provide the description of the main representatives of each type of clustering algorithms.

2.5.2.1 Partitioning Algorithms

Partitioning clustering algorithms preform division of a dataset into a predefined number of clusters through an iterative process [140]. At each step of the clustering procedure, clustering objects are reassigned from one cluster to another in order to optimize the clustering objective. The number of clusters has to be set in advance, which is their major drawback. Optimal number of clusters is typically defined using internal clustering evaluation indices calculated for a range of the number of clusters [140] (detailed explanation is provided in Section 2.5.3). The algorithms are suitable for both static and time series data [133, 134].

The basic partitioning clustering algorithm is the k-means algorithm [131, 140]. It has been extensively used in the clustering of large databases due to its favourable computational complexity of approximately $O(N)$, where N is the number of clustering objects. The algorithm represents a cluster by a centroid, which is determined as an average of the elements in the cluster. The clustering objective function is the sum of squared distances between clustering objects and their corresponding centroids [131, 140]:

$$E = \sum_{j=1}^{k} \sum_{i=1}^{N_j} \left\| x_i^j - c_j \right\|^2, \tag{2.56}$$

where x_i^j is the i-th clustering object in the j-th cluster, c_j is the centroid of the j-th cluster, N_j is the number of elements in the j-th cluster, k is the total number of clusters and $\|\cdot\|$ is the distance measure.

In the first iteration, cluster centroids are chosen randomly from the analysed dataset and the rest of the data are allocated to the closest centroid according to the selected distance measure (the Euclidian distance is usually used). Following this, centroids of newly formed clusters are calculated and the whole process is repeated. The clustering procedure continues until the convergence criterion is reached (the objective function stops decreasing or the same centroids are calculated in the successive stages of the clustering procedure) [131, 140].

The clustering result of the k-means is highly affected by the choice of the initial centroids and the algorithm does not necessarily converge to the global optimum [131, 140]. Thus, the k-means algorithm is usually repeated several times with different initial representative objects (for the same total number of clusters) and clustering result that corresponds to the best value of the objective function represents the final output of the algorithm. In addition, the algorithm is sensitive to outliers and noise as these elements can significantly influence the calculation of cluster centres, and cannot identify non-spherical clusters [131, 140].

In [141] the k-means++ clustering algorithm was suggested in order to address the problem of the selection of initial centroids. The greater distribution of initial centroids across the dataset is achieved by choosing the first initial centroid randomly from the entire dataset, and then selecting the remaining initial centroids through a two-stage procedure. The two-stage process involves the identification of the closest current centroid for each non-representative clustering object, and the selection of the new centroid according to the weighted probability distribution with weights proportional to the previously computed distances. In order to increase the robustness of the k-means algorithm to outliers, the k-medoids approach was developed [140]. Instead of representing clusters by centroids, the k-medoids uses actual clustering objects that are the closest to clusters' centroids as cluster representatives (so-called cluster medoids). The Partitioning Around Medoids (PAM) algorithm is the most popular representative of the k-medoids approach. However, lower sensitivity to outliers is accompanied with higher computational burden ($O(k(N-k)^2)$ for a single iteration) compared to the classical k-means [140, 142]. The PAM variants, such as the Clustering Large Application (CLARA) and Clustering Large Applications based upon RANdomized Search (CLARANS) algorithm, were proposed to reduce computational complexity [140, 142]. The CLARA applies the PAM clustering to a random sample extracted from the analysed dataset, while the CLARANS relies on the randomized search for updating a certain number of current medoids at each iteration. Still, the CLARA algorithm cannot produce good clustering results if the random sample does not contain all the best medoids from the entire dataset, and the CLARANS requires the number of medoid substitutions to be defined in advance.

All the above-mentioned partitioning algorithms perform "hard" or "crisp" clustering, meaning each clustering object is allocated to a single cluster [133, 140]. As opposed to

this clustering approach, the fuzzy c-means algorithm assigns all clustering objects to all clusters with a certain membership degree [132, 143]. The membership degrees of all clustering objects with respect to all clusters are grouped into a membership matrix and the element of the matrix is calculated using the following expression [143]:

$$u_{ij} = \frac{1}{\sum_{l=1}^{k}\left(\frac{d^2(x_i,c_j)}{d^2(x_i,c_l)}\right)^{1/(m-1)}}, \tag{2.57}$$

where u_{ij} is the membership degree of the *i*-th clustering object with respect to the *j*-th cluster, x_i is the *i*-th clustering object, c_j is the centroid of the *j*-th cluster, $d(x_i, c_j)$ is the Euclidean distance between the *i*-th clustering object and the *j*-th fuzzy centroid, *k* is the number of clusters, and *m* is the fuzziness level ($m \in (1,\infty)$, *m* is usually 2).

The fuzzy centroid is defined as follows [143]:

$$c_j = \frac{\sum_{i=1}^{N_j}(u_{ij})^m x_i}{\sum_{i=1}^{N_j}(u_{ij})^m}, \tag{2.58}$$

where N_j is the number of objects in the *j*-th cluster.

Similar to the k-means clustering, the objective function of the fuzzy c-means algorithm is the sum of distances between fuzzy centroids and cluster elements [143]:

$$J = \sum_{j=1}^{k}\sum_{i=1}^{N_j}(u_{ij})^m \left\|c_j - x_i\right\|^2. \tag{2.59}$$

The fuzzy c-means method is also characterized with linear computational complexity, which makes it suitable for large datasets [132].

2.5.2.2 Hierarchical Algorithms

Hierarchical clustering (HC) algorithms perform clustering by organizing objects into a "hierarchical" structure [131, 140]. Depending on the way the hierarchical structure is obtained, they can be divided into agglomerative (bottom-up approach) and divisive (top-down approach). The former considers all clustering objects as individual clusters at the beginning of the clustering process, and then iteratively merges them into a single large cluster. On the other hand, the divisive algorithm starts with one cluster containing all

clustering objects and divides this cluster into smaller ones during the process. Divisive algorithms have been significantly less utilised than agglomerative ones due to a large number of ways in which a set of objects can be partitioned into two subsets (2^{N-1}-1 possible divisions in case of N clustering objects) [132, 140]. The decision on merging or splitting of clusters is made on the basis of the similarity between clusters, which is calculated using distance and linkage measure [131, 140]. Linkage measures specify how similarity between clusters is assessed and the most commonly used are: single, complete, average (weighted and unweighted) and Ward's [140]. Single and complete linkage measure requires the computation of the distance between the two closest and farthest members of the clusters, respectively, while average linkage is based on the average distance between all pairs of objects in two clusters. Unweighted average linkage takes into account the number of elements in clusters as well. Ward's linkage measure merges the pair of clusters that provides the minimum increase in the sum of squared inter-cluster distances.

A dendrogram is usually used for the graphical representation of the clustering results. It shows which clusters are grouped (in the case of bottom-up) or divided (in the case of top-down) at each step of the clustering process [140]. An example of the dendrogram is given in Figure 2.9. Clusters are represented by nodes, whereas the vertical axis of the dendrogram shows the similarity measure between clusters.

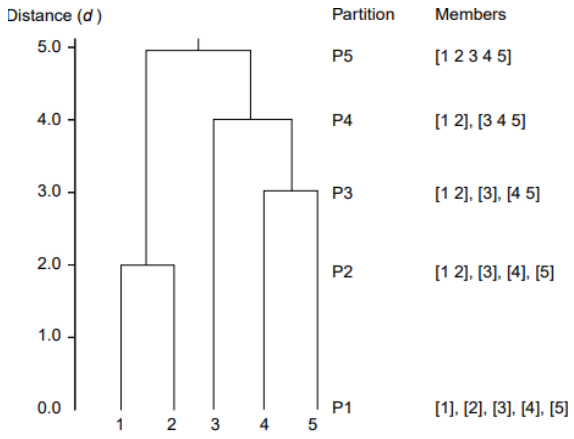

Figure 2.9 Graphical representation of the dendrogram (adopted from [144])

As opposed to the partitioning algorithms, the HC does not require the number of clusters to be defined in advance. However, the problem of selecting the optimal number of clusters still remains. The best number of clusters can be estimated using internal clustering evaluation indices [145] (as in the case of the partitioning algorithms) or by

inspecting the dendrogram structure (e.g., a large change in the similarity measure indicates that considerably dissimilar clusters are merged at that stage of the clustering process [144]).

One of the drawbacks of the HC algorithms is that the merging or division of clusters cannot be corrected once it has been carried out [140]. Additionally, the HC methods are characterized by high computational complexity (at least $O(N^2)$), are sensitive to outliers and have difficulty in identifying non-spherical-shaped clusters [140]. Several algorithms on the basis of the classical HC were proposed to address some of these issues, such as the balanced iterative reducing and clustering using hierarchies (BIRCH) and the clustering using representatives (CURE) [133, 134]. The BIRCH algorithm uses a set of features to describe the cluster and organizes these sets into a clustering feature tree that represents cluster hierarchy [140]. The tree structure is responsible for high computational efficiency ($O(N)$), however, the algorithm fails to identify non-spherical clusters as it is based on radius criterion, and relies on the limited amount of information about clustering objects [140]. On the other hand, the CURE represents a cluster by a set of "well scattered points", which enables the algorithm to identify arbitrary shaped clusters [146]. The first cluster representative is chosen as the farthest one from the cluster centroid (average of elements within the cluster), while each next representative point is selected as the farthest one from the previously chosen points. These representatives are then "moved towards" the cluster centroid proportionally to a predefined parameter value in order to reduce the impact of outliers on the clustering result. The distance between two clusters is defined as the minimum distance between any two representative points from the clusters. Unlike the traditional HC, the CURE requires the number of clusters to be chosen in advance. Given that the worst-case time complexity is $O(N^2\log(N))$, the CURE uses a random data sample in the case of large datasets.

2.5.2.3 Model-based Algorithms

The key assumption in the model-based clustering of time series is that the analysed data can be produced by a stochastic or an ANN-based model [133]. The main disadvantages of these clustering methods are the requirement for specifying model structure in advance (mainly relying on user experience) and slow processing time of large datasets [133].

The most popular stochastic models used for data representation are Hidden Markov Models (HMMs) and different variants of Autoregressive Integrating Moving Average (ARIMA) models [134, 135]. HMMs are described by [132, 147]:

- a discrete set of unobserved states;
- a discrete set of observations;
- an initial state probability distribution;
- a transition matrix (defines the probability of moving from one state to another);
- an emission matrix (defines the probability of generating a certain output value from a certain system state).

The current model output is defined by the current state and emission distribution, while the model state at the current time step depends on the state at the previous time step and transition distribution function [132]. HMM parameters for the given set of observations are usually estimated using the Baum-Welch algorithm, which maximizes the likelihood of the observations being produced by the HMM [147, 148]. The number of states has to be set in advance, which is one of the major disadvantages of these models [148].

ARIMA model for non-stationary time series (i.e., time series with mean or variance varying with time) is given by [149, 150]:

$$(1-\sum_{j=1}^{p}\Phi_j B^j)(1-B)^d X_t = \theta_0 + \left(1-\sum_{j=1}^{q}\theta_j B^j\right)e_t, \tag{2.60}$$

where X_t is the value of time series X at time step t, p is the autoregressive order, q is the moving average order, d is the order of differencing, (Φ_1,…,Φ_p) is a set of autoregressive coefficients that model the correlation between X_t and its preceding values, (θ_1,…, θ_q) is a set of moving average coefficients, θ_0 is the deterministic trend term (often neglected), $e(t)$ is the Gaussian white noise, and B is an operator with the following characteristic: $B^p X_t = X_{t-p}$.

In the case of the stationary time series, the order of the differencing is equal to zero, and the following variant of the ARIMA model, autoregressive moving average (ARMA) model is used [150]:

$$(1-\sum_{j=1}^{p}\Phi_j B^j)X_t = \theta_0 + \left(1-\sum_{j=1}^{q}\theta_j B^j\right)e_t, \tag{2.61}$$

where θ_0 is related to the mean of the time series, μ, i.e., $\theta_0 = \mu\left(1 - \sum_{j=1}^{p} \Phi_j\right)$.

Another two special cases of the ARIMA model are autoregressive (AR) model [150]:

$$(1 - \sum_{j=1}^{p} \Phi_j B^j) X_t = \theta_0 + e_t, \tag{2.62}$$

and moving average (MA) model [150]:

$$X_t = \mu + \left(1 - \sum_{j=1}^{q} \theta_j B^j\right) e_t, \tag{2.63}$$

where $\theta_0 = \mu\left(1 - \sum_{j=1}^{p} \Phi_j\right)$.

The maximum likelihood method has been typically used in the parameter estimation process of ARIMA models [150].

Data clustering using HMMs and ARIMA models usually involves [147, 149]:

- fitting of models to all individual clustering objects in the dataset or initial clusters,
- calculation of similarity between models (e.g., based on the similarity in values of model parameters [149, 151], probability of a clustering object being generated by models initially derived for other objects [147, 152], etc.), and
- application of other clustering algorithm to the previously computed similarity measures in order to obtain final clusters.

The most widely used ANN-based clustering model is the Kohonen self-organizing map (SOM) that transforms clustering data from high-dimensional space into a two-dimensional network structure [133, 153]. Each neuron/unit in the map is represented by a *d*-dimensional vector (a prototype vector), where *d* is the dimension of the clustering objects. At the beginning of the clustering process, initial values are assigned to prototypes and then each clustering object (i.e., input vector) is presented to the SOM to identify its best matching unit (BMU). The BMU corresponds to the prototype that is the closest to the input vector according to the Euclidean distance. After identifying the BMU for the given input vector, the BMU as well as a certain number of units in its neighbourhood are updated. The number of neighbourhood units being updated reduces

during the training procedure; in the beginning, almost the whole map represents the neighbourhood of the BMU, whereas only the BMU is updated at the final step. Therefore, the SOM relies on the "topology preserving" approach, meaning that clustering objects that are close to each other in the original data space are mapped into topologically closed SOM units [153]. The major drawback of SOM application is a large number of user-defined parameters (the number and spatial layout of SOM neurons, the mechanism of BMU update) as well as potential misrepresentation of the original space density [132].

2.5.2.4 Density-based Algorithms

Density-based clustering algorithms define clusters "as dense regions in the data space, separated by sparse regions", which allows them to identify arbitrary shaped clusters [140]. One of the basic density-based algorithms is Density Based Spatial Clustering of Applications with Noise (DBSCAN), which identifies dense regions on the basis of the minimum number of objects (*MinPts*) in the ε neighbourhood of cluster objects [154]. Objects that are left unassigned to any cluster/dense region at the end of the clustering procedure correspond to outliers (noise data). However, the proper identification of clusters is highly dependent on these two input parameters, ε and *MinPts* [146]. Given that the DBSCAN is not suitable for datasets characterized by different local densities in different regions of the data space, the Ordering points to identify the clustering structure (OPTICS) algorithm was developed [155]. The algorithm does not produce a single clustering result but a "density-based cluster ordering" that does not require a single global parameter setting [155]. The ordering contains the information about "intrinsic cluster structure" of the analysed dataset, and can be obtained by running the DBSCAN for a large number of combinations of input parameters [155].

Another popular clustering method is the Density-based clustering (DENCLUE) algorithm that organizes the clustering dataset into a map consisting of d-dimensional hypercubes, where d is the dimension of clustering objects [156]. Only data from highly populated hypercubes and their neighbourhood hypercubes are actually used in the clustering, which in turn provides the computational complexity of $O(N\log(N))$ [132]. The identification of clusters relies on the kernel density estimation approach [156]. Namely, the local maxima of the overall density function of the relevant data (the density function is estimated using the Gaussian kernel) correspond to cluster representatives,

and the closest local maximum is determined for each clustering object using the hill-climbing technique. Clustering objects associated with the same local maximum are allocated to the same cluster. However, the estimation of optimal parameters of the density function can be mathematically challenging and time-consuming in the case of high dimensional clustering data [157].

2.5.2.5 Grid-based Algorithms

Grid-based algorithms operate by dividing the data space into a certain number of cells and conducting the clustering process using statistics about clustering objects within the cells (e.g., the number of elements within the cell, the average, minimum, and maximum of the attributes of clustering objects in the cell) [140]. They have been widely used for spatial data clustering. The computational time usually depends on the number of cells, not on the size of the analysed dataset.

2.5.3 Clustering Evaluation Measures

The evaluation of clustering quality can be carried out using external or internal indices [133]. External indices determine the similarity between the results of the clustering algorithm and the known partitions (the ground truth) that have to be defined by human experts using prior information about the clustering data. Some of the commonly used external indices are [133, 134, 158]:

- Cluster purity: For each cluster produced by the clustering procedure and each known partition/class, the number of common clustering objects is computed and the dominant class is determined for each cluster:

$$CP = \frac{1}{N}\sum_{i=1}^{k} \underset{1\le j\le k}{max}\left|G_j \cap C_i\right|, \tag{2.64}$$

  where C is a set of clusters obtained using the clustering algorithm, G is a set of the clusters known *a priori*, k is the number of clusters, $|\cdot|$ is the number of elements in the set, and N is the total number of clustering objects.

- Cluster similarity measure:

$$Sim(G, C) = \frac{1}{k}\sum_{i=1}^{k} \underset{1\le j\le k}{max}\left(Sim(G_j, C_i)\right), \tag{2.65}$$

$$Sim(G_j, C_i) = \frac{2|G_j \cap C_i|}{|G_j| + |C_i|}, \tag{2.66}$$

- Rand index:

$$Rand = \frac{a+d}{a+b+c+d}, \tag{2.67}$$

where *a* is the number of pairs of objects assigned to the same cluster in both sets, *G* and *C*, *b* is the number of pairs of objects assigned to the same cluster in *G*, but to different clusters in *C*, *c* is the number of pairs of objects assigned to the same cluster in *C*, but to different clusters in *G*, and *d* is the number of pairs of objects that do not belong to the same cluster neither in *G* nor *C*.

- Jaccard score:

$$Jaccard = \frac{a}{a+b+c}. \tag{2.68}$$

In case the ground truth is not available (which is a common situation in practical clustering tasks), internal measures, based on the assessment of intra-cluster and inter-cluster similarity, are used for the evaluation of clustering results [133]. The most popular internal measures are [140, 144, 159, 160]:

- Mean squared error (MSE): The MSE index calculates the average distance between a clustering object and its corresponding cluster representative:

$$MSE = \frac{1}{N}\sum_{i=1}^{N} d^2\left(x_i, w_{j:x_i \in \Omega_j}\right), \tag{2.69}$$

where x_i is the *i*-th clustering object, w_j is a representative of the *j*-th cluster, Ω_j is a set of objects in the *j*-th cluster, *N* is the total number of objects, $d(\cdot)$ is the distance measure.

- Clustering dispersion index (CDI): The CDI is defined as a ratio of the average distance between the objects within the same cluster and the average distance between the representatives of clusters:

$$CDI = \frac{\sqrt{\frac{1}{k}\sum_{j=1}^{k} \overline{d}^2(\Omega_j)}}{\overline{d}(W)}, \tag{2.70}$$

$$\overline{d}^2(\Omega_j) = \frac{1}{2N_j}\sum_{x_i \in \Omega_j} d^2(x_i, \Omega_j), \tag{2.71}$$

$$d^2(x_i, \Omega_j) = \frac{1}{N_j}\sum_{y\in\Omega_j} d^2(x_i, y), \tag{2.72}$$

where k is the number of clusters, W is a set of cluster representatives, y is an element of the j-th cluster, N_j is the number of objects in the j-th cluster.

- Mean index adequacy (MIA): The MIA index, similar to the MSE index, is calculated on the basis of the average distances between clustering objects and their cluster representatives:

$$MIA = \left(\frac{1}{k}\sum_{j=1}^{k} d^2\left(w_j, \Omega_j\right)\right)^{1/2}, \tag{2.73}$$

- Within cluster sum of squares to between cluster variation ratio (WCBCR): The WCBCR is computed using the distances between each clustering object and its corresponding cluster representative, and the distances between cluster representatives:

$$WCBCR = \frac{\sum_{j=1}^{k}\sum_{x_i\in\Omega_j} d^2(x_i, w_j)}{\sum_{1\le q<p}^{k} d^2(w_p, w_q)}, \tag{2.74}$$

- Silhouette index (SI):

$$SI\left(x_i^j\right) = \frac{b\left(x_i^j\right) - a(x_i^j)}{max\{a\left(x_i^j\right), b(x_i^j)\}}, \tag{2.75}$$

$$b\left(x_i^j\right) = \min_{1\le l\le k, l\ne j}\left\{\frac{\sum_{y\in\Omega_l} d\left(x_i^j, y\right)}{|\Omega_l|}\right\}, \tag{2.76}$$

$$SI = \frac{1}{N}\sum_{i=1}^{N} SI(x_i^j), \tag{2.77}$$

where $SI\left(x_i^j\right)$ is the SI index for the i-th clustering object in the j-th cluster, $a(x_i^j)$ is the average distance between the i-th object and all other objects in its cluster, $b(x_i^j)$ is the smallest average distance between the i-th object and the remaining clusters, $|\Omega_l|$ is the number of objects in the l-th cluster, and SI is the global index used for assessing the overall quality of the clustering result. The value of $SI\left(x_i^j\right)$ is within the range [-1, 1], with values close to 1 indicating high compactness of

the cluster containing the *i*-th clustering object and separation of the *i*-th clustering object from other clusters.

Lower values of all afore-mentioned internal indices, with the exception of the SI, imply better clustering results in terms of separation and compactness of clusters. These indices have been commonly used to address the problem of selecting the optimal number of clusters for a given dataset. The most common approach is to perform the clustering procedure for a range of the number of clusters, calculate the chosen clustering evaluation index for each clustering result and select the best number of clusters according to the optimal value of the evaluation index [140, 145, 160]. In the case of the MSE, CDI, MIA and WCBCR, the optimal index value is determined using the elbow method: the values of the clustering index are plotted against the number of clusters and the optimal index value (and the corresponding optimal number of clusters) is located at the knee of the curve. On the other hand, in the case of the SI, the maximum of all values computed for each clustering procedure indicates the best number of clusters.

2.6 Summary

This chapter presented the state-of-the-art of the methods for dynamic equivalent modelling of power plants and networks. System identification-based techniques were identified as more adequate for equivalent modelling of electrical networks with converter-interfaced sources compared to conventional approaches (i.e., the modal analysis and coherency-based methods). Furthermore, a comprehensive review of the most commonly used unsupervised data mining techniques, clustering algorithms, was given. The choice of the optimal number of clusters is one of the main issues, while high dimensionality and adequate distance metric represent additional concerns in time series clustering. The chapter also discussed the typical approaches for overcoming the afore-mentioned issues.

3 Probabilistic Analysis and Modelling of HRES Plant for System Stability Studies

3.1 Introduction

Traditional representation of RESs as negative constant power loads in power system stability simulations is not acceptable anymore due to their considerable installation capacity, and consequently non-negligible contribution to power system stability performance [20]. On the other hand, the use of detailed dynamic models of RES power plants in system level studies can result in high computational time, and full-scale models often cannot be exchanged between different system operators due to confidentiality issues [19-21]. In order to obtain system stability results within reasonable computational time without compromising their accuracy, equivalent modelling of RES power plants can be adopted [20]. This chapter performs exploratory studies on equivalent modelling of HRES plant for four types of system stability problems (small-disturbance, transient, frequency and long-term voltage stability). The methodology for identifying the most probable impact of HRES plant on the above-mentioned categories of power system stability is described. The typical contribution of the HRES plant to the relevant power system stability behaviour represents the main input for the development of the preliminary EMs of HRES plant for small-disturbance, transient, frequency and long-term voltage stability studies. The aim of the chapter is to provide a foundation for further investigation of the most probable annual contribution of HRES plant to power system

stability and the design of robust EMs capable of representing the whole HRES plant in annual system stability simulations.

3.2 Methodology

Methodology for assessing the influence of HRES plant on four types of system stability (small-disturbance, transient, frequency and voltage) of the system and development of preliminary EMs of HRES plant for the considered system stability analyses is illustrated in Figure 3.1. Dashed rectangles in Figure 3.1 mark inputs and outputs of different stages within the procedure. The presented procedure is applicable to any technology mix in the HRES plant.

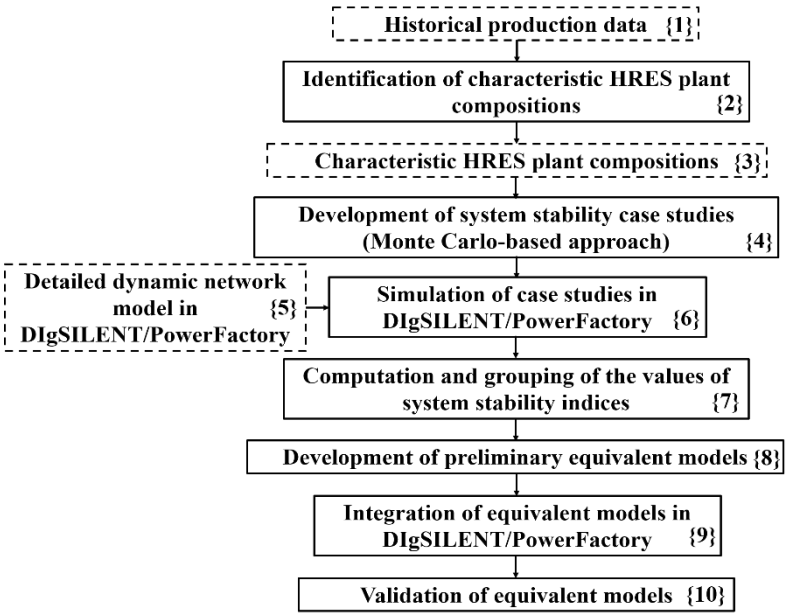

Figure 3.1 The methodology for analysing the impact of HRES plant on system stability and developing preliminary EMs of HRES plant for system stability studies

The assessment of the impact of the HRES plant on system stability is performed on the basis of characteristic annual HRES plant operating scenarios (so-called plant compositions), which in turn eliminates the need for investigating all possible HRES plant operating scenarios. These plant compositions are defined by applying an unsupervised data mining technique to the historical production profile of the considered HRES plant. A probabilistic Monte Carlo (MC) approach is used for taking into consideration uncertainties in production and location of individual technologies in the HRES plant. The behaviour of the HRES plant in small-disturbance, transient, frequency and long-term voltage stability of the system is analysed on the basis of the least damped

electromechanical mode, shape of real power response of the HRES plant in time domain, frequency nadir and the maximum rate of change of frequency (RoCoF), and critical point of real power-voltage (P-V) curve (load margin and critical bus voltage), respectively. HRES plant compositions resulting in similar system stability results are represented by a common EM. In this way, a set of EMs suitable for modelling the investigated HRES plant operating conditions in system stability simulations is obtained.

The stages of the methodology are described in detail in the following sections.

3.2.1 Identification of Characteristic Hybrid Renewable Energy Source Plant Compositions

The patterns in HRES plant production profiles are determined by applying a clustering method to a historical dataset of real power outputs of individual technologies in the HRES plant (block {2} in Figure 3.1). Production levels of individual plants are grouped into a vector at each time step in the considered historical time period and the vectors are used as inputs to the clustering process. The fuzzy c-means clustering algorithm is used for data clustering. It was selected due to its low computational complexity ($O(N)$, where N is the number of clustering objects) as the historical dataset is large, its property to perform "soft" clustering, which is especially useful in case of clusters not being well separated [132], and its proven efficiency in application in similar clustering tasks in the past [70, 161, 162]. The fuzzy c-means algorithm represents each cluster by its centroid that corresponds to characteristic HRES plant composition.

As the number of clusters has to be defined in advance, internal clustering evaluation indices, based on assessing inter-cluster and intra-cluster similarity, have been commonly used for estimating the optimal number of clusters [160]. In this study, a combination of three widely applied clustering indicators, MSE, CDI, and MIA, is used [160]. The clustering process is repeated for a range of the number of clusters, the chosen index is calculated for each clustering result and then plotted against the number of clusters. The optimal number of clusters (according to the considered clustering indicator) is located at the knee of the curve. If the knee is not noticeable, it can be estimated using the two-tangent method described in [160] (the method is illustrated in Figure 3.2). The two-tangent method is based on visual inspection of the knee location

and drawing tangents to the parts of the curve on either side of the estimated knee location. The knee of the curve is then located at the intersection of the tangents. The final number of clusters, that is, the number of characteristic HRES plant compositions, is determined as the median value of the number of clusters identified by the MSE, CDI and MIA clustering indices.

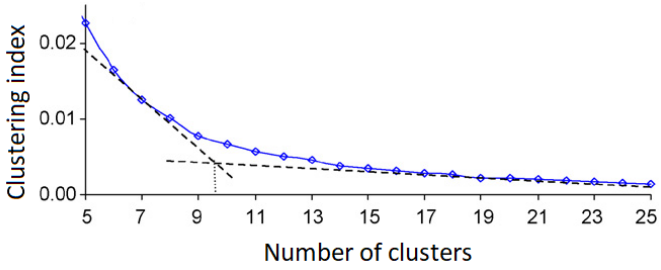

Figure 3.2 The illustration of the two-tangent method for estimating the knee of the curve (adapted from [160])

3.2.2 Development of System Stability Case Studies

In order to identify the most probable influence of the HRES plant on power system stability and propose the preliminary structures of EMs capable of representing HRES plant behaviour in system stability studies throughout the whole year, system stability case studies (CSs) are generated on the basis of characteristic annual HRES plant compositions (block {4} in Figure 3.1). Uncertainties in production of individual plants and their location within the HRES plant (in terms of the distance from the PCC) are modelled using the probabilistic MC approach. In each MC CS, real power outputs of individual plants are sampled uniformly from the pre-specified ranges defined on the basis of typical annual plant compositions. Similarly, the uniform probability distribution is used for random sampling of the lengths of lines connecting individual plants to the PCC from the pre-defined range of values.

3.2.3 Simulation of Case Studies in DIgSILENT/PowerFactory

MC CSs designed in the previous step of the methodology are simulated in DIgSILENT/PowerFactory software package using the detailed HRES plant model and the model representing the rest of the power system (block {6} in Figure 3.1). For each MC CS, four types of system stability simulations are carried out as follows:

- *Small-disturbance stability* analysis involves the modal analysis of the whole system, which determines all system eigenvalues using the classical QR transformation method [102].

- *Transient and frequency stability* studies are carried out by performing electromechanical simulations for the chosen disturbances. Three-phase self-clearing fault is selected as an external system disturbance in transient stability studies. The fault location and duration are the same in all CSs. On the other hand, an increase in the total system load is chosen as a disturbance in frequency stability analysis. (*Note*: A single disturbance was simulated in transient and frequency stability simulations due to the small size of the test system (presented in Section 3.3). Chapter 4 will provide a procedure for generating a set of the most probable disturbances during the year.) Real power response of the HRES plant at the PCC and system frequency response are recorded in each transient and frequency stability simulation, respectively.
- *Long-term voltage stability* analysis is performed by computing P-V curves at the system buses. The P-V curve method represents one of the most reliable long-term voltage stability indices and can be simulated in DIgSILENT/PowerFactory environment with little computational burden [163]. Long-term voltage stability limit is determined by increasing the system load gradually until the load flow calculation stops converging. The increase in the system load in the first iteration is 0.5% of its initial value, while the change of the system demand in the following iterations varies between 0.01% and 2% (recommended values in DIgSILENT/PowerFactory [164]). Step size reduces as the system approaches the long-term voltage stability limit. Real power outputs of individual plants in the HRES plant remain constant in long-term voltage stability study, while the external system covers the mismatch between the analysed demand and HRES plant power production.

3.2.4 Computation and Grouping of the Values of System Stability Indices

Following system stability simulations of MC CSs in DIgSILENT/PowerFactory, the contribution of a MC HRES plant composition to each of the investigated categories of power system stability is assessed in the following way:

- *Small-disturbance stability*: The impact of different HRES plant compositions on small-disturbance stability of the system is assessed on the basis of the parameters

of electromechanical oscillation modes. Only electromechanical modes are taken into consideration in the analysis as these modes are the ones that persist longest and thus determine the overall system dynamic behaviour [102]. Small-disturbance stability problems in power systems are commonly caused by insufficient damping torque, which implies that a reliable assessment of the least damped mode is needed for controlling power system operation [165]. Therefore, for each MC CS, the damping and frequency of the least damped (the critical) electromechanical mode are determined, and these parameters are used for comparing HRES plant compositions from the perspective of their influence on small-disturbance stability of the system.

- *Transient stability*: The shape of real power response of the HRES plant at the PCC is a criterion for differentiating HRES plant compositions in terms of their contribution to transient stability of the system. (*Note*: Given that the SGs in the small test system used in this preliminary study are located within the investigated HRES plant and that some of the considered HRES plant operating points do not contain any of SG-based power plants in service, transient stability indices such as transient stability index (TSI) and critical clearing time could not be computed. Thus, real power time-domain responses of the HRES plant were chosen for analysing the transient stability performance of the test system.) Reactive power responses of the HRES plant are not considered in this exploratory study.

- *Frequency stability*: Frequency nadir and the maximum RoCoF represent typical parameters used for frequency stability assessment [163], and thus are determined for each frequency response from the simulated MC CSs. Frequency nadir corresponds to the lowest frequency value following a disturbance, whereas the RoCoF is a time derivative of the system frequency [163]. The maximum RoCoF is calculated as the maximum of average RoCoF values over a moving window [166]:

$$RoCoF_{Max} = \max_i RoCoF_i = \max_i \left(\frac{1}{n}\sum_{k=1}^{n}\frac{\Delta f_k}{T_s}\right), \tag{3.1}$$

where $RoCoF_i$ is the average RoCoF for the *i*-th measurement window, T_s is the sampling time, Δf_k is the variation in frequency within the *k*-th sampling period, *n* is the number of sampling periods in the measurement window. As

recommended in [167], the sampling period of 100 ms and window size of 500 ms are adopted in this study.

- *Long-term voltage stability*: The load margin (i.e., the difference between the load level at which voltage collapse occurs and the initial load level) and the voltage of the bus that collapses first are used to analyse the impact of the HRES plant on long-term voltage stability of the system.

For each type of system stability, the obtained system stability results are grouped according to their similarity, which in turn provides the information about MC CSs resulting in similar system stability performance. The groups/clusters of system stability results represent a basis for EM development and their number determines the number of EMs required for representing the considered HRES plant operating scenarios in system stability simulations.

3.2.5 Development of Preliminary Equivalent Models

An EM is developed for each cluster of system stability results, and the following sections describe EM structure and parameter estimation process for the considered categories of power system stability.

3.2.5.1 Small-disturbance Stability Study

In [168] the reduction of the model order was achieved by clustering all modes produced by the modal analysis according to similarity in damping and frequency, whereas EM development in this study takes into consideration only electromechanical modes as small-disturbance stability is associated with the rotor angle oscillations [169]. Each cluster of critical electromechanical modes is represented by a mode (so-called a representative critical electromechanical mode) whose damping and frequency correspond to the mean values of damping and frequency of all modes in the cluster. Furthermore, a representative HRES plant composition for each cluster is defined as one of the simulated plant compositions resulting in the critical electromechanical mode that corresponds to a cluster medoid (the cluster medoid is one of the simulated electromechanical modes in the cluster being the most similar to the representative critical mode).

EM structure is derived from time domain electromechanical simulations carried out for each representative HRES plant composition. The electromechanical simulations are carried out in DIgSILENT/PowerFactory software using the full-scale dynamic model of the HRES plant. A small increase in the total TN load of 1% is chosen as a system disturbance. The lengths of all connecting lines are set at the average of line lengths simulated in the MC procedure. Voltage and real power responses at the PCC are recorded in the simulations and these responses represent a basis for EM parameter estimation.

The EM is developed in the form of a TF with the input and output signal corresponding to the deviation of voltage and real power at the PCC from their pre-disturbance values, respectively. The full EM structure is as follows:

$$P_{EM}(t) = \begin{cases} P_{ss}, t < t_{start} \\ P_{ss} + \mathcal{L}^{-1}\big(TF(s)\big)\big(u_{PCC}(t) - u_{PCC,ss}\big), t \geq t_{start} \end{cases}, \tag{3.2}$$

where $P_{EM}(t)$ is the real power output of the EM in MW, P_{ss} is the total HRES plant production at pre-disturbance state in MW, $\mathcal{L}^{-1}$ stands for the inverse Laplace transform, $TF(s)$ is the TF in s-domain, $u_{PCC}(t)$ is voltage at the PCC in p.u., $u_{PCC,ss}$ is the pre-disturbance voltage at the PCC in p.u., and t_{start} is the time of occurrence of the system disturbance.

TF denominator has two complex poles corresponding to the representative critical electromechanical mode for a given cluster. When it comes to TF numerator, its parameters are estimated through an iterative optimization process using System Identification Toolbox in Matlab [170]. In this process, voltage and real power responses at the PCC obtained in previously simulated time domain electromechanical simulations are used as TF input and output, respectively. The order of TF numerator is gradually increased starting from the structure with a single zero. For each TF numerator order, TF parameters were estimated using the Levenberg-Marquardt algorithm, which is a line-search algorithm that can be seen as an intermediate between the gradient-descent and Gauss-Newton method [20, 170]. The objective of the optimization procedure is to minimize the difference between TF output and the simulated real power response of the detailed HRES plant model:

$$\min_{\theta} RMSE = \min_{\theta} \sqrt{\frac{1}{n}\sum_{i=1}^{n}(P_{ORG,i} - P_{EM,i})^2}, \tag{3.3}$$

where *RMSE* is root mean squared error, θ is a set of unknown TF parameters, n is the number of simulated time steps, $P_{ORG,i}$ is the real power response obtained in the electromechanical simulation at the i-th time step, and $P_{EM,i}$ is EM output at the i-th time step (obtained using (3.2)). The optimization terminates when there is no considerable improvement in *RMSE* value between two consecutive iterations. Following parameter estimation, the Best Fit Value (BFV) is calculated using (3.4) [20]:

$$BFV(\%) = 100 \cdot \left(1 - \left|\frac{\sum_{i=1}^{n}(P_{ORG,i} - P_{EM,i})}{\sum_{i=1}^{n}(P_{ORG,i} - \overline{P}_{ORG})}\right|\right), \tag{3.4}$$

where $\overline{P}_{ORG}$ is the average of real power response of the detailed HRES plant model to the small system disturbance. The optimal TF parameters correspond to the lowest TF numerator order with the BFV above a pre-defined threshold (80% is adopted in the study [20]).

3.2.5.2 Transient and Frequency Stability Study

The structure of a grey-box EM for transient and frequency stability studies is the same: the model is in the form of an equivalent SG or WF depending on the analysed HRES plant composition. The equivalent is connected directly to the PCC. The WF model is used for representing the cluster of system stability results produced by HRES plant compositions consisting of converter-connected technologies only. (*Note*: In the case of the test system and data used in this study (described in Section 3.3 and Section 3.4), the WF within the HRES plant had the largest share in the total HRES plant production most of the time during the year compared to the other converter-connected technologies in the test HRES plant, and thus, was chosen for modelling plant compositions without SGs in service.)

The equivalent SG is represented by the classical, second-order, machine model [102]:

$$\frac{dw}{dt} = \frac{1}{2H}\left(T_m - T_e - K_D(w-1)\right), \tag{3.5}$$

$$\frac{d\delta}{dt} = w_0(w-1), \tag{3.6}$$

where w is rotor speed in p.u., H is inertia constant in seconds, T_m and T_e are mechanical and electrical torque, respectively, in p.u., K_D is damping coefficient in p.u., δ is rotor angle in electrical radians, and $w_0 = 2\pi f$ is the referent rotor speed in rad/s.

The parameters of the SG model include the SG rated capacity, inertia constant and damping coefficient. The SG rated capacity is defined on the basis of the analysed HRES plant production and the SG rated power factor (the value of 0.85 is adopted in this study), while the remaining two equivalent SG parameters are obtained through a parameter estimation procedure.

The equivalent WF consists of a number of identical doubly-fed induction generators (DFIGs) connected in parallel. The number of individual DFIGs in service is defined by the total WF production (i.e., the analysed HRES plant power output) and the rated power of individual units as it is assumed that units in operation generate the rated power output. A detailed description of the WF control system is given in Section 3.3. All parameters of the equivalent WF control system model correspond to the default/recommended values in [164], except the proportional gain and integral time constant of PI controllers responsible for maintaining WF real and reactive power output at the reference values that are estimated in the parameter optimization procedure.

In order to estimate the unknown parameters of EM for transient stability simulations, a representative real power response of a cluster is defined as an average of all responses in the cluster. Similarly, representative frequency nadir and maximum RoCoF of a cluster correspond to an average of the frequency nadir and maximum RoCoF values assigned to the particular cluster, respectively. (*Note*: Even though cluster medoid is a more common representative of a cluster of time series data compared to cluster average [133], the average of cluster responses is chosen in transient stability study due to the uniformity. The cluster average is used for defining representative of clusters of system stability results in other three preliminary system stability studies (the average of damping and frequency of the electromechanical modes in cluster for small-disturbance stability, the average of the RoCoF and frequency nadir in cluster for frequency stability, and the average of load margin and critical bus voltage in cluster for long-term voltage stability).) In addition, for both types of system stability studies, representative HRES plant production of a cluster is determined as an average of the power outputs of MC CSs allocated to the given cluster.

The unknown EM parameters (the inertia constant and damping coefficient in the case of the SG equivalent, and the gain and time constant of the PI controllers in the case of the WF equivalent) are estimated through the iterative procedure. At each iteration of the procedure, EM parameters are sampled from the pre-defined ranges, a transient/frequency system stability simulation is performed for a given combination of parameter values, and EM accuracy is assessed. In this procedure, the real power output of the equivalent SG/WF corresponds to the representative HRES plant production for the particular cluster. In the case of transient stability study, EM performance is evaluated by comparing the time domain real power response produced by the EM with the representative real power response of the relevant cluster as follows:

$$EM_{Err}^{Trans}(\%) = 100 \cdot \frac{1}{T} \cdot \sum_{t=1}^{T} \left| \frac{P_t^{EM,i} - P_t^{REP,i}}{P_t^{REP,i}} \right|, \tag{3.7}$$

where T is the total number of simulated time steps, $P_t^{EM,i}$ is the output of the EM for the i-th cluster at time step t, and $P_t^{REP,i}$ is the value of the representative response for the i-th cluster at time step t.

When it comes to frequency stability studies, the suitability of EM for representing HRES plant compositions from a particular cluster of frequency stability results is assessed as follows:

$$EM_{Err}^{Freq}(\%) = 100 \cdot \sqrt{{\Delta_{Fnadir}}^2 + {\Delta_{RoCoF}}^2}, \tag{3.8}$$

$$\Delta_{Fnadir} = \frac{F_{nadir}^{EM,i} - F_{nadir}^{REP,i}}{F_{nadir}^{REP,i}}, \tag{3.9}$$

$$\Delta_{RoCoF} = \frac{RoCoF^{EM,i} - RoCoF^{REP,i}}{RoCoF^{REP,i}}, \tag{3.10}$$

where Δ_{Fnadir} and Δ_{RoCoF} is the EM error in the frequency nadir and maximum RoCoF, respectively, $F_{nadir}^{EM,i}$ and $RoCoF^{EM,i}$ are the frequency nadir and maximum RoCoF obtained using the EM for the i-th cluster, respectively, and $F_{nadir}^{REP,i}$ and $RoCoF^{REP,i}$ are the representative frequency nadir and maximum RoCoF of the i-th cluster, respectively.

The combination of EM parameters resulting in the minimum value of the $EM_{Err}^{Trans}/EM_{Err}^{Freq}$ index is the best combination of the parameter values for the EM for transient/frequency stability studies.

3.2.5.3 Long-term Voltage Stability

Each cluster of critical points of P-V curves is described by a representative critical point, which is determined as a mean of the values of load margin and critical bus voltage allocated to the cluster. As in the case of transient and frequency stability study, representative HRES plant production of a cluster is computed as a mean value of the power outputs of MC CSs assigned to the cluster. The EM structure for long-term voltage stability studies is illustrated in Figure 3.3. EM is in the form of a parallel combination of a SG (PV type) (*Equivalent SG* in Figure 3.3) and a shunt inductor/capacitance (*Shunt* in Figure 3.3), which is connected to the low voltage side of the transformer connecting the whole HRES plant to the PCC (T_{HRES} in Figure 3.3) through a step-up transformer (T_{EM} in Figure 3.3) and a line (L_{EM} in Figure 3.3).

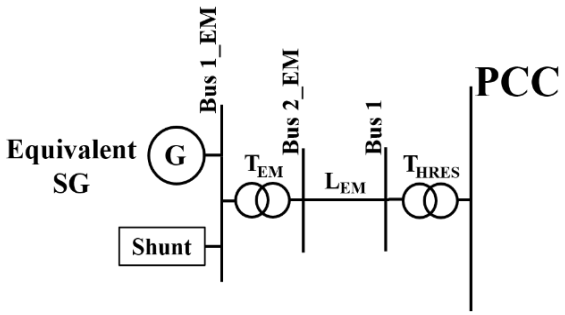

Figure 3.3 Illustration of the EM structure for long-term voltage stability study in DIgSILENT/PowerFactory

The EM structure relies on the work presented in [171]. In [171] a capability curve of a VPP, i.e., a plant comprising a number of RESs and responsive loads spatially distributed across the network, with a single point of connection to the TN was developed to enable participating the VPP in system balancing services. For each possible real power output of the VPP, the minimum and maximum reactive power limits were identified using the optimal power flow (OPF)-based approach. However, different technology mixes in the VPP with the same total real power output can be characterized by considerably different reactive power capabilities. The method in [171] does not provide the guidelines on how to select the reactive power limits for a specific VPP composition. Equivalent modelling of HRES plant presented in this thesis extends the work from [171] by not requiring the

reactive power limits to be determined for all possible plant compositions and defining a single (representative) maximum reactive power limit for a number of HRES plant operating scenarios.

The set of EM parameters includes: the shunt size, the maximum reactive power production of the SG for the analysed SG real power output (Q_{max}), the rated capacity of the SG and step-up transformer, the short-circuit ratio of the step-up transformer (u_k) and the length of the connecting line. The rated capacities of the SG and step-up transformer are the same, and calculated based on the SG real power output (i.e., the total production of the analysed HRES plant composition) and the Q_{max} value. It is assumed that the step-up transformer has no copper loses and the length of the connecting line is equal to the average of the line lengths simulated in the MC procedure.

The shunt size, and the parameters Q_{max} and u_k are estimated through the iterative process that is the same as the one used for defining the unknown parameters of EMs for transient and frequency stability studies. In this stage of the methodology, the real power output of the equivalent SG is equal to the representative HRES plant output for the considered cluster. For each combination of EM parameters, EM accuracy, i.e., the difference between the critical point of the P-V curve produced by the EM and the representative critical point of the relevant cluster, is calculated as follows:

$$EM_{Err}^{Volt}(\%) = 100 \cdot \sqrt{(\Delta_{LM})^2 + (\Delta_{CritBus})^2}, \tag{3.11}$$

$$\Delta_{LM} = \frac{P_{crit}^{EM,i} - P_{crit}^{REP,i}}{P_{crit}^{REP,i}}, \tag{3.12}$$

$$\Delta_{CritBus} = \frac{u_{crit}^{EM,i} - u_{crit}^{REP,i}}{u_{crit}^{REP,i}}, \tag{3.13}$$

where Δ_{LM} and $\Delta_{CritBus}$ is the EM error in terms of the value of load margin and critical bus voltage, respectively, $P_{crit}^{EM,i}$ and $u_{crit}^{EM,i}$ are the load margin and critical bus voltage produced by the EM for the *i*-th cluster, respectively, and $P_{crit}^{REP,i}$ and $u_{crit}^{REP,i}$ are the representative load margin and critical bus voltage of the *i*-th cluster, respectively. The combination of Q_{max}, u_k, and shunt size resulting in the minimum value of the EM_{Err}^{Volt} index represents the optimal combination of parameter values.

3.2.6 Integration of Equivalent Models into DIgSILENT/PowerFactory

DIgSILENT/PowerFactory software provides a feature to automatically select the EM from the set of models stored in the software library. Given that EMs of the HRES plant for transient, frequency and long-term voltage stability studies are in the form of a SG or WF, corresponding built-in models available in DIgSILENT/PowerFactory software are used for creating a set of these EMs in the software library.

When it comes to the EMs of the HRES plant for small-disturbance stability studies (which are in the form of a TF), these models are implemented in DIgSILENT/PowerFactory environment using built-in DIgSILENT Simulation Language (DSL) [164]. Due to DSL requirements, TF (3.2) has to be transformed into the control canonical state-space model. The TF parameters obtained in the previous step of the equivalent modelling procedure are used for calculating the parameters of the corresponding state-space matrices as follows:

$$z_{TF,P}\,(s) = \frac{b_0 s^n + b_1 s^{n-1} + \cdots + b_{n-1} s + b_n}{s^n + a_1 s^{n-1} + \cdots + a_{n-1} s + a_n}, \tag{3.14}$$

$$\begin{gathered} \frac{dx(t)}{dt} = Ax(t) + B\big(u_{PCC}(t) - u_{PCC,ss}\big) \\ z_{TF,P}\,(t) = Cx(t) + D\big(u_{PCC}(t) - u_{PCC,ss}\big), \\ P_{EM}(t) = P_{ss} + z_{TF,P}\,(t) \end{gathered} \tag{3.15}$$

$$A = \begin{bmatrix} 0 & 1 & 0 & \cdots & 0 \\ 0 & 0 & 1 & \cdots & 0 \\ \vdots & \vdots & \vdots & \ddots & \vdots \\ 0 & 0 & 0 & \cdots & 1 \\ -a_n & -a_{n-1} & -a_{n-2} & \cdots & -a_1 \end{bmatrix}, B = \begin{bmatrix} 0 \\ 0 \\ \vdots \\ 0 \\ 1 \end{bmatrix}, D = b_0\,, \tag{3.16}$$

$$C = [(b_n - a_n b_0) \quad (b_{n-1} - a_{n-1} b_0) \quad \ldots \quad (b_2 - a_2 b_0) \quad (b_1 - a_1 b_0)], \tag{3.17}$$

where $z_{TF,P}\,(s)$ is the TF in *s*-domain (obtained when estimating EM parameters), $z_{TF,P}\,(t)$ is the output of the state-space model, and *A*, *B*, *C* and *D* are state-space matrices.

The implementation of state-space EM in DIgSILENT/PowerFactory network model requires an interface in the form of a controllable, constant power load (see Figure 3.4). The load is connected at the PCC and its dynamic behaviour is controlled by the developed EM. Thus, dynamic model designed in DSL environment receives the

information about the pre-disturbance voltage at the PCC and voltage at the PCC at the current time step ($u_{PCC,ss}$ and $u_{PCC}(t)$ in Figure 3.4, respectively) from the network simulation model, and computes the output signal (reference real power of the load marked by $P_{EM}(t)$ in Figure 3.4) at the current time step according to (3.14)-(3.17). Real power at the PCC ($P_{PCC}(t)$ in Figure 3.4) corresponds to the EM output ($P_{EM}(t)$ in Figure 3.4). The reactive power output of the EM is set at the value of the reactive power output of the whole HRES plant at the pre-disturbance state for the considered HRES plant operating point. Modal analysis applied to the system with the EM of the HRES plant instead of the detailed HRES plant dynamic model identifies critical electromechanical mode for the given HRES plant composition on the basis of real power response of the EM, i.e., the structure of the TF-based EM.

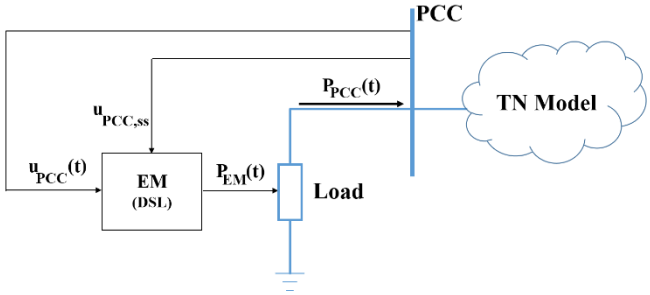

Figure 3.4 Illustration of the concept of EMs for small-disturbance stability studies in DIgSILENT/PowerFactory

3.2.7 Validation of Equivalent Models

For each type of system stability studies, EM validation is performed by simulating all previously defined MC CSs (i.e., cases used for EM development) using EM of the HRES plant instead of the detailed plant model (block {10} in Figure 3.1). For each MC CS and system stability analysis, EM performance is assessed by comparing system stability results obtained using the detailed and EM of the HRES plant. The following index is computed for each small-disturbance stability simulation:

$$EM_{Err}^{Small}(\%) = 100 \cdot \sqrt{{\Delta_{\sigma,i}}^2 + {\Delta_{Freq,i}}^2}, \tag{3.18}$$

$$\Delta_{\sigma,i} = \frac{\sigma^{EM} - \sigma^i}{\sigma^i}, \tag{3.19}$$

$$\Delta_{Freq,i} = \frac{Freq^{EM} - Freq^{i}}{Freq^{i}}, \tag{3.20}$$

where $\Delta_{\sigma,i}$ and $\Delta_{Freq,i}$ are EM error in terms of the damping and frequency of the critical electromechanical mode of the *i*-th CS, respectively, σ^{i} and $Freq^{i}$ are the damping and frequency of the critical electromechanical mode for the *i*-th CS simulated using the detailed plant model, respectively, σ^{EM} and $Freq^{EM}$ are the damping and frequency of the critical electromechanical mode for the *i*-th CS simulated using the EM, respectively.

The accuracy of the developed models for transient, frequency and long-term voltage stability studies is assessed using the indices described by (3.7), (3.8), and (3.11), respectively, with the representative cluster values in these expressions being replaced by the corresponding values obtained by simulating the relevant CS using the full-scale HRES plant dynamic model.

3.3 Test System

The test HRES plant, together with the test TN, is shown in Figure 3.5. The whole system is modelled in DIgSILENT/PowerFactory software package 2020 [164]. The HRES plant contains six renewable generation and storage technologies: a WF, PV plant, run-of-river HPP, biomass plant, biogas plant and BESS. The HRES plant configuration corresponds to an optimal techno-economic solution for the southern part of Greece defined in [172]. Individual plants in the HRES plant are connected to a common 110 kV bus (Bus 16 in Figure 3.5), which is further connected to a 230 kV external TN through a transformer (the grid connection point of the transformer is the PCC of the HRES plant – Bus 17 in Figure 3.5) and four lines (one line is in parallel with two lines connected in series). The external TN (External Grid in Figure 3.5) is modelled as an infinite bus (i.e., as a voltage source with constant voltage amplitude and frequency [102]). System load (connected to Bus 17 in Figure 3.5) is represented by static exponential load model without frequency dependent components. Line and transformer parameters are adopted from [105, 173, 174].

Installation capacities and dynamic model order of individual plants in the test HRES plant are given in Table 3.1. Models of individual plants include the dynamic model of a generation/storage technology and its corresponding control system. The rated power factor of 0.85 is adopted for all SGs, while the capability curves of SGs correspond to

the one given in [175]. The PV plant, WF and BESS operate with a unity power factor, and their capability curves are adopted from [176-178]. The library of DIgSILENT/PowerFactory software package contains the dynamic models of all individual technologies represented in the test HRES plant.

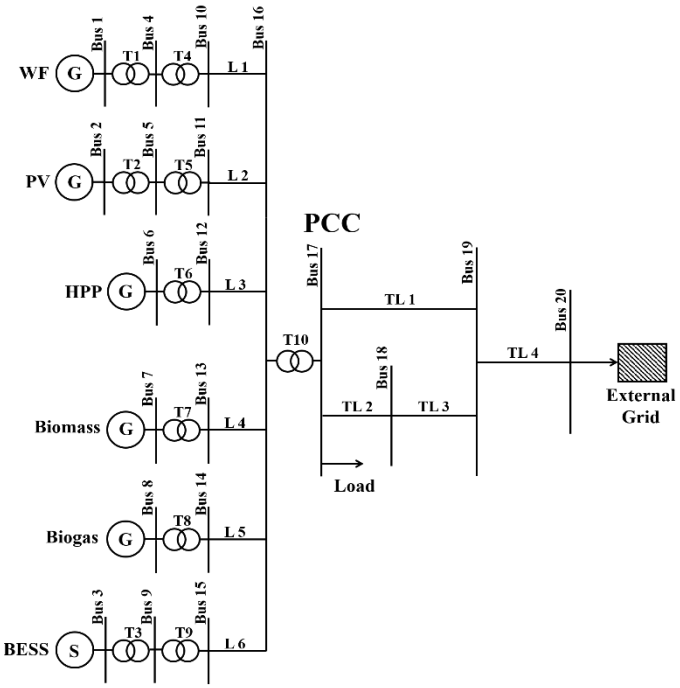

Figure 3.5 The schematic diagram of the test system

Table 3.1 Installation capacities and the order of models of individual plants in the test HRES plant

	Aggregate model of WF	Aggregate model of PV plant	HPP	Biomass plant	Biogas plant	BESS
Rated capacity (MVA)	170	265	295	76.5	76.5	125
Model order	17	14	13	14	11	9
Overall model order	78					

The standard fifth-order SG model is used for modelling the hydro generator in the HRES plant, while the standard sixth-order model is used for the biomass and biogas SGs [102]. SG dynamic parameters are adopted from [173].Governors of type IEEEG3, IEEEG1 and GAST are used in the hydro, biomass and biogas generator control system, respectively [102]. The excitation systems of all SGs are modelled by IEEE DC1A exciter [102]. The parameters of the governor and excitation systems correspond to typical values given in [179, 180]. Both the PV plant and the WF consist of a number of

identical individual units connected in parallel and are represented in DIgSILENT software by corresponding aggregate models (AMs) obtained by scaling up the model of individual units [164]. AM parameters depend on the number of individual units in service, which is determined according to the total production of the RES plant and the rated power of individual units (2 MW for both types of plants), as it is assumed that units in operation generate the rated power output.

The WF consists of DFIGs represented by a generic type 3 wind generator model suitable for large scale stability studies. The model has a structure similar to the one proposed by Western Electricity Coordinating Council (WECC) [22] and International Electrotechnical Commission (IEC) [181] and is available in DIgSILENT/PowerFactory [164]. The control system (illustrated in Figure 3.6) contains pitch control (which includes a PI controller, servo motor represented by a first-order control system, and the minimum and maximum limits of the change and the rate of change of pitch angle), wind turbine and drive train dynamics, which provide the mechanical power of a wind generator. The rotor-side converter controller, which regulates the rotor voltage, is also included in the control system [182]. The rotor-side converter control system relies on two PI-control loops connected in series: a slow (outer) power control loop that provides referent rotor currents based on the deviation of WF real and reactive power from the reference values, and a fast (inner) rotor current control loop that generates referent rotor voltage based on the difference between the measured and referent rotor currents. The proportional gain and integral time constants of the PI controllers in the outer control loop (k_P, k_Q and T_P, T_Q, respectively), and of the PI controllers in the inner loop (k_d, k_q and T_d, T_q, respectively) represent the unknown parameters of the equivalent WF model for transient and frequency stability studies. The WF control system also contains the fault-ride-through capability, the reactive power injection for supporting the terminal voltage, the reactive current injection priority during a fault, the limitation in terms of the rate of real current recovery after a fault, and the total current limitation. Furthermore, under-/over-voltage, under-/over-speed, and rotor overcurrent (crowbar) protection are included in the WF control system.

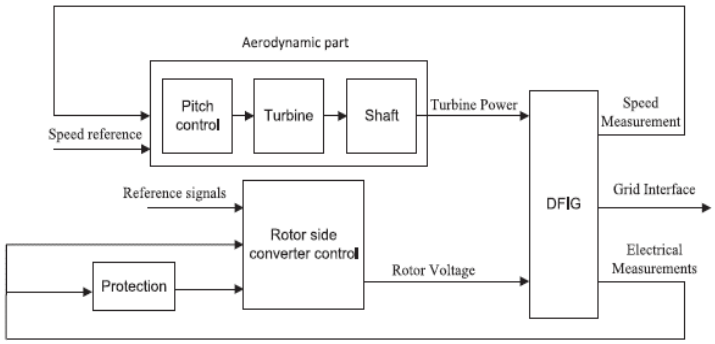

Figure 3.6 The schematic diagram of the WF control system (adopted from [182])

A type 4 wind generator model is used to represent PV units. Both wind generators and PV units can be represented by a type 4 model in stability studies since the converter decouples the dynamics of the source on the DC part from the rest of the power system [182]. This is also suggested by the WECC Renewable Energy Modeling Task Force [23], which develops a PV model by slightly modifying the type 4 wind generator model. The Full Converter Connected (FCC) model used in the study has a similar structure to [22, 181] and is also available in DIgSILENT/PowerFactory [164]. The generator system is represented by a static voltage source (a built-in static generator model in DIgSILENT/PowerFactory), which is typically used for modelling non-rotating generators [183]. The control system of the PV plant (shown in Figure 3.7) maintains real and reactive power at the PV plant connection bus at their referent values by regulating the voltage of the static voltage source. The PV plant control system contains all controllers and protection mechanisms suggested in [22, 181] (the fault-ride-through capability, the reactive power injection for supporting the terminal voltage, the reactive current injection priority during faults, the limitation in terms of the rate of real current recovery after a fault, the total current limitation, the real power reduction in case of an over-frequency event, the over/under-voltage protection and the over/under-frequency protection).

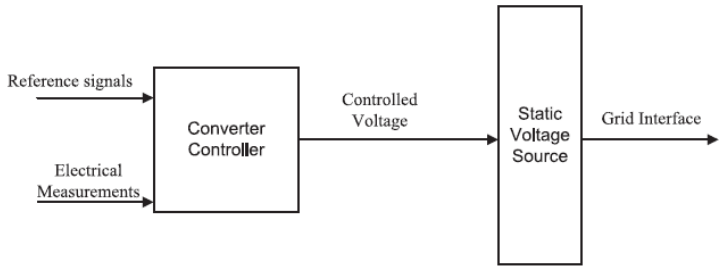

Figure 3.7 The schematic diagram of the PV plant control system (adopted from [182])

The BESS is modelled as a voltage source equipped with the appropriate control system described in detail in [184], [185]. The voltage source model takes into account the battery state of charge and battery internal losses modelled by a constant resistance. The battery voltage varies linearly with the battery state of charge, and battery terminal voltage limits are taken into account as well. The battery control system contains a frequency controller (a proportional control with a dead band), which provides an additional input to a real power-voltage controller. Apart from the input signal generated by the frequency control, the real power-voltage controller has reference real power and terminal voltage values as inputs. The real power control is a PI controller, whereas the voltage control is a slow integrator. The battery control system also incorporates a charge controller with reactive current priority during a fault, and the state-of-charge, the total current and the apparent power limits.

3.4 Case Studies

A one-year historical HRES plant production dataset with a one-hour sampling rate was generated based on typical annual solar irradiation, wind speed, electricity price and demand profiles in the southern part of Greece [172]. At each time step, power outputs of individual technologies in the HRES plant were determined through an optimization procedure with the aim of maximizing demand provision while minimizing total plant costs. Thus, the number of rows in the historical HRES plant production dataset corresponds to the number of time steps in the investigated historical period, while the number of columns in the dataset is equal to the number of individual technologies in the HRES plant (i.e., each row in the dataset is a historical HRES plant composition).

The first stage of the methodology involves the identification of characteristic annual HRES plant compositions on the basis of historical plant production data using the fuzzy c-means clustering algorithm. The change of the clustering evaluation indices MSE, CDI and MIA with the number of clusters, together with the indication of the optimal number of clusters, is shown in Figure 3.8. Given that the knee of the curve is not noticeable for any of the clustering indices, the two-tangent method presented in [160] is used for estimating the knee (as shown in Figure 3.8). The MSE, CDI and MIA indices suggest different number of clusters: 9, 5 and 11, respectively. Therefore, the fuzzy c-means method divides the historical dataset into nine groups. Nine typical annual plant compositions are given in Table 3.2.

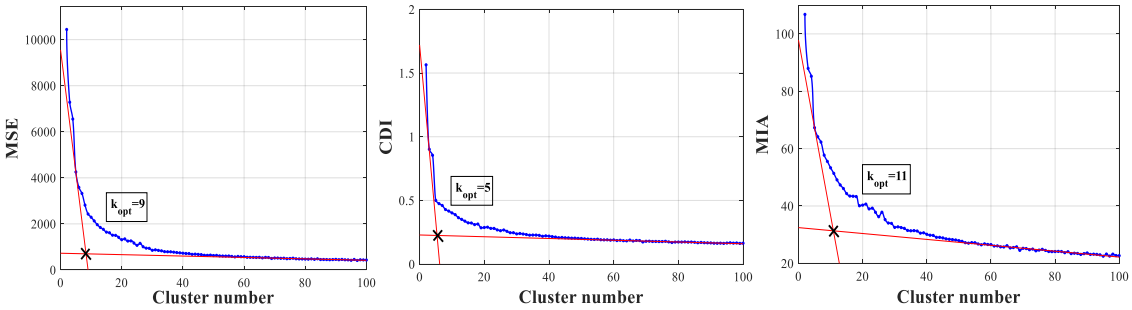

(a) (b) (c)

Figure 3.8 The change of the MSE (a), CDI (b) and MIA (c) with the number of clusters in the case of historical HRES plant production data clustering

Table 3.2 Characteristic annual HRES plant compositions (base power is the rated power of the individual plant)

Cluster number	HRES plant composition					
	WF (%)	PV plant (%)	HPP (%)	Biomass plant (%)	Biogas plant (%)	BESS (%)
1	7.1	1.5	0	84.2	75.8	0
2	94.1	2.3	0	0	0	0
3	45.9	4.5	0	62.6	18.3	1.4
4	74.1	30.2	0	0	0	-10.9
5	16.5	9.8	0	0	0	72.9
6	87.1	72.5	0	0	0	-0.3
7	11.8	49.8	0	0	0	-1.2
8	14.1	1.5	43.6	0	0	0.1
9	10.6	76.2	0	0	0	-44.3

Probabilistic MC procedure involves generating a thousand MC simulations per characteristic annual HRES plant composition (the choice of the number of MC simulations is explained in Section 4.4). In each MC simulation, lengths of connecting lines (lines L 1 – L 6 in Figure 3.5) are sampled uniformly between 0.5 km and 5 km (in case of larger variation in line lengths it would be less probable for the individual plants to be connected to the same TN bus). The variation in the length of connecting lines of the PV plant and WF represents the variation in the distance of dominant (in terms of power production value) individual units in these plants from the PCC. Namely, the PV plant and WF are modelled as a single aggregated plant in the detailed HRES plant dynamic model, whereas in reality these plants consist of a large number of spatially distributed units. Depending on weather conditions (i.e., wind speed and solar irradiance intensity in the case of the WF and PV plant, respectively) it might occur that individual units located in a certain part of the plant have larger power output compared to the remaining units, which could then be represented in the AM of the PV plant and WF by

modifying the length of the respective connecting line to the PCC. Even though the remaining individual plants within the test HRES plant (i.e., the HPP, biomass and biogas plant, and BESS) do not contain spatially distributed individual units, the lengths of their connecting lines are varied in MC simulations as well, in order to investigate the influence of the lengths of connecting lines (i.e., the proximity of the relevant plant to the PCC) on the overall transient response of the HRES plant and ultimately on the stability performance of the system.

As for uncertainties in short-term production forecast, in each set of 1,000 MC simulations, the power output of each individual plant is sampled uniformly in the range of ±5% around the corresponding value in the typical HRES plant composition. A single TN operation point is considered in all cases – the TN demand (represented by the load connected to Bus 17 in Figure 3.5) corresponds to an average annual HRES plant production of 155 MW. The set of 9,000 MC CSs is simulated for each of four types of system stability studies using the test system presented in Figure 3.5. The obtained system stability results as well as developed EMs are presented in the following sections.

3.4.1 Small-disturbance Stability Study

As mentioned in Section 3.2.4, the focus of small-disturbance stability analysis is on electromechanical modes. The least damped (the critical) electromechanical mode is defined for each MC simulation and shown in Figure 3.9 (a). Given that only three out of nine typical annual HRES plant compositions (i.e., compositions 1, 3, and 8) have at least one SG-based power plant in service, electromechanical modes are present only in the case of these three plant compositions. The results of small-disturbance stability analysis of the above-mentioned three HRES plant compositions can be divided into two groups as shown in Figure 3.9 (a).

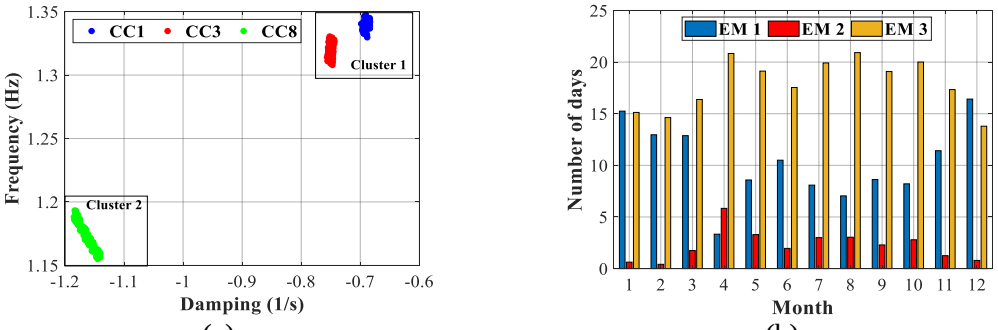

(a) (b)

Figure 3.9 (a): Small-disturbance system stability results (CC: characteristic HRES plant composition); (b) The expected time of use of EMs during the year

Cluster 1 contains the results of the MC CSs based on compositions 1 and 3 that are characterized by two SGs (the biomass and biogas power plant) in operation. These two compositions result in the least damped and fastest electromechanical mode (on average, -0.72 1/s and 1.33 Hz, respectively) among the recorded critical electromechanical modes. The second cluster includes composition 8, i.e., the composition with the HPP as a single SG in service. Electromechanical modes produced by cluster 2 have frequency and damping of about 1.17 Hz and -1.16 1/s, respectively. Therefore, all analysed MC CSs can be divided into three groups (two groups of cases producing electromechanical modes and a group of cases without an SG-based power plant in service) based on their impact on small-disturbance stability of the system.

Three clusters of MC cases indicate that three EMs are required for representing the considered HRES plant operating conditions in small-disturbance stability studies. The expected number of days per month covered by each of the equivalents is shown in Figure 3.9 (b). Cluster/EM 3 and 1 represent around 60% and 30% of the historical dataset, respectively, while the remaining EM 2 covers less than 10% of the data. EM 3 is a dominant equivalent in each month, except during the winter period when both EM 1 and EM 3 have similar time of use.

The parameters of the representative electromechanical mode (given in Table 3.3) are used for specifying the complex poles of TFs for clusters 1 and 2, meaning EM 1 and 2 are in the form of the second-order TF. In the case of EM 3, that is, HRES plant compositions without SGs in service, TF poles cannot be initialized in advance. In this case both TF numerator and denominator coefficients are estimated in the parameter estimation procedure.

In order to estimate TF numerator for EM 1 and EM 2, and the whole TF structure for EM 3, time domain electromechanical simulations are performed for representative HRES plant compositions of the three clusters. Representative HRES plant composition for cluster 1 and 2 is a simulated HRES plant composition that results in the cluster medoid, i.e., the critical electromechanical mode that is the most similar to representative electromechanical mode for the given cluster. (*Note*: Identifying a representative HRES plant composition as an average of plant compositions associated with the analysed cluster (i.e., calculating the mean of real power outputs from the cluster per individual

technology) can result in a representative plant composition considerably different from the compositions in the cluster if these compositions are very diverse. As a result, due to the high sensitivity of the small-disturbance stability results to system operating point, the representative plant composition obtained in this way would be characterized by the critical electromechanical mode different from the representative mode of the given cluster. This was the case with cluster 1 containing plant compositions 1 and 3. Adopting the cluster medoid approach for defining the representative HRES plant composition solved the issue.) Table 3.3 shows the parameters of the cluster medoids for clusters 1 and 2. Representative mode and cluster medoid for cluster 2 are identical, whereas the difference between the parameters of the representative mode and cluster medoid for cluster 1 is around 3% (only 0.02 1/s) and 0.8% for damping and frequency value, respectively. Small difference between the parameters of the representative cluster mode and cluster medoid justifies the use of the selected electromechanical simulations for specifying TF numerator. As aforementioned, a representative plant composition for a cluster of electromechanical modes is a simulated MC plant composition that results in the critical electromechanical mode corresponding to a cluster medoid. Given that plant compositions in cluster 3 do not produce electromechanical modes, the representative HRES plant composition for this cluster is defined as an average of HRES plant compositions assigned to this cluster.

A small increase in the system load (represented by load connected to Bus 17 in Figure 3.5) of 1% is used as a system disturbance in electromechanical simulations. The simulations last 10 seconds and the disturbance occurs at t=1 second. The lengths of all connecting lines (L 1- L 6 in Figure 3.5) are set at 2.75 km as it corresponds to the average of the line lengths simulated in the MC procedure. Deviation of real power response at the PCC from its pre-disturbance steady state value is shown in Figure 3.10 for all electromechanical simulations.

Table 3.3 The representative critical electromechanical mode and cluster medoid for clusters 1 and 2

	Representative mode		Cluster medoid	
Cluster	Damping (1/s)	Frequency (Hz)	Damping (1/s)	Frequency (Hz)
1	-0.72	1.33	-0.70	1.34
2	-1.16	1.17	-1.16	1.17

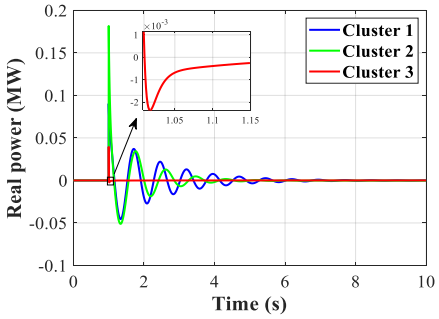

Figure 3.10 Deviation of real power responses at the PCC (obtained in electromechanical simulations) from their pre-disturbance steady state values

TF parameter estimation process (relying on power responses presented in Figure 3.10) terminates when the improvement in the RMSE value between two consecutive iterations becomes smaller than 0.01%. The obtained expressions for TFs for all three EMs are as follows:

$$TF_{EM\,1} = \frac{-2370s^2-857.5s-446.4}{s^2+1.44s+70.3}, \tag{3.21}$$

$$TF_{EM\,2} = \frac{-3621s^2+3414s-1103}{s^2+2.32s+55.65}, \tag{3.22}$$

$$TF_{EM\,3} = \frac{-420.1s^3+2.24\cdot10^4s^2+1.23\cdot10^5s-1.61\cdot10^4}{s^3+330.2s^2+1.15\cdot10^4s+8295}. \tag{3.23}$$

EM 3 is characterized by three real poles: -290.86 1/s, -38.6 1/s, and -0.74 1/s. (*Note*: Given that the deviation of the real power response of the HRES plant from the pre-disturbance value is insignificant for EM 3 (see Figure 3.10), and plant compositions associated with EM 3 do not produce electromechanical modes, another option for the HRES plant representation in the case of plant compositions with converter-connected technologies only is a negative constant power load model (instead of $TF_{EM\,3}$).)

MC CSs generated by plant compositions 1, 3 and 8 are simulated in DIgSILENT/PowerFactory using the corresponding EMs instead of the detailed HRES plant dynamic model. Figure 3.11 illustrates the error of EM 1 and EM 2 in terms of the damping and frequency of the critical electromechanical mode in the form of boxplots. Outliers are marked by red asterisks, whereas whiskers cover 99.3% of data in the case of normal distribution. The EM implemented in DIgSILENT/PowerFactory results in the representative critical electromechanical mode of the relevant cluster as EM parameters

do not depend on HRES plant power production, and thus, EM error is determined by the difference between the parameters of the representative mode and the actual critical electromechanical mode for a given MC CS. As seen in Figure 3.11, developed models have slightly higher accuracy in terms of the frequency of the critical electromechanical mode than in the case of damping value. The error in the damping value is between -4% and 4.5% for most of the cases represented by EM 1, whereas the error in the frequency value for EM 1 as well as the error in the damping and frequency for EM 2 is within (-1, 1)% for almost all simulated cases.

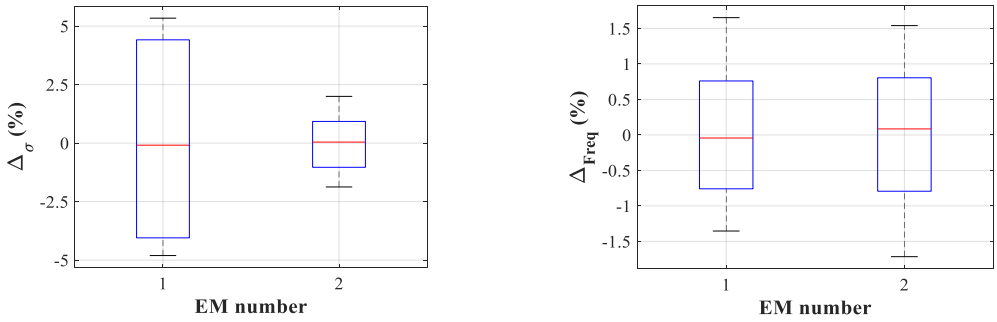

(a) (b)

Figure 3.11 MC CSs used for model development: EM accuracy in terms of damping (a) and frequency (b) of the critical electromechanical mode

3.4.2 Transient Stability Study

In all MC CSs, a three-phase self-clearing short-circuit fault occurs at Bus 18 (see Figure 3.5) at t=1 s and lasts for 100 ms. The total duration of simulations is 10 seconds. The obtained 9,000 HRES plant real power responses can be divided into four clusters according to similarity in time, meaning four DEMs are required for representing the considered HRES plant operating scenarios in transient stability simulations. Four clusters of power responses, together with cluster representative responses (shown in black), are presented in Figure 3.12.

Power responses generated by HRES plant compositions with SGs in service are divided into two clusters: cluster 1 (responses from typical plant composition 1) and cluster 2 (responses from typical plant compositions 3 and 8). Table 3.4 provides the information about the total HRES plant production, SG share and the type of SGs in operation for typical HRES plant compositions 1, 3 and 8. As can be seen, the clustering of power responses depends on SG share in plant composition and the type of SGs in service (the total HRES plant output is similar for all compositions). Namely, compositions 1 and 3 contain the same two SGs in service (the biomass and biogas power plant), but the SG share in plant composition 3 is about a half of that in plant composition 1. On the other

hand, the participation of SGs in the HRES plant production for compositions 1 and 8 is similar, but plant composition 8 has the HPP as a single SG in operation.

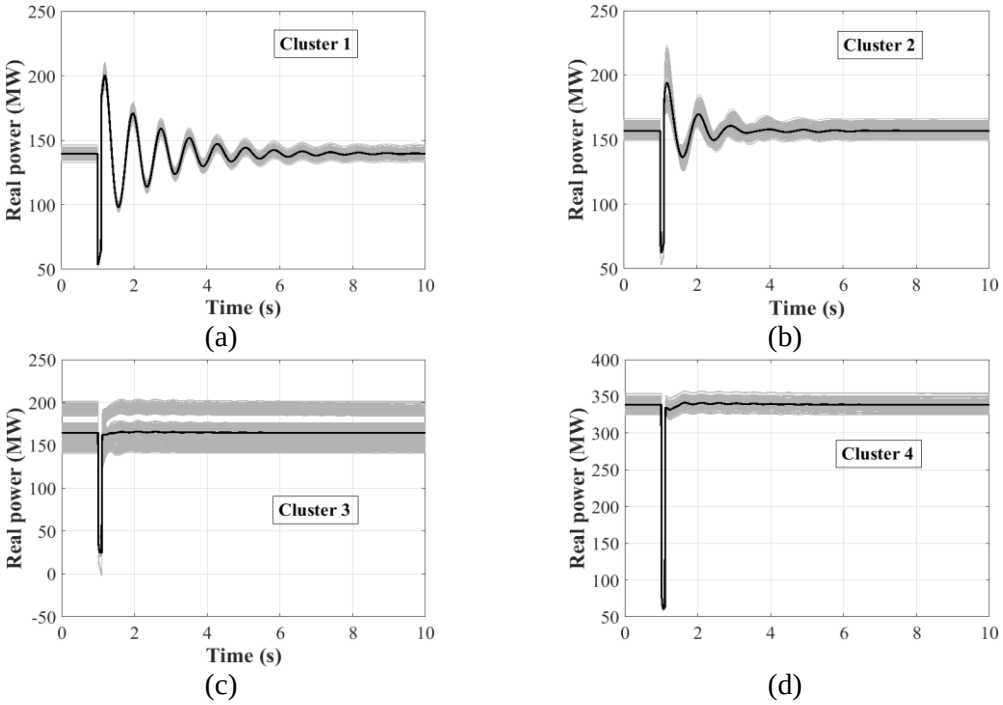

Figure 3.12 Simulated HRES plant real power responses (grey) and representative responses (black) ((a): Cluster 1; (b): Cluster 2; (c): Cluster 3; (d): Cluster 4)

Table 3.4 Total HRES plant production, SG share and type of SGs in service for typical plant compositions containing SGs

Cluster	Composition	HRES plant output (MW)	SG share (%)	SG in service
1	1	138.4	88.4	biomass and biogas power plant
2	3	153.6	40.3	biomass and biogas power plant
	8	156.7	82.1	HPP

MC real power responses produced by compositions containing converter-connected technologies only are divided into two clusters (cluster 3 and 4) mainly due to significant difference in the pre-disturbance HRES plant power output. Cluster 4 contains the responses from a single plant composition, composition 6, with the steady state HRES plant production of around 340 MW. On the other hand, the pre-disturbance HRES plant power output for compositions 2, 4, 5, 7, and 9 in cluster 3 is between 140 MW and 190 MW.

Figure 3.13 presents the expected time of use of EMs during the year, which was determined using the historical production dataset. EM 3 and EM 1 represent around a

half and quarter of the historical dataset, respectively, while EM 2 and EM 4 cover about 15% and 5% of the data, respectively. EM 3 is a dominant model in each month, except in January, February and December when EM 1 and EM 3 are expected to be used similar number of days.

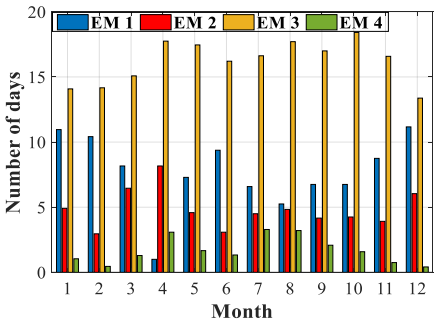

Figure 3.13 The expected time of use of EMs for transient stability studies

Clusters 1 and 2 are represented by an equivalent SG, while an equivalent WF is used for modelling responses from the remaining two clusters (compositions with converter-connected technologies only). The ranges of values used for estimating the unknown equivalent SG parameters are: (1, 10) s for the inertia constant, and (1, 100) p.u. for the damping coefficient. When it comes to the equivalent WF model, it is assumed that the parameters of the two PI controllers in the outer control loop are the same (as recommended in [164]). The same assumption is adopted for the parameters of the PI controllers in the inner loop [164]. In the parameter estimation procedure, the proportional gain of the PI controllers in the outer loop was varied from 0.1 p.u. to 5 p.u., while the range of (0.01, 0.1) p.u. was used for the gain of the PI controllers in the inner loop. The range of (0.01, 0.1) s and (0.005, 0.05) s was adopted for the time constants of the PI controllers in the outer and inner loop, respectively. The minimum and maximum limits of the ranges used in the estimation process were established by the trial-and-error method.

For each cluster, the representative HRES plant production (P_{HRES}^{REP}), EM parameters as well as the accuracy of EM for the representative plant response (used for EM parameter estimation) are given in Table 3.5. EM 1 and 2 have similar inertia constant values, but the damping coefficient for EM 2 is considerably larger than for EM 1 (this is expected as oscillations in power responses from cluster 1 last about 8 seconds, while they disappear within 4 seconds in the case of cluster 2, as shown in Figure 3.12 (a) and (b)). For both equivalent WF models, the parameters of the PI controllers in the inner loop are

almost identical to the default values used for modelling the WF in the detailed HRES plant dynamic model. All four EMs are characterized by high accuracy for the representative case - the average deviation of EM real power responses from the representative cluster responses (i.e., EM_{Err}^{Trans} value) is between 0.21% (EM 3) and 1.22% (EM 1).

Table 3.5 Representative HRES plant production, EM parameters and EM accuracy for the representative case

EM	P_{HRES}^{REP} (MW)	H (s)	K_D (p.u.)	k_P, k_Q (p.u.)	T_P, T_Q (s)	k_d, k_q (p.u.)	T_d, T_q (s)	EM_{Err}^{Trans} (%)
1	140	7.5	21.25	-	-	-	-	1.22
2	157	8	59.5	-	-	-	-	1.00
3	164	-	-	2.6	0.07	0.05	0.01	0.21
4	338	-	-	0.8	0.03	0.05	0.01	0.29

In order to further assess EM accuracy, all previously developed MC CSs were simulated using four EMs instead of the full-scale HRES plant dynamic model. Figure 3.14 shows the obtained EM_{Err}^{Trans} values for each EM in the form of boxplots. All EMs are capable of reproducing the real power response of the detailed HRES plant model with high accuracy. The median EM error for EM 1 and EM 2 is about 1.2%, whereas the 50th percentile of EM_{Err}^{Trans} values for EM 3 and EM 4 is 0.4% and 0.25%, respectively. Furthermore, the maximum EM_{Err}^{Trans} value for EM 1-4 is around 1.5%, 1.3%, 1.1% and 0.6%, respectively.

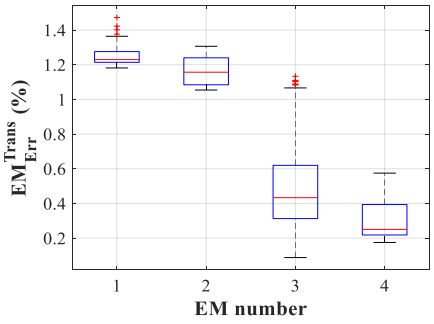

Figure 3.14 MC CSs used for model development: The accuracy of EMs of the HRES plant for transient stability studies

3.4.3 Frequency Stability Study

Figure 3.15 illustrates frequency nadir in the case of nine typical HRES plant compositions for an increase of 50% in the total system load (classified as a large contingency in [186]). As can be seen, there is no significant drop in the frequency

responses; the frequency nadir is between 49.64 Hz and 49.89 Hz (frequency is calculated in DIgSILENT/PowerFactory software package as a rate of change of the phase angle of the voltage at the PCC). In order to obtain more realistic system stability results with a mid-size system disturbance (about (10 - 20)% of the global load [186]), the external TN (External Grid in Figure 3.5) has to be represented by a SG with the rated capacity smaller than 400 MVA. Thus, in frequency stability studies, the external TN is represented by the SG with the installation capacity of 384 MVA as the parameters for this generator size are available in [173]. The standard sixth-order model is used for modelling the generator, whereas the IEEE DC1A exciter and IEEEG1 governor represent the SG control system [102].

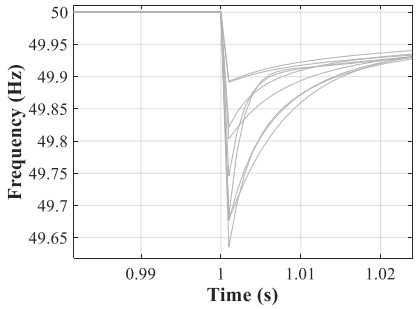

Figure 3.15 Frequency nadir for typical HRES plant compositions in the case of a 50% load increase and the external TN represented by the infinite bus

An increase of 10% in the total system load was used as a system disturbance in all MC CSs [186]. Frequency stability results (the maximum RoCoF and frequency nadir) for all analysed cases are presented in Figure 3.16 (a). As can be seen, the obtained results can be divided into three clusters/groups. Cluster 1 includes the results from HRES plant composition 8, which is the only plant composition with the HPP in service (the HPP is the only SG in operation). Cluster 2 contains MC CSs produced by plant compositions 1 and 3 with two SGs in service (the biomass and biogas power plant), while all plant compositions consisting of converter-connected technologies only are allocated to cluster 3. As expected, cluster 3 is characterized by the smallest frequency nadir and the largest RoCoF. The representative values of the maximum RoCoF and frequency nadir, together with the representative HRES plant production, are given in Table 3.6 for each cluster, and these values are used in the EM parameter estimation procedure.

The expected time of use of the EMs during the year is shown in Figure 3.16 (b). EM 3 represents around 60% of the historical data and is a dominant model in each month, except during the winter (the January-March and November-December periods) when

EM 2 is used a considerable number of days per month as well. EM 2 is an adequate equivalent for about 30% of the historical dataset, whereas EM 1 covers less than 10% of the data.

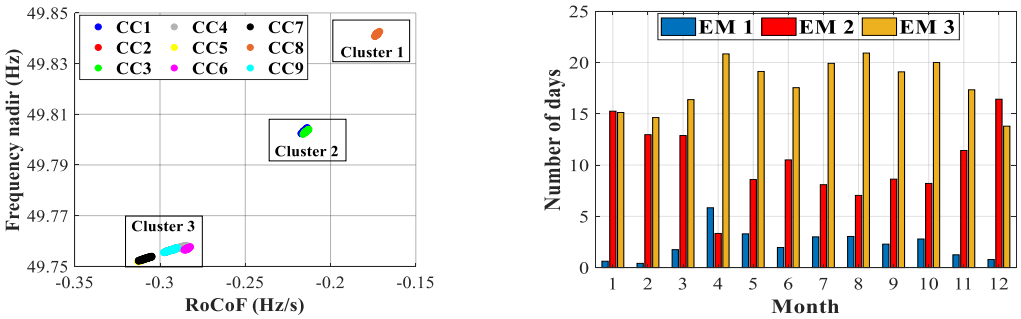

(a) (b)

Figure 3.16 (a): Frequency system stability results (CC: characteristic HRES plant composition); (b) The expected time of use of EMs during the year

Table 3.6 The representatives of clusters of frequency stability results

Cluster	P_{HRES}^{REP} (MW)	Frequency nadir (Hz)	RoCoF (Hz/s)
1	157	49.84	-0.17
2	146.1	49.80	-0.21
3	194	49.76	-0.30

The equivalent SG is developed for clusters 1 and 2, whereas the equivalent WF model is used for representing cluster 3. The ranges of values used for estimating the parameters of the equivalent SG model are the same as for transient stability study. As for the equivalent WF model, the gain of the PI controllers in the outer loop was varied between 1 p.u. and 5 p.u., while the range of (0.005, 0.1) p.u. was adopted for the gain of the PI controllers in the inner loop. The range of (0.005, 0.05) s was used for the integral time constants of all PI controllers. EM parameters and accuracy for the representative CS are given in Table 3.7. The EM_{Err}^{Freq} value is determined by the error in RoCoF value for all three equivalents as EMs provide frequency nadir values almost identical to the representative ones. Still, the RoCoF error is below 1% for all EMs. The RoCoF error in absolute units is between 0.3 mHz/s (EM 2) and 1.2 mHz/s (EM 1).

Table 3.7 The parameters of EMs for frequency stability studies

EM	H (s)	K_D (p.u.)	k_P, k_Q (p.u.)	T_P, T_Q (s)	k_d, k_q (p.u.)	T_d, T_q (s)	EM_{Err}^{Freq} (%)	Δ_{Fnadir} (%)	Δ_{RoCoF} (%)
1	2.5	10.2	-	-	-	-	0.7	0	-0.7
2	1.7	5.1	-	-	-	-	0.14	-0.01	-0.14
3	-	-	2.5	0.01	0.01	0.01	0.24	-0.01	-0.24

Figure 3.17 presents the results of EM validation for all MC CSs used for model development. The maximum frequency nadir error is 0.12%, whereas the maximum RoCoF error is around 5%. Still, the median RoCoF error for EM 1, EM 2 and EM 3 is -0.18%, -1.07% and 1.3%, respectively. EM 1 has the highest accuracy, which is expected as it covers MC CSs produced by a single plant composition 8.

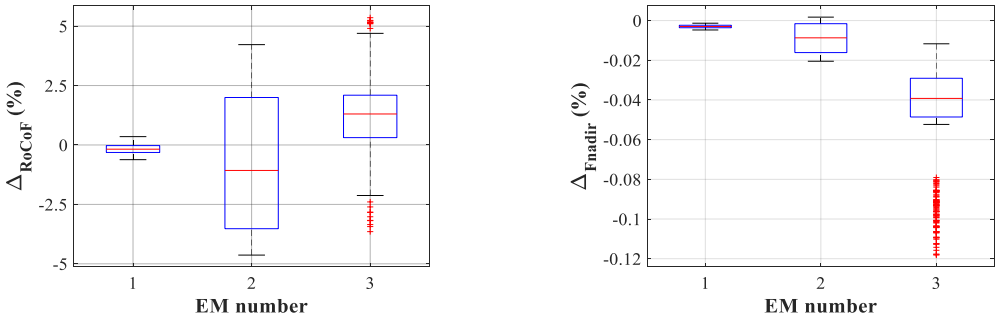

(a) (b)

Figure 3.17 MC CSs used for EM development: EM accuracy in terms of RoCoF (a) and frequency nadir (b)

Figure 3.18 presents the RoCoF and frequency nadir error expressed in absolute units (i.e., in mHz/s and mHz, respectively) for all three EMs. In [187] the RoCoF error of 0.1 Hz/s was stated as the maximum acceptable error from end-user's side according to an extensive survey. As can be seen, all three equivalents satisfy the accuracy requirement. As for the frequency nadir error, unlike in the case of EM 1 and EM 2, the inaccuracy in frequency nadir value is larger than the maximum allowed frequency measurement error of 10 mHz ([167]) for almost all cases in cluster 3. Among cases represented by EM 3, MC CSs generated by plant composition 6 have the highest frequency nadir error; Δ_{Fnadir} value for these cases is almost three times larger than the corresponding value for the remaining cases in cluster 3 (48 mHz compared to 17 mHz). This is due to characteristic plant composition 6 being characterized by significantly larger HRES plant power production compared to the representative HRES plant production and the power output of other plant compositions represented by EM 3.

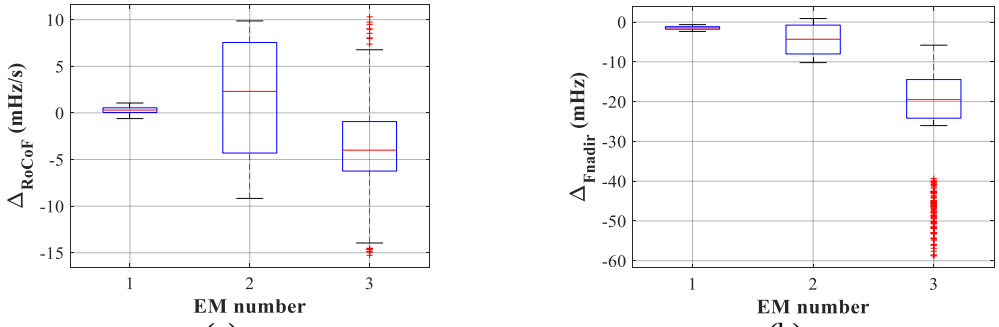

(a) (b)

Figure 3.18 MC CSs used for EM development: EM accuracy in absolute units in terms of RoCoF (a) and frequency nadir (b)

3.4.4 Long-term Voltage Stability Study

Long-term voltage stability results for all MC CSs, together with the indicated clusters, are shown in Figure 3.19 (a). Given that the minimum recorded critical bus voltage value over all MC simulations is about 0.5 p.u., it can be concluded that the test system is not prone to long-term voltage stability, as otherwise voltage collapse would have happened at much higher value of critical bus. In the case of long-term voltage stability analysis, MC CSs can be grouped into five clusters and the data about cluster representatives are given in Table 3.8. Clusters 1 and 5 consist of MC CSs produced by a single plant composition – composition 8 and 6, respectively. Characteristic HRES plant composition 8 is the only composition with the HPP in service (the HPP is also the only SG in operation). Plant composition 6 has significantly larger total HRES plant output compared to other plant compositions, and the WF and PV plant provide the total plant production. Cluster 2 represents the remaining HRES plant compositions with SGs in service - compositions 1 and 3 (the biomass and biogas power plants are in operation). Clusters 3 and 4 are generated by typical plant compositions having only converter-connected technologies in service: cluster 3 contains compositions 5, 7 and 9, while compositions 2 and 4 belong to cluster 4. Compositions belonging to cluster 4 are characterized by dominant production from the WF. On the other hand, the HRES plant production is mainly provided by the BESS in the case of plant composition 5, whereas compositions 7 and 9 are characterized by the dominant production from the PV plant.

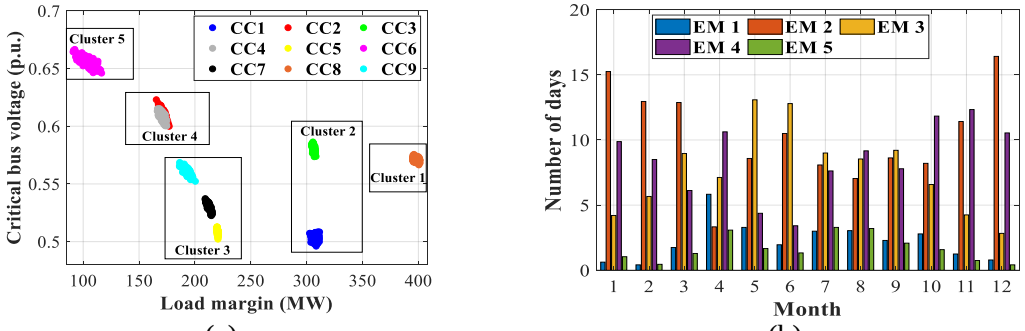

(a) (b)

Figure 3.19 (a): Long-term voltage system stability results (CC: characteristic HRES plant composition); (b) The expected time of use of EMs during the year

Duration of clusters per month, that is, the expected time of use of the EMs, is presented in Figure 3.19 (b). EM 2 – 4 are the most dominant models in almost every month during the year. EM 2 and EM 4 cover about 35% and 30% of the data, respectively, while

around a quarter of the historical production dataset is assigned to EM 3. The remaining two EMs represent around 5% of the data each.

Table 3.8 The representatives of clusters of long-term voltage stability results

Cluster	Load margin (MW)	Critical bus voltage (p.u.)	P_{HRES}^{REP} (MW)
1	398	0.57	159.1
2	307.2	0.54	148.2
3	208.6	0.53	155.7
4	171	0.61	181.1
5	103.9	0.66	341.6

The final step in the study involves EM development for each of the five previously defined clusters. The parameter Q_{max} was estimated from the range of (-0.9, 0.9) p.u. in the optimization process, the parameter u_k was varied from 5% to 30%, while the shunt size was defined using the range of (0, 200) Mvar. The length of the line connecting the equivalent SG to the PCC is set at 2.75 km as it corresponds to the average of the line lengths simulated in the MC procedure. In the EM parameter estimation process, SG power output is equal to the representative HRES plant output for the particular cluster (given in Table 3.8). The parameters of all five EMs as well as the deviation of EM results from the representative long-term voltage stability results are given in Table 3.9. Lack of reactive power support in the case of converter-connected plants is reflected in the low value of parameter Q_{max}. Shunt inductor is required in the case of EM 1 and EM 2, whereas shunt capacitor is needed for EM 4 and EM 5. EM 3 does not require any shunt element. The difference between the load margin value and critical bus voltage obtained using the EMs and the corresponding representative values is on average 4% and 2.7%, respectively, while the maximum of both Δ_{LM} and $\Delta_{CritBus}$ indices is around 5%. EM 2 is characterized by the lowest accuracy in terms of critical bus voltage, because cluster 2 is the most dispersed cluster in terms of critical bus voltage values.

Table 3.9 The parameters of EMs for long-term voltage stability studies

EM	Q_{max} (p.u.)	u_k (%)	Shunt size (Mvar)	EM_{Err}^{Volt} (%)	Δ_{LM} (%)	$\Delta_{CritBus}$ (%)
1	0.75	0.5	100	4.77	-4.27	-2.12
2	0.25	3.5	20	6.24	-3.86	4.90
3	-0.30	3.5	0	3.88	3.26	2.10
4	-0.50	5	-90	5.83	4.68	-3.48
5	-0.30	7	-80	4.07	3.95	0.98

Model accuracy is further assessed using all 9,000 MC CSs. The errors in the values of load margin and critical bus voltage (i.e., the Δ_{LM} and $\Delta_{CritBus}$ indicators given by (3.12) and (3.13), respectively) are computed for each MC simulation and shown in Figure 3.20

in the form of boxplots. Figure 3.20 indicates that the developed EMs are sufficiently accurate. The deviation of the load margin and critical bus voltage values produced by EMs from the accurate values is below 5% for the majority of the analysed cases. EM 3 is characterized by the lowest accuracy in terms of load margin, with the 95th percentile of the error being equal to 12.4%, while the remaining models have similar Δ_{LM} values (the 95th percentiles for these models are below 7%). This is expected as cluster 3 is the most dispersed cluster in terms of the load margin values of the allocated cases. When it comes to the critical bus voltage, around 75% of the simulated cases are characterized by the error within the range of (-5, 5)%. EM 2 has the highest error (as in the case of representative cases used for parameter estimation), with the 95th percentile of the error being equal to 13.6%.

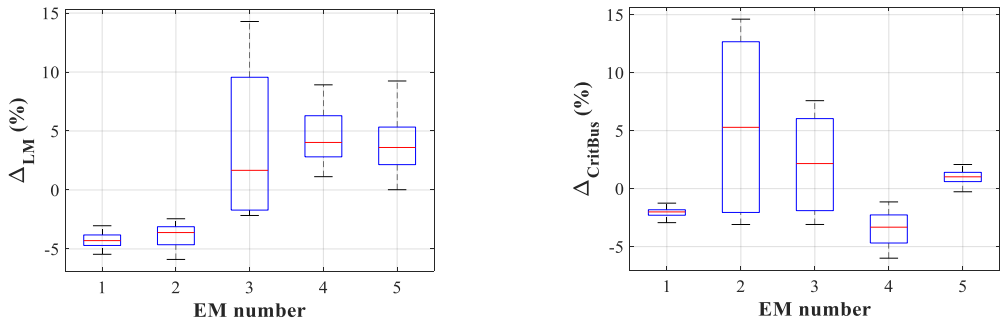

Figure 3.20 MC CSs used for EM development: EM accuracy in terms of load margin (a) and critical bus voltage (b)

3.4.5 Discussion

In each of the considered system stability study, the introduced uncertainties in the power output and location of the individual plants in the HRES plant do not have a considerable impact on power system stability performance. Table 3.10 summarizes EM characteristics and the clusters/groups of plant compositions represented by a common EM for all four types of system stability studies. In all four system stability analyses, plant compositions with converter-connected technologies only are not grouped together (i.e., cannot be represented by the same EM) with any plant composition having SGs in service. HRES plant compositions with the biomass and biogas power plant (compositions 1 and 3) are clustered together, and the composition with the HPP in operation (composition 8) represents a single cluster in all system stability studies except

in the case of transient stability study. In addition, the grouping of plant compositions for small-disturbance and frequency stability studies is the same.

Table 3.10 EM characteristics and clusters of typical plant compositions for all four types of system stability studies

Stability	EM type	No. of EMs	Min EM order	Max EM order	Clusters of plant compositions
Small-disturbance	black-box	3	2	3	(1, 3); (8); (2, 4-7, 9)
Transient	grey-box	4	2	17	(1); (3, 8); (2, 4, 5, 7, 9); (6)
Frequency	grey-box	3	2	17	(8); (1, 3); (2, 4-7, 9)
Long-term voltage	grey-box	5	2	2	(8); (1, 3); (5, 7, 9); (2, 4); (6)

Equivalent modelling of the test HRES plant provides a considerable simplification of the mathematical model of the plant. Namely, the detailed HRES plant dynamic model contains 78 differential equations, whereas EM order is between 2 and 17 (the equivalent WF model for transient and frequency stability simulations). The number of EMs required for representing the considered operating conditions of the test HRES plant in system stability simulations ranges from three (small-disturbance and frequency stability) to five (long-term voltage stability). It should be noted that EMs were developed on the basis of a single TN operating point.

The EM structure for small-disturbance stability analysis corresponds to a black-box model, while EMs for the remaining three system stability studies are grey-box equivalents. The equivalent second-order SG and the equivalent WF (for plant compositions with converter-connected technologies only) were chosen as grey-box equivalents in transient and frequency stability studies, whereas only the equivalent SG was used in long-term voltage stability analysis. The equivalent SG could not represent HRES plant compositions without SGs in service in transient and frequency stability studies as it could not provide non-oscillatory real power responses and high RoCoF values, respectively, associated with the dynamic behaviour of converter-connected technologies. Unlike the grey-box equivalents for transient and frequency stability that are directly connected to the PCC, EM for long-term voltage stability studies is connected to the PCC in the same way as individual SG-based plants within the HRES plant, i.e., through a line and two transformers (see Figure 3.5). Introducing impedances between the equivalent SG and the PCC was necessary in order to obtain acceptable error values

in both load margin and critical bus voltage value, in particular in the case of HRES plant compositions comprising converter-connected technologies only. In the case of the equivalent SG directly connected to the PCC, large reduction in reactive power capability of the equivalent SG is needed in order to obtain low load margin in the case of HRES plant compositions without SG-based plants in service, which in turn results in a considerable reduction in pre-disturbance network voltage magnitudes, and consequently large error in critical bus voltage value (compared to the results obtained with the detailed HRES plant model). Increasing reactive power capability of the equivalent SG results in an increase in pre-disturbance network voltage magnitudes and a reduction in the error in critical bus voltage, but the error in load margin value significantly increases. The line between two transformers used in the EM configuration does not have a significant impact on EM accuracy due to its small length (2.75 km – the average of line lengths simulated in the MC procedure). However, the line was retained in the EM structure to preserve the way of connecting individual SG-based plants within the HRES plant to the PCC. In long-term voltage stability studies, the equivalent WF was not used for representing plant compositions with converter-connected technologies only (as it was the case with transient and frequency stability) as long-term voltage stability analysis is a static stability study, and generator dynamic parameters and control systems have no impact on long-term voltage stability results.

In the case of small-disturbance stability studies a second-order TF was chosen for the simulation of the critical (least damped) electromechanical mode instead of a second-order SG model due to the complexity of HRES plant configuration and high sensitivity of small-disturbance stability results to variations in operating point. Namely, given that HRES plant can contain a variety of synchronous and non-synchronous technologies, there is a possibility of HRES plant compositions with different total HRES plant production resulting in similar critical electromechanical mode, and thus, being allocated to a single cluster and represented by a common EM. In case an equivalent second-order SG is developed for such a cluster, the equivalent SG (with a single set of inertia constant and damping coefficient values) would have to produce similar electromechanical modes for potentially significantly different total HRES plant outputs (i.e., the equivalent SG production levels). On the other hand, the TF-based model parameters (i.e., TF coefficients) are constant and independent on the plant power output, meaning the TF-

based EM produces the electromechanical mode corresponding to the cluster representative (for which the EM was developed) for all plant compositions within the relevant cluster regardless of differences in their total HRES plant production.

Grey-box models are more physically intuitive than their black-box counterparts, but require more details about HRES plant configuration. In the case of transient and frequency stability studies, EM for HRES plant compositions without SGs in service is in the form of the equivalent WF, which corresponds to an appropriately scaled detailed dynamic model of the WF in the HRES plant, and thus needs the information about wind generator parameters as well as the structure and parameter values of its control system. The detailed dynamic data might be protected by data confidentiality laws, which in turn could limit the application of these models in practice in case the entity developing EM is not the entity having access to the full-scale dynamic HRES plant model. On the other hand, the black-box model for small-disturbance stability study relies on the measured/simulated plant responses only, which means that the eventual data confidentiality issue could be overcome by sharing only measurements or simulated plant responses between different entities. Furthermore, in the case of transient stability results, plant composition 6 had to be separated from the other plant compositions with converter-connected technologies only due to the difference in the pre-disturbance HRES plant production. In case the shape of the deviation of real power response at the PCC from the initial pre-disturbance value was analysed, that is, in case the shape of response in time domain was decoupled from HRES plant operating point, all compositions containing only converter-connected technologies could be allocated to a single cluster. Also, in the case of frequency stability studies, the accuracy of EM 3 for MC CSs generated by composition 6 is lower compared to the other cases from the same cluster. On the other hand, the TF-based structure used in small-disturbance stability studies has a potential to be suitable for a wider range of operating conditions compared to grey-box EMs, as its inputs and outputs are the deviations of voltage and real power responses at the PCC from their pre-disturbance values, respectively.

3.5 Summary

The chapter provided the procedure for identifying the influence of the HRES plant on power system stability performance during the year and presented the results of the exploratory study towards development of EMs of HRES plant for small-disturbance,

transient, frequency and long-term voltage stability studies. The test system contains the HRES plant comprising a range of RES and storage technologies, and connected to the external network through a single PCC.

Identification of the annual impact of the HRES plant on the system stability is based on characteristic annual HRES plant compositions, which eliminates the issue of high computational time required for analysing all possible HRES plant operating points. Unsupervised clustering technique is used for determining typical plant compositions from the historical dataset. Probabilistic MC approach relying on characteristic plant compositions and a single TN operating point produced the results for investigated system stability problems (small-disturbance, transient, frequency and long-term voltage stability). The obtained system stability results were divided into groups according to similarity, and these groups provided the information about typical plant compositions having similar influence on the analysed category of power system stability. Development of the procedure for determining the typical annual impact of the HRES plant on power system stability represents the first original contribution of this thesis.

Preliminary EMs of HRES plant for the considered types of system stability were developed for each group of system stability results. Results obtained with the test system indicate that the behaviour of the whole HRES plant in system stability studies can be represented by a few models throughout the year. The presented exploratory study paves the way towards development of robust EMs of HRES plants suitable for a wide range of HRES plant and TN operating conditions, and system disturbances. The guidelines for developing EMs of HRES plants for the afore-mentioned system stability simulations represent the second original contribution of this thesis.

The following chapters of the thesis will focus on equivalent modelling of HRES plants for transient stability studies as the interest is in the overall system dynamic behaviour and stability following disturbances, as opposed to previous work on HRES plant where the focus was mainly on its economic/energy contributions to power system operation. It is assumed that all individual RES plants within the HRES plant are equipped with the fault ride through capability (a typical requirement for RESs these days [188]), and thus, do not trip during a fault in the system, which then places the focus of the research on system dynamic behaviour following the initial, small, period of fault duration.

Furthermore, DEMs for transient stability simulations have to take into consideration longer time period following a disturbance compared to equivalents for frequency stability studies typically designed to result in as accurate as possible frequency nadir and RoCoF values and often using simple/reduced order models of individual technologies, which in turn complicates the analysis of HRES plant contribution to the overall system dynamic behaviour.

4 Data-driven Equivalent Modelling of HRES Plant for Power System Transient Stability Studies

4.1 Introduction

This chapter presents the methodology for development of DEM of HRES plants, incorporating different renewable generation and storage technologies, suitable for reliable assessment of the overall transient stability of the realistic, large power systems. Given that the transient stability of a power system is determined by a complex interaction between all elements in the system, HRES plant power responses having different shape in time domain may result in very similar (if not the same) transient stability performance of the system. Therefore, developing equivalents from the perspective of the overall transient stability status is more important and more useful for practical large system studies than development of highly accurate dynamic models of HRES plant as seen from the PCC. In this modelling approach, HRES plant power responses associated with similar global transient stability behaviour are represented by a common DEM regardless of dissimilarities in shape. Transient stability index (TSI) is used for system stability assessment, and consequently for the evaluation of the model performance. The proposed DEM is in the form of a TF with voltage and real/reactive power at the PCC as an input and output, respectively. Separate TFs are developed for

real and reactive power responses. The methodology is illustrated on a number of CSs using two HRES plant configurations.

4.2 Methodology and Model Development

Figure 4.1 illustrates the flow chart of the methodology for developing DEMs of HRES plants for transient stability studies that should provide sufficiently accurate global system stability results. Inputs and outputs of different stages in the procedure are marked by dashed rectangles. The methodology relies on historical plant production data, statistical data about TN short-circuit fault performance and unsupervised data mining techniques (clustering methods).

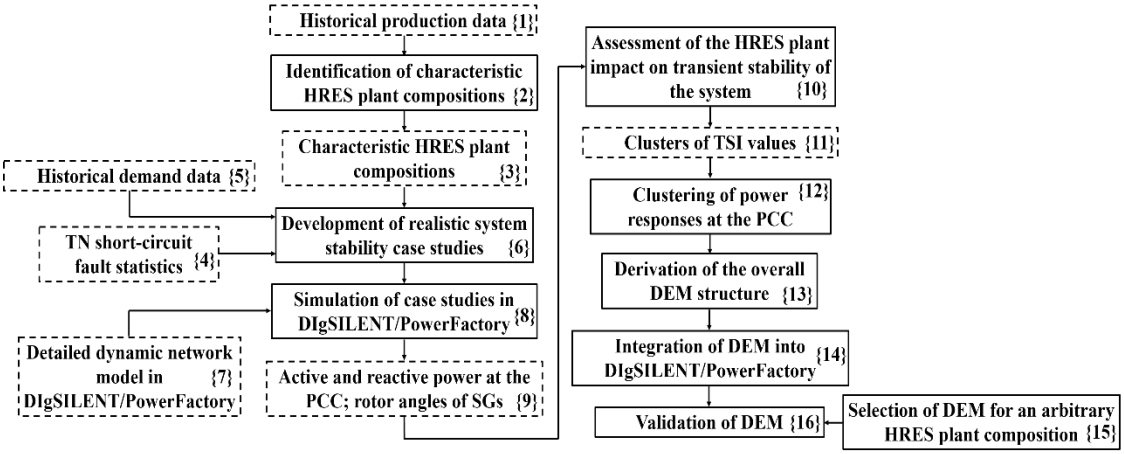

Figure 4.1 The flow chart of the methodology for developing TF-based DEMs of HRES plants for transient stability studies

Firstly, a set of historical real power outputs of individual plants within the HRES plant is divided into groups according to similarity in operating conditions of the HRES plant, i.e., HRES plant compositions, using an unsupervised clustering technique (block {2} in Figure 4.1). In this way, characteristic HRES plant compositions (block {3} in Figure 4.1) during the year, or any other pre-specified time period, are identified. The use of typical instead of all possible plant compositions results in low computational complexity of the equivalent modelling procedure.

Realistic system stability CSs used for DEM development are generated in a probabilistic manner (block {6} in Figure 4.1) and provide the most probable annual HRES plant dynamic performance in transient stability analysis. Typical HRES plant compositions and TN short-circuit fault statistics, as well as uncertainties in production and location of individual plants in the HRES plant, represent a basis for defining CSs. System stability

simulations are carried out in DIgSILENT/PowerFactory environment using the detailed HRES plant and TN dynamic model (block {8} in Figure 4.1).

Given that the aim is developing a DEM from the perspective of the overall system stability results, the influence of HRES plant power responses (obtained in the previously defined CSs) on transient stability of the power system is assessed on the basis of the value of TSI – a widely used global transient stability indicator (block {10} in Figure 4.1). In order to define HRES plant responses resulting in similar transient stability performance of the system (that is, similar TSI values), groups/clusters of TSI values (block {11} in Figure 4.1) are identified through an unsupervised clustering process. The number of TSI clusters defines the number of DEMs required for representing the HRES plant in transient stability studies. HRES plant responses resulting in TSI values allocated to the same cluster (block {12} in Figure 4.1) are represented by a common DEM, regardless of their dissimilarities in shape.

Prior to DEM development (block {13} in Figure 4.1), power responses are z-normalized as total HRES plant production varies across CSs. Separate parts of DEM are used for modelling real and reactive power responses of the HRES plant, but they have the same structure – two blocks connected in series. The first block produces z-normalized power response, which represents an input to the second block that performs inverse z-normalization to obtain power response in absolute units. The block for simulating z-normalized power response is characterized by a time-varying structure – its structure is different for pre-fault, fault and post-fault period. The DEM output is constant before and during the fault (DEM produces different power outputs during these time periods), while a TF is used for simulating power response following the fault clearance. Voltage and real/reactive power at the PCC are TF input and output signals, respectively. A representative system stability CS is defined for each group of HRES plant power responses. Voltage and power responses at the PCC obtained in corresponding dynamic simulation are used for estimating DEM parameters.

Finally, DEM is integrated into the TN model in DIgSILENT/PowerFactory at the PCC (block {14} in Figure 4.1) and its accuracy is assessed on the basis of the difference between TSI values produced by the detailed and equivalent plant model for the same system operating conditions and disturbances (block {16} in Figure 4.1). The selection

of the adequate DEM that should be used in transient stability studies at a particular time of the year is performed on the basis of similarity between the forecasted operating condition of the HRES plant and characteristic HRES plant compositions (block {15} in Figure 4.1).

The first stage in the equivalent modelling procedure that concerns the identification of characteristic annual HRES plant compositions (block {2} in Figure 4.1) is presented in Section 3.2.1, and thus, will not be described in this chapter. Detailed description of the remaining steps involved in the modelling procedure is given in the following sections.

4.2.1 Development of Realistic System Stability Case Studies

Given that the idea of the presented modelling methodology is to develop DEMs able to reflect realistic, the most probable HRES plant dynamic behaviour in transient stability analysis during a year, HRES plant power responses used for DEM development are generated on the basis of representative conditions in the system. The application of characteristic annual HRES plant compositions, along with TN short-circuit fault statistical data, provides the most likely annual HRES plant responses in transient stability studies.

Uncertainties in production of individual plants and their location within the HRES plant (in terms of the distance from the PCC), as well as uncertainties in TN self-clearing short-circuit faults and total system demand are modelled using probabilistic MC approach. In each MC CS, real power outputs of individual plants are sampled uniformly from the pre-specified ranges centred around their outputs in characteristic HRES plant compositions. Similarly, the uniform probability distribution is used for random sampling of the lengths of lines connecting individual plants to the PCC from the pre-defined range of values. The historical system demand data are divided into clusters according to the clusters of historical plant production data and the time instance of the observations from the production and demand datasets. In each MC simulation, total system demand level is varied around the corresponding cluster centroid using the same range as in the case of typical annual plant compositions.

As for TN disturbances, in each MC simulation, the location, type and impedance of TN short-circuit fault are selected in a probabilistic manner using TN fault statistics. The procedure is based on the methodology described in [189]. Fault location is chosen by

sampling a random number R uniformly from range [0, 1] and comparing it with the probabilities of a fault occurring at TN buses and lines (see Figure 4.2). The probability of fault occurrence at the i-th TN element is defined as follows [189]:

$$P_i = \frac{f_i}{\sum_{i=1}^{M} f_i}, \tag{4.1}$$

where f_i is the annual fault rate of the i-th TN element and M is the number of TN buses and lines. The i-th TN element is chosen for fault location if the following is satisfied:

$$\sum_{j=1}^{i-1} P_j < R \leq \sum_{j=1}^{i} P_j. \tag{4.2}$$

In case a line fault is selected, the position of the fault along the line is defined according to the uniform probability distribution function.

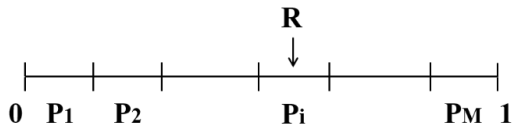

Figure 4.2 The illustration of fault location sampling (adapted from [189])

Fault type is chosen in a similar way as fault location, i.e., by comparing a random number with the probabilities of occurrence of four fault types (single-line-to-ground (LG), double line-to-ground (LLG), line-to-line (LL) and three-phase (LLL) fault) at the selected TN element. The selection of the i-th fault type is performed according to (4.1) and (4.2), but with P_i and f_i representing the probability of occurrence and annual rate of the i-th fault type at the chosen TN element, respectively, and M equal to four (the total number of the considered fault types). Finally, fault impedance is sampled from the pre-specified range ((0-20) Ω [190]) using the uniform probability distribution.

Different fault locations along lines, all four fault types and non-zero fault impedance are simulated to ensure generation and analysis of realistic annual HRES plant power responses in transient stability studies. Using only LLL faults in the equivalent modelling process would result in DEM capable of representing the worst-case scenario in the network, i.e., the least probable plant performance in transient stability analyses. Asymmetrical short-circuit faults, i.e., LG, LL and LLG, which result in less severe system conditions compared to LLL faults, are much more likely to occur in real power

systems. Similarly, adopting a single fault location along a line and zero fault impedance would result in unrealistic system stability performance because all locations along a line are prone to short-circuit fault occurrence and short-circuit faults always occur with a certain value of fault impedance, respectively.

4.2.2 Simulation of Case Studies in DIgSILENT/PowerFactory

Transient stability analysis of MC CSs is performed in DIgSILENT/PowerFactory software package using the detailed dynamic model of the HRES plant and TN model. The full-scale dynamic model of the HRES plant contains detailed dynamic models of all individual technologies and their control systems, which take into account all relevant protection mechanisms. Real and reactive power responses of the HRES plant at the PCC, along with the rotor angles of all SGs in the system are recorded in the simulations.

4.2.3 Assessment of the Hybrid Renewable Energy Source Plant Impact on Transient Stability of the System

HRES plant power responses are analysed on the basis of their effect on the overall transient stability of the system. For that purpose, TSI (4.3) is calculated for each MC CS [182]:

$$TSI = \frac{360° - \delta_{max}}{360° + \delta_{max}} \cdot 100\%, \tag{4.3}$$

where δ_{max} is the maximum difference between rotor angles of any two SGs in the system at the same time instance. In case δ_{max} is larger than 360 degrees, the TSI is negative and the system is considered to be transiently unstable.

The MC CSs that result in similar TSI values are grouped together and represented by a common DEM, meaning the number of resulting TSI clusters determines the number of DEMs. The Kernel Density Estimation (KDE) method identifies the groups of similar TSI values. The approach is based on the estimation of the probability density function (PDF) of TSI values using the kernel function (4.4) [140]:

$$\hat{f}_h(x) = \frac{1}{Nh}\sum_{i=1}^{N} K\left(\frac{x - x_i}{h}\right) = \frac{1}{N}\sum_{i=1}^{N} K_h(x - x_i), \tag{4.4}$$

where $K()$ is the kernel function that models the contribution of the individual sample x_i to the overall data density, h is the bandwidth (a positive smoothing parameter), N is the

number of samples in the considered dataset (the number of calculated TSI values in this analysis), and $K_h(t) = K(t/h)/h$. The kernel function has to satisfy the following conditions:

$$K(w) \geq 0, \forall w, \tag{4.5}$$

$$K(w) = K(-w), \forall w, \tag{4.6}$$

$$\int_{-\infty}^{+\infty} K(w)dw = 1. \tag{4.7}$$

The standard Gaussian function with zero mean and standard variance of one is used in this analysis, as it is the most common choice for the kernel function [140, 191]. Thus, the expression for the kernel density estimator is:

$$\hat{f}_h(x) = \frac{1}{Nh}\frac{1}{\sqrt{2\pi}}\sum_{i=1}^{N} e^{-(x-x_i)^2/2h^2}. \tag{4.8}$$

Estimation of the optimal bandwidth of the kernel function represents the most critical step of the KDE application, as the bandwidth determines the shape of the estimated PDF. Very small values of the parameter *h* usually result in under-smoothed PDF estimates, whereas the kernel function overfits the underlying PDF in case of large bandwidths. The impact of the bandwidth value on the shape of the kernel function is illustrated in Figure 4.3. In this study, solve-the-equation plug-in method is used for automatic estimation of the optimal value of the parameter *h* (more details on the selection of the optimal bandwidth are provided in Section 4.2.3.1).

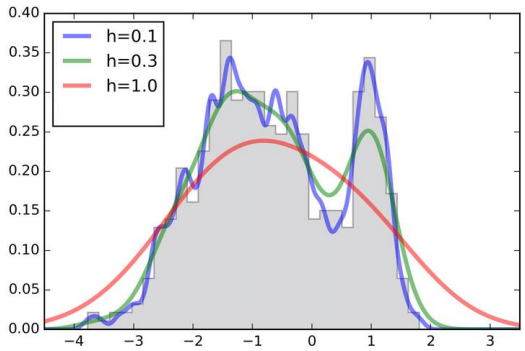

Figure 4.3 The illustration of the impact of the bandwidth value on the shape of the kernel function (adopted from [192])

Clusters of TSI values are determined based on the local maxima of the estimated PDF [140]. For each clustering object *x* (calculated TSI value), the nearest local maximum of the estimated PDF is determined through a step-wise hill-climbing procedure [140]. In the case of the Gaussian kernel function, the step-wise hill-climbing procedure is performed using (4.9)-(4.11):

$$x^0 = x, \tag{4.9}$$

$$x^{j+1} = x^j + \delta \frac{\nabla \hat{f}_h(x^j)}{\left\|\nabla \hat{f}_h(x^j)\right\|}, \tag{4.10}$$

$$\nabla \hat{f}_h(x^j) = \frac{1}{Nh^3} \sum_{i=1}^{N} \frac{1}{\sqrt{2\pi}} e^{-\left(x^j - x_i\right)^2 / 2h^2} \left(x_i - x^j\right), \tag{4.11}$$

where $\nabla \hat{f}_h(x^j)$ and $\left\|\nabla \hat{f}_h(x^j)\right\|$ is the gradient and the magnitude of the gradient of the kernel density estimator at x^j, respectively, and δ is a small positive number that controls the speed of convergence (the value of 0.1 is adopted). The procedure terminates when $\hat{f}_h(x^{j+1})$ (calculated using (4.8)) becomes lower than $\hat{f}_h(x^j)$, and x^j then represents the nearest local maximum for the considered clustering object. TSI values having the same nearest local maximum are assigned to the same cluster.

Unlike the fuzzy c-means clustering algorithm, which could have been equally used for this purpose, the KDE method does not require the number of clusters to be set in advance, it can identify arbitrary shaped clusters and has strong mathematical background. The drawback of the KDE approach is its computational complexity (due to the need for computing the density estimate and local maximum for each clustering object, and estimating the optimal bandwidth value [191]), and difficulty in obtaining a "reasonable nonparametric density estimation" in the multivariate settings ("the curse of dimensionality") [157]. This, however, was not the case in this study nor it will be in the case of development of DEM of any practical HRES plant as the clustering dataset is one-dimensional and its size is determined by the number of typical HRES plant compositions that cannot be unreasonably large.

4.2.3.1 The Estimation of the Optimal Bandwidth Value for the Kernel Function

The adequacy of the bandwidth value for the considered dataset is commonly assessed using the asymptotic mean integrated squared error (AMISE), a criterion for measuring the accuracy of the kernel density estimator, due to its simple mathematical dependence

on the parameter *h* [157, 193]. The AMISE represents a large sample approximation to the mean integrated squared error (MISE), i.e., it is obtained by omitting higher order terms from the expression for the MISE as follows (more detailed derivation of the expression for the AMISE is given in Appendix A.1) [157, 193]:

$$\begin{aligned} MISE\left(\hat{f}_h(x)\right) &= E\left[ISE\left(\hat{f}_h(x)\right)\right] = E\left[\int\left(\hat{f}_h(x)-f(x)\right)^2 dx\right] = \\ &= \int E\left[\left(\hat{f}_h(x)-f(x)\right)^2\right] dx = \int MSE\left(\hat{f}_h(x)\right) dx \end{aligned}, \tag{4.12}$$

$$MSE\left(\hat{f}_h(x)\right) = Var\left(\hat{f}_h(x)\right) + \left(Bias\left(\hat{f}_h(x)\right)\right)^2, \tag{4.13}$$

$$Var\left(\hat{f}_h(x)\right) = \frac{f(x)R(K)}{Nh} + o\left(\frac{1}{Nh}\right), \tag{4.14}$$

$$Bias\left(\hat{f}_h(x)\right) = \frac{1}{2}h^2\mu_2(K)f''(x) + o(h^2), \tag{4.15}$$

$$MISE\left(\hat{f}_h(x)\right) = \frac{R(K)}{Nh} + \frac{1}{4}h^4\left(\mu_2(K)\right)^2 R\left(f''(x)\right) + o\left(\frac{1}{Nh} + h^4\right), \tag{4.16}$$

where $f(x)$ is the unknown true PDF, $ISE\left(\hat{f}_h(x)\right)$, $MSE\left(\hat{f}_h(x)\right)$, $Var\left(\hat{f}_h(x)\right)$ and $Bias\left(\hat{f}_h(x)\right)$ is the integrated squared error, mean squared error, variance and bias of the estimated PDF, respectively, $R(g)$ is the roughness of function g defined as $R(g) = \int (g(x))^2 dx$, $\mu_2(g)$ is the second moment of function g, $\mu_2(g) = \int x^2 g(x)dx < \infty$. The *o()* stands for the little-o notation and is defined as:

$$a_N = o(b_N) \text{ as } N \to \infty, \text{ if and only if } \lim_{N\to\infty}\left|\frac{a_N}{b_N}\right| = 0, \tag{4.17}$$

where a_N and b_N are sequences of real numbers.

Bases on the expression for the MISE (4.16), the AMISE criterion is defined as follows:

$$AMISE\left(\hat{f}_h(x)\right) = \frac{R(K)}{Nh} + \frac{1}{4}h^4(\mu_2(K))^2 R(f''(x)). \tag{4.18}$$

The optimal *h* value for the kernel function minimizes the value of the AMISE criterion:

$$\frac{\partial}{\partial h} AMISE\left(\hat{f}_h(x)\right) = 0 => \ h_{opt} = \left(\frac{R(K)}{NR(f'')(\mu_2(K))^2}\right)^{1/5}. \tag{4.19}$$

The previous expression (4.19) contains a single unknown parameter $R(f'')$, and the solve-the-equation plug-in method is chosen to address this issue as it has demonstrated superior performance, both theoretically and empirically, over a number of other techniques [194]. The method is based on replacing $R(f'')$ with an adequate estimate determined through an iterative procedure. Namely, the integrated squared density derivative functionals, $R(f^{(s)})$, for even s can be written in the following form [191], [157]:

$$R(f^{(s)}) = \int \left(f^{(s)}(x)\right)^2 dx = (-1)^s \int f^{(2s)}(x) f(x) dx, \tag{4.20}$$

$$r = 2s, \tag{4.21}$$

$$\Psi_r = \int f^{(r)}(x) f(x) dx = E\left[f^{(r)}(x)\right]. \tag{4.22}$$

An estimator for Ψ_r, $\widehat{\Psi}_r$, is defined as follows [191], [157]:

$$\widehat{\Psi}_r = \frac{1}{N}\sum_{i=1}^{N} \hat{f}_h^{\,(r)}(x_i) = \frac{1}{N^2 g_r^{r+1}} \sum_{i=1}^{N}\sum_{j=1}^{N} K^{(r)}\left(\frac{x_i - x_j}{g_r}\right), \tag{4.23}$$

$$g_r = \left[-\frac{2K^{(r)}(0)}{\mu_2(K)\Psi_{r+2}N}\right]^{1/(r+3)}, \tag{4.24}$$

where $\hat{f}_h^{\,(r)}(x_i)$ is the estimate of the r-th derivative of the PDF $f(x)$ at $x=x_i$, and g_r is the optimal bandwidth for the $\widehat{\Psi}_r$ estimate. Expression (4.23) demonstrates that the estimator for Ψ_r recognizes that the PDF and density derivative functionals might require different optimal bandwidths [194]. The optimal g_r value (4.24) corresponds to the value that eliminates the main bias term from the expression of the asymptotic mean squared error (AMSE) for Ψ_r estimation (detailed derivation of (4.24) is given in Appendix A.2).

According to (4.19) – (4.22), the expression for the optimal bandwidth is:

$$h_{opt} = \left(\frac{R(K)}{N\Psi_4(\mu_2(K))^2}\right)^{1/5}, \tag{4.25}$$

while the expression for g_4 according to (4.24) for r=4 is:

$$g_4 = \left[-\frac{2K^{(4)}(0)}{\mu_2(K)\Psi_6 N}\right]^{1/7}. \tag{4.26}$$

Combining (4.25) and (4.26), g_4 can be expressed as a function of the h_{opt} value:

$$g_4 = \left[-\frac{2K^{(4)}(0)\mu_2(K)\Psi_4}{R(K)\Psi_6}\right]^{1/7} h_{opt}^{5/7}. \tag{4.27}$$

Finally, the solve-the-equation-plug-in method estimates the optimal bandwidth value using the following equation:

$$\hat{h}_{opt} = \left(\frac{R(K)}{N\hat{\Psi}_4(\tilde{g}_4)\mu_2(K)^2}\right)^{1/5}, \tag{4.28}$$

where $\hat{\Psi}_4(\tilde{g}_4)$ is computed using (4.23) with the optimal bandwidth $\tilde{g}_4$ defined according to (4.27) as follows:

$$\tilde{g}_4 = \left[-\frac{2K^{(4)}(0)\mu_2(K)\hat{\Psi}_4}{R(K)\hat{\Psi}_6}\right]^{1/7} \hat{h}_{opt}^{5/7}, \tag{4.29}$$

with $\hat{\Psi}_4$ and $\hat{\Psi}_6$ computed using (4.23), and g_4 and g_6, respectively, that are specified by (4.24). Equation (4.28) can be solved using the Newton-Raphson method.

As the estimates for $\hat{\Psi}_4$ and $\hat{\Psi}_6$ in (4.23) depend on a higher density derivative functional, iterative procedure is applied for their computation. A two-stage approach is most commonly used [191]. Density derivative functionals in the first iteration are calculated using the normal scale rule, which assumes that the underlying PDF (i.e., the unknown true PDF of the considered dataset) corresponds to the normal distribution with zero mean and variance equal to the variance of the analysed dataset (detailed derivation of (4.30) is provided in Appendix A.3) [157]:

$$\hat{\Psi}_r = \frac{(-1)^{r/2} r!}{(2\sigma)^{r+1}\left(\frac{r}{2}\right)!\sqrt{\pi}}, \tag{4.30}$$

where σ is the standard deviation of the considered dataset.

Therefore, the steps in the estimation of the optimal bandwidth for the PDF estimate using the two-stage solve-the-equation-plug-in method are as follows:

1. Computation of the standard deviation of the analysed dataset, σ

2. Computation of the estimators of the density functionals $\widehat{\Psi}_6$ and $\widehat{\Psi}_8$ using the normal scale rule (4.30)
3. Calculation of intermediate bandwidths g_4 and g_6 using (4.24)
4. Computation of the estimators of the density functionals $\widehat{\Psi}_4$ and $\widehat{\Psi}_6$ using (4.23)
5. Final optimal bandwidth is a solution of (4.28).

The solve-the-equation-plug-in method is illustrated on a following simple example. Let assume that the original PDF is a combination of two normal PDFs:

$$f(x) = 0.5 \cdot \frac{1}{\sigma_1\sqrt{2\pi}} e^{-\frac{(x-\mu_1)^2}{2\sigma_1^2}} + 0.5 \cdot \frac{1}{\sigma_2\sqrt{2\pi}} e^{-\frac{(x-\mu_2)^2}{2\sigma_2^2}}, \tag{4.31}$$

where μ_1 and μ_2 is the mean of the first and second normal PDF, respectively, and, σ_1 and σ_2 is the standard deviation of the first and second normal PDF, respectively. The adopted parameters of the normal PDF are: $\mu_1 = 2$, $\sigma_1 = 2$, and $\mu_2 = 20$, $\sigma_2 = 3$.

A set of *N*=1,000 random numbers is generated according to the previously specified mix of normal PDFs (i.e., the original PDF), and this dataset is used for estimating the PDF using the KDE approach. The two-stage solve-the-equation-plug-in method for computing the optimal bandwidth value is performed as follows:

1. The standard deviation of the dataset is defined as follows:

$$\sigma = \sqrt{\frac{1}{N-1}\sum_{i=1}^{N}(x_i - x_{mean})^2} = 9.36, \tag{4.32}$$

where x_i is the *i*-th element of the dataset, and x_{mean} is the dataset average.

2. The estimators of the density functionals $\widehat{\Psi}_6$ and $\widehat{\Psi}_8$ are computed using (4.30):

$$\widehat{\Psi}_8 = \frac{(-1)^4 8!}{(2\sigma)^9 4!\sqrt{\pi}} = 3.35 \cdot 10^{-9}, \tag{4.33}$$

$$\widehat{\Psi}_6 = \frac{(-1)^3 6!}{(2\sigma)^7 3!\sqrt{\pi}} = -8.40 \cdot 10^{-8}. \tag{4.34}$$

3. Bandwidths g_4 and g_6 are computed using (4.24), and the values for $\widehat{\Psi}_6$ and $\widehat{\Psi}_8$ obtained in the previous step of the procedure:

$$g_6 = \left[-\frac{2K^{(6)}(0)}{\mu_2(K)\widehat{\Psi}_8 N}\right]^{1/9} = 5.35, \tag{4.35}$$

$$g_4 = \left[-\frac{2K^{(4)}(0)}{\mu_2(K)\widehat{\Psi}_6 N}\right]^{1/7} = 4.33, \tag{4.36}$$

where:

$$K^{(r)}(x) = (-1)^r H_r(x)K(x) = (-1)^r \left[\sum_{j=0}^{r/2}(-1)^j \frac{(2j)!}{2^j j!}\binom{r}{2j} x^{r-2j}\right]\frac{1}{\sqrt{2\pi}}e^{-x^2/2}, \tag{4.37}$$

$$\mu_2(K) = \int x^2 K(x)dx = \int x^2 \frac{1}{\sqrt{2\pi}}e^{-x^2/2}dx = 1, \tag{4.38}$$

with $H_r(x)$ representing the *r*-th Hermite polynomial.

4. The estimators of the density functionals $\widehat{\Psi}_4$ and $\widehat{\Psi}_6$ are computed using (4.23) and the values of g_4 and g_6 calculated in the previous step of the procedure:

$$\widehat{\Psi}_6 = \frac{1}{N^2 g_6^7}\sum_{i=1}^{N}\sum_{j=1}^{N} K^{(6)}\left(\frac{x_i - x_j}{g_6}\right) = -8.48 \cdot 10^{-6}, \tag{4.39}$$

$$\widehat{\Psi}_4 = \frac{1}{N^2 g_4^5}\sum_{i=1}^{N}\sum_{j=1}^{N} K^{(4)}\left(\frac{x_i - x_j}{g_4}\right) = 1.33 \cdot 10^{-4}. \tag{4.40}$$

5. The optimal bandwidth is obtained from (4.28) using the values of $\widehat{\Psi}_4$ and $\widehat{\Psi}_6$ calculated in the previous step of the procedure:

$$\tilde{g}_4 = \left[-\frac{2K^{(4)}(0)\mu_2(K)\widehat{\Psi}_4}{R(K)\widehat{\Psi}_6}\right]^{1/7} \hat{h}_{opt}^{5/7} = 2.01 \cdot \hat{h}_{opt}^{5/7}, \tag{4.41}$$

$$\hat{h}_{opt} = \left(\frac{R(K)}{N\widehat{\Psi}_4(\tilde{g}_4)(\mu_2(K))^2}\right)^{1/5} = \left(\frac{\frac{1}{\sqrt{2\pi}}}{1000 \cdot \widehat{\Psi}_4(\tilde{g}_4) \cdot 1}\right)^{1/5}, \tag{4.42}$$

where:

$$R(K) = \int\left(K(x)\right)^2 dx = \int\left(\frac{1}{\sqrt{2\pi}}e^{-x^2/2}\right)^2 dx = \frac{1}{2\sqrt{\pi}}. \tag{4.43}$$

Solving (4.42) using the Newton-Raphson method gives the optimal bandwidth value:

$$\hat{h}_{opt} = 0.77. \tag{4.44}$$

4.2.4 Clustering of Power Responses at the Point of Common Coupling

The clustering of calculated TSI values leads to groups/clusters of real and reactive power responses of the HRES plant that need to be represented by a common DEM. Prior to model development though, the power responses have to be normalized as HRES plant production varied from one simulation to the next. Z-normalization (4.45) is used for that purpose [195]:

$$z(t) = \frac{Y(t) - Y_{mean}}{SD\_Y}, \tag{4.45}$$

$$Y_{mean} = \frac{1}{n}\sum_{i=1}^{n} Y_i, \tag{4.46}$$

$$SD\_Y = \sqrt{\frac{1}{n-1}\sum_{i=1}^{n}(Y_i - Y_{mean})^2}, \tag{4.47}$$

where $z(t)$ is the z-standardized power response, $Y(t)$ is power response in absolute units, Y_{mean} is the average value of the overall power response in absolute units, SD_Y is the standard deviation of the power response in absolute units, n is the number of samples, and Y_i is instantaneous value of power response in absolute units at the i-th time step.

For each cluster of z-normalized power responses, a representative response is defined and used for estimating DEM parameters in the next stage of the equivalent modelling procedure. First, z-normalized real and reactive power responses obtained in the same MC CS are grouped into a single vector. Then, a vector characterized by the minimum sum of squared Euclidean distances from the other vectors in the cluster is determined and named a representative vector. Real and reactive power response from the representative vector are representative z-normalized real and reactive power response, respectively, whereas the MC case that results in the representative power response is a representative CS of the cluster.

4.2.5 Derivation of the Overall Dynamic Equivalent Model Structure

Block diagram of the DEM developed for each cluster of power responses is shown in Figure 4.4. The real and reactive power responses at the PCC are modelled by separate parts of the DEM though they have the same structure defined by (4.48) and (4.49):

$$z_{EQ,Y}(t) = \begin{cases} 0, & t < t_{fault} \\ z_{Fault,Y}, & t_{fault} \le t \le t_{clear}, \\ z_{TF,Y}(t), & t > t_{clear} \end{cases} \tag{4.48}$$

$$Y_{EQ}(t) = Y_{SS} + z_{EQ,Y}(t) \cdot SD_Y^{rep}, \tag{4.49}$$

where $z_{EQ,Y}(t)$ is the z-normalized power response of the model, t_{fault} is the moment of fault occurrence, t_{clear} is the moment of fault clearing, $z_{Fault,Y}$ is the value of z-normalized power response of the model during the fault, $z_{TF,Y}(t)$ is the z-normalized power response of the model after the fault clearance, $Y_{EQ}(t)$ is the power response at the PCC in absolute units (after inverse z-transformation), Y_{SS} is the total power output of the plant before the disturbance, SD_Y^{rep} is the standard deviation of the representative power response in absolute units.

Equation (4.48) corresponds to the simulation of z-normalized power response (marked by blue solid rectangles in Figure 4.4), whereas (4.49) represents the application of inverse normalization to obtain power response in absolute units (marked by blue dashed rectangles in Figure 4.4). The DEM part described by (4.48) is characterized by different structures for pre-fault, fault and post-fault time periods. It can be seen from (4.48) that the z-normalized power response before the disturbance is equal to zero as the system is in steady state before the fault occurrence. The z-normalized power response during the fault is assumed to be constant as fault duration is short compared to post-fault recovery period. The average of the representative z-normalized power response during the fault is adopted for modelling the response during this time period (z_{Fault}).

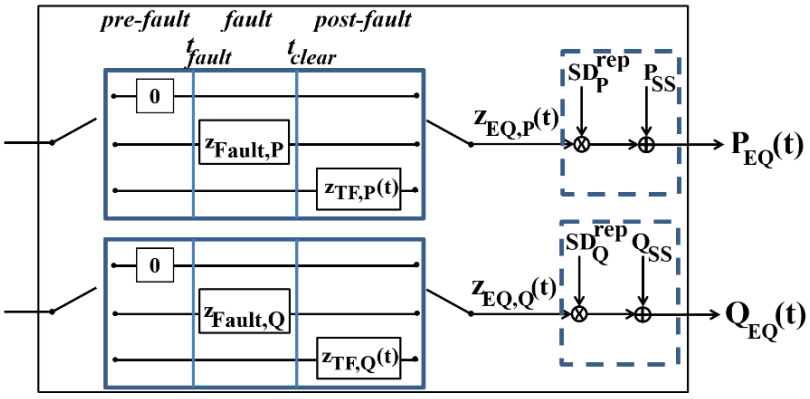

Figure 4.4 Block diagram of TF-based DEM

The z-normalized power response after the fault clearing is produced by a TF with voltage at the PCC as an input. Different TFs are used for modelling real and reactive power response of the HRES plant. TF parameters are determined through an iterative optimization procedure using voltage and z-normalized power response at the PCC from the representative MC CS as TF input and output, respectively. The TF numerator and denominator order are gradually increased starting from the minimum first order. For each TF order, TF parameters are estimated in the same way as in the case of TF-based EM for small-disturbance stability studies presented in Chapter 3 (i.e., using the Levenberg-Marquardt algorithm). The objective of TF parameter estimation is to minimize the sum of squared differences between the representative z-normalized power response and TF output:

$$\min_{\theta} \varepsilon(\theta) = \min_{\theta} \sum_{t=1}^{n} (z_{ORG}^{rep}(t_k) - z_{EQ}^{rep}(t_k))^2, \tag{4.50}$$

where θ is a set of TF parameters, n is the number of the considered time steps, $z_{ORG}^{rep}(t_k)$ is the representative z-normalized power response at the k-th time step, and $z_{EQ}^{rep}(t_k)$ is the TF output for the representative CS at the k-th time step. The Levenberg-Marquardt optimization terminates when there is no considerable improvement in the value of $\varepsilon(\theta)$ between two consecutive iterations (the value of 0.01% is adopted in this study).

Following TF parameter estimation, the BFV is then calculated using (4.51) [19, 20]:

$$BFV\ (\%) = 100 \cdot \left(1 - \frac{\left\| z_{ORG}^{rep}(t) - z_{EQ}^{rep}(t) \right\|}{\left\| z_{ORG}^{rep}(t) - \overline{z}_{ORG}^{rep} \right\|}\right), \tag{4.51}$$

where $\overline{z}_{ORG}^{rep}$ is the average of the representative z-normalized power response during the post-fault recovery period. The BFV value of 100% corresponds to the perfect match between the representative z-normalized response and TF output, whereas the zero value indicates that TF output signal is a constant signal corresponding to the average of the representative response. The parameter optimization process terminates, that is, the optimal TF order and TF parameters are determined, when the BFV becomes larger than a pre-specified threshold. The threshold of 80% is adopted in this methodology [19, 20].

Finally, for transformation of z-normalized response into power response in absolute units the mean value and standard deviation of the actual power response are needed (see (4.45)). However, this information cannot be known in advance for an arbitrary operating

condition and short-circuit fault without measuring or simulating HRES plant response. Therefore, HRES plant power output in steady state for a given forecasted plant composition and the standard deviation of the representative power response in absolute units (SD_Y^{rep}) are used instead of the mean value and standard deviation of the actual power response, respectively.

4.2.6 Integration of Dynamic Equivalent Model into DIgSILENT/PowerFactory

Built-in DSL is used for designing DEMs of the HRES plant in DIgSILENT/PowerFactory environment [164]. As in the case of the TF-based model for small-disturbance stability studies presented in Chapter 3, the TF-part of the DEM (4.48) has to be transformed into the control canonical state-space model due to DSL requirements. The approach given in Section 3.2.6 is used for transforming the TF-part of the model into the state-space model, and it will be repeated here for clarity:

$$z_{TF,Y}(s) = \frac{b_0 s^n + b_1 s^{n-1} + \cdots + b_{n-1} s + b_n}{s^n + a_1 s^{n-1} + \cdots + a_{n-1} s + a_n}, \tag{4.52}$$

$$\begin{matrix} \frac{dx(t)}{dt} = Ax(t) + Bu_{PCC}(t) \\ z_{TF,Y}(t) = Cx(t) + Du_{PCC}(t) \end{matrix}, \tag{4.53}$$

$$A = \begin{bmatrix} 0 & 1 & 0 & \cdots & 0 \\ 0 & 0 & 1 & \cdots & 0 \\ \vdots & \vdots & \vdots & \ddots & \vdots \\ 0 & 0 & 0 & \cdots & 1 \\ -a_n & -a_{n-1} & -a_{n-2} & \cdots & -a_1 \end{bmatrix}, B = \begin{bmatrix} 0 \\ 0 \\ \vdots \\ 0 \\ 1 \end{bmatrix}, D = b_0\,, \tag{4.54}$$

$$C = [(b_n - a_n b_0) \quad (b_{n-1} - a_{n-1} b_0) \quad \ldots \quad (b_2 - a_2 b_0) \quad (b_1 - a_1 b_0)], \tag{4.55}$$

where $z_{TF,Y}(s)$ is the TF-part of the DEM (obtained when estimating DEM structure) in *s*-domain, and *A*, *B*, *C* and *D* are state-space matrices.

Similar to the equivalent for small-disturbance stability studies described in Chapter 3, the implementation of DEM in DIgSILENT/PowerFactory network model requires an interface in the form of a controllable, constant power load. The load is connected at the PCC and its real and reactive power responses during dynamic simulations are controlled

according to (4.48), (4.49) and (4.52) – (4.55). The illustration of the DEM concept in DIgSILENT/PowerFactory software is presented in Figure 4.5.

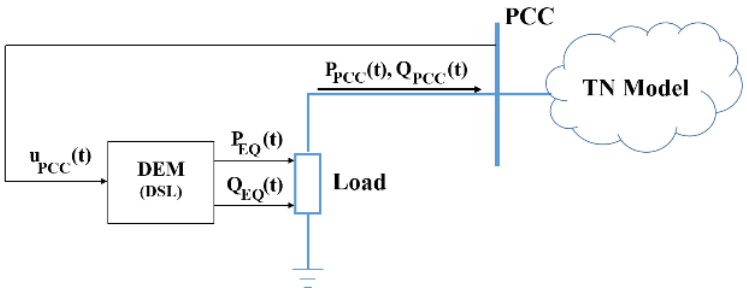

Figure 4.5 Illustration of the concept of TF-based DEMs in DIgSILENT/PowerFactory

Thus, dynamic model developed in DSL environment receives a signal from the network simulation model, voltage at the PCC ($u_{PCC}(t)$ in Figure 4.5), as an input, performs computations defined in (4.48), (4.49) and (4.52) – (4.55), and provides pre-specified output signals – reference real and reactive power of the load ($P_{EQ}(t)$ and $Q_{EQ}(t)$ in Figure 4.5, respectively). Real and reactive power injected at the PCC ($P_{PCC}(t)$ and $Q_{PCC}(t)$ in Figure 4.5, respectively) correspond to the DEM outputs. The integration time step of the DSL computations is equal to the time step of dynamic network simulations. A set of DEMs, one per cluster of power responses, is created and stored in the software library. DIgSILENT/PowerFactory software provides a feature to automatically select the DEM from the set of available DEMs and assigned it to the load model in order to simulate HRES plant dynamic behaviour at the PCC in transient stability simulations.

4.2.7 Selection of Dynamic Equivalent Model for an Arbitrary Hybrid Renewable Energy Source Plant Composition

Clustering of MC CSs according to the similarity in their TSI values may divide power responses associated with a single characteristic HRES plant composition into different clusters. In order to perform selection of DEM at any time of the year knowing HRES plant composition only, the most adequate model for each characteristic plant composition is chosen as the model corresponding to the cluster containing the largest share of responses produced by this plant composition.

When it comes to an arbitrary HRES plant operating condition, the corresponding DEM is the best model for the characteristic annual plant composition which is the most similar (composition) to the given plant composition (similarity between plant compositions is assessed based on their Euclidean distance). Figure 4.6 illustrates the procedure for

choosing the DEM for a new/arbitrary HRES plant composition (the inputs and outputs of the procedure are marked by dashed rectangles). First, the Euclidean distance between the new plant composition and each of the typical HRES plant compositions is calculated (block {1} in Figure 4.6), with P_j^{new}, $P_j^{typ,i}$, N_{ind}, and N_{typ} in Figure 4.6 corresponding to the power output of the *j*-th individual plant in the case of the new plant composition, the power output of *j*-th individual plant in the case of the *i*-th typical plant composition, the number of individual plants within the HRES plant, and the total number of typical plant compositions, respectively. Then, the minimum of the computed Euclidean distances is defined (block {2} in Figure 4.6), and the typical plant composition corresponding to the minimum Euclidean distance (*Min_Typ* in Figure 4.6) is the most similar to the investigated new plant composition. The adequate DEM for the new HRES plant composition is the best DEM for the typical *Min_Typ* plant composition.

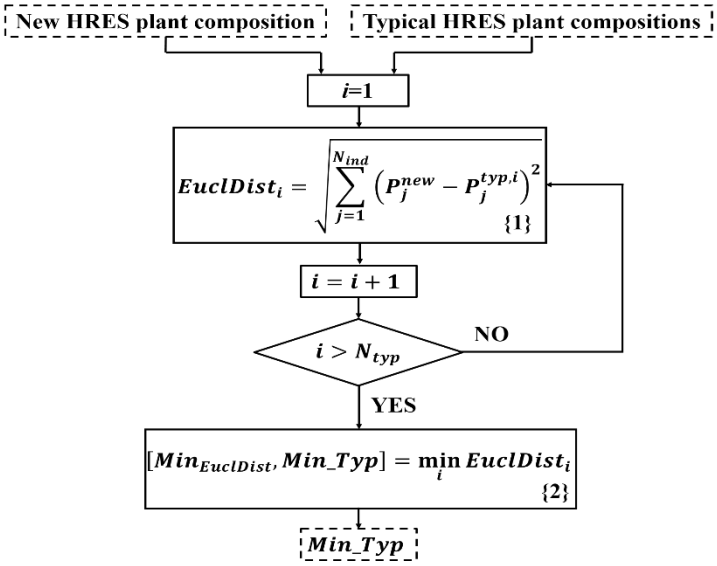

Figure 4.6 The illustration of the selection of the adequate DEM for an arbitrary HRES plant composition

4.2.8 Validation of Dynamic Equivalent Model

Evaluation of DEM performance is carried out in DIgSILENT/PowerFactory software package for a range of system operating conditions and TN short-circuit faults. Model accuracy is assessed from the point of view of the overall transient stability of the system, i.e., the error in TSI value:

$$TSI_{Err}(\%) = \left|\frac{TSI_{ORG} - TSI_{EQ}}{TSI_{ORG}}\right| \cdot 100\%, \tag{4.56}$$

where TSI_{ORG} and TSI_{EQ} are TSI values obtained using the detailed dynamic model and DEM of the HRES plant, respectively.

4.3 Test System

The methodology is tested using two CSs involving HRES plant configurations shown in Figure 4.7. HRES plants are connected to the same TN represented by the standard IEEE 9-bus model [173]. The test systems are modelled in DIgSILENT/PowerFactory software package 2020 [164].

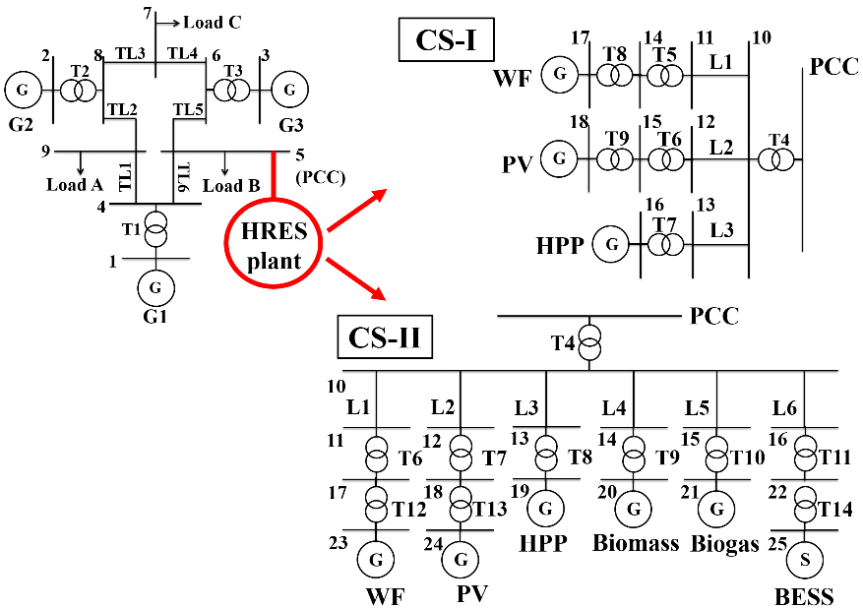

Figure 4.7 The schematic diagram of the test HRES plants and IEEE 9-bus network (G: generation technology; S: storage technology)

The HRES plant in CS-I consists of three individual plants, namely a WF, a PV plant and a run-of-river HPP, whereas the HRES plant in CS-II includes, in addition to the above a biomass plant, biogas plant and BESS, i.e., six individual plants in total. Installation capacities and dynamic model order of individual plants in both HRES plants are given in Table 4.1. Models of individual plants include the dynamic model of a generation/storage technology and its corresponding control system. The HRES plant from CS-II corresponds to the HRES plant used in the CS presented in Chapter 3, and the dynamic modelling of this HRES plant is described in detail in Section 3.3.

All individual plants in CS-I have the same rated capacity in order to prevent any single energy source dominating the dynamic behaviour of the HRES plant. The rated capacity of 210 MVA is chosen as it results in the median participation of the HRES plant in

supplying the total system demand (in the case of the data used in the study) of about 25%, and, thus, provides similar participation of all four power plants in the test system (the HRES plant and three SGs in the test TN) in the total system production. As in the case of the HPP within the HRES plant from CS-II, the hydro generator in the HRES plant from CS-I has a rated power factor of 0.85, and is represented by the standard fifth-order SG model, while IEEEG3 governor and IEEE DC1A exciter comprise the hydro generator control system. Modelling of the PV plant and WF in the HRES plant from CS-I is the same as for the relevant individual plants in the HRES plant from CS-II (detailed description is provided in Section 3.3).

Table 4.1 Installation capacities and model order of the test HRES plants

	CS-I			CS-II					
	AM of WF	AM of PV plant	HPP	AM of WF	AM of PV plant	HPP	Biomass plant	Biogas plant	BESS
Rated capacity (MVA)	210	210	210	170	265	295	76.5	76.5	125
Model order	17	14	13	17	14	13	14	11	9
Overall model order	44			78					

4.4 Case Studies

The production data used in CS-I concern the total production of run-of-river HPPs, PV plants and WFs in Central-Northern Italy for the four-year period 2015-2018. The data with a one-hour sampling rate are available in [196]. As the missing values account for less than 1% of the dataset, no interpolation was conducted. Historical HRES plant production data were scaled so that the maximum production of each individual plant during the analysed period is equal to its rated power. When it comes to CS-II, the historical HRES plant production dataset is the same as the one used in Chapter 3.

In CS-I historical demand data are obtained from the total demand in Central Italy during the four-year period 2015-2018 [196], while the demand data in CS-II correspond to the typical annual demand profile in the southern part of Greece [172]. In both CSs, historical demand data were scaled so that the maximum load level corresponds to the sum of rated

real powers of SGs in the TN and the maximum HRES plant production from the historical dataset. The scaled historical demand data are assigned to three loads in the TN model (see Figure 4.7). The production of SGs in the TN is defined using OPF. The OPF objective is to minimize the total generation cost of SGs in the TN (generation cost functions are adopted from [197]), while satisfying the specified total system load and considering the constraints in terms of real and reactive power outputs of SGs, bus voltage magnitude, line and transformer loadings.

For each characteristic annual HRES plant composition, 1,000 MC simulations are performed. The number of MC simulations was chosen according to the following expression [198]:

$$\varepsilon_r = \frac{\Phi^{-1}\left(1-\frac{\delta}{2}\right)\sqrt{\frac{\sigma_S^2(X)}{N_{CC}\cdot N_S}}}{E_S(X)}, \tag{4.57}$$

where ε_r is the estimated error of the sample mean, Φ^{-1} is the inverse of the standard Gaussian function with zero mean and standard deviation of one, δ is the confidence level, σ_S^2 is the sample variance, N_{CC} is the number of characteristic annual HRES plant compositions, N_S is the number of MC simulations per each of the characteristic annual HRES plant compositions, E_S is the sample mean, and X is the sampled random variable with ($N_{CC}\cdot N_S$) samples, i.e., TSI values obtained from MC simulations. For N_S=1000, and a confidence level of 99% (δ=0.01), the ε_r value was around 0.1% for both CSs presented in this chapter, meaning the adopted number of MC simulations per characteristic annual HRES plant composition provides a satisfactory low error of the sample mean.

As in the case of the CS presented in previous Chapter 3, in each set of 1,000 simulations, the lengths of lines connecting individual plants to the PCC (i.e., lines marked as "*Lx*" in Figure 4.7, where *x* is the number that goes from 1 to 3 and 6 in CS-I and CS-II, respectively) are sampled uniformly between 0.5 km and 5 km. The uncertainties in power outputs of individual technologies in the HRES plant are modelled by uniformly varying power output of each individual plant in the range of ±5% around the typical HRES plant composition. The same approach is applied to the centroids of historical demand clusters. Probabilistic fault simulation is carried out using TN fault statistics given in Table 4.2 [199, 200]. LG faults are applied on phase A, while LL and LLG faults

involve phases B and C. When it comes to the sampling of fault location along a line, it is assumed that all positions along the line have the same probability of being affected by the fault. The fault impedance is sampled uniformly from the range (0-20)Ω [190].

The plant responses are simulated for 10 s with the sampling rate of 1 ms and with a fault occurring at 1 s. The same fault duration of 100 ms was used in all MC simulations. The simulations are performed in MATLAB and DIgSILENT/PowerFactory (system stability studies) environment.

Table 4.2 Statistical data about TN fault performance (fault rate/year) [199, 200]

230 kV Bus	Fault type		LG	LLG	LL	LLL
	Fault distribution		0.73	0.17	0.06	0.04
	Fault rate	0.08	0.0584	0.0136	0.048	0.0032
230 kV Line	Fault type		LG	LLG	LL	LLL
	Fault distribution		0.76	0.14	0.06	0.04
	Fault rate	1.57	1.1932	0.2198	0.0942	0.0628

4.4.1 Case Study - I

4.4.1.1 Model Development

The changes of the values of the MSE, CDI and MIA with the number of clusters in the case of historical data clustering are presented in Figure 4.8. Given that the knee of the curve is not noticeable for any of the clustering indices, the two-tangent method described in [160] is used for estimating the knee (as shown in Figure 4.8).

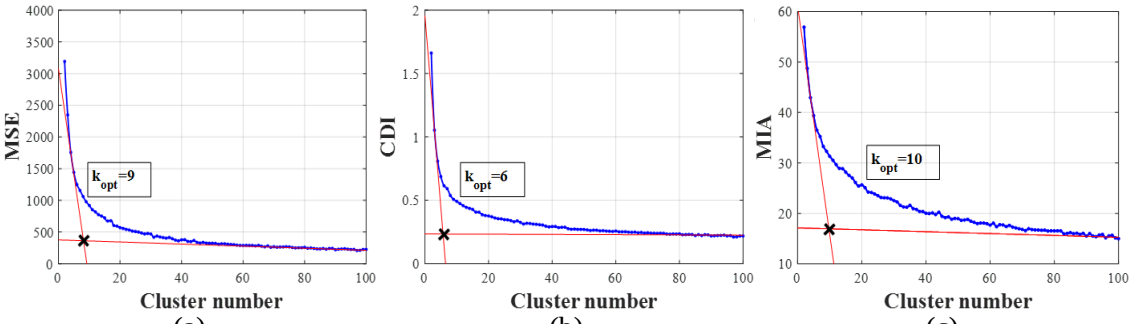

Figure 4.8 CS-I: The change of the MSE (a), CDI (b) and MIA (c) with the number of clusters in the case of historical HRES plant production data clustering

The MSE, CDI and MIA indices suggest different optimal number of clusters to be used in the fuzzy c-means clustering, i.e., 9, 6 and 10, respectively (as shown in Figure 4.8). Thus, the median value is chosen and the production data set was divided into nine

clusters, which are presented in Figure 4.9 (a) in the form of boxplots. Outliers are marked by red asterisks, whereas whiskers cover 99.3% of data in the case of normal distribution. Also, nine clusters of total TN demand corresponding to nine clusters of plant compositions are defined according to the time instance of demand and production data samples (see Figure 4.9 (b)). Characteristic annual HRES plant compositions and total demand levels are defined by the respective cluster centroids and given in Table 4.3.

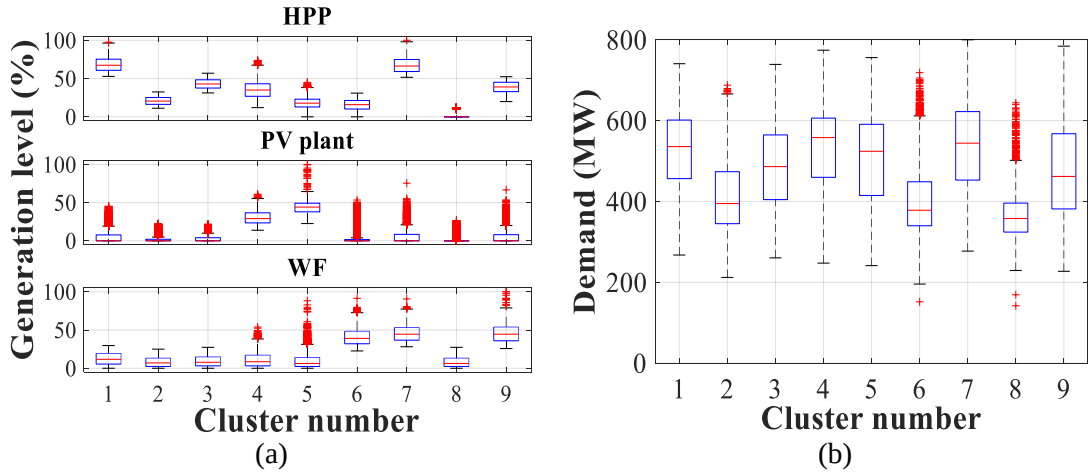

Figure 4.9 CS-I: Clusters of HRES plant compositions (a) and total demand levels (b) (base power for the production levels is the rated power, 210 MVA)

Table 4.3 CS-I: Characteristic annual HRES plant compositions and total demand levels (base power for the production levels is the rated power, 210 MVA)

Cluster number	HRES plant composition			Demand (MW)
	HPP (%)	PV plant (%)	WF (%)	
1	67.36	3.48	12.68	528
2	21.34	2.07	7.89	415
3	43.04	2.75	8.89	485
4	33.63	29.98	10.44	534
5	19.20	43.51	7.91	510
6	16.35	2.55	39.81	403
7	65.83	4.05	44.82	535
8	0	1.16	7.75	365
9	38.63	4.04	44.26	474

Figure 4.10 (a) shows the PDF of TSI values estimated using the KDE approach (the optimal bandwidth of the kernel function is 0.33 according to the solve-the-equation plug-in method). A great majority of MC simulations is characterized by the TSI being within the range of 80-85, meaning there is no significant variation in transient stability status regardless of considerable variation in system operating conditions and disturbances. (*Note*: There have been no cases of slow-interaction converter-driven instability (this category of power system stability is related to the slow dynamic

interactions of the controllers of power electronic-based devices with the slow-response components in power systems such as the electromechanical dynamics of SGs and some generator controllers [169]).) Step-wise hill-climbing method identifies two local maxima corresponding to TSI values of 80.6 and 84.3. This means that two DEMs are required for representing the HRES plant in transient stability studies throughout the year. Two corresponding TSI clusters are shown in Figure 4.10 (b) in the form of boxplots.

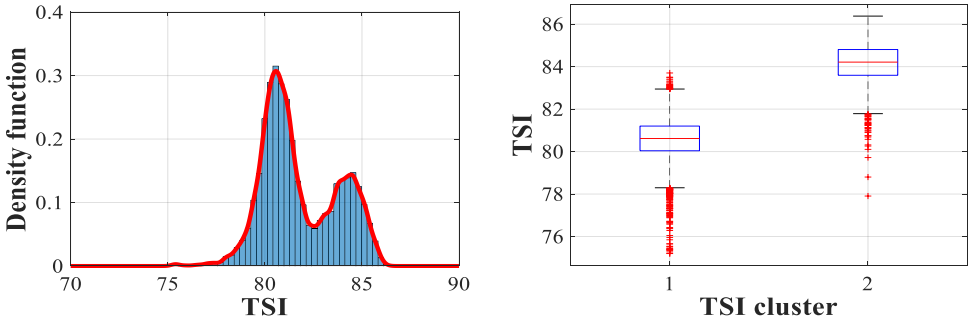

Figure 4.10 CS-I: Histogram-PDF of TSI values (a) and TSI clusters (b)

The number of MC cases produced by the same typical plant composition is defined for each TSI cluster and given in Table 4.4. It can be seen that for each characteristic HRES plant composition, a great majority of (if not all) 1,000 MC simulations belong to the same TSI cluster, regardless of differences in location, type and resistance of short-circuit faults. Therefore, the value of TSI is predominantly determined by HRES plant operating condition, and thus, the selection of the adequate DEM at any time of the year can be performed on the basis of HRES plant composition only. The typical annual HRES plant compositions 6, 7 and 9 (the WF loading is about 40% in those compositions) belong to TSI cluster 2, i.e., they can be represented by DEM 2, whereas the remaining typical generation compositions, 1-5 and 8, are assigned to DEM 1 (about 73% of the historical data can be represented by DEM 1). The expected time of use of the corresponding DEMs (defined based on the historical production dataset) is shown in Figure 4.11. DEM 1 could be confidently used in transient stability simulations pretty much throughout the whole year, except during the first three months of the year when both models cover approximately the same number of days and therefore are equally good for modelling the HRES plant in stability studies.

Table 4.4 CS-I: Number of MC CSs per TSI cluster

	CC 1	CC 2	CC 3	CC 4	CC 5	CC 6	CC 7	CC 8	CC 9
TSI cluster 1	890	1000	1000	1000	995	69	14	1000	37
TSI cluster 2	110	0	0	0	5	931	986	0	963

CC=characteristic HRES plant composition

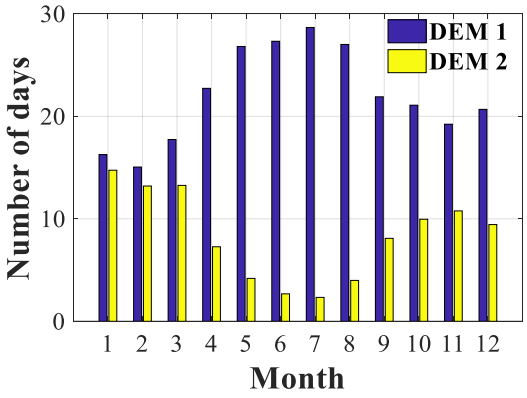

Figure 4.11 CS-I: The expected time of use of DEMs

As described in Section 4.2.4, z-normalized real and reactive power responses at the PCC are divided into groups using the information about the allocation of MC simulations to the two TSI clusters. Clusters of z normalised power responses, along with representative z-normalised responses shown in black thick curve, are presented in Figure 4.12. As can be seen, responses of considerably different shape are grouped together and assigned to the same DEM, which indicates that focusing on highly accurate representation of HRES plant power responses in time domain is unnecessary from the perspective of obtaining reliable results about the most probable overall transient stability status of the system during a year. Table 4.5 provides the information about the parameters of the developed DEMs: TF order, the value of z-normalised power response during fault duration, as well as standard deviation of the representative power response. The proposed equivalent modelling yields significant simplification (from 44 to 11 states) in HRES plant modelling for transient stability assessment of the system with embedded HRES plant. The mathematical model for the dominant equivalent (i.e., the model that can be used most of the time during the year), DEM 1, is as follows (the mathematical model of DEM 2 is given in Appendix B.1.1):

$$z_{Fault,P}(t) = -6.50;\ z_{Fault,Q}(t) = 9.59, \tag{4.58}$$

$$z_{TF,P}(t) = \int^{-1}\left[\frac{-7.4s^5-750.8s^4-1951s^3-1.8\cdot10^4s^2+8141s+2122}{s^5+182.1s^4+715.1s^3+1.1\cdot10^4s^2+2.8\cdot10^4s+3.8\cdot10^4}\right]u_{PCC}(t), \tag{4.59}$$

$$z_{TF,Q}(t) = \mathcal{L}^{-1}\left[\frac{-0.2s^6+101s^5+298.7s^4+4782s^3-667.9s^2+1.1\cdot10^4 s-4492}{s^6+71.9s^5+558.9s^4+5015s^3+2.4\cdot10^4 s^2+4.2\cdot10^4 s+2.6\cdot10^4}\right] u_{PCC}(t), \quad (4.60)$$

$$P_{EQ}(t) = P_{Ss} + 2.04 z_{EQ,P}(t);\ Q_{EQ}(t) = Q_{Ss} + 3.49 z_{EQ,Q}(t), \quad (4.61)$$

where $\mathcal{L}^{-1}$ is inverse Laplace transformation and $u_{PCC}(t)$ is the magnitude of voltage at the PCC.

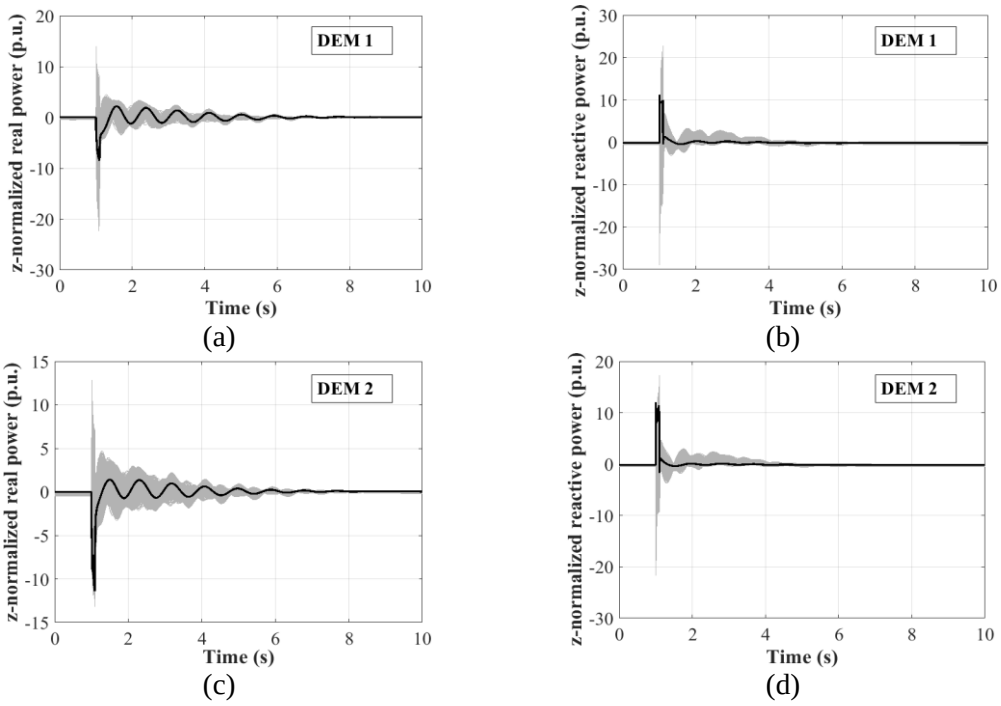

Figure 4.12 CS-I: Z-normalized simulated responses (grey) and representative responses (black) ((a): DEM 1 - real power; (b): DEM 1 - reactive power; (c): DEM 2 - real power; (d): DEM 2 - reactive power)

Table 4.5 CS-I: Parameters of the DEMs

	Real power			Reactive power		
	TF order	$z_{Fault,P}$	SD_P^{rep} (MW)	TF order	$z_{Fault,Q}$	SD_Q^{rep} (Mvar)
DEM 1	5	-6.50	2.04	6	9.59	3.49
DEM 2	6	-8.51	2.19	4	9.66	3.90

4.4.1.2 Assessment of Model Accuracy

The first part of model accuracy assessment is based on MC CSs used for model development. All 9,000 previously defined MC cases are simulated using the equivalent instead of the detailed dynamic model of the HRES plant and the error in TSI value is computed for each MC simulation. The TSI_{Err} indicator given by (4.56) is shown in Figure 4.13 (a) in the form of boxplots for all analysed cases (a boxplot per DEM). The

maximum TSI_{Err} indicator is around 6% and the median TSI_{Err} is below 0.5% for both DEMs, which demonstrates their high accuracy.

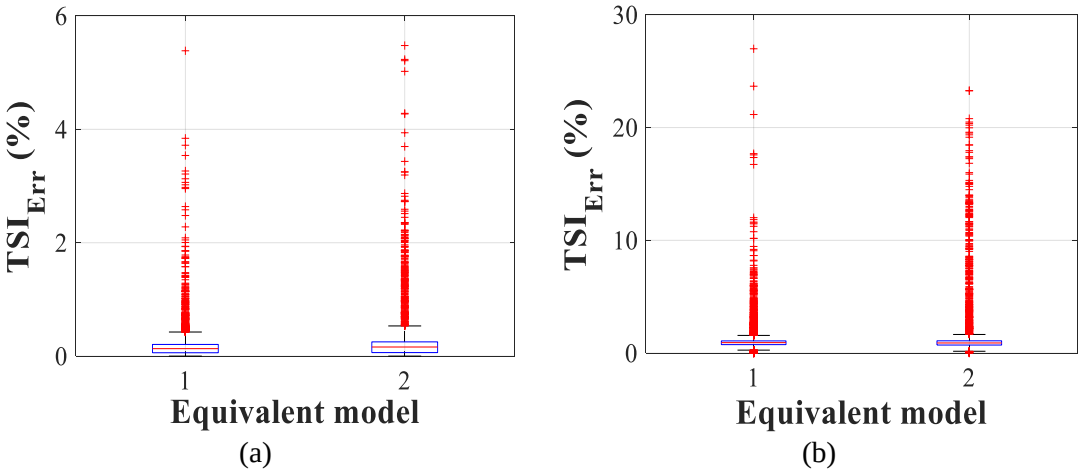

Figure 4.13 CS-I: Error in TSI values for trained (a) and untrained (b) CSs

In order to further test model robustness, the second part of model performance evaluation involves untrained CSs. Namely, the hourly data about the total production of HPPs, PV plants and WFs and total demand in the analysed region during the year of 2019 are used for generating system operating scenarios. TN short-circuit faults are defined in the same way as in the case of initial MC simulations. Results of model testing are shown in Figure 4.13 (b). Model accuracy is slightly lower than in the case of trained CSs, as there are about 100 MC cases characterized by the TSI_{Err} indicator being within the range of (10-30)%. Still, the median error in TSI values is around 1% for both DEMs.

The accuracy of the DEMs is also compared to the case when the whole HRES plant is replaced by a "negative" constant power load model (NCPLM) as done in many system stability studies. The NCPLM accuracy is assessed using the MC CSs developed based on the data from the year of 2019 (i.e., untrained cases that were used for DEM validation). Figure 4.14 compares CDFs of the error in TSI values (TSI_{Err} index) for the NCPLM and the developed DEMs. As illustrated in Figure 4.14, the use of the NCPLM doubles the median TSI error: it increases from 0.9% for the proposed DEMs to 2.5% for the NCPLM. In addition, TSI_{Err} indicator is below 4% for 90% of the simulated transient stability simulations in the case of the NCPLM, whereas this number is below 1.6% for the developed DEMs.

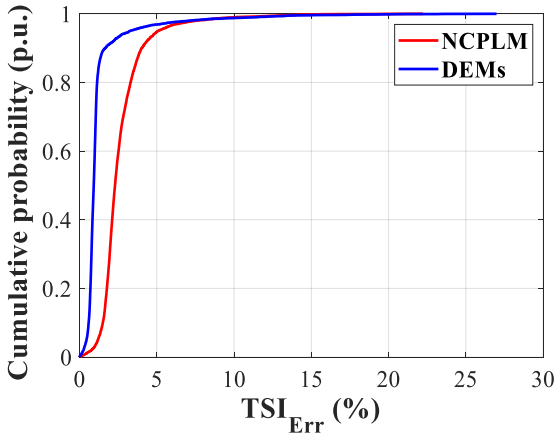

Figure 4.14 CS-I: Test 2019 year: CDF of the error in TSI values for the NCPLM (red) and DEMs developed using the proposed methodology (blue)

Additionally, though not necessarily required for the purpose that the DEM is developed for, the assessment of DEM accuracy is performed by comparing the time domain responses of the detailed dynamic model of the HRES plant and the responses of the equivalent model. The mismatch between the power responses produced by the detailed HRES plant dynamic model and DEM is investigated for MC CSs from the relevant TSI cluster (i.e., the training dataset used for DEM development) as well as for corresponding cases from the test year (2019) that can be represented by the given DEM. Given that the adopted fault duration is 100 ms in all simulations and the period after fault clearing is relevant for TSI calculation, only the period after fault clearing is analysed.

The difference between power responses (in absolute units) produced by the detailed and equivalent model is calculated at each time step of the simulation using the following index:

$$\Delta Y(t_k) = \frac{Y_{EQ}(t_k) - Y_{ORG}(t_k)}{Y_{ORG}(t_k)} \cdot 100\%, \tag{4.62}$$

where t_k is the k-th time step of the simulation, $Y_{ORG}(t_k)$ and $Y_{EQ}(t_k)$ is real/reactive power output of the detailed and equivalent model, respectively, at the k-th time step.

The results of the analysis for the dominant model, DEM 1, are shown in Figure 4.15 and Figure 4.16, while the results for DEM 2 are illustrated in Appendix B.1.1 (Figure B.1 and Figure B.2). Figure 4.15 and Figure 4.16 illustrate the values of index (4.62) calculated for each power response belonging to the training DEM 1 and for each power

response from the year 2019 that can be represented by DEM 1, respectively. The index is calculated for real and reactive power responses separately. The values of the index are shown in the form of boxplots at characteristic time steps of the simulations. In the case of the training dataset, the deviation of real power responses of DEM 1 from the original real power responses (i.e., responses produced by the detailed model) is between -1.9% and 2.4% at each time step for most of the cases. As for the reactive power responses from this dataset, DEM 1 accuracy is slightly lower; DEM 1 error at each time step is between -5.1% and 0.8% for most of the responses. However, in most of the cases with DEM 1 error for reactive power responses that is above ±10%, small reactive power output of the HRES plant in the pre-disturbance state (below 5 Mvar) is a cause of high values of index given by (4.62). When it comes to DEM 1 accuracy for the test year (2019), the maximum observed values of index (4.62) for real and reactive power responses are higher than in the case of the training data, however, the overall DEM 1 accuracy is similar to the one obtained with the training DEM 1 dataset. For most of the responses in this case, the DEM 1 error at each time step after fault clearing is within the range [-1.9, 2.3]% and [-6, 2.1]% for real and reactive power responses, respectively. Similar to the training dataset, the DEM 1 accuracy for reactive power responses from the test dataset is lower compared to the real power responses from the same dataset mainly due to small values of the total reactive power output of the HRES plant in pre-fault state resulting in high values of index (4.62).

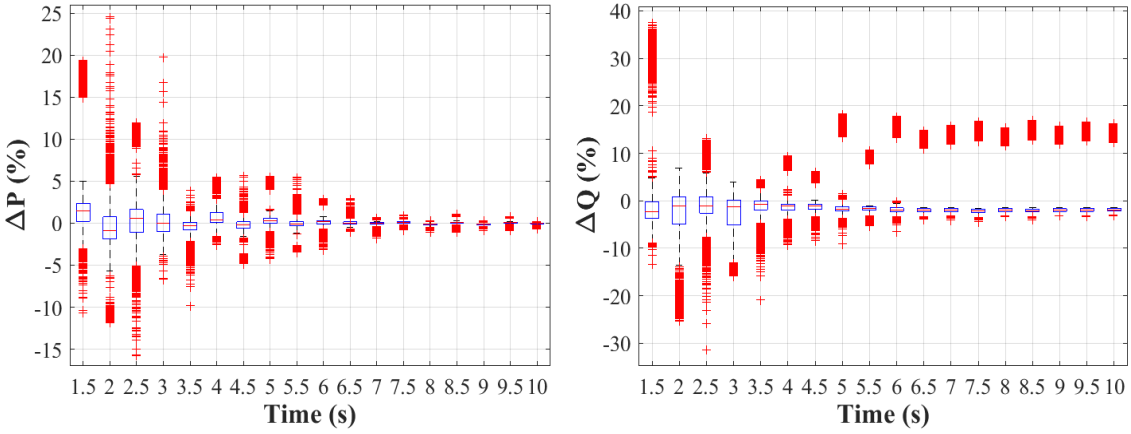

Figure 4.15 CS-I: Training DEM 1 dataset: Comparison between the power responses of the detailed model and DEM 1 ((a): real power, (b): reactive power)

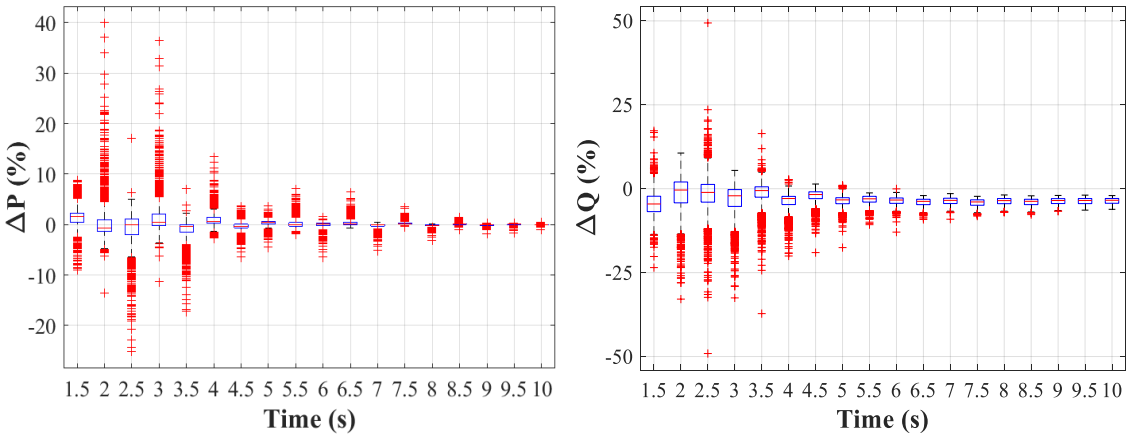

Figure 4.16 CS-I: Test 2019 year: Comparison between the power responses of the detailed model and DEM 1 ((a): real power, (b): reactive power)

When it comes to the training dataset for DEM 2, even though the maximum value of index given by (4.62) is about 15% and 50% in the case of real and reactive power responses, respectively, the error for most of the cases is below 2% and 8% for real and reactive power at each time step after fault clearing, respectively. The accuracy of DEM 2 in terms of the shape of real power responses in time domain for the test year (2019) is similar to the accuracy for real power in the case of the training DEM 2 dataset. As for the reactive power responses from the test year, DEM 2 accuracy is lower compared to the training dataset, i.e., the value of index (4.62) is within the range [-22, 2.5]% for most of the cases at all time steps after the fault clearing. As in the case of DEM 1, low reactive power output of the HRES plant is the main reason for high values of index (4.62) in the case of reactive power responses.

4.4.1.3 The Impact of Input Data on the Accuracy of Dynamic Equivalent Model

4.4.1.3.1 The Impact of the Historical Period Duration

In order to assess the effect of the size of historical HRES plant production dataset on DEM accuracy, DEMs of the considered HRES plant were developed on the basis of three shorter historical periods: six-month winter (Period I: 01/01/2017-15/03/2017; 16/09/2017-31/1/2017), six-month summer (Period II: 16/03/2017 – 15/09/2017), and one-month period (Period III: March of 2017) that can be considered as the worst-case scenario in terms of historical data availability. The data from the year of 2017 are used

for DEM development as they are characterized by the most dissimilar HRES plant production profiles compared to the plant compositions used for DEM validation.

The fuzzy c-means clustering algorithm identified six characteristic HRES plant compositions in Period I and four typical plant compositions in the remaining two periods. The plant compositions are given in Table 4.6, together with the compositions from the original four-year historical period. None of the sets of typical HRES plant compositions from the reduced historical periods contains the composition characterized by similar production of the HPP and WF of about 40% (original composition 9). Composition without the HPP in operation was identified in Period I only, while both six-month periods do not contain the composition characterized by similar production of the HPP and PV plant of about 30% (original composition 4). For each typical HRES plant composition in the considered reduced historical periods, the most similar plant composition from the original four year-period is given in Table 4.6 in bold. Similarity to original compositions 3 and 5, original composition 2, and original compositions 4 and 7 in the case of the six-month winter, six-month summer, and one-month period, respectively, is limited as the maximum difference between the outputs of the individual technologies in the original and reduced historical periods is about 10%.

A single eleventh-order DEM is sufficient for representing all compositions in Period I, while two DEMs are required for Period II and Period III. The orders of models in Period II are 11 and 8, while both equivalents developed based on one-month data are characterized by ten differential equations.

Table 4.6 CS-I: Typical HRES plant compositions for different historical period duration

Cluster number	Original historical production dataset			Period I				Period II				Period III			
	HPP (%)	WF (%)	PV (%)	HPP (%)	WF (%)	PV (%)		HPP (%)	WF (%)	PV (%)		HPP (%)	WF (%)	PV (%)	
1	67.4	13.3	3.8	66.7	17.1	4.3	**1**	18.2	9.8	43.4	**5**	67.3	14.1	4.7	**1**
2	21.3	8.6	1.9	16.4	47.3	2.3	**6**	39.4	11.6	5.3	**3**	35.3	10.0	41.2	**4**
3	43.0	9.5	2.9	0	9.4	1.4	**8**	20.7	42.7	8.2	**6**	26.9	14.2	2.0	**2**
4	33.6	10.5	30.5	33.6	12.6	3.4	**3**	12.0	9	2.0	**2**	57.3	51.0	6.4	**7**
5	19.2	8.6	43.8	56.6	53.8	3.5	**7**								
6	16.3	40.0	2.9	21.7	8.9	36.5	**5**								
7	65.8	44.8	4.8												
8	0	7.6	1.0												
9	38.6	44.8	3.8												

The accuracy of the new DEMs is evaluated using already defined MC CSs for the year of 2019. Figure 4.17 shows the CDFs of the TSI error for the DEMs derived on the basis

of the reduced historical periods as well as for the original DEMs. The 50th and 90th percentile of the CDFs of the TSI error for all DEMs developed based on the three reduced historical datasets are about 2.3% and 4%, respectively, which does not represent a considerable reduction in the overall model accuracy compared to the original DEMs derived using the whole four-year historical period (0.9% and 1.6% correspond to the 50th and 90th percentile, respectively, of the CDF of TSI_{Err} indicator for these DEMs). Given that the same level of model accuracy was achieved for all three reduced historical periods, the correlation between the duration of historical period and TSI error is not linear, i.e., larger historical dataset does not necessarily provide higher model accuracy. As the median TSI error of 2.3% was obtained for DEMs derived using only one-month recordings, this value can be considered as the maximum median TSI error for DEMs of the considered HRES plant developed on the basis of any historical period.

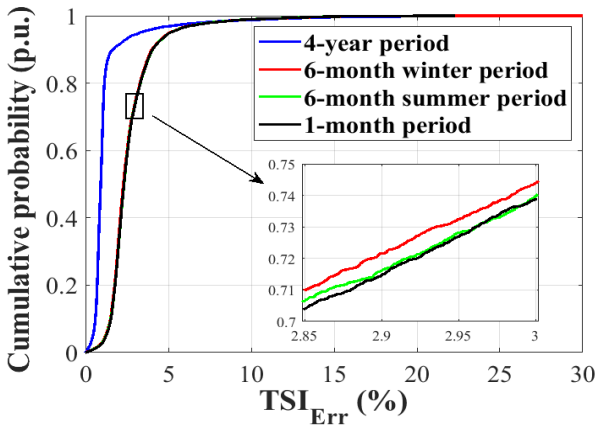

Figure 4.17 CS-I: CDFs of TSI error for DEMs developed using four-year (blue), six-month winter (red), six-month summer (green), and one-month (black) period

4.4.1.3.2 The Impact of the Sampling Rate of Historical Production Data

The impact of data sampling rate on DEM accuracy is investigated for one-month historical period, the March of 2017, as a worst-case scenario. As the original historical data for the test HRES plant are available with a one-hour sampling rate, the data were resampled at six-hour time steps in order to perform this analysis. MC CSs for the year of 2019 (defined for the DEMs developed using the original historical dataset) are used for assessing DEM accuracy. Figure 4.18 illustrates CDFs of TSI error for DEMs derived on the basis of the one-month recordings with two different sampling rates. Very similar, almost identical values of TSI_{Err} indicator were obtained for both sets of DEMs, meaning

historical data sampling rate does not have significant impact on the accuracy of TSI value. The reason for a high match between the two CDFs is the ability of the fuzzy c-means clustering algorithm to identify almost identical typical monthly HRES plant compositions regardless of data sampling rate (characteristic plant compositions for the one-month period for one- and six-hour sampling rates are given in Table 4.7).

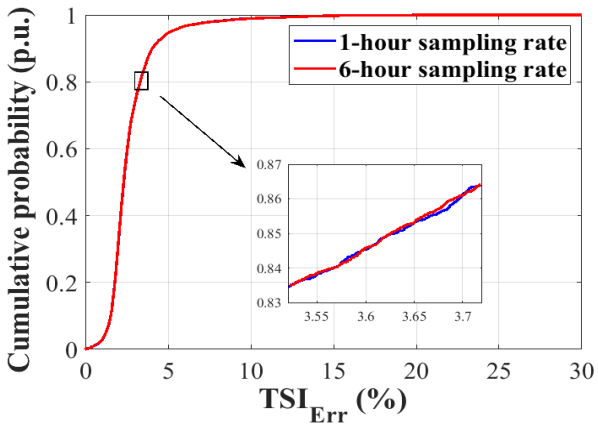

Figure 4.18 CS-I: CDFs of TSI error for DEMs developed using the one-month data with one-hour (blue) and six-hour (red) sampling rate

Table 4.7 CS-I: Typical HRES plant compositions for the one-month historical period with one- and six-hour sampling rates

Cluster number	One-hour sampling rate			Six-hour sampling rate		
	HPP (%)	WF (%)	PV (%)	HPP (%)	WF (%)	PV (%)
1	67.3	14.1	4.7	70.4	14.5	4.8
2	35.3	10.0	41.2	35.4	11.3	37.3
3	26.9	14.2	2.0	23.4	13.2	2.7
4	57.3	51.0	6.4	61.2	52.1	9.9

4.4.1.3.3 The Impact of the Unavailability of Historical Production Data of Individual Plants

In case historical data for a single individual plant in the HRES plant are not available but the real power output of the whole HRES plant was recorded, then the data for this plant can be obtained by simply subtracting the sum of real power outputs of the remaining individual technologies from the total HRES plant production. However, if production data of the whole HRES plant or more than one individual technology are not available, then artificial production data have to be generated. Artificial production dataset can be produced using one of the following approaches:

- Production data of non-dispatchable RES plants, such as PV plants, WFs and run-of-river HPPs, can be generated on the basis of measured solar irradiance, wind speed and streamflow at the plant location, respectively, and corresponding

equations for converting primary energy source into plant power output. In case measurements are not available, relevant PDFs can be used for modelling variation in solar irradiance, wind speed and streamflow.

- Production data of dispatchable individual plants can be obtained as the outputs of the optimal economic dispatch of the HRES plant. The objective of the optimization process is to minimize the total plant costs while meeting the pre-specified HRES plant production profile.

In order to assess the impact of missing historical production data on DEM performance, two scenarios for generating artificial historical data are analysed:

- Scenario I - assuming production data unavailability for a single plant, the WF in this example;
- Scenario II - assuming production data unavailability for all individual plants in the HRES plant.

Scenario II represents the worst-case scenario in terms of the unavailability of historical data of individual plants in the HRES plant. Still, it should be noted that it is highly unlikely that there would be absolutely no information about real power output of any individual technology in an operating HRES plant.

Given that wind speed and solar irradiance measurements, as well as the relevant PDFs of wind speed and solar irradiance, for the considered region were not available, the artificial historical data for the considered scenarios were generated by varying the available data within the ±20% range, i.e., by multiplying the available historical data by a random number sampled uniformly from the range [0.8 – 1.2]. It is assumed that inaccuracies due to the conversion of wind speed and solar irradiance value into power plant output, availability/operation status of power plant, wake effect in the WF, shading effect on PV panels, etc., can be taken into account by adopting the maximum error of ±20%.

Following the generation of the artificial historical data, all steps in the proposed equivalent modelling procedure were performed. In the case of unavailability of historical production data of the WF, the number of characteristic annual HRES plant

compositions in the artificial historical dataset is six, while the number of typical plant compositions in Scenario II is seven. These compositions are given in Table 4.8, along with nine typical compositions identified in the original historical dataset. Typical plant compositions obtained from the artificial datasets are similar to the original ones to a great extent. However, unlike in the case of the original historical data, the sets of typical plant compositions in Scenario I and Scenario II do not contain the compositions with similar share of the HPP and PV plant/WF in the total HRES plant output (original compositions 4 and 9, respectively). In addition, characteristic plant compositions in Scenario I do not include a composition with converter-connected technologies only.

Table 4.8 CS-I: Typical annual HRES plant compositions for original and artificial historical datasets

Cluster number	Original historical production dataset			Scenario I			Scenario II		
	HPP (%)	WF (%)	PV (%)	HPP (%)	WF (%)	PV (%)	HPP (%)	WF (%)	PV (%)
1	67.4	13.3	3.8	37.5	10.5	4.8	44.4	10.5	4.8
2	21.3	8.6	1.9	13.0	8.6	2.9	24.6	10.5	4.8
3	43.0	9.5	2.9	55.8	45.7	5.7	22.4	8.6	41.9
4	33.6	10.5	30.5	20.2	41.0	3.8	56.0	46.7	5.7
5	19.2	8.6	43.8	22.6	9.5	41.0	69.0	16.2	4.8
6	16.3	40.0	2.9	64.0	14.3	4.8	0	9.5	2.9
7	65.8	44.8	4.8				21.2	42.9	3.8
8	0	7.6	1.0						
9	38.6	44.8	3.8						

As in the case of the original historical production dataset, in both scenarios, two DEMs are required for modelling the whole HRES plant during the year. Furthermore, there is no considerable difference in the order of the derived DEMs: in Scenario I the order of DEMs is 8 and 10, in Scenario II the order of DEMs is 10 and 12, while original DEMs (i.e., DEMs developed on the basis of the original historical data) are characterized by 10 and 11 states. The accuracy of the DEMs developed using the artificial historical data is assessed on the basis of both sets of MS CSs used for the validation of the original DEMs. The results of the evaluation of the original DEMs and DEMs developed in Scenario I and II are compared in Figure 4.19 using the CDFs of the TSI error (a few values of TSI error in Scenario I and Scenario II between 30% and 50% are not shown in Figure 4.19 (a) to enable easier comparison between the results for the training data and the test 2019 year). Additionally, the values of the 50^{th} and 90^{th} percentile of TSI error for all three sets of DEMs are given in Table 4.9. It can be seen that the lack of historical data of individual plants has almost no effect on DEM accuracy. In the case of

9,000 MC CSs used for the development of the original DEMs, the median TSI_{Err} is almost the same for all three sets of DEMs, while the 90th percentile of TSI error for DEMs from Scenario I and II is higher than the corresponding value for the original DEMs by only 0.04% and 0.02%, respectively. As for the test 2019 year, the median TSI_{Err} of DEMs from Scenario I and II (0.88% and 0.84%, respectively) is insignificantly smaller than the median TSI_{Err} value for the original DEMs (0.91%). The reason for this is slightly greater similarity of the data from the test 2019 year with the artificial HRES plant production profiles than with the original historical data (2015-2018).

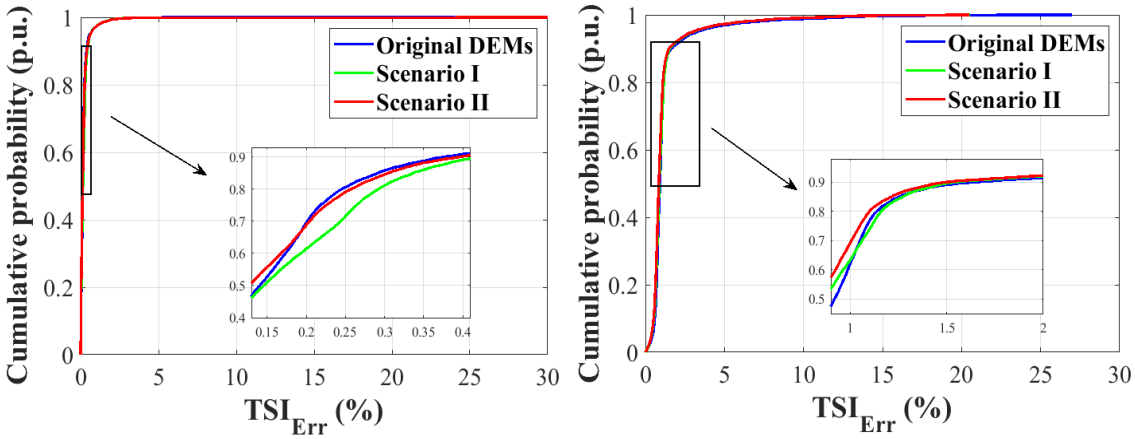

Figure 4.19 CS-I: CDFs of TSI_{Err} indicator for the original DEMs (blue), DEMs from Scenario I (green) and DEMs from Scenario II (red) ((a): MC CSs used for the development of the original DEMs; (b): MC CSs from the test 2019 year)

Table 4.9 CS-I: TSI error for original and artificial historical datasets

	MC CSs used for the original DEM development			MC CSs from the year of 2019		
	Original DEMs	Scenario I	Scenario II	Original DEMs	Scenario I	Scenario II
50th percentile of TSI error	0.14%	0.15%	0.13%	0.91%	0.88%	0.84%
90th percentile of TSI error	0.38%	0.42%	0.40%	1.60%	1.54%	1.50%

The issue of historical data unavailability may also arise in case of the integration of new individual plants into the existing HRES plant after developing DEMs for the initial HRES plant design. In this situation, the adequacy of the already developed DEMs for representing new HRES plant configuration can be assessed by comparing TSI values produced by these DEMs and the detailed dynamic model of the new HRES plant in probabilistic transient stability simulations. Given that historical datasets required for transient stability analysis cannot be available for new individual plants prior to their

commissioning, artificial historical data have to be generated as previously described. If, following the transient stability analysis, the use of the existing DEMs results in large errors in TSI values (see discussion in Section 4.4.3) then new set of DEMs has to be developed. The analysis in Section 4.4.1.3.1 has shown, however, that both one-month and six-month historical production data result in the same DEM accuracy. Therefore, the production of individual technologies recorded during the first month of operation of the new HRES plant can be used for the development of the new DEMs, and if necessary periodically updated as more data become available.

4.4.2 Case Study - II

4.4.2.1 Model Development

The historical HRES plant production dataset used in this CS-II corresponds to the one used for the test HRES plant in Chapter 3, meaning the results of the clustering of historical production data using the fuzzy c-means algorithm are the same. Thus, the optimal number of clusters in the historical plant production dataset is nine (the change of the clustering indices MSE, CDI and MIA with the number of clusters is shown in Figure 3.8). Nine typical annual plant compositions and corresponding demand levels (identified as in CS-I) are given in Table 4.10 (characteristic plant compositions are the ones given in Table 3.2) and yield 9,000 MC simulations, i.e., 9,000 TSI values. Nine clusters of historical production and demand data are presented in Appendix B.2.1 in the form of boxplots (Figure B.3 and Figure B.4, respectively).

Table 4.10 CS-II: Characteristic annual HRES plant compositions and total demand levels (base power for the production levels is the rated power of the individual plant)

Cluster number	HRES plant composition						Demand (MW)
	WF (%)	PV plant (%)	HPP (%)	Biomass plant (%)	Biogas plant (%)	BESS (%)	
1	7.1	1.5	0	84.2	75.8	0	378
2	94.1	2.3	0	0	0	0	371
3	45.9	4.5	0	62.6	18.3	1.4	367
4	74.1	30.2	0	0	0	-10.9	446
5	16.5	9.8	0	0	0	72.9	450
6	87.1	72.5	0	0	0	-0.3	463
7	11.8	49.8	0	0	0	-1.2	447
8	14.1	1.5	43.6	0	0	0.1	370
9	10.6	76.2	0	0	0	-44.3	451

Figure 4.20 (a) shows the PDF of the TSI values estimated using the KDE approach (the optimal bandwidth of the kernel function is 0.13). Similar to CS-I, all MC cases result in

transiently stable behaviour of the system with small variation in the TSI values. (*Note*: As in the case of CS-I, there have been no cases of slow-interaction converter-driven instability.) The estimated PDF is characterized by three local maxima, corresponding to the TSI values of 78.3, 81.2 and 92.5, which means that three DEMs are required for modelling the annual performance of the considered HRES plant in transient stability studies. Three TSI clusters are presented in Figure 4.20 (b).

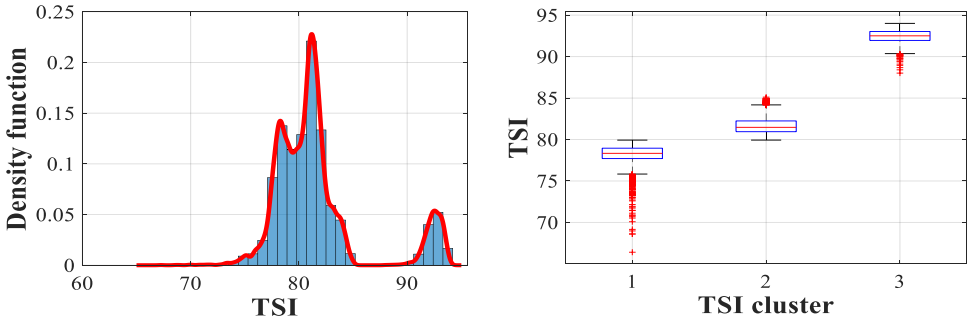

Figure 4.20 CS-II: Histogram-PDF of TSI values (a) and TSI clusters (b)

As in CS-I, majority of the responses resulting from modelling uncertainties associated with fault performance, total system demand and plant output for a given plant composition is clustered in one TSI cluster (the number of MC CSs from each typical plant composition per TSI cluster is given in Table 4.11). Thus, as in the previous CS, the choice of the DEM at any time of the year can be carried out having the information about the HRES plant composition only. DEM 1 is the most suitable for HRES plant compositions 1, 3 and 8 (compositions with at least one SG in service), while the sixth typical composition, characterized by high production from both the WF and PV plant, is represented by DEM 3. DEM 2 is the most adequate model for the remaining production profiles.

Table 4.11 CS-II: Number of MC CSs per TSI cluster

	CC 1	CC 2	CC 3	CC 4	CC 5	CC 6	CC 7	CC 8	CC 9
TSI cluster 1	1000	119	991	10	196	0	99	991	91
TSI cluster 2	0	881	9	990	804	0	901	9	909
TSI cluster 3	0	0	0	0	0	1000	0	0	0

CC=characteristic HRES plant composition

Figure 4.21 shows the expected time of use of DEMs during the year. DEM 3 has the smallest data coverage and accounts for less than 5% of the historical dataset, whereas DEM 1 and 2 correspond to around 40% and 55% of the dataset, respectively. DEM 2 is

a dominant model in every month, except in winter when DEM 1 and 2 have similar time of use.

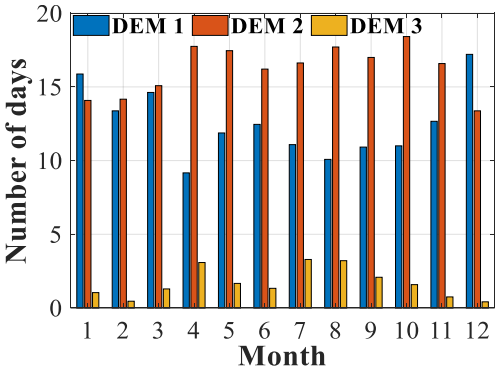

Figure 4.21 CS-II: The expected time of use of DEMs

Clusters of z-normalised power responses at the PCC are presented in Figure 4.22, with representative z-normalised power response shown in black thick curve.

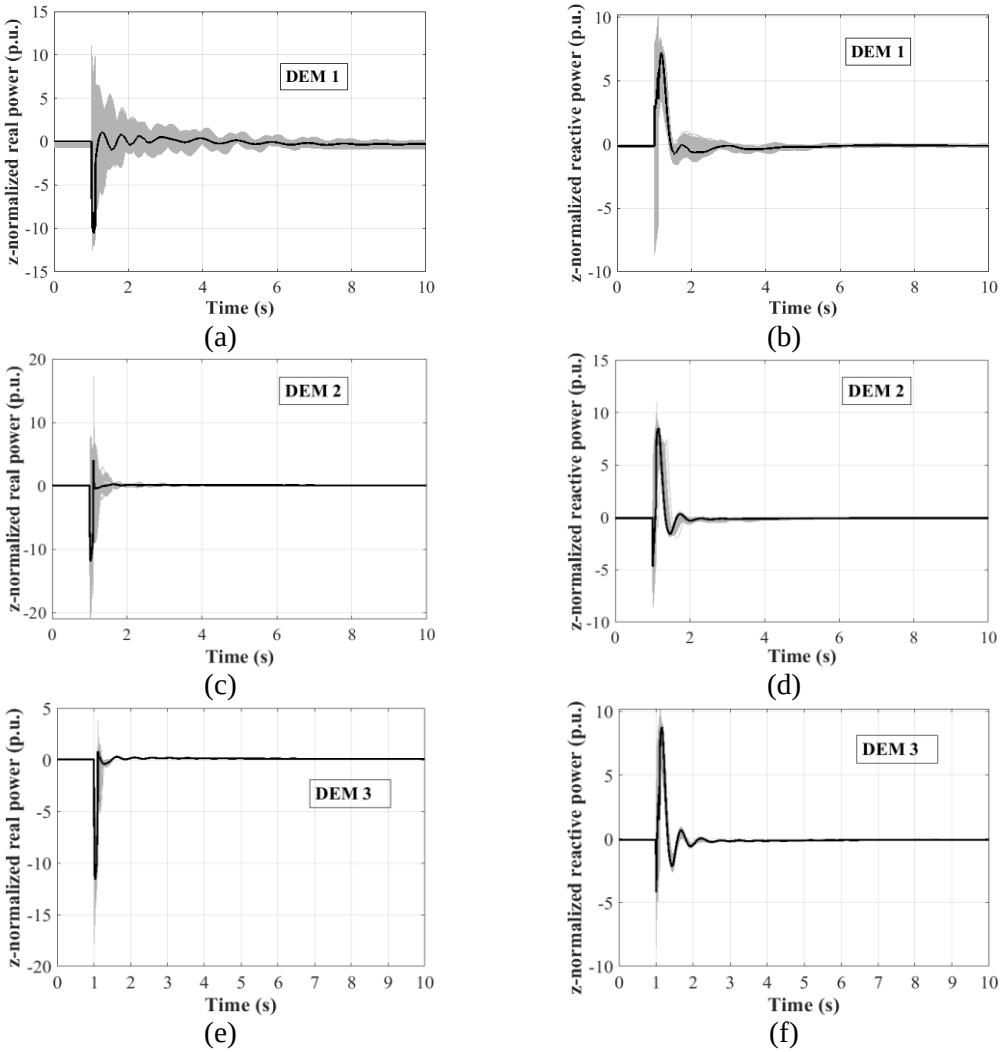

Figure 4.22 CS-II: Z-normalized simulated responses (grey) and representative responses (black) ((a): DEM 1 - real power; (b): DEM 1 - reactive power; (c): DEM 2 - real power; (d): DEM 2 - reactive power; (e): DEM 3 - real power; (f): DEM 3 - reactive power)

Table 4.12 provides the information about equivalent model parameters for both real and reactive power. The model order of DEMs 1, 2 and 3 is 11, 8, and 9, respectively, which is considerably smaller than the model order of the detailed HRES plant model (78 state variables). The full mathematical model of the dominant equivalent, DEM 2, is given by (4.63-4.66) (the mathematical models of the remaining equivalents are provided in Appendix B.2.2 and B.2.3):

$$z_{Fault,P}(t) = -9.69;\ z_{Fault,Q}(t) = -1.68, \tag{4.63}$$

$$z_{TF,P}(t) = \mathcal{L}^{-1}\left[\frac{3.5s^6+3\cdot10^3s^5+1.2\cdot10^4s^4+4.3\cdot10^5s^3-4.9\cdot10^6s^2+1.5\cdot10^7s+1.5\cdot10^6}{s^6+581.7s^5+7.4\cdot10^4s^4+1.3\cdot10^6s^3+1.5\cdot10^7s^2+1\cdot10^8s+2\cdot10^7}\right]u_{PCC}(t), \tag{4.64}$$

$$z_{TF,Q}(t) = \mathcal{L}^{-1}\left[\frac{7.3s^2+157.3s-14.2}{s^2+11.5s+141.7}\right]u_{PCC}(t), \tag{4.65}$$

$$P_{EQ}(t) = P_{Ss} + 1.11z_{EQ,P}(t);\ Q_{EQ}(t) = Q_{Ss} + 5.36z_{EQ,Q}(t). \tag{4.66}$$

Table 4.12 CS-II: Parameters of the DEMs

	Real power			Reactive power		
	TF order	$z_{Fault,P}$	SD_P^{rep} (MW)	TF order	$z_{Fault,Q}$	SD_Q^{rep} (Mvar)
DEM 1	5	-9.51	2.15	6	3.87	10.34
DEM 2	6	-9.69	1.11	2	-1.68	5.36
DEM 3	6	-8.87	4.52	3	1.51	4.96

4.4.2.2 Assessment of Model Accuracy

Model accuracy is tested by simulating 9,000 previously defined MC CSs with the developed DEMs and comparing TSI values obtained in the case of the detailed and equivalent plant model. Figure 4.23 (a) illustrates the error in TSI values for all three DEMs in the form of boxplots. The maximum error in TSI values is below 20% for all MC simulations. Furthermore, median TSI_{Err} indicator (4.56) for all three DEMs is below 1%, confirming that the equivalent modelling approach provides DEMs of high accuracy.

As in CS-I, the suitability of the NCPLM for representing the whole HRES plant is analysed based on the MC CSs used for DEM evaluation. Figure 4.23 (b) compares CDFs of the error in TSI values for the NCPLM and developed models. As can be seen, the use of the NCPLM instead of the proposed DEMs results in larger TSI error in this CS as well. For the NCPLM, the 50th and 90th percentile of TSI_{Err} indicator are 4% and 5.6%,

respectively. On the other hand, the developed DEMs are characterized by the 50th and 90th percentile of TSI error of around 1% and 2.9%, respectively.

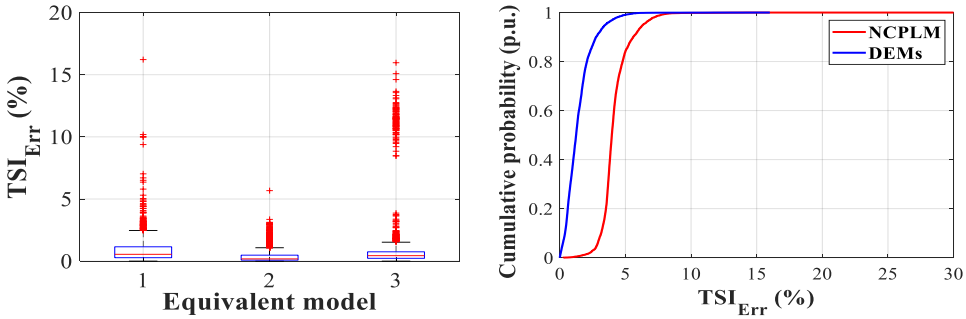

(a) (b)

Figure 4.23 CS-II: (a): Model accuracy; (b): CDF of the error in TSI values for the NCPLM (red) and DEMs developed using the proposed methodology (blue)

The mismatch between the shape of time domain power responses (after the fault clearing) produced by the detailed and equivalent model is analysed as well (as in CS-I). For each DEM, the index given by (4.62) is calculated for all MC cases allocated to the relevant TSI cluster. The results for the dominant equivalent, DEM 2, are shown in this chapter (see Figure 4.24), whereas the results for DEM 1 and DEM 3 are given in Appendix B.2.2 and B.2.3, respectively (Figure B.5 and Figure B.6, respectively).

As seen in Figure 4.24 (a), in the case of real power responses, DEM 2 error is between -2% and 2% at each time step of the simulation after the fault clearing for almost all MC cases, and the error reduces to almost zero after four seconds of the simulation. When it comes to reactive power, model accuracy is slightly lower. Though the maximum DEM 2 error is around -21%, the value of index (4.62) is within the range [-2, 5]% at each time step after the fault clearing for most of the analysed cases. In addition, the highest median error for reactive power responses among all time steps in the post-fault period is 3.7%.

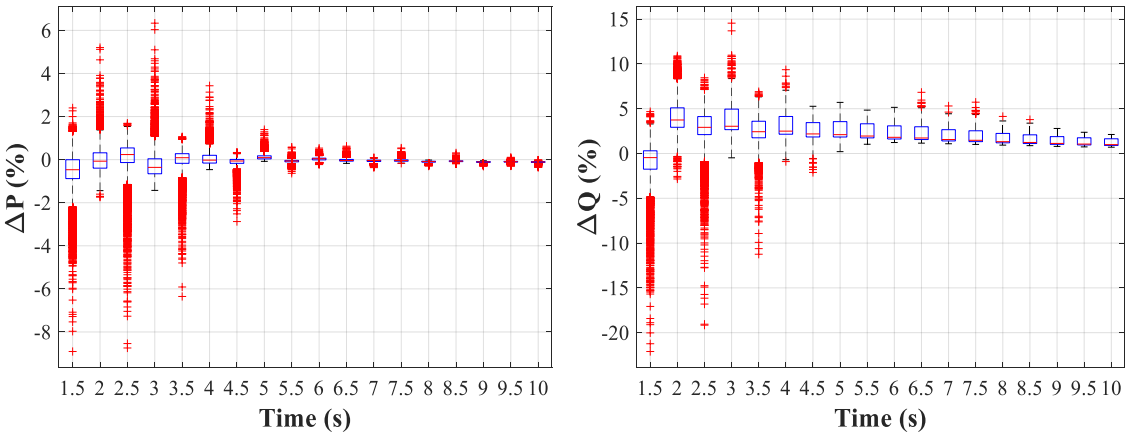

(a) (b)

Figure 4.24 CS-II: Training DEM 2 dataset: Comparison between the power responses of the detailed model and DEM 2 ((a): real power, (b): reactive power)

The accuracy of DEM 1 for real power responses is almost the same as in the case of DEM 2. When it comes to reactive power responses, the maximum DEM 1 error is 50%. However, for most of the cases in TSI cluster 1, the value of index given by (4.62) is within the range [-12, 7]% at each time step after the fault clearing. DEM 3 is characterized by the smallest error in terms of the shape of real and reactive power responses in time domain among all equivalents. The maximum value of index (4.62) is only 0.6% in the case of real power. The accuracy of DEM 3 in the case of reactive power responses is slightly lower, but the error is below 2% for most of the cases at each time step after the fault clearing. Still, it should be noted that TSI cluster 3 is the smallest cluster with only 1,000 MC CSs produced by characteristic HRES plant composition 6.

4.4.3 Discussion

The basic assumption of the proposed equivalent modelling procedure is model development on the basis of the most probable HRES plant dynamic behaviour/responses in annual transient stability studies of the system. The typical annual short-circuit faults are used for simulating the corresponding HRES plant power responses, which are then used for TF parameter estimation. Given that the procedure for DEM development is the same for any power system, cases resulting in lower TSI values will be used for model development only if they represent the most probable annual disturbances, i.e., if the typical global transient stability performance of the system during the year is characterized by TSI values closer to zero. Therefore, as the model development relies on highly probable disturbances, the accuracy of the DEM is expected to be lower in the case of low-probability disturbances (i.e., outliers) compared to the DEM performance for typical annual disturbances. This difference in the DEM performance for high- and low-probability disturbances will exist in any power system regardless of its typical annual transient stability status, i.e., whether the system is generally very stable, or less stable, during the year.

Whether TSI error associated with the application of DEM can be considered sufficiently small or not depends on the desired accuracy in TSI value, which can be different depending on the original TSI value, i.e., TSI value obtained using the detailed HRES plant dynamic model and proximity to transient stability limit. Theoretically, the TSI values can be in the range from -100 to 100. The system is more stable if the TSI value

is closer to 100, while the system stability boundary corresponds to zero TSI value. In both CSs presented in this chapter, the simulated TSI values were far away from the transient stability limit (TSI values were in the range 70-95). Thus, even a considerable TSI error of 50%, calculated by (4.56), would not result in an inaccurate assessment of the transient stability status of the system. The actual errors in TSI value obtained when comparing performance of the detailed model and DEMs were within a few percent, which implies that the transient stability status of the system with DEMs remains practically the same as with the full-scale HRES plant dynamic model. Even if the original TSI values were much smaller, say about 5, the 50% error would give a range between 2.5 and 7.5, which still corresponds to the transient stability behaviour and status of the system with the detailed model. Based on the above, one could safely set a (very) conservative limit on the TSI error of 20% which would guarantee practically the same transient behaviour of the system. Furthermore, transient stability assessment of the system is typically carried out by checking only whether the calculated TSI is positive, i.e., whether the system is stable or not. Therefore, the least rigorous assessment of DEM accuracy would be according to transient stability status of the system indicated by the detailed and equivalent model. DEM certainly cannot be considered suitable for representing the HRES plant in transient stability studies if TSI values produced by the original model and DEM indicate opposite system stability status, that is, if TSI value obtained using the detailed model is positive and DEM results in negative TSI, or vice versa.

Relative error (given by (4.62)) is used for assessing model accuracy in terms of the shape of time domain HRES plant power responses as it can present the model accuracy in a more identifiable way compared to the error in absolute units. Namely, defining a threshold for differentiating between the acceptable and non-acceptable model performance is more intuitive in the case of relative error than in the case of error in absolute units. For instance, the error of 20 MW cannot indicate whether the model performance is acceptable or not as this would depend on the size of the plant, i.e., its power output. On the other hand, the relative error, in case of previously mentioned absolute error of 20 MW and assumed base value of 200 MW (i.e., the denominator in (4.62)), would be 10%, which can be used as an indicator of satisfactory model accuracy. The only situation when the use of relative error can provide misleading results about model performance is in the case of small error in absolute units and small base value

(which was the case when the highest relative error values were observed for reactive power responses in CSs). In these cases, small error in absolute units that has no practical significance can result in large relative error. Given that the pre-disturbance real power output of the whole HRES plant is above 100 MW for more than 85% of the considered MC cases (all investigated cases in CS-I and CS-II), and the pre-disturbance reactive power output of the HRES plant is below 10 Mvar (relative reactive power error can have high value in the case of small reactive power production in absolute units and small reactive power error in absolute units, as explained above) for about 25% of all analysed MC cases in CS-I and CS-II, relative model error can be safely used for assessing the accuracy of the developed DEMs in terms of the shape of time domain HRES plant power responses.

4.5 Summary

This chapter presented the data-driven methodology for dynamic equivalent modelling of HRES plants for transient stability studies. The focus of the study was on the development of DEMs of HRES plant suitable for the sufficiently accurate assessment of the overall system transient stability as described by TSI value. The proposed equivalent modelling approach is based on typical annual HRES plant dynamic responses in transient stability simulations generated using historical plant production data and TN fault statistics. The dynamic model is in the form of two TFs with voltage, and real and reactive power at the PCC as the input and outputs, respectively. Developed data-driven methodology for equivalent dynamic modelling of HRES plant represents the third original contribution of this thesis.

The methodology was tested on two HRES plant configurations connected to the same TN. In both CSs, a few low-order DEMs were required for representing the plant in system transient stability analyses throughout the year. The median error in transient stability assessment for a wide range of operating conditions and TN short-circuit faults was below 1% for all DEMs of the test HRES plants. In addition, the proposed DEMs outperformed a common model of RES power plants in system studies (the NCPLM representation) in terms of TSI accuracy. Even though the models were not developed with the aim of obtaining highly accurate HRES plant power responses in time domain,

the relative difference between the values of real and reactive power produced by the detailed and equivalent model was below about 2.5% and 12%, respectively, during the post-fault period for most of the analysed cases.

The presented modelling approach is robust to the size of the historical dataset (in terms of the duration of the historical period), sampling rate and availability of data for individual technologies in the HRES plant. The procedures for generating artificial production datasets in case of historical data unavailability were also proposed. Furthermore, the required level of DEM accuracy for obtaining reliable overall transient stability results was discussed.

Considering high accuracy of transient stability assessment and low order of the equivalent models, the proposed methodology can clearly provide computationally efficient and accurate large network transient stability analysis with embedded HRES plants. The proposed approach is highly suitable for practical applications as only the information about the forecasted HRES plant composition and typical HRES plant production profiles is needed for selecting the most appropriate DEM from the library of previously developed models at any time during the year. It should be noted that the network topology was assumed to be the same in all pre-disturbances operating conditions as well as following a fault disturbance (i.e., all simulated faults were self-clearing faults). The number of models in the library is not critical from the perspective of computational time for performing dynamic security assessment as these models can be developed offline and stored in the library for future use.

The DEMs presented in this chapter were developed from the perspective of the accuracy of the global transient stability status, which represents a departure from the typical approach in dynamic equivalent modelling of power plants and networks that requires highly accurate plant/network responses in time domain. In order to investigate whether focusing on the reproduction of time domain power responses of the detailed plant model can improve the accuracy of transient stability assessment of the system provided by the TF-based DEMs, the following Chapter 5 introduces the methodology for dynamic equivalent modelling of HRES plant for transient stability studies from the perspective of the shape of time domain HRES plant power responses at the PCC.

5 Deep Learning-based Equivalent Modelling of HRES Plant for Power System Transient Stability Studies

5.1 Introduction

This chapter presents the methodology for developing DEM of HRES plant for transient stability studies that relies on deep learning method. The methodology represents a further assessment of the data-driven dynamic equivalent modelling of HRES plant described in previous Chapter 4. The principle difference between the data-driven and deep learning-based modelling procedures is that the accuracy of TF-based equivalents (presented in Chapter 4) was assessed on the basis of TSI value, while the error of DEM developed in this chapter is defined according to the dissimilarity between time domain responses of the detailed plant dynamic model and DEM. TF-based DEMs were derived from the perspective of the overall transient stability status described by TSI value, without paying attention to the shape of HRES plant power responses. The main focus of the deep learning-based methodology is on the reproduction of time domain HRES plant power responses obtained by the detailed dynamic plant model and the application of DEM at any time of the year based on the information about the forecasted HRES plant operating condition only.

5.2 Methodology and Model Development

The deep learning-based methodology for equivalent modelling of HRES plants for system transient stability analysis is illustrated in Figure 5.1. Inputs and outputs of the various steps in the methodology are represented by dashed rectangles. As in the case of the data-driven equivalent modelling, the deep learning-based procedure generates realistic CSs used for model development through probabilistic MC simulations relying on characteristic annual HRES plant compositions (determined based on historical HRES plant production dataset) and TN short-circuit fault statistics. Clustering algorithm-based approach enables the identification of the groups/clusters of HRES plant power responses (obtained from realistic MC CSs) similar in time, and these clusters represent a basis for the development of a set of DEMs.

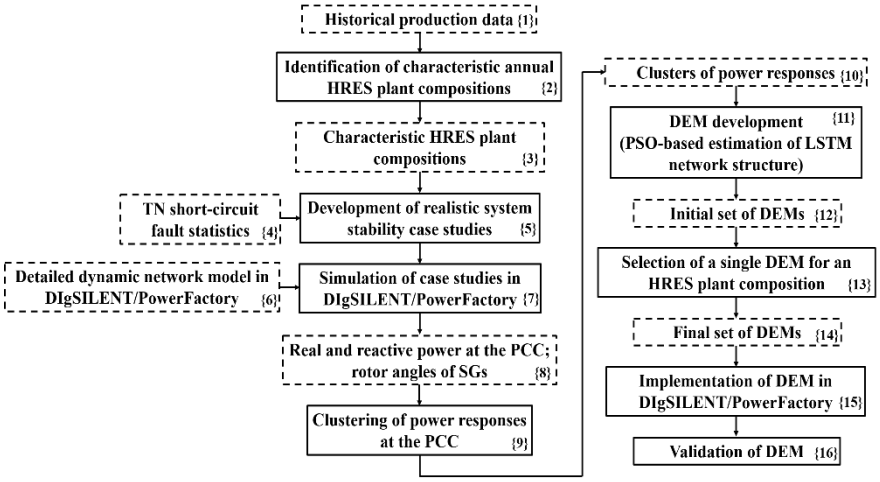

Figure 5.1 The flow chart of the methodology for developing LSTM-based DEMs of HRES plants for transient stability studies

A DEM is developed per group of similar HRES plant power responses in Matlab environment. As in the case of the TF-based models, the DEM comprises two blocks connected in series. The first block is an LSTM neural network with real and imaginary part of the positive sequence voltage, and z-normalized real and reactive power at the PCC as inputs and outputs, respectively. Z-normalized responses represent inputs to the second block that transforms normalized responses into power responses in absolute units. In order to reduce computational time, the LSTM network training is performed on a subset of power responses from the relevant cluster. The particle swarm optimization (PSO) algorithm is used for identifying the adequate LSTM network structure. The application of DEMs developed in this way depends on both HRES plant composition and characteristics of TN short-circuit fault as clustering of HRES plant power responses

may divide the responses produced by a single typical plant composition into different clusters. Therefore, a practical approach for identifying the most adequate DEM for each typical plant composition is proposed, which in turn enables the selection of DEM at any time of the year knowing only HRES plant operating scenario.

Finally, DEM is integrated into the TN dynamic model in DIgSILENT/PowerFactory software and its accuracy is evaluated in terms of both, the shape of time domain HRES plant power responses and the global transient stability performance of the system using the TSI. The methodology is illustrated on the IEEE 9-bus network model with the HRES plant consisting of three non-dispatchable RESs (the WF, PV plant and HPP). The test system and data correspond to the ones used in CS-I in Chapter 4.

The proposed deep learning-based methodology and the modelling procedure in [99] utilize the same deep learning architecture. The key novelties introduced by the approach presented in this thesis are: a structured identification of the optimal LSTM network topology (trail-and-error method was applied in [99]), comprehensive DEM evaluation and analysis of the impact of DEMs on system transient stability through the assessment of the DEM accuracy based on system TSI value.

The first three stages of the modelling procedure, i.e., the identification of characteristic annual HRES plant compositions, development of realistic CSs and simulation of CSs in DIgSILENT/PowerFactory, are the same as in the data-driven equivalent modelling methodology (Section 3.2.1, Section 4.2.1, and Section 4.2.2), and thus will not be described in this chapter. The remaining steps in the deep learning-based methodology are explained in detail in the following sections.

5.2.1 Clustering of Power Responses at the Point of Common Coupling

As in the case of the data-driven equivalent modelling, the simulated HRES plant power responses had to be z-normalized (using (4.45)-(4.47)) first, as the pre-disturbance HRES plant power production was not the same in the analysed MC CSs. Real and reactive power responses at the PCC from the same MC CS are grouped into a single vector and these vectors are used in the clustering of HRES plant responses (block {9} in Figure 5.1).

As mentioned in Chapter 2, partitioning, hierarchical and model-based clustering algorithms have been typically used for time series clustering. The agglomerative (bottom-up) HC algorithm with the unweighted average linkage is chosen in this study for grouping HRES plant power responses according to similarity in time. Unlike the partitioning algorithms, the HC is a deterministic algorithm (the dendrogram is always the same as it does not depend on the initial cluster centers) and does not require the number of clusters to be defined *a priori* [140]. Furthermore, the HC with the average linkage is not sensitive to noise and outliers [140]. As for model-based clustering, the structure of models and a criterion for assessing their similarity have to be specified in advance, and then another clustering algorithm (e.g. the partitioning or HC) has to be applied to the previously computed similarity measures. Even though the HC algorithm has quadratic computational complexity, computational time is not an issue when developing DEMs for any HRES plant as the clustering dataset size is defined by the number of typical plant compositions and MC CSs per composition, and these numbers cannot be unreasonably high.

The unweighted average linkage is based on the average distance between all pairs of clusters' objects and thus represents a compromise between two extremes, single and complete linkage (based on the distance between the two closest and furthest objects, respectively) [140, 160]. Unlike the weighted average linkage, the unweighted linkage takes into account the size of the clusters as well. When it comes to the distance measure, the standard Euclidean distance is chosen as it has been widely used for clustering time series data [133]. The optimal number of clusters, which has to be specified following the HC clustering procedure, is defined in the same way as in the case of the historical HRES plant production data clustering, that is, using the MSE, CDI and MIA clustering evaluation indices.

5.2.2 Dynamic Equivalent Model Development

5.2.2.1 The Structure of Long Short Term Memory-based Dynamic Equivalent Model

A DEM is designed for each cluster of HRES plant power responses (block {11} in Figure 5.1). Block diagram of LSTM-based DEM is shown in Figure 5.2. The DEM consists of two blocks connected in series: an LSTM network and inverse z-normalization part (marked by dashed rectangle in Figure 5.2). (*Note*: Given that NARX

and LSTM networks are less sensitive to the vanishing gradient problem compared to classical RNNs, and have been successfully applied in dynamic equivalent modelling of ADNs [95, 96, 99], these two ANN types were initial candidates for equivalent modelling of HRES plants. However, when applied to the data used in this study, NARX networks demonstrated worse generalization performance and longer training time compared to LSTM networks (on average, NARX-based models were characterized by about three times higher model error and four times longer time required for model development compared to LSTM-based equivalents). In addition, LSTM networks outperformed NARX networks in the modelling of dynamic systems in [99, 123].)

The LSTM network in the proposed DEM structure has 10 inputs in total - normalized deviations of real and imaginary part of the positive sequence voltage at the PCC from their pre-disturbance values (normalization is performed using the rated voltage value) at the current time step and at four previous time steps [95, 96, 99]. (*Note*: Unlike in the case of the TF-based models with voltage magnitude as a single input signal, the real and imaginary part of voltage at the PCC were chosen as model inputs as they provided better LSTM network performance compared to voltage magnitude as the only model input.) Real and imaginary part of the positive sequence voltage at the PCC at time step *t* are denoted by $u_{PCC,1,r}[t]$ and $u_{PCC,1,i}[t]$, respectively, in Figure 5.2, while their pre-disturbance values are denoted by $u_{PCC,1,r\_ss}$ and $u_{PCC,1,i\_ss}$, respectively. Z-normalized real and reactive power responses at the PCC are LSTM outputs. The LSTM network consists of LSTM and fully connected (FC) hidden layers. LSTM layers, as described in Section 2.4.1.3, contain recurrently connected LSTM memory cells with four multiplicative gates (the input, input modulation, output and forget gate) that minimize the possibility of the occurrence of the vanishing gradient problem by controlling the information content stored in and exported from the cell [117, 122]. On the other hand, FC layers contain ordinary neurons and at least one FC layer is usually stacked upon the last LSTM layer in the network in order to project the LSTM layer output into the dimensional space of the network output [99, 201].

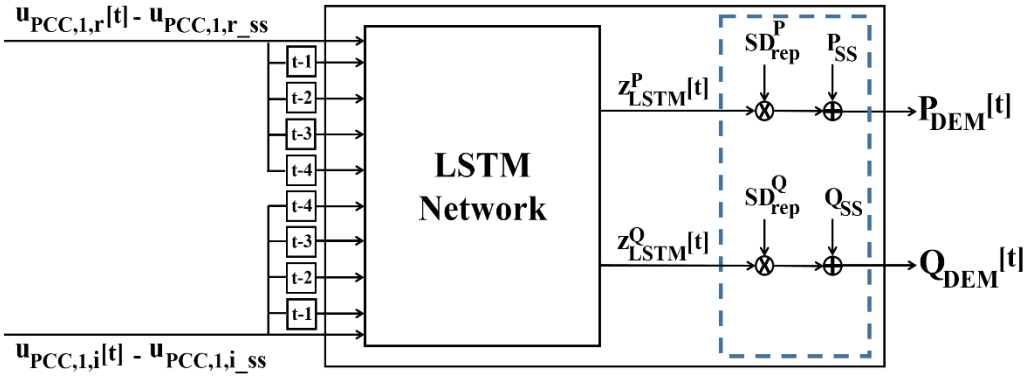

Figure 5.2 Block diagram of LSTM-based DEM

The LSTM network training involves the estimation of the elements of weight and bias matrices of LSTM and FC layers. The total number of estimable parameters in an LSTM layer is:

$$NoParam_{LSTM} = 4 \cdot N_{LSTMcell} \cdot N_{PreLayer} + 4 \cdot N_{LSTMcell}^2 + 4 \cdot N_{LSTMcell}, \quad (5.1)$$

where $N_{LSTMcell}$ is the number of LSTM cells in the LSTM layer, and $N_{PreLayer}$ is the size (the number of elements) in the previous network layer. In case the given LSTM layer is the first layer in the LSTM network, $N_{PreLayer}$ refers to the number of inputs of the LSTM network (10 in this case). The addends in expression (5.1) correspond to the number of elements of the weight matrices between the input and the forget, input, input modulation and output gate, the number of elements of the weight matrices between the last time step of the hidden state and the forget, input, input modulation and output gate, and the number of elements of bias vectors for all four gates.

The number of estimable parameters in an FC layer is:

$$NoParam_{FC} = N_{FCneuron} \cdot N_{PreLayer} + N_{FCneuron}, \quad (5.2)$$

where $N_{FCneuron}$ is the number of neurons in the FC layer. The first addend in (5.2) represents the number of elements of the weight matrix between the FC layer and the previous layer in the network, while the second one is the size of the bias vector for the FC layer.

An example of an LSTM network topology with 2 LSTM layers (each containing 2 LSTM cells) and 2 FC layers (with 6 and 2 neurons each) is given in Figure 5.3. Circles in Figure 5.3 represent ordinary neurons in FC layers. As seen in Figure 5.3, the LSTM network is a fully-connected network, i.e., all elements of one layer are connected to all

elements in the next layer in the LSTM network structure. At each time step during the simulation, the values of LSTM network input signals, i.e., the real and imaginary part of positive sequence voltage at the PCC at the current and four previous time steps, are propagated through the LSTM network. The outputs of LSTM cells within each of the LSTM layers in the LSTM network are calculated according to (2.41) – (2.46), whereas the outputs of the regular neurons in FC layers are computed using (2.37) and (2.38). According to (5.1) and (5.2), the total number of estimable parameters in the given LSTM network is 176, whereas the number of estimable parameters per LSTM layer 1, LSTM layer 2, FC layer 1, FC layer 2 is 104, 40, 18, 14, respectively.

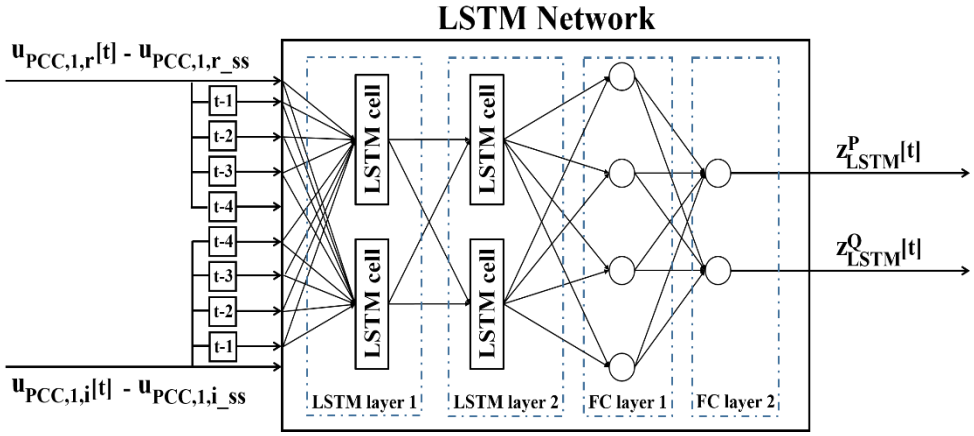

Figure 5.3 The illustration of LSTM network structure

As in the case of the TF-based DEMs, the inverse z-normalization part of DEM transforms z-normalized power responses into power responses in absolute units, which means that the information about the mean value and standard deviation of power response in absolute units is needed (see (4.45)). However, unlike in the data-driven modelling approach, the representative response/CS is not defined for a cluster of HRES plant power responses. Therefore, inverse z-normalization is performed using the power production of a given forecasted HRES plant composition at the pre-disturbance state and the mean value of the standard deviations of all power responses in the relevant cluster (so-called representative standard deviation), instead of the average and standard deviation of the actual power response in absolute units, respectively.

The mathematical expression for real and reactive power output of DEM at each time step of simulation is given by (5.3):

$$Y_{DEM}[t] = z_{LSTM}^{Y}[t] \cdot SD_{rep}^{Y} + Y_{SS}, \tag{5.3}$$

where $Y_{DEM}[t]$ is the DEM real/reactive power output at time step *t*, $z_{LSTM}^{Y}[t]$ is the z-normalized real/reactive power output of the LSTM network at time step *t*, SD_{rep}^{Y} is the representative standard deviation for real/reactive power responses from the corresponding cluster, and Y_{SS} is the total HRES plant real/reactive power output at the pre-disturbance state for the analysed case.

5.2.2.2 Estimation of Long Short-Term Memory Network Structure

The procedure for defining the optimal LSTM network architecture (the number of hidden layers and LSTM cells/neurons per LSTM/FC hidden layer) is illustrated in Figure 5.4. The appropriate number of LSTM and FC hidden layers in the LSTM network is determined by iteratively increasing the number of layers until there is no significant improvement in the total DEM error for all responses in the cluster (the value of 1% is adopted as a threshold). (*Note*: The expression for the total DEM error is given later in this section.) For a specified number of hidden layers, the optimal number of LSTM cells/neurons per LSTM/FC layer is estimated using the PSO algorithm.

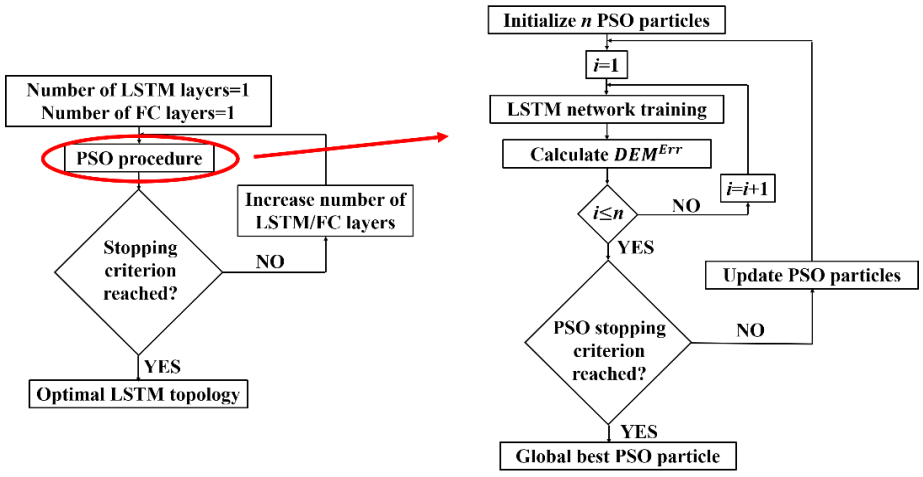

Figure 5.4 Estimation of the optimal LSTM network architecture

The PSO algorithm has proven to be suitable for complex non-convex optimization problems [202]. Small number of the PSO parameters as well as the adequacy of their default/recommended values for a wide range of optimization problems are one of the reasons for its popularity [203, 204]. Furthermore, the PSO algorithm is characterized by the computational complexity of *O*(*n*log*n*), where *n* is the number of candidate solutions, which makes it less computationally demanding than another commonly used heuristic

optimization method - genetic algorithm (quadratic computational complexity), and is specified as one of the most suitable optimization techniques for deep learning tasks in [202].

The algorithm finds the optimal solution for the considered optimization task using a group of PSO potential solutions (particles) that form a population (so-called swarm) [203, 204]. Each PSO particle is described by two features: its position in the search space and its velocity. Both the position and velocity are vectors with the size determined by the number of the optimization variables. The algorithm choses the positions and velocities of the particles randomly in the first iteration, and then it dynamically updates the velocity, and consequently the position, of each PSO particle in the following iterations. The velocity update of a PSO particle is carried out taking into account the distance of the current position of the particle in the search space from its best previous position (the so-called local best) and from the best position of any particle in the whole swarm (the so-called global best). The global and local best positions are defined with respect to the PSO cost function values of the particles. The change in the velocity and position of the *d*-th component of the *i*-th PSO particle is performed as follows [205]:

$$v_{i,k+1}^{d} = wv_{i,k}^{d} + c_1 r_1 \left(pbest_{i,k}^{d} - x_{i,k}^{d}\right) + c_2 r_2 \left(gbest_{k}^{d} - x_{i,k}^{d}\right), \tag{5.4}$$

$$x_{i,k+1}^{d} = x_{i,k}^{d} + v_{i,k+1}^{d}, \tag{5.5}$$

where $v_{i,k}^{d}$ and $x_{i,k}^{d}$ are *d*-th component of the velocity and position vector of the *i*-th PSO particle at the *k*-th iteration, respectively, w is the inertia weight, c_1 and c_2 are the acceleration constants, $pbest_{i,k}^{d}$ is *d*-th component of the local best of the *i*-th PSO particle at the *k*-th iteration, $gbest_{k}^{d}$ is *d*-th component of the global best at the *k*-th iteration, and r_1 and r_2 are random numbers chosen uniformly from the range (0, 1).

The inertia weight provides a balance between the local and global exploration [204, 205]. Higher inertia weight values facilitate the global search, while lower values encourage the local search. The inertia weight can have a constant value (the values of 0.7 and 0.8 are recommended in [203]), vary randomly, or decrease from a relatively large value (a value close to one [204]) to a small value during the optimization process enabling the algorithm to perform the global search at the beginning and focus on the

small neighbourhood around the PSO particle at the end of the process [206, 207]. The movement of the PSO particle towards the local and global best is determined by the constants c_1 and c_2, respectively [203, 205]. The optimal values for these PSO parameters are between 1.5 and 1.7 [203]. When it comes to the swarm size, the typical values between 20 and 50 have provided a satisfactory performance of the PSO algorithm for various optimization problems [203-205, 207].

In this study, the PSO particles correspond to the number of LSTM cells/neurons per LSTM/FC hidden layer and the LSTM network is trained for each PSO particle (i.e., LSTM network architecture). The adequacy of the LSTM network architecture for the considered cluster of power responses is assessed on the basis of DEM accuracy in terms of the shape of time domain HRES plant power responses for all MC CSs in the cluster. Alternatively, the number of hidden layers could have been estimated through the direct application of the PSO procedure. This would eliminate the iterative search, however, the computational time for identifying the optimal LSTM network structure would be higher (the LSTM network training would have to be carried out for unnecessary large number of layers), and it would ultimately provide the same result as the iterative search. Given that the PSO is designed for continuous variables and the number of LSTM cells/neurons per hidden layer is a discrete variable, each component of the PSO particle is replaced by the closest integer value following the position update [203].

The PSO cost function is based on the calculation of the difference between detailed and equivalent model power responses at each time step after fault clearing. The accuracy of DEM power responses after fault clearing is considered to be more important than that during the fault as: i) the post-fault responses are relevant for transient stability assessment of the system; ii) the fault duration is significantly shorter than the post-fault time period; iii) dynamic models used in transient stability simulations are not suitable for electromagnetic transients. The following DEM relative error is calculated for each MC real and reactive power response in the cluster and each time step after fault clearing:

$$DEM\_Y_{i,t}^{Err} = \frac{Y_{DEM\ i,t} - Y_{ORG\ i,t}}{Y_{ORG\ i,t}} \cdot 100\%, \tag{5.6}$$

where $DEM\_Y_{i,t}^{Err}$ is DEM relative error for real/reactive power response, $Y_{ORG\ i,t}$ is the real/reactive power output of the detailed HRES plant dynamic model and $Y_{DEM\ i,t}$ is the

real/reactive power output of the DEM calculated using (5.3); all for the *i*-th MC CS and time step *t*.

Following this, at each of the considered time steps, the 95th percentile of the computed $DEM\_Y_{i,t}^{Err}$ values is calculated and the maximum of the obtained percentiles is defined:

$$95PCTL_Y = \max_{1+N_{Flt} \le t \le N_T} 95PCTL\left(\left\{\left|DEM\_Y_{i,t}^{Err}\right|\right\}_{1 \le i \le N_{Resp}}\right), \tag{5.7}$$

where 95*PCTL* stands for the 95th percentile, N_{Resp} is the number of MC CSs in the relevant cluster, N_{Flt} is the number of time steps during the fault duration, and N_T is the total number of simulated time steps. $DEM\_Y_{i,t}^{Err}$ is calculated using (5.6).

Finally, the PSO cost function is defined as a total DEM error for real and reactive power responses as follows:

$$PSO_{Cost} = DEM^{Err} = \sqrt{(95PCTL_P)^2 + \left(95PCTL_Q\right)^2}, \tag{5.8}$$

where DEM^{Err} is the total DEM error, and $95PCTL_P$ and $95PCTL_Q$ are computed using (5.7).

In order to reduce computational burden, each LSTM network is trained on a subset of power responses from the corresponding cluster. The MC CSs used for the LSTM network training are chosen equidistantly from the range defined by the values of all cluster's z-normalized power responses at the time of the first swing peak. Given that clusters are usually not perfectly compact, the time of the first swing peak was chosen as the most convenient, practical, time step in power responses for identifying a spread of responses within a cluster. Differences in the shape of responses allocated to a single cluster result in the time of the first swing peak not being the same for all cluster responses. Thus, the relevant time step used for specifying the range for selecting the responses corresponds to the time of the first swing peak for the majority of the responses in the cluster. Separate ranges are created for real and reactive power responses, and a half of the cases is chosen from each of them. Cases used for the LSTM network training include a training set (for estimating network parameters) and a validation set, and both

datasets are chosen as previously described. The ratio of the size of the training and validation dataset is 70/30 [96].

Figure 5.5 illustrates the selection of five training/validation responses from a cluster of z-normalized real power responses (the total number of training/validation cases is ten in this example).

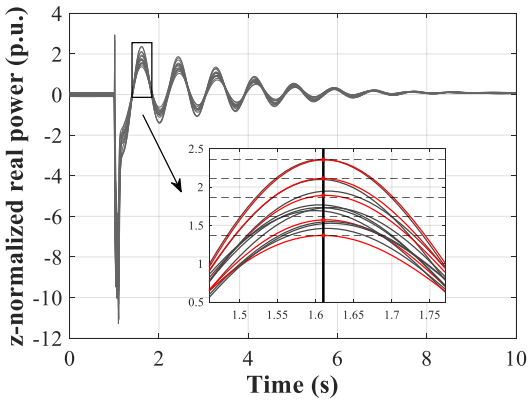

Figure 5.5 Illustration of the selection of the training/validation cases from a cluster of z-normalized real power responses

The time of the first swing peak for most of the responses is 1.61 s. Dashed black lines in the zoomed part of the figure indicate equidistant intervals from the range defined by the values of the responses at 1.61 s. A training/validation response corresponds to the response having the value at 1.61 s that is the closest to the one defined by a dashed line (the training/validation responses are shown in red in Figure 5.5).

The LSTM network cost function is based on mean squared DEM error (averaging is performed across all time steps after fault occurrence and all training/validation responses):

$$LSTM_{Cost} = \frac{1}{N_{SubResp}} \sum_{i=1}^{N_{SubResp}} \frac{1}{N_T} \left(DEM_i^{SumErr,Flt} + DEM_i^{SumErr,AftFlt} \right), \quad (5.9)$$

$$DEM_i^{SumErr,Flt} = \sum_{t=1}^{N_{Flt}} WeightFact \cdot \left(\left(\frac{DEM\_P_{i,t}^{Err}}{100} \right)^2 + \left(\frac{DEM\_Q_{i,t}^{Err}}{100} \right)^2 \right), \quad (5.10)$$

$$DEM_i^{SumErr,AftFlt} = \sum_{t=1+N_{Flt}}^{N_T} \left(\left(\frac{DEM\_P_{i,t}^{Err}}{100} \right)^2 + \left(\frac{DEM\_Q_{i,t}^{Err}}{100} \right)^2 \right), \quad (5.11)$$

where $N_{SubResp}$ is the number of training/validation MC CSs, $DEM_i^{SumErr,Flt}$ and $DEM_i^{SumErr,AftFlt}$ is the sum of the values of squared DEM relative error per each time

step during the fault duration and post-fault period for the *i*-th MC CS, respectively, and *WeightFact* is the weight factor (the value of 0.01 is adopted in this study).

The LSTM network training process is focused on DEM outputs and not on LSTM outputs (z-normalized power responses) as power responses in absolute units are ultimately relevant for performing transient stability simulations. The weight factor *WeightFact* is introduced to reduce the impact of DEM error during the fault duration on the LSTM network training. Unlike in the case of the PSO cost function, time steps during the fault cannot be excluded from the LSTM cost function as DEM is to be used in simulations starting from fault occurrence and the LSTM learning algorithm calculates the gradient of the LSTM cost function with respect to trainable network parameters at each time step of the training responses. The BPTT in combination with the standard Adam optimizer with default hyper-parameter values are used for the LSTM network training [99]. The Adam optimizer is computationally efficient and utilizes the advantages of two other methods, AdaGrad and RMSProp (adequate for sparse gradients and non-stationary objective functions, respectively), and thus usually outperforms other optimization techniques [99, 112, 208]. Given that the LSTM cost function has to be differentiable due to the calculation of the gradient of the cost function with respect to estimable parameters (i.e., elements of weight and bias matrices), and the information about the LSTM error (i.e., the difference between the target outputs and actual LSTM outputs) has to be available at every time step, the PSO cost function based on the 95^{th} percentile of DEM error (given by (5.8)) could not be chosen. Early stopping method is used for terminating the LSTM network training. In the initial iterations of the network training, both the training and validation error, i.e., the values of the LSTM cost function for the training and validation data, respectively, decrease. At a certain iteration of the training, the overfitting of the training data begins and the validation error begins to increase, while the training error continues to decrease. Early stopping method terminates the network training after a pre-defined number of consecutive iterations (six is adopted in this study [89]) during which there was an increase in the validation error, and LSTM network parameters are set to the values obtained in the iteration that is associated with the minimum validation error [89].

The whole PSO procedure is carried out in Matlab environment, with the Matlab default values for the PSO acceleration coefficients – 1.5. When it comes to the inertia weight, Matlab adapts the parameter over PSO iterations according to the change in the global best PSO solution (the default range of values is [0.1, 1.1]). The PSO algorithm terminates when the cost function value has stabilized, i.e., when the maximum change in the global best PSO cost function value over 10 consecutive iterations is below 1%. The optimal swarm size and the number of training CSs for the LSTM network training are defined by developing DEM of the largest cluster for a range of their values and selecting the combination that provides the best balance between the total DEM error and computational burden.

5.2.3 Selection of a Single Dynamic Equivalent Model for a Hybrid Renewable Energy Source Plant Composition

The previous step in the equivalent modelling procedure provides an initial set of DEMs (block {12} in Figure 5.1). The allocation of MC CSs/responses to clusters depends on both HRES plant operating condition and characteristics of TN short-circuit fault (location, type and impedance). Clustering of z-normalized HRES plant power responses according to similarity in time divides MC power responses produced by a single characteristic HRES plant composition into different clusters, meaning there is a set of DEMs associated with each typical plant composition. In order to perform selection of DEM at any time of the year knowing only HRES plant operating scenario, the most adequate model for each characteristic plant composition is identified (block {13} in Figure 5.1). The suitability of the *p*-th initial DEM for the *q*-th typical plant composition is assessed on the basis of the accuracy of the *p*-th DEM for the *q*-th composition's MC responses assigned to the *p*-th cluster and the number of these responses:

$$IdxDEM_p^q(\%) = \frac{DEM^{Err,RespRel_p^q}}{N_{RespRel_q^p}}, \tag{5.12}$$

where $IdxDEM_p^q$ is the index calculated for the *p*–th DEM and *q*-th typical plant composition, $DEM^{Err,RespRel_p^q}$ is the total DEM error calculated for the *q*-th composition's MC responses in the *p*-th cluster (5.8), and $N_{RespRel_q^p}$ is the number of the *q*-th composition's MC responses in the *p*-th cluster.

The index defined by (5.12) is calculated for each typical plant composition and its set of DEMs. The DEM having the lowest index value is the most suitable DEM for the particular plant composition. In this way, the final set of DEMs required for representing HRES plant dynamic performance in annual transient stability studies is obtained (block {14} in Figure 5.1). (*Note*: When selecting the best DEM for a typical plant composition, the data-driven methodology relies only on the number of responses per cluster from the considered plant composition. The main reason for not taking into account the TF-based model accuracy with respect to TSI value, in the data-driven approach, is that the TSI index is considered to be a robust index that can sufficiently well represent stability status of the system. Furthermore, the accuracy of the TF-based model with respect to TSI was not defined for a group of HRES plant responses in the model development procedure, and almost all (if not all) responses produced by a single typical plant composition were allocated to the same cluster in both CSs presented in Chapter 4. In the case of the deep learning-based methodology, the LSTM-based model accuracy in terms of the shape of plant real/reactive power responses was defined for a group of real/reactive power responses as the maximum 95^{th} percentile of the error across all time steps after fault clearing (see (5.7)).)

Finally, the DEM for an arbitrary HRES plant operating condition is the best DEM for the typical plant composition which is the most similar to the given plant composition. As in the case of the data-driven equivalent modelling, similarity between plant compositions is assessed according to their Euclidean distance (a composition is treated as a vector whose components are power outputs of individual RESs in the HRES plant). The diagram illustrating the process of selecting the adequate DEM for a new HRES plant operating point is shown in Figure 4.6, as the process is the same as in the case of the data-driven methodology.

5.2.4 Integration of Dynamic Equivalent Model in DIgSILENT/PowerFactory

A set of DEMs is developed in Matlab and stored in a user-defined folder in the form of Matlab mat-files. Transient stability studies are performed in DIgSILENT/PowerFactory environment and DIgSILENT/PowerFactory communicates with Matlab mat-files (i.e., DEMs) through a Matlab m-file interface. The interaction between

DIgSILENT/PowerFactory and Matlab during transient stability simulations is shown in Figure 5.6. At each time step of simulation:

i) The Matlab m-file interface transfers the required DEM inputs (real and imaginary parts of the positive sequence voltage at the PCC at the current time step and four previous time steps - $u_{PCC,1,r}[t\text{-}4{:}t]$ and $u_{PCC,1,i}[t\text{-}4{:}t]$ in Figure 5.6, respectively) from DIgSILENT/PowerFactory environment to the adequate Matlab mat-file (DEM). DIgSILENT/PowerFactory calculates DEM input signals based on the magnitude and angle of the positive sequence voltage at the PCC ($u_{PCC,1}[t]$ and $\varphi_{PCC,1}[t]$ in Figure 5.6, respectively) obtained by applying the method of symmetrical components on phase voltages at the PCC ($u_{PCC,a}[t]$, $u_{PCC,b}[t]$, and $u_{PCC,c}[t]$ in Figure 5.6);

ii) The Matlab mat-file (DEM) is simulated in Matlab software and provides real and reactive power at the PCC at the current time step ($P_{DEM}[t]$ and $Q_{DEM}[t]$ in Figure 5.6, respectively);

iii) DEM outputs are sent to DIgSILENT/PowerFactory through the Matlab m-file interface;

iv) DIgSILENT/PowerFactory assigns DEM outputs to the real and reactive power output of a controllable, constant power load connected at the PCC (the same approach is used as in the case of TF-based DEM implementation). The dynamic load response is controlled by the DEM, i.e., real and reactive power injected at the PCC ($P_{PCC}[t]$ and $Q_{PCC}[t]$ in Figure 5.6, respectively) correspond to DEM output values.

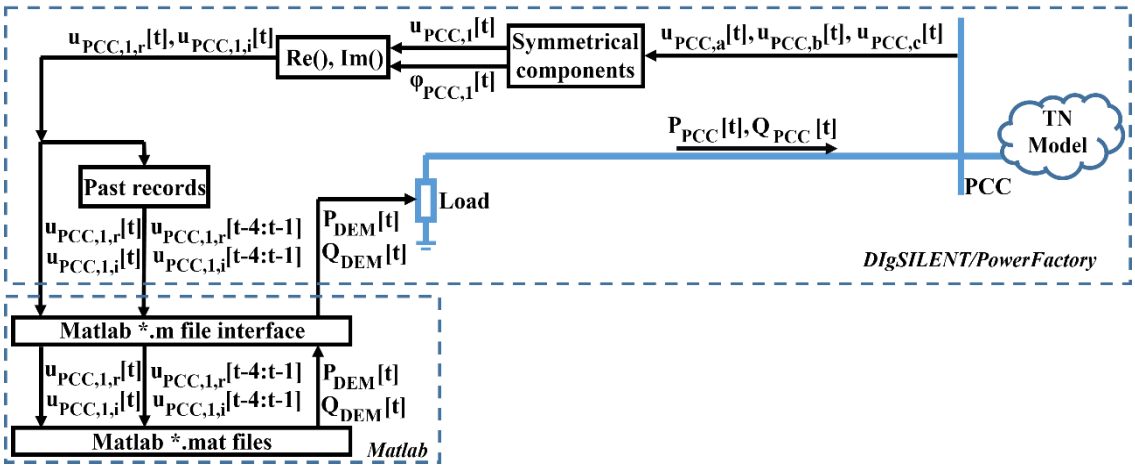

Figure 5.6 Illustration of DEM implementation in DIgSILENT/PowerFactory

5.2.5 Validation of Dynamic Equivalent Model

DEM performance is validated in DIgSILENT/PowerFactory software for a large number of system operating points and disturbances. DEM accuracy for the *i*-th case in terms of the shape of time domain power response is assessed according to the maximum relative difference between the responses of the detailed and equivalent model over all time steps after fault clearing:

$$DEM_{i,Y}^{Err,SingleCS} = \max_{1+N_{Flt} \le t \le N_T} \left| DEM\_Y_{i,t}^{Err} \right|, \tag{5.13}$$

$$DEM_{i}^{Err,SingleCS} = \sqrt{\left(DEM_{i,P}^{Err,SingleCS}\right)^2 + \left(DEM_{i,Q}^{Err,SingleCS}\right)^2}, \tag{5.14}$$

where $DEM_{i,Y}^{Err,SingleCS}$ is the DEM relative error for a single *i*-th real/reactive power response, $DEM_{i}^{Err,SingleCS}$ is the total DEM error for a single *i*-th CS, and $DEM\_Y_{i,t}^{Err}$ is computed using (5.6). Equation (5.13) is in fact the expression (5.7) for a single transient stability simulation.

DEM accuracy is further assessed from the perspective of the global transient stability status measured by TSI value. TSI error is calculated in the same way as in the data-driven modelling procedure, that is, using (4.56).

5.3 Case Study

The methodology is illustrated on the test system presented in Figure 5.7. The test system consists of the HRES plant (the WF, PV plant and HPP) and the IEEE 9-bus network, and is the same as the test network model used in CS-I in Chapter 4. The detailed description of the models of individual plants in the HRES plant is given in Section 4.3.

5.3.1 Model Development

Given that the test system and data correspond to the ones used in CS-I in Chapter 4, the results of the fuzzy c-means clustering of the historical HRES plant production data (nine characteristic annual HRES plant compositions and system demand levels given in Table 4.3) as well as simulated MC power responses at the PCC are the same as in CS-I in

Chapter 4. However, unlike in the case of the data-driven equivalent modelling, in this CS HRES plant power responses are analysed from the perspective of their similarity in time using the HC algorithm.

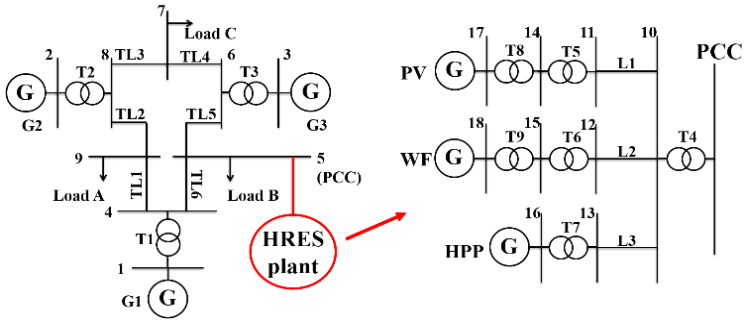

Figure 5.7 The schematic diagram of the test HRES plant and IEEE 9-bus network (G: generation technology)

Given that the number of clusters produced by the HC algorithm corresponds to the number of DEMs of the HRES plant, the optimal number of clusters cannot be unreasonably large. Therefore, the clustering evaluation indices were calculated for the number of clusters from 2 to 30. The clustering process provides 12 clusters of z-normalized HRES plant power responses as the application of the elbow method on the values of MSE, CDI and MIA indices in the considered range results in 8, 12, and 12 clusters, respectively. The change of the values of the clustering indices with the number of clusters is presented in Figure 5.8.

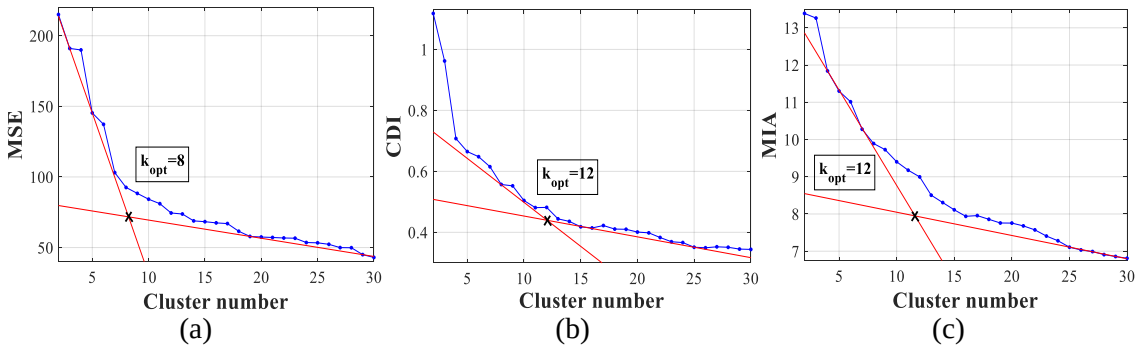

Figure 5.8 The change of the MSE (a), CDI (b) and MIA (c) with the number of clusters in the case of the HC clustering of HRES plant power responses

Table 5.1 shows the total number of responses as well as the number of MC CSs produced by each characteristic plant composition per cluster of z-normalized HRES plant power responses. About 90% of all 9,000 MC responses is allocated to seven clusters: cluster 1, 3, 4, 6, 8-10, with clusters 1, 6, 8 and 10 containing more than 1,000 responses (the largest cluster is cluster 10 with 2,519 responses). According to (5.12), the selection of a certain DEM for the representation of all responses from a typical plant composition

depends on the ratio of the DEM accuracy for the responses produced by this plant composition that are allocated to the respective cluster (i.e., the cluster used for estimating the DEM structure) and the number of these responses. The lower the index (5.12) is, the more suitable DEM for representing all responses from the typical plant composition is. If the size of a cluster is considerably smaller than the size of the other obtained clusters (e.g., clusters 11 and 12 in this CS), for any typical plant composition, index given by (5.12) for this small cluster will certainly have much higher value compared to the indices calculated for the remaining clusters. As a result, the DEM developed on the basis of this cluster will not be used for representing the HRES plant in annual transient stability simulations. This, in turn, implies that there is no need for highly accurate identification of the optimal number of clusters of HRES plant power responses as very small clusters will not be included in the set of the best DEMs of the given HRES plant, and thus, will be eliminated from the equivalent modelling procedure. (*Note*: The computational time associated with the development of LSTM-based models could be reduced by not designing LSTM networks for very small clusters of HRES plant responses.)

Table 5.1 Number of MC CSs per cluster of HRES plant power responses

	Total no. CSs	CC 1	CC 2	CC 3	CC 4	CC 5	CC 6	CC 7	CC 8	CC 9
C 1	1673	85	2	46	69	10	19	191	1000	251
C 2	372	6	4	29	87	83	81	23	0	59
C 3	447	193	0	15	1	0	0	210	0	28
C 4	203	68	0	0	0	0	1	102	0	32
C 5	169	48	0	0	1	0	0	33	0	87
C 6	1381	518	0	5	16	13	55	419	0	355
C 7	105	0	0	57	16	23	9	0	0	0
C 8	1645	51	22	412	451	328	318	0	0	63
C 9	402	4	142	39	59	95	42	1	0	20
C 10	2519	20	830	393	293	441	466	1	0	75
C 11	18	0	0	4	7	7	0	0	0	0
C 12	66	7	0	0	0	0	9	20	0	30

CC=characteristic HRES plant composition
C=cluster of z-normalized HRES plant power responses

Figure 5.9 presents z-normalized real and reactive power responses allocated to cluster 1 and cluster 9, which are the clusters with low and high compactness level, respectively (the remaining clusters are given in Appendix C). Cluster 1 consists of all responses produced by plant composition 8 that contains converter-connected technologies only

(these responses are shown in black in Figure 5.9 (a) and (b)) and certain number of responses from each of the remaining plant compositions with the HPP in operation (see Table 5.1), which in turn reduces its compactness level (for real power responses in particular).

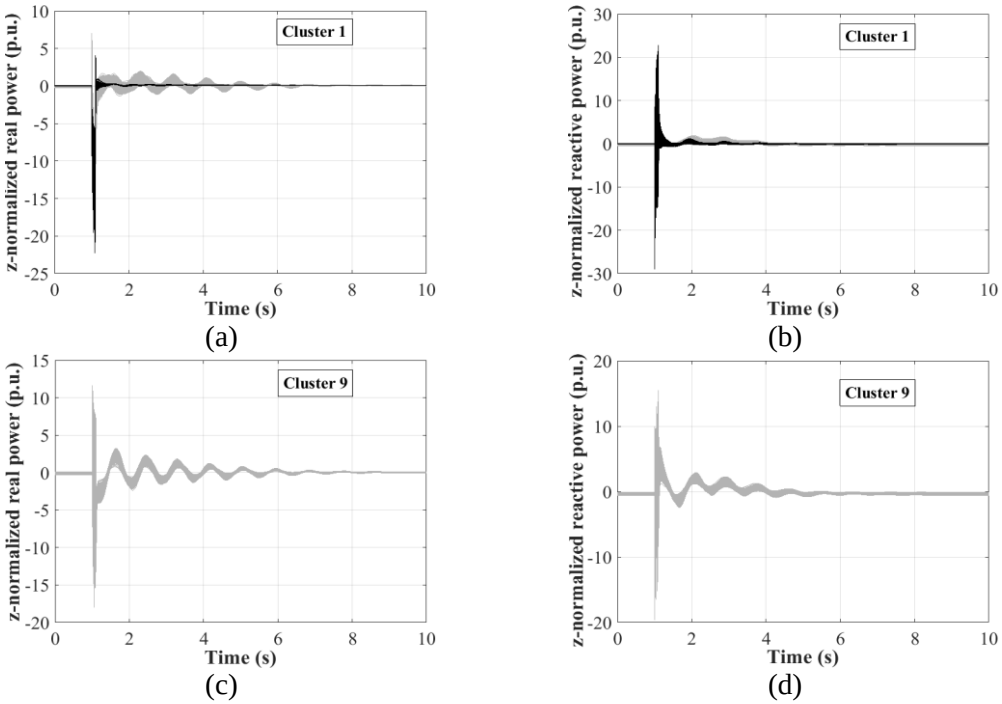

Figure 5.9 Clusters of z-normalized power responses ((a): Cluster 1 - real power; (b): Cluster 1 - reactive power; (c): Cluster 9 - real power; (d): Cluster 9 - reactive power) (black lines in (a) and (b) are responses produced by plant composition 8 without the HPP in service)

In order to identify the optimal number of training responses for the LSTM network training and the optimal number of PSO particles, DEM of the largest cluster (cluster 10) is developed for 10, 50, 100, and 500 training cases, and 20, 30, 40 and 50 PSO particles. The model development (i.e., the PSO procedure) was conducted in Matlab environment of the Computational Shared Facility of the University of Manchester using an 8-core Intel Xeon E5-2650 v2 at 2.6 GHz and 64 GB of RAM, and one Nvidia v100 Volta GPU. For each of the considered combinations of the number of training responses and the PSO swarm size, the following index, based on the total DEM error and the computational burden associated with DEM development, is calculated:

$$OptComb = CompTime \cdot DEM^{Err}, \tag{5.15}$$

where *CompTime* is the computational time of the PSO procedure expressed in hours and DEM^{Err} is the DEM error defined by (5.8).

The *OptComb* values for all combinations are given in Table 5.2 and the minimum value of *OptComb* index, that is, the best trade-off between DEM accuracy and computational time, is obtained for 50 training cases and 30 PSO particles (the shaded cell in Table 5.2). Thus, the PSO swarm size of 30, and 50 training and 20 validation (the adopted ratio of the size of training and validation dataset is 70/30) responses are used in the LSTM network training. Clusters 11 and 12 contain 18 and 66 responses, respectively, and thus, 50 training and 20 validation responses cannot be used for the training of LSTM networks for these two clusters. Therefore, the number of training and validation responses for these clusters is set at 70% and 30% of the total number of responses in the cluster, respectively (e.g., the number of training and validation responses for cluster 11 is 8 and 3, respectively).

Table 5.2 Identification of the optimal number of training cases and PSO particles

PSO swarm size\No. training cases	10	50	100	500
20	507	353	571	401
30	388	323	578	504
40	386	663	998	756
50	864	470	1487	782

An LSTM network is designed for each of the twelve clusters of z-normalized HRES plant power responses and computational time for identifying the optimal LSTM network topology varied from 6 h (DEM 1) to 48.5 h (DEM 3). DEMs for all clusters contain LSTM network with 2 FC layers. When it comes to the number of LSTM layers, DEMs for clusters 2, 5, 7 and 12 have only one layer, DEM for cluster 3 has 3 layers, while the remaining DEMs are characterized by 2 layers.

The LSTM network topology (i.e., the number of LSTM cells/neurons per LSTM/FC layer) for clusters with more than 1,000 responses (i.e., clusters 1, 6, 8, and 10) is given in Table 5.3. In addition, the number of estimable parameters per LSTM and FC layer as well as for the whole LSTM network are also shown in Table 5.3. The data for the remaining clusters are given in Appendix C (Table C.1). The LSTM network for cluster 6 contains the smallest number of estimable parameters (15,444) over all 12 LSTM network topologies. On the other hand, the LSTM network structure for cluster 9 (2 LSTM layers with 231 and 300 LSTM cells each, and 2 FC layers with 188 and 2 neurons each) has the largest number of parameters that need to be estimated (918,974).

Table 5.3 The LSTM network structure and the number of LSTM network estimable parameters for selected clusters

Cluster	LSTM layers	FC layers	No. parameters per LSTM layer	No. parameters per FC layer	Total no. parameters
C 1	(10; 161)	(850; 2)	(840; 110,768)	(137,700; 1,702)	251,010
C 6	(18; 10)	(938; 2)	(2,088; 1,160)	(10,318; 1,878)	15,444
C 8	(283; 12)	(1000; 2)	(332,808; 14,208)	(13,000; 2,002)	362,018
C 10	(10; 55)	(150; 2)	(840; 14,520)	(8,400; 302)	24,062

It should be noted that the estimation of the optimal LSTM network topology for each of the twelve clusters is carried out independently of the dynamic network simulations. Transient stability simulations are performed first, and their outputs, i.e., HRES plant power responses, are then clustered and used for defining LSTM network architecture per cluster. Performing the estimation of the optimal LSTM network topologies using a group of distributed computers (as it has been done in this research) can considerably reduce the computational time of the overall dynamic equivalent modelling process.

The accuracy of the initial set of DEMs is assessed by simulating the developed models for all MC CSs in the corresponding cluster. These simulations were performed in Matlab, and DEM inputs correspond to real and imaginary part of the positive sequence voltage at the PCC from the relevant MC CS simulated in DIgSILENT/PowerFactory using the detailed HRES plant dynamic model. For each of the twelve DEMs, Figure 5.10 (a) illustrates DEM error (calculated using (5.7) and (5.8)) for all responses in the relevant cluster. DEM error for real power responses (i.e., the largest 95^{th} percentile of relative error values per time step after fault clearing) is below 5% for all clusters. For all DEMs, the accuracy for reactive power responses is lower compared to real power responses mainly due to small values of reactive power in absolute units (see (5.6)). The best model accuracy is obtained for DEM 11 (the total DEM error is 1.1%), but this cluster contains only 18 MC CSs. The highest DEM error for real and reactive power responses is 4.2% (DEM 10) and 11.7% (DEM 1), respectively. Low values of HRES plant reactive power output (the median of the pre-disturbance values is -3.7 Mvar) are the main cause of high DEM 1 error.

The most suitable DEM is selected for each characteristic HRES plant composition according to the values shown in Figure 5.10 (b) (the values are computed using (5.12)). The coloured cell and bold font in the column indicates the best DEM for the particular typical plant composition. As can be seen in Figure 5.10 (b), the initial set of twelve models can be reduced to only four DEMs - DEM 1, 6, 8 and 10, with DEM 8 and DEM

6 representing 4 and 3 out of 9 typical plant compositions, respectively, i.e., 78% of all plant compositions.

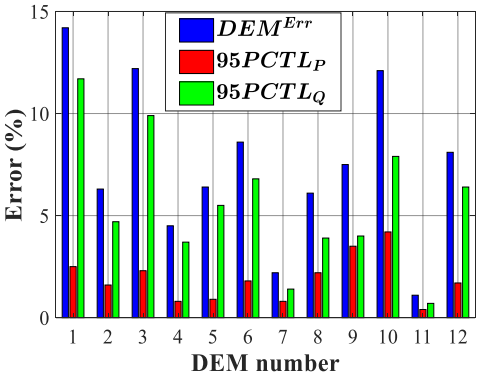

(a)

DEM number	1	2	3	4	5	6	7	8	9
12	0.600	NaN	NaN	NaN	NaN	0.756	0.430	NaN	0.247
11	NaN	NaN	0.175	0.143	0.129	NaN	NaN	NaN	NaN
10	0.420	**0.013**	0.028	0.041	0.028	0.030	13.454	NaN	0.232
9	6.665	0.044	0.190	0.091	0.087	0.140	23.159	NaN	0.447
8	0.183	0.561	**0.012**	**0.012**	**0.012**	**0.013**	NaN	NaN	0.231
7	NaN	NaN	0.033	0.119	0.070	0.211	NaN	NaN	NaN
6	**0.014**	NaN	1.245	0.380	0.492	0.147	**0.024**	NaN	**0.026**
5	0.063	NaN	NaN	3.600	NaN	NaN	0.376	NaN	0.056
4	0.051	NaN	NaN	NaN	NaN	2.830	0.043	NaN	0.181
3	0.041	NaN	1.558	25.839	NaN	NaN	0.062	NaN	0.334
2	1.033	3.175	0.152	0.056	0.055	0.058	0.426	NaN	0.120
1	0.154	6.299	0.292	0.252	1.898	1.222	0.163	**0.009**	0.065

Typical plant composition

(b)

Figure 5.10 (a): Total DEM error (blue), DEM error for real (red) and reactive (green) power responses for all clusters; (b): The values of *IdxDEM* index for all plant compositions and DEMs (NaN: there are no MC CSs from the particular plant composition in the cluster)

5.3.2 Assessment of Model Accuracy

DEM validation is carried out using the same CSs as in the case of the TF-based models presented in Chapter 4: MC CSs utilized for DEM development and non-training CSs from the year of 2019. All cases are simulated in DIgSILENT/PowerFactory using the best DEM for each typical plant composition (i.e., using only DEMs 1, 6, 8 and 10) instead of the detailed HRES plant dynamic model. For each MC CS, both the error in terms of the shape of HRES plant power response (i.e., the maximum relative error across all time steps after the fault clearing) and TSI error are computed as specified in Section 5.2.5.

DEM error in reproducing time domain HRES plant real and reactive power responses for MC CSs used for DEM development is shown in Figure 5.11 (a) in the form of CDFs (solid lines). In the case of real power, the maximum difference between the detailed and equivalent model response over all time steps after fault clearing is below 1.4% and 5.8% for the 50% and 95% of the analysed 9,000 MC CSs, respectively. When it comes to the error in the shape of reactive power responses, the 50th and 95th percentile are equal to 5.6% and 20.4%, respectively. However, the median and 95th percentile of reactive power errors expressed in absolute units is only 1.2 Mvar and 3.9 Mvar, respectively. In order to investigate the change in the accuracy of equivalent HRES plant representation due to the use of only four DEMs instead of initial twelve models, model error is calculated for

each individual real and reactive power response obtained using all twelve DEMs in simulations. The CDFs of the obtained values are shown in Figure 5.11 (a) as dashed lines. When all twelve models are used for modelling the HRES plant, the 50th percentile of the error for real and reactive power responses is 0.8% and 3.7%, respectively, while the corresponding 95th percentiles are 3.4% and 9.2%. Therefore, the use of a single DEM for all responses produced by a typical plant composition does not have a significant impact on the accuracy of real power responses – the increase in the 50th and 95th percentile of the error is 0.6% and 2.4%, respectively. However, when it comes to reactive power responses, the increase in the median error (the 50th percentile) due to the use of four instead of twelve DEMs is about 2%, while the 95th percentile of the error is more than twice as large as the corresponding value for initial twelve models (e.g., only 4% of 9,000 MC CSs has error higher than 10% in the case of twelve models, while that percentage rises to 20% in the case of four DEMs used in simulations).

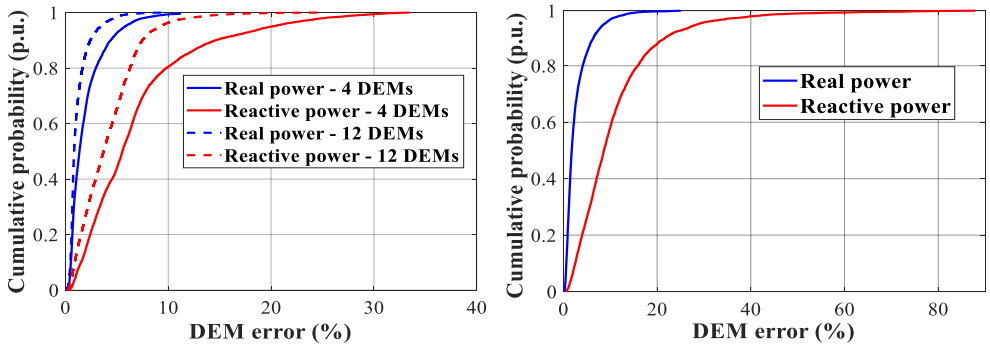

Figure 5.11 (a): CDFs of DEM error for real and reactive power responses for the training CSs when four (solid lines) and twelve (dashed lines) are used in simulations; (b): CDFs of DEM error for real and reactive power responses for the test 2019 year

Results of DEM accuracy assessment in terms of the shape of power responses for the non-training MC CS from the 2019 year are presented in Figure 5.11 (b) in the form of CDFs. As expected, DEM accuracy is slightly lower compared to the set of CSs used for model development. The median value of the maximum difference between detailed and equivalent model real and reactive power responses after fault clearing is 1.8% and 8.8%, respectively, while the corresponding 95th percentiles are 8.7% and 28.6%. As in the case of MC CSs used for DEM development, the 50th and 95th percentile of reactive power errors expressed in absolute units are 1.2 Mvar and 3 Mvar, respectively. In addition, Figure 5.12 illustrates the boxplots of DEM_Q^{Err} values at characteristic time steps after fault clearing for the dominant models DEM 6 (represents plant compositions 1, 7 and 9) and DEM 8 (represents plant compositions 3-6). Only three seconds after fault occurrence are shown in Figure 5.12 as model error reduces practically to zero at later

time steps for most of the MC CSs. Both DEMs have few cases (less than 10) with the maximum error higher than 80%. However, the relative difference between the responses of the detailed and equivalent model at each time step after fault clearing is below 9% and 5% for the majority of the cases represented by DEM 6 and DEM 8, respectively.

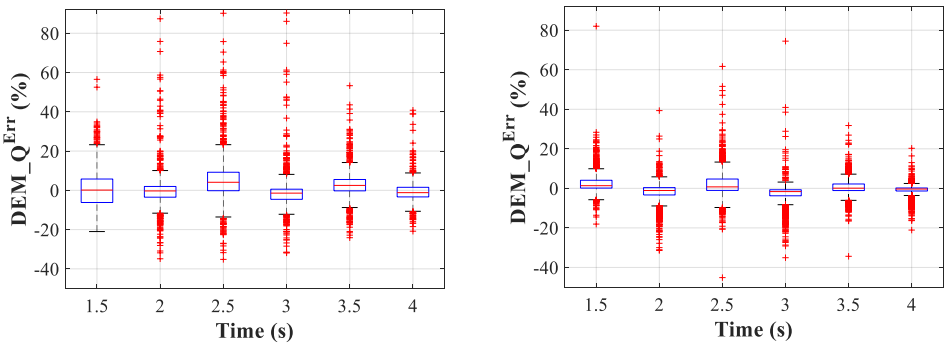

Figure 5.12 Non-training MC CSs for 2019 year: boxplot of DEM 6 (a) and DEM 8 (b) error in terms of the shape of reactive power responses for characteristic time steps after fault clearing

As afore-mentioned, the LSTM-based equivalents are evaluated in terms of the global transient stability status described by TSI value as well. Figure 5.13 presents the CDFs of TSI error for both MC CSs used for DEM development (training CSs) and non-training MC CSs from the test 2019 year. In the case of the 9,000 training cases, the 50th and 95th percentile of TSI error is 0.1% and 0.6%, respectively. When it comes to the non-training CSs, the accuracy of the models is slightly lower: the 50th and 95th percentile of the TSI error is about 0.7% and 3%, respectively.

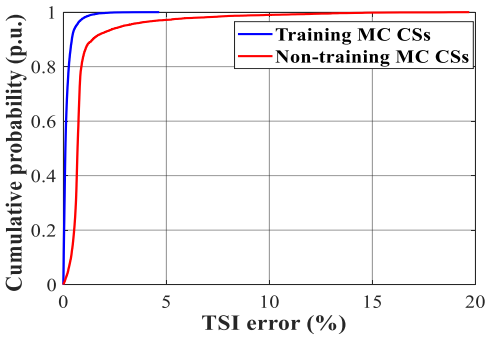

Figure 5.13 CDF of TSI error for the training (blue) and non-training (red) MC CSs

5.3.2.1 Comparison of the Accuracy of Long Short-Term Memory Network-based and Transfer Function-based Dynamic Equivalent Models

This section provides the analysis on the difference in the performance of DEMs developed using the data-driven and deep learning-based methodologies in terms of the

ability to reproduce HRES plant power responses in time domain obtained by the detailed plant dynamic model and accuracy of the overall transient stability results (TSI value). The comparison is carried out for the non-training MC CS from the test 2019 year.

Figure 5.14 illustrates the CDFs of the error in terms of the shape of HRES plant power responses (calculated using (5.13)) for both types of models. As can be seen, both types of DEMs are characterized by similar levels of accuracy in the case of real power responses: the 50th and 95th percentiles of the error of the LSTM-based models are smaller than the corresponding values of the TF-based DEMs by only about 0.4% and 1.3%, respectively. When it comes to reactive power, the median error of the TF-based models is 7.8%, which is smaller than the median error of the LSTM-based models by 1%. However, the 95th percentile of the TF-based models is higher than the corresponding value for the LSTM-based equivalents by around 25%, meaning the LSTM-based models are characterized by smaller number of cases with high error (above 20%). For both TF-based and LSTM-based models, the pre-disturbance reactive power output of the HRES plant was below 10 Mvar in about 50% of the cases when the error for reactive power was above 20%. Even though it was expected to obtain better accuracy in terms of the shape of time domain HRES plant power responses with LSTM-based models than with TF-based models, both types of DEMs resulted in a similar performance. It should be noted that the error of LSTM-based models is affected by the use of a single best DEM for all responses from a typical HRES plant composition (responses with significantly different shape in time domain are simulated using the same LSTM network).

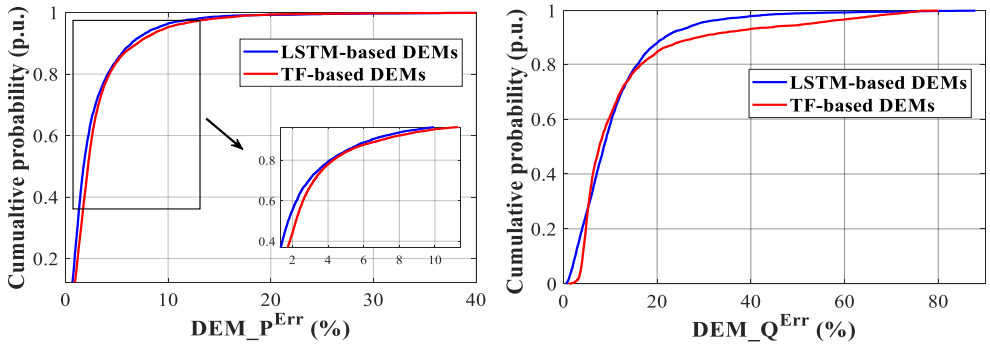

Figure 5.14 Non-training MC CSs for 2019 year: CDF of DEM error in terms of the shape of real (a) and reactive (b) power responses (blue: LSTM-based models, red: TF-based models)

In order to further investigate the difference in the capability of reproducing HRES plant power responses in time domain and assess whether one type of DEMs outperforms the other during the certain period of the year, the relative error values of the LSTM-based

and TF-based models are compared for each month in the test 2019 year. Figure 5.15 shows the 50th and 95th percentile of the DEM_P^{Err} and DEM_Q^{Err} values for the LSTM-based and TF-based models for each month in the year. In the case of HRES plant real power responses, the LSTM-based and TF-based equivalents are characterized by similar monthly performance, with the LSTM-based models having slightly better performance in each month. For both types of DEMs, monthly median error values are similar to the overall median error (i.e., the error determined for the whole year - Figure 5.14 (a)). The difference between the median error of the TF-based and LSTM-based models per month varies from 0.2% to 1.3%, with the maximum difference observed in October. As for the 95th percentiles of the error, the only months with the difference above 1% are April and September-December, with the maximum difference of 7.6% occurring in September. Both types of DEMs have the lowest error in November, while the worst performance of the LSTM-based and TF-based model is observed in January and October, respectively.

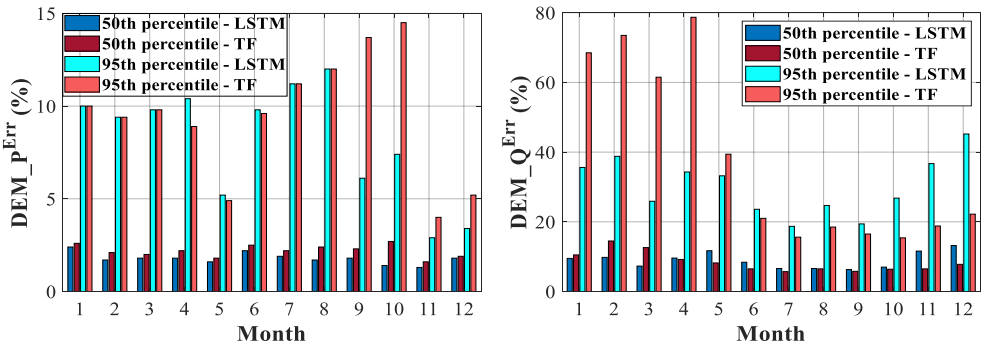

(a) (b)

Figure 5.15 Non-training MC CSs for 2019 year: the 50th and 95th percentile of the error in terms of the shape of real (a) and reactive (b) power responses per month for the LSTM-based and TF-based models

In the case of reactive power responses, the LSTM-based models outperform the TF equivalents in February and March, whereas the opposite is true for November and December (see Figure 5.15 (b)). The overall performance of both types of equivalents is similar in the remaining period of the year, with the differences being mainly in the number of cases characterized by high model error (above 20%). The range of values for the median error per month is (6.3, 11.7)% and (5.7, 14.5)% for the LSTM-based and TF-based equivalents, respectively. In February, March, November and December, the difference between the 50th percentiles of the error of the TF-based and LSTM-based models is around 5%. When it comes to the 95th percentile of the error, the value for the TF-based models is larger by around 30% and smaller by about 20% than the

corresponding value for the LSTM-based equivalents in the February-March and November-December period, respectively.

The main reason for lower accuracy of the TF-based models in February and March is that TF-based DEM 2, which has higher error in terms of the shape of reactive power responses compared to TF-based DEM 1 (see Section 4.4.1.2), covers a considerable number of days in this time period. On the other hand, in the test 2019 year, LSTM-based DEM 8 is a dominant model (i.e., a model used most of the days in a month) among deep learning-based equivalents, except during November and December when LSTM-based DEM 6 covers a considerable number of days per month as well. As shown in Figure 5.12, LSTM-based DEM 6 is characterized by lower reactive power accuracy than LSTM-based DEM 8, which in turn deteriorates the performance of the LSTM-based models in the last two months of the year.

As for the accuracy in the global transient stability status, Figure 5.16 (a) compares the CDFs of TSI error for the LSTM-based and TF-based equivalents. As can be seen, both types of equivalents have similar performance in terms of TSI values as well: the 50^{th} and 95^{th} percentile of TSI error for the LSTM-based models is only smaller by 0.2% and 0.3%, respectively, than the corresponding values of the TF-based DEMs (0.9% and 3.3%, respectively). Furthermore, as seen in Figure 5.16 (b), there is no significant variation in the performance of the models over months in the test 2019 year (the LSTM-based models have slightly better performance than the TF-based equivalents in each month). For both types of DEMs, the median TSI error values per month are within the range of 0.05% around the corresponding overall median error, whereas the 95^{th} percentiles of TSI error per month vary between about 1.5% and 5%. Still, the maximum difference between the 95^{th} percentiles of the TSI error of the TF-based and LSTM-based models per month is only 1%.

The previous analysis has shown that developing DEM of HRES plant on the basis of time domain plant power responses does not provide significant improvement in model accuracy in terms of both HRES plant power responses and the global transient stability status (in particular). Therefore, reliable transient stability assessment of the system can be provided by DEMs not taking into account the shape of power responses at the PCC and focusing only on the contribution of the HRES plant to the overall transient stability behaviour of the system.

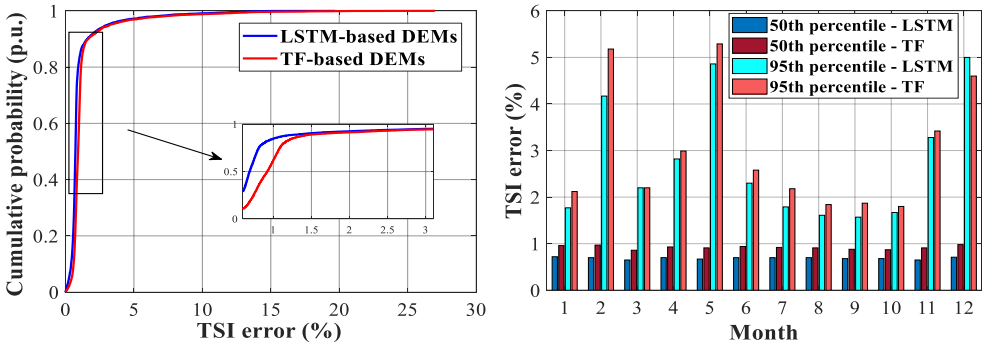

Figure 5.16 Non-training MC CSs for 2019 year: (a) CDF of TSI error of the LSTM-based (blue) and TF-based (red) models; (b) the 50th and 95th percentile of TSI error per month for the LSTM-based and TF-based models

5.4 Summary

The chapter presented the procedure for dynamic equivalent modelling of HRES plant based on historical plant production data, clustering algorithms and deep learning technique. DEM of HRES plant was developed taking into consideration the shape of HRES plant power responses at the PCC in time domain. Deep learning-based methodology for dynamic equivalent modelling of HRES plants represents the fourth original contribution of the thesis.

The methodology, illustrated on the HRES plant comprising three non-dispatchable RESs, results in a set of LSTM network-based DEMs capable of representing the HRES plant in system transient stability studies throughout the year. Furthermore, and possibly more importantly, the modelling procedure includes a practical approach for selecting a small number of the most appropriate DEMs that can be used in annual transient stability simulations knowing only HRES plant operating conditions (the power output of individual RESs). Only four DEMs were required for representing the test HRES plant in transient stability studies during the year with the median TSI error below 0.7%, and the median value of the maximum relative difference between detailed and equivalent model real and reactive power responses of 1.8% and 8.8%, respectively.

The LSTM-based DEMs were compared with the TF-based models, derived based on the minimization of the TSI error only, to ascertain the level of detail and accuracy in DEM development necessary for system transient stability studies. Both types of DEMs resulted in a very similar error in terms of the reproduction of time domain real power

responses (within 1.3%) and TSI value (within 0.3%). When it comes to reactive power responses, the TF-based models are characterized by larger number of cases with model error above 20% (the difference between the 95^{th} percentiles of the error of TF-based and LSTM-based models is around 25%). The comparative analysis of two types of equivalents demonstrated that taking into account the shape of time domain HRES plant power responses when performing dynamic equivalent modelling of HRES plant is not necessary for accurate assessment of the transient stability of the system.

6 Limitations of the Reliance on Assessment of the Contribution of Spatially Distributed HRES Plant to Real System Operation

6.1 Introduction

Previous Chapters 3-5 presented the analysis of the impact of HRES plant with a single PCC on power system stability behaviour and described methodologies for developing EMs of HRES plant with a single PCC for system stability studies. The focus of this chapter is on HRES plants with multiple points of connection to the TN, that is, spatially widely distributed HRES plants at TN level. The chapter discusses the typical principles of operation of distributed HRES plants as well as the potential negative effect of this operation on power system dynamic performance. The influence of a common management of distributed HRES plant on transient stability of the system is analysed using a distributed HRES plant integrated into a simplified model of a large interconnected transmission system comprising four TNs. The distributed HRES plant consists of a number of WFs and PV plants spread across the transmission system.

6.2 The Concept of Operation of Spatially Distributed HRES Plant

In order to obtain more stable and controllable power output from small RESs connected at the DN voltage level, the concept of a VPP was proposed [171]. In the literature the VPP commonly refers to an aggregation of geographically distributed devices, which can include small-scale generation sources as well as energy storage systems and controllable loads [171]. VPP components are connected to a number of buses in DN, and the whole VPP has a single point of connection to the TN (as illustrated in Figure 6.1).

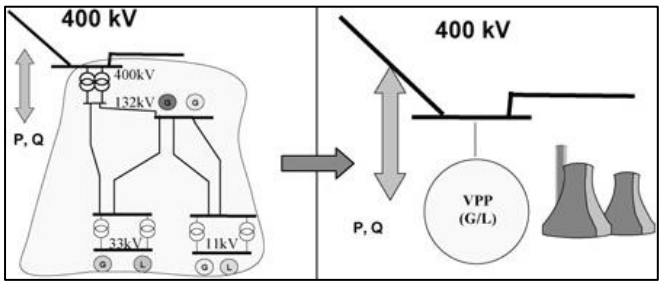

Figure 6.1 The illustration of the VPP concept (adopted from [171])

Unlike in the case of single small RES power plants, VPPs have the capacity and controllability to participate in markets and system management [171]. The participation of the VPP in markets is based on the single VPP operation profile obtained by aggregating/combining operation profiles of individual VPP components, meaning the whole VPP is seen as a single entity from the perspective of market operators. The dispatch of VPP components is then optimized by maximizing plant revenue while satisfying the total VPP power output specified by market-based transactions. Apart from taking part in market activities, VPPs can also contribute to local network management and provide balancing services to transmission system operator (TSO). A DN operator requires the information about the scheduled operating positions, response characteristics and cost data of all VPP components in order to include the VPP in local network management. On the other hand, the above-mentioned data together with the information about local network topology and constraints are needed for representing the whole VPP and local network by a single aggregation profile at the TN supply point, and thus making the VPP balancing capabilities available to TSO.

In this thesis the spatially distributed HRES plant refers to an aggregation of RES plants (energy storage systems can be included as well) geographically spread across the TN. In other words, the distributed HRES plant corresponds to a VPP concept for TN voltage

level, meaning the principle of operation of both distributed HRES plants and VPPs is the same. In a great majority of papers on VPP operation and management, the optimal VPP dispatch is determined by maximising VPP revenue while satisfying the requested VPP power production [209]. The contribution of the optimal economic dispatch of VPPs to power system stability (in particular system dynamic performance) has been commonly neglected [209]. However, the location and power output of distributed HRES plant/VPP components at the given time period affect the optimal economic dispatch of the remaining generators in the system as well. Operating positions of system generators together with the system loading condition at the given time period define power flows in the network, and consequently the voltage profiles and line loadings in the whole system. Apart from influencing the static behaviour of the network, the power outputs of the system generators also affect the dynamic performance of the whole network.

In future power systems with a considerable number of integrated RES plants and decommissioned conventional power plants, preserving power system stability will be more challenging, and thus, optimal economic dispatch of generation units may violate system dynamic limits. Certain distributed HRES plant/VPP composition can be the most optimal with respect to HRES plant/VPP revenues, but its dynamic characteristics in combination with the dynamic responses of the associated optimal economic schedule of the remaining system generators can have a detrimental effect on power system stability. Under such conditions, it might be necessary to make a shift from the traditional economic carbon reduction-driven dispatch of generation units only to the dispatch additionally governed by system dynamics/stability analysis. In other words, system dynamic stability may become a determining constraint when deciding on the dispatch of the spatially distributed HRES plant/VPP for a particular time period. This is similar to a concept of security constrained OPF or security constrained generator scheduling with the emphasis on renewable generation scheduling/utilisation.

In order to investigate to what extent and under which conditions the selection of the operating schedule of distributed HRES plant components (i.e., spatial HRES plant composition) affects system dynamic performance, system-level dynamic studies have to be performed. Unlike in the case of HRES plants presented in Chapters 3-5, a DEM cannot be used for representing the distributed HRES plant in system stability

simulations due to its multiple points of connection to the TN. In case there are individual plants within the distributed HRES plant with a common point of connection to the TN, they can be represented by an EM; otherwise each HRES plant component has to be modelled separately. The following section provides the analysis on the differences in power system stability status due to variations in the dispatch of HRES plant components for the same total HRES plant output. The focus is on transient stability of the system. This is similar to generic studies of the effect of proliferation of RESs on system transient stability with a difference that in this case it is assumed that a single aggregator or a groups of aggregators are offering a "VPP type of service" to a TN. The aim is to demonstrate that by offering certain energy delivery to TN, the aggregators might be constrained in a way, as they would need to consider what effects their particular deployment of RESs (part of their portfolio) might have on the overall TN dynamic performance. If this planned deployment, based on available resources (wind and sun), could affect system transient stability (in this particular case) or other performance attributes of TN, the aggregator may not be able to deliver initially offered/promised service. This clearly could lead to either reduced profit for them or a need to re-negotiate the contracts.

6.3 Analysing the Impact of Spatial HRES Plant Composition on Transient System Stability

6.3.1 Test System

The test system is a simplified, realistic representation of a 255-bus equivalent of four interconnected real TNs in Europe comprising 42 SGs and 178 loads. Figure 6.2 presents the schematic diagram of the test system, with SGs/loads connected to the same bus represented by a single SG/load symbol. The network structure consisting of 220 kV and 400 kV levels is divided into four areas connected by 17 tie-lines (TLs). A less detailed diagram of the test network indicating TLs between the areas is shown in Figure 6.3. The 6 out of 17 TLs are 400 kV lines (red lines in Figure 6.2 and Figure 6.3), while the remaining TLs are 220 kV lines (green lines in Figure 6.2 and Figure 6.3). The SGs in the test network represent thermal and hydro power plants, while the HRES plant in the test system consists of RESs (WFs and PV plants) that are spatially widely distributed in four areas. Figure 6.2 provides the information about the locations of RES power plants in the Current (blue wind turbine symbols) and Future (orange wind turbine and orange

PV panel symbols) RES state (detailed explanation of RES states is given in Section 6.3.3). As in the case of SGs and system loads, RES plants of the same technology that are connected to the grid at the same bus are represented by a single symbol.

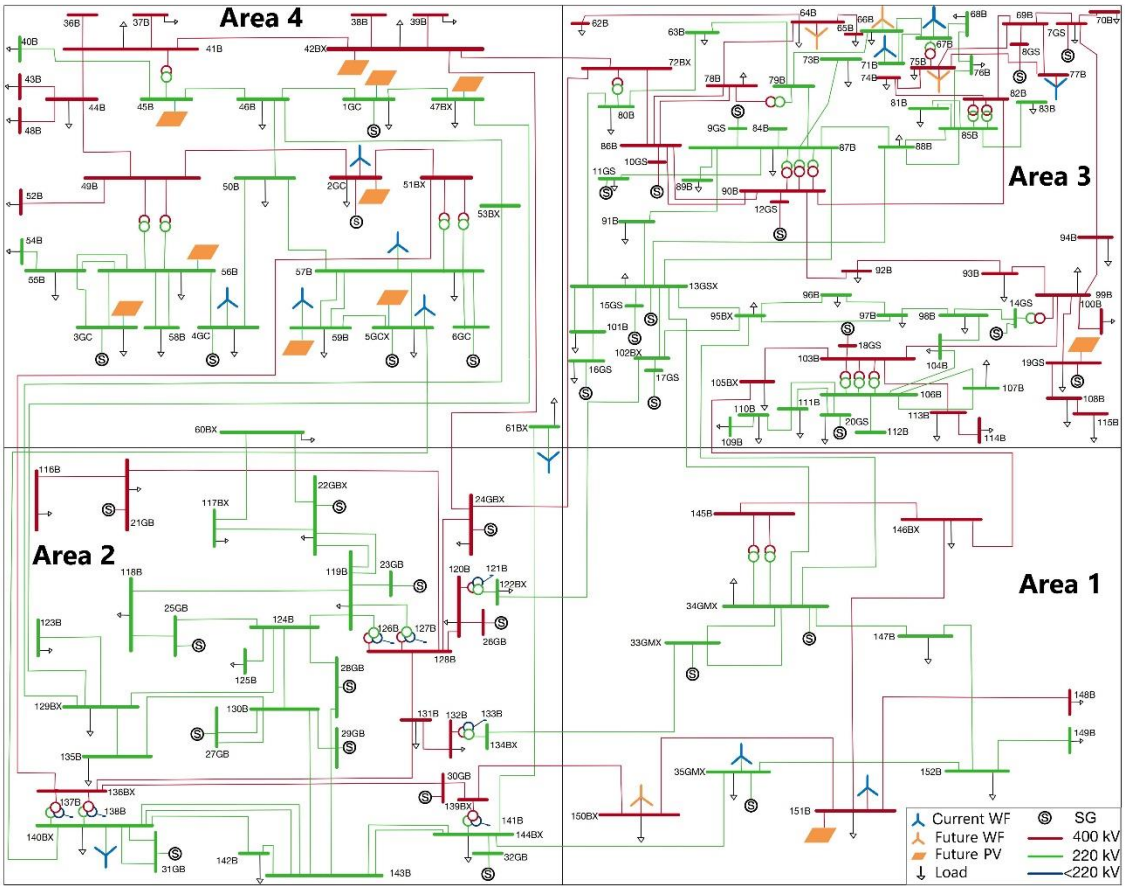

Figure 6.2 The schematic diagram of the test system

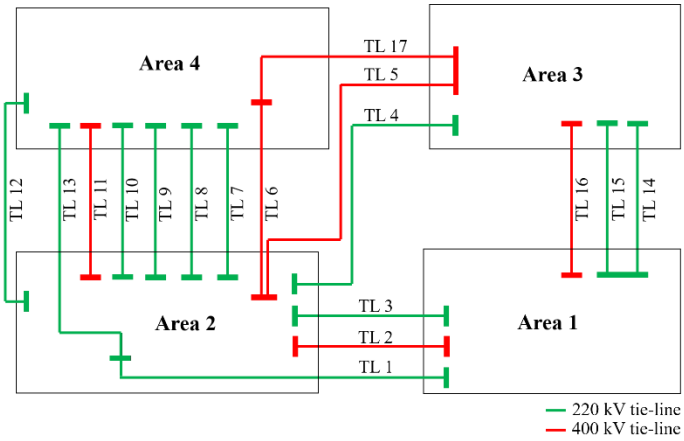

Figure 6.3 The less detailed schematic diagram of the test system indicating TLs between the areas

The test system is developed in DIgSILENT/PowerFactory software environment. The standard sixth- and fifth-order SG model is used for modelling thermal and hydro power plants, respectively, while the control systems of SGs include excitation systems and governors. The parameters of SG dynamic models and SG controllers were provided by the respective TSOs, whereas the SG cost functions were adopted from [210] according to the similarity in the plant type and rated capacity. Wind turbines and PV units are represented by DFIGs and FCC units, respectively. As in the case of the test systems presented in Chapters 3-5, RES power plants comprise a number of identical units connected in parallel. The number of units in operation is defined by the total power production of the RES power plant, as it is assumed that units in service operate at the rated real power output (2 MW). In this study, it is assumed that PV plants operate with a unity power factor, while a wind generator produces 0.25 Mvar [211]. The dynamic models of WFs and PV plants, and their control systems correspond to the ones used in the test networks in Chapters 3-5 (detailed description of the dynamic modelling of RES power plants is provided in Section 3.3). The loads in the test network are modelled using a constant impedance model.

6.3.2 Methodology

The procedure for assessing the influence of spatial HRES plant composition on transient system stability performance relies on the probabilistic modelling of power production of individual RESs in the HRES plant and probabilistic representation of the transient stability results (the flow chart is presented in Figure 6.4). Adequate PDFs are used for generating random power outputs of individual RES plants for the considered system loading conditions. A number of system disturbances at various locations in the network are simulated for each operating point, and TSI, a widely used index for transient stability assessment, is calculated for each simulation. The most probable (representative) TSI for the particular system operating condition is determined according to the PDF estimated using the obtained TSI values. The representative TSIs are then used for investigating the impact of spatial HRES plant composition on the overall transient stability behaviour of the system. (*Note*: Given that the spatially distributed HRES plant in the test system contains non-dispatchable RESs with the production determined by the weather conditions, the analysis presented in this chapter is also applicable to the case of a single owner of each individual RES plant in the test system.) The procedure comprises four parts: Part I, Part III, and Part IV, which are mainly focused on data analysis, are

performed in Matlab R2020a, while Part II (system stability analysis) is carried out in DIgSILENT/PowerFactory 2020 environment [164]. Following sections describe each part of the procedure in detail.

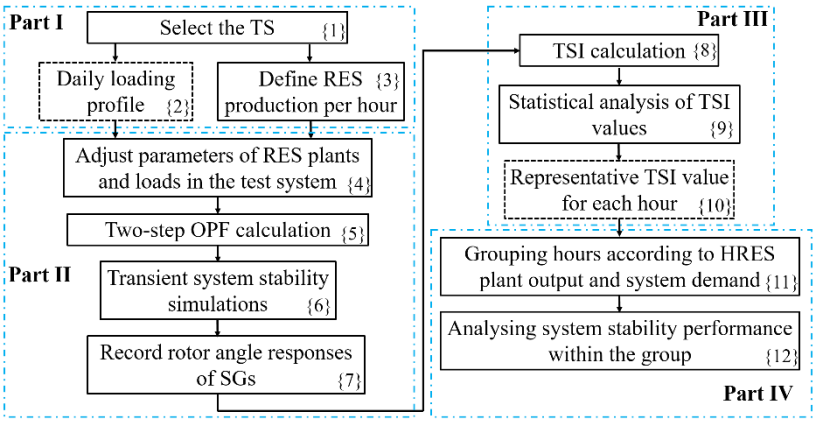

Figure 6.4 The flow chart of the procedure for assessing the impact of spatial HRES plant composition on transient stability of the system

6.3.2.1 Part I

Part I of the procedure illustrated in Figure 6.4 provides the system load level and power production of all non-dispatchable RESs, i.e., PV plants and WFs, in the network. Firstly, a test scenario (TS) used for a 24-hour transient stability assessment of the system is chosen from a pre-defined set of TSs (block {1} in Figure 6.4). Each TS is associated with a particular daily system loading profile (block {2} in Figure 6.4), and the location and rated capacity values of RESs (so-called RES state, which is described in detail in Section 6.3.3). Then, for each hour in the chosen TS, the power outputs of RES plants within the HRES plants are defined in a probabilistic manner (block {3} in Figure 6.4) by sampling RES production from the predefined PDFs. In case historical RES plant production data or historical wind speed and solar irradiation measurements are available, these data can be used for defining hourly production profiles of RES power plants instead of the PDFs.

In the case of WFs, it is assumed that the wind speed follows a Weibull distribution with a shape parameter of 2.2 and scale parameter of 11.1 [212]:

$$f(v)=\begin{cases}\frac{k}{\varphi}\left(\frac{v}{\varphi}\right)^{k-1}e^{-(v/\varphi)^k} & v\geq 0\\ 0 & v<0\end{cases}, \tag{6.1}$$

where v is the wind speed, k is the shape parameter and φ is the scale parameter. The power production for the sampled wind speed is obtained from a typical wind turbine power curve presented in Figure 6.5 (a) [213].

When it comes to PV plants, the daily PV production curve shown in Figure 6.5 (b) is used for defining plant power output [182, 214] (the normalization is carried out using the rated capacity of the PV plant). In order to take into account uncertainties in power production, for each PV plant, the value from the PV curve for the given hour is multiplied by a random factor generated using a beta distribution [214]:

$$f(x)=\frac{\Gamma(a+b)}{\Gamma(a)\Gamma(b)}x^{a-1}(1-x)^{b-1}, x \in [0,1], \tag{6.2}$$

where Γ stands for the gamma function, and a and b are the PDF parameters. In this study the following values are adopted for the beta distribution parameters: a=13.7 and b=1.3 [182].

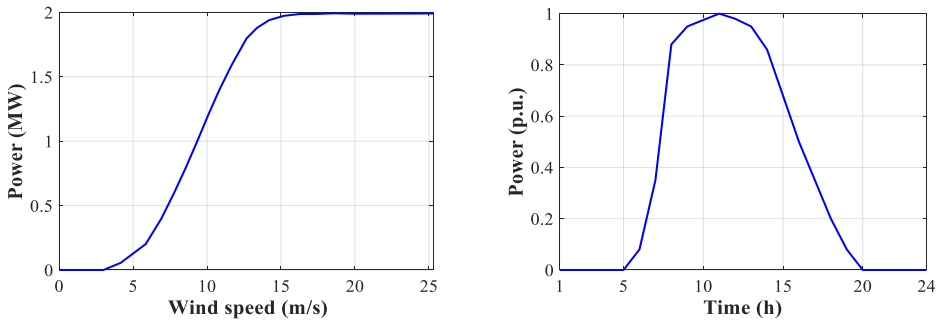

(a) (b)

Figure 6.5 (a): Wind turbine power curve [213]; (b): Daily PV plant production curve [182, 214] (the base power is the rated PV plant capacity)

The assumptions about wind and PV generation output presented above facilitate the generation of realistic daily power production profiles of RES power plants in the test system.

6.3.2.2 Part II

Part I of the procedure provides the dispatch of RES units in the system, while the pre-disturbance power outputs of SGs in the network are defined by the OPF calculation performed in Part II.

In order to take into consideration the reduction in the total system inertia level due to HRES plant integration, it is assumed that each SG in the test network is an equivalent

representation (an equivalent SG) of an SG power plant comprising four identical units. The rated capacity and power dispatch of the equivalent SG for an operating condition correspond to the sum of rated capacities and power outputs, respectively, of the individual units in the relevant SG plant that are in service in the case of the given operating condition (it is assumed that individual units in service have the same operating point):

$$S_{EqSG_i}^{N_{EqSG_i}^{unit}} = \sum_{j=1}^{N_{EqSG_i}^{unit}} S_{unit,EqSG_i^j} = N_{EqSG_i}^{unit} \cdot S_{unit,EqSG_i^j}, \tag{6.3}$$

$$P_{EqSG_i}^{N_{EqSG_i}^{unit}} = \sum_{j=1}^{N_{EqSG_i}^{unit}} P_{unit,EqSG_i^j} = N_{EqSG_i}^{unit} \cdot P_{unit,EqSG_i^j}, \tag{6.4}$$

where $N_{EqSG_i}^{unit}$ is the number of units represented by the *i*-th equivalent SG (the equivalent SG of the *i*-th SG plant), that is, the number of units in service in the *i*-th SG plant, for the given operating condition (the maximum number of units in service is equal to four), $S_{EqSG_i}^{N_{EqSG_i}^{unit}}$ and $P_{EqSG_i}^{N_{EqSG_i}^{unit}}$ is the rated capacity and real power output of the *i*-th equivalent SG representing $N_{EqSG_i}^{unit}$ units, respectively, $S_{unit,EqSG_i^j}$ and $P_{unit,EqSG_i^j}$ is the rated capacity and real power output of the *j*-th individual unit in the *i*-th SG plant, respectively (all units in the plant are identical). The relation between the reactive power output of the *i*-th equivalent SG representing $N_{EqSG_i}^{unit}$ units ($Q_{EqSG_i}^{N_{EqSG_i}^{unit}}$) and the reactive power of individual units in service in the *i*-th SG plant ($Q_{unit,EqSG_i^j}$) is analogous to (6.4).

In order to ensure the specified minimum operational reserve, the maximum real power limit of individual units in the *i*-th SG plant is defined as follows:

$$P_{unit,EqSG_i^j}^{max} = p_{unit,EqSG_i^j}^{max} \cdot S_{unit,EqSG_i^j}, \tag{6.5}$$

$$p_{unit,EqSG_i^j}^{max} = (1 - Reserve_{unit,EqSG_i^j}) \cdot PF_{nom,unit,EqSG_i^j}, \tag{6.6}$$

where $P_{unit,EqSG_i^j}^{max}$ and $p_{unit,EqSG_i^j}^{max}$ is the maximum real power limit in MW and p.u., respectively, $Reserve_{unit,EqSG_i^j}$ is the spare reserve in p.u., and $PF_{nom,unit,EqSG_i^j}$ is the

rated power factor; all for the *j*-th individual unit in the *i*-th SG plant. A fixed spare reserve of 15% is adopted in the study for all individual units in all SG plants [182].

The minimum real power limit and reactive power limits of individual units in the *i*-th SG plant are specified as follows:

$$P^{min}_{unit,EqSG_i^j}=p^{min}_{unit,EqSG_i^j}\cdot S_{unit,EqSG_i^j}, \tag{6.7}$$

$$Q^{min}_{unit,EqSG_i^j}=q^{min}_{unit,EqSG_i^j}\cdot S_{unit,EqSG_i^j}, \tag{6.8}$$

$$Q^{max}_{unit,EqSG_i^j}=q^{max}_{unit,EqSG_i^j}\cdot S_{unit,EqSG_i^j}, \tag{6.9}$$

where $P^{min}_{unit,EqSG_i^j}$ and $p^{min}_{unit,EqSG_i^j}$ is the minimum real power limit in MW and p.u., respectively, $Q^{min}_{unit,EqSG_i^j}$ and $q^{min}_{unit,EqSG_i^j}$ is the minimum reactive power limit in Mvar and p.u., respectively, $Q^{max}_{unit,EqSG_i^j}$ and $q^{max}_{unit,EqSG_i^j}$ is the maximum reactive power limit in Mvar and p.u., respectively; all for the *j*-th individual unit in the *i*-th SG plant.

The real and reactive power limits in MW and Mvar, respectively, of the *i*-th equivalent SG representing $N^{unit}_{EqSG_i}$ units can be obtained based on (6.3) and (6.4):

$$\begin{aligned} P^{max,N^{unit}_{EqSG_i}}_{EqSG_i} &= N^{unit}_{EqSG_i}\cdot P^{max}_{unit,EqSG_i^j} = N^{unit}_{EqSG_i}\cdot p^{max}_{unit,EqSG_i^j}\cdot S_{unit,EqSG_i^j} = \\ &= p^{max}_{unit,EqSG_i^j}\cdot S^{N^{unit}_{EqSG_i}}_{EqSG_i} \end{aligned}, \tag{6.10}$$

where $P^{max,N^{unit}_{EqSG_i}}_{EqSG_i}$ is the maximum real power limit in MW for the *i*-th equivalent SG representing $N^{unit}_{EqSG_i}$ units. Analogous expressions can be obtained for the remaining real and reactive power limits in absolute units for the *i*-th equivalent SG representing $N^{unit}_{EqSG_i}$ units.

When it comes to the real and reactive power limits in p.u. of the *i*-th equivalent SG, they are equal to the respective limits of individual units in the *i*-th SG plant according to (6.10):

$$p^{max}_{EqSG_i}=P^{max,N^{unit}_{EqSG_i}}_{EqSG_i}\Big/S^{N^{unit}_{EqSG_i}}_{EqSG_i}=\left(p^{max}_{unit,EqSG_i^j}\cdot S^{N^{unit}_{EqSG_i}}_{EqSG_i}\right)\Big/S^{N^{unit}_{EqSG_i}}_{EqSG_i}=p^{max}_{unit,EqSG_i^j}, \tag{6.11}$$

where $p_{EqSG_i}^{max}$ is the maximum real power limit in p.u. of the *i*-th equivalent SG. Analogous expressions can be obtained for the remaining real and reactive power limits in p.u. of the *i*-th equivalent SG. In this study, the adopted minimum and maximum reactive power limits in p.u. are -0.6 p.u. and 0.8 p.u., respectively [163, 211], whereas the minimum real power limit values are obtained from the respective TSOs.

The determination of the optimal economic dispatch of SG plants in the network represents a mixed-integer optimization problem as power outputs of SG plants and the number of SG units in service in each plant (which define the rated capacity values of SG plants (see (6.3))) have to be defined. The given optimization task can be mathematically formulated as follows:

$$
\begin{gathered}
min \sum_{i=1}^{N_{EqSG}} Cost_{EqSG_i} = min \sum_{i=1}^{N_{EqSG}} \left(a_i \left(P_{EqSG_i}^{OPF} \right)^2 + b_i P_{EqSG_i}^{OPF} + c_i \right) \\
P_k - P_{gk} + P_{dk} = 0, k = 1, \dots, N_{bus}, \\
P_k = V_k \sum_{l=1}^{N_{bus}} V_l Y_{kl} \cos(\theta_k - \theta_l - \psi_{kl}), k = 1, \dots, N_{bus}, \\
Q_k - Q_{gk} + Q_{dk} = 0, k = 1, \dots, N_{bus}, \\
Q_k = V_k \sum_{l=1}^{N_{bus}} V_l Y_{kl} \sin(\theta_k - \theta_l - \psi_{kl}), k = 1, \dots, N_{bus}, \\
P_{EqSG_i}^{min,OPF} \le P_{EqSG_i}^{OPF} \le P_{EqSG_i}^{max,OPF}, i = 1, \dots, N_{EqSG}, \\
P_{EqSG_i}^{min,OPF} = p_{unit,EqSG_i^j}^{min} \cdot N_{EqSG_i}^{FinUnit} \cdot S_{unit,EqSG_i^j}, i = 1, \dots, N_{EqSG}, \\
P_{EqSG_i}^{min,OPF} = p_{unit,EqSG_i^j}^{max} \cdot N_{EqSG_i}^{FinUnit} \cdot S_{unit,EqSG_i^j}, i = 1, \dots, N_{EqSG}, \\
Q_{EqSG_i}^{min,OPF} \le Q_{EqSG_i}^{OPF} \le Q_{EqSG_i}^{max,OPF}, i = 1, \dots, N_{EqSG}, \\
Q_{EqSG_i}^{min,OPF} = q_{unit,EqSG_i^j}^{min} \cdot N_{EqSG_i}^{FinUnit} \cdot S_{unit,EqSG_i^j}, i = 1, \dots, N_{EqSG}, \\
Q_{EqSG_i}^{max,OPF} = q_{unit,EqSG_i^j}^{max} \cdot N_{EqSG_i}^{FinUnit} \cdot S_{unit,EqSG_i^j}, i = 1, \dots, N_{EqSG}, \\
\sqrt{\left(P_{EqSG_i}^{OPF} \right)^2 + \left(Q_{EqSG_i}^{OPF} \right)^2} \le S_{EqSG_i}^{OPF} = N_{EqSG_i}^{FinUnit} \cdot S_{unit,EqSG_i^j}, i = 1, \dots, N_{EqSG}, \\
0 \le N_{EqSG_i}^{FinUnit} \le 4, i = 1, \dots, N_{EqSG}, \\
V_k^{min} \le V_k \le V_k^{max}, k = 1, \dots, N_{bus}, \\
Line_{loading,m} \le Line_{loading,m}^{max}, m = 1, \dots, N_{line}, \\
TR_{loading,n} \le TR_{loading,n}^{max}, n = 1, \dots, N_{TR},
\end{gathered}
\quad , \qquad (6.12)
$$

where: $Cost_{EqSG,i}$ is the generation cost for the *i*-th equivalent SG, a_i, b_i, and c_i are the coefficients of the cost function for the *i*-th equivalent SG, $P_{EqSG_i}^{OPF}$ and $Q_{EqSG_i}^{OPF}$ are the real and reactive power output values of the *i*-th equivalent SG that are obtained from the OPF, respectively, P_k and Q_k is the net real and reactive power injection at the *k*-th bus,

respectively, P_{gk} and Q_{gk} is the sum of real and reactive power outputs of the equivalent SGs and individual RES plants within the HRES plant that are connected to the *k*-th bus, respectively, P_{dk} and Q_{dk} is the real and reactive power of the load connected to the *k*-th bus, respectively, V_k is the voltage magnitude of the *k*-th bus, Y_{kl} and ψ_{kl} is the magnitude and phase angle of the complex admittance matrix element at the position (*k*, *l*), respectively, θ_k is the phase angle of the voltage at the *k*-th bus, $N_{EqSG_i}^{FinUnit}$ (a discrete variable) is the number of units represented by the *i*-th equivalent SG that is obtained from the OPF, $P_{SG_i}^{min,OPF}$ and $P_{EqSG_i}^{max,OPF}$ is the minimum and maximum real power limit in MW of the *i*-th equivalent SG representing $N_{EqSG_i}^{FinUnit}$ units, $Q_{EqSG_i}^{min,OPF}$ and $Q_{EqSG_i}^{max,OPF}$ is the minimum and maximum reactive power limits in Mvar of the *i*-th equivalent SG representing $N_{EqSG_i}^{FinUnit}$ units, respectively, $S_{EqSG_i}^{OPF}$ is the rated capacity of the *i*-th equivalent SG representing $N_{EqSG_i}^{FinUnit}$ units, V_k^{min} and V_k^{max} are the minimum and maximum voltage limits for the *k*-th bus, respectively, $Line_{loading,m}$ is the loading of the *m*-th line, $Line_{loading,m}^{max}$ is the maximum loading of the *m*-th line, $TR_{loading,n}$ is the loading of the *n*-th transformer, $TR_{loading,n}^{max}$ is the maximum loading of the *n*-th transformer, N_{EqSG}, N_{bus}, N_{line}, and N_{TR} are the number of equivalent SGs, buses, lines and transformers in the network, respectively. The constraints for all bus voltage magnitudes are 0.9 p.u. and 1.1 p.u., whereas the maximum allowed line and transformer loading is 100%.

Given that the whole system is modelled in DIgSILENT/PowerFactory environment and this software package does not have a tool for solving the mixed-integer non-linear optimization task described by (6.12), the given optimization problem is divided into two parts, each of them representing a non-linear OPF with continuous variables. Thus, the OPF is conducted twice for each hour during the day in order to determine both the power dispatch of equivalent SGs as well as the required number of units represented by each equivalent SG (i.e., the required number of units in service in each SG plant). The first OPF gives the information about the rated capacity values and preliminary operating points of equivalent SGs, whereas the second OPF provides the final power dispatch of equivalent SGs according to the capacity values provided by the first OPF.

6.3.2.2.1 Two-step Optimal Power Flow Procedure

The two-step OPF calculation is carried out in DIgSILENT/PowerFactory environment using the detailed network model. The logarithmic barrier interior point algorithm for nonlinear optimization based on the Newton method is used for solving the OPF problem [215] (the only available optimization algorithm for nonlinear optimization tasks in DIgSILENT/PowerFactory [164]).

When performing the first OPF, all equivalent SGs are in operation and have the maximum rated capacity ($N_{EqSG_i}^{unit}$ is equal to four, that is, it is assumed that all four individual units in each plant are in service). The objective of the first OPF is to minimize the total generation cost of SG plants while satisfying the specified total system load, and considering equivalent SG and network constraints. The first OPF problem can be formulated as follows:

$$\begin{gathered} min \sum_{i=1}^{N_{EqSG}} Cost_{EqSG_i} = min \sum_{i=1}^{N_{EqSG}} \left(a_i \left(P_{EqSG_i}^{4,OPF\,1} \right)^2 + b_i P_{EqSG_i}^{4,OPF\,1} + c_i \right) \\ P_k - P_{gk} + P_{dk} = 0, k = 1, \dots, N_{bus}, \\ P_k = V_k \sum_{l=1}^{N_{bus}} V_l Y_{kl} \cos(\theta_k - \theta_l - \psi_{kl}), k = 1, \dots, N_{bus}, \\ Q_k - Q_{gk} + Q_{dk} = 0, k = 1, \dots, N_{bus}, \\ Q_k = V_k \sum_{l=1}^{N_{bus}} V_l Y_{kl} \sin(\theta_k - \theta_l - \psi_{kl}), k = 1, \dots, N_{bus}, \\ P_{EqSG_i}^{min,4,OPF\,1} \le P_{EqSG_i}^{4,OPF\,1} \le P_{EqSG_i}^{max,4}, i = 1, \dots, N_{EqSG}, \\ Q_{EqSG_i}^{min,4} \le Q_{EqSG_i}^{4,OPF\,1} \le Q_{EqSG_i}^{max,4}, i = 1, \dots, N_{EqSG}, \\ \sqrt{\left(P_{EqSG_i}^{4,OPF\,1} \right)^2 + \left(Q_{EqSG_i}^{4,OPF\,1} \right)^2} \le S_{EqSG_i}^{4}, i = 1, \dots, N_{EqSG}, \\ V_k^{min} \le V_k \le V_k^{max}, k = 1, \dots, N_{bus}, \\ Line_{loading,m} \le Line_{loading,m}^{max}, m = 1, \dots, N_{line}, \\ TR_{loading,n} \le TR_{loading,n}^{max}, n = 1, \dots, N_{TR}, \end{gathered} \quad , \quad (6.13)$$

where: $P_{EqSG_i}^{4,OPF\,1}$ and $Q_{EqSG_i}^{4,OPF\,1}$ are the real and reactive power output values of the *i*-th equivalent SG representing four units that are obtained from the first OPF, respectively, P_k and Q_k is the net real and reactive power injection at the *k*-th bus, respectively, $P_{EqSG_i}^{max,4}$ is the maximum real power limit in MW of the *i*-th equivalent SG representing four units, $P_{SG_i}^{min,4,OPF\,1}$ is the minimum real power limit in MW of the *i*-th equivalent SG representing four units that is used in the first OPF calculation, $Q_{EqSG_i}^{min,4}$ and $Q_{EqSG_i}^{max,4}$ are

the minimum and maximum reactive power limits in Mvar of the *i*-th equivalent SG representing four units, respectively, $S^{4}_{EqSG_i}$ is the rated capacity of the *i*-th equivalent SG representing four units. The values of $P^{max,4}_{EqSG_i}$, $Q^{min,4}_{EqSG_i}$, and $Q^{max,4}_{EqSG_i}$ are calculated using (6.10) for the number of units equal to four ($N^{unit}_{EqSG_i} = 4$), while the $S^{4}_{EqSG_i}$ is defined based on (6.3) for four units in service. The constraints for all bus voltage magnitudes are 0.9 p.u. and 1.1 p.u., whereas the maximum allowed line and transformer loading is 100%.

In the first OPF calculation the actual minimum real power limits of individual units are not considered. Instead, the minimum real power limit for all individual units is set to zero. Consequently, the minimum real power limit of all equivalent SGs in the first OPF ($P^{min,4,OPF\,1}_{EqSG_i}$ in (6.13)) is zero. Zero minimum real power limit is adopted to make possible the disconnection of an equivalent SG representing four units from the network (this corresponds to disconnecting the whole SG plant from the network). The minimum real power limit of zero value enables the dispatch of the *i*-th equivalent SG in the first OPF calculation to take any value between zero and the maximum real power limit of the *i*-th equivalent SG (calculated according to (6.10) for the number of units equal to four). In case the real power production of the *i*-th equivalent SG obtained from the first OPF ($P^{4,OPF\,1}_{EqSG_i}$) is below the actual minimum real power limit for a single unit in the *i*-th SG plant ($P^{min}_{unit,EqSG^{j}_{i}}$ in (6.7)), then not even a single unit in service can provide such a low power output, and the whole *i*-th equivalent SG representing four units (i.e., the whole *i*-th SG plant) is disconnected from the network. On the other hand, using the actual, non-zero, minimum real power limits of individual units in the first OPF calculation would result in non-zero minimum real power limits of equivalent SGs ($4 \cdot P^{min}_{unit,EqSG^{j}_{i}}$ according to (6.10), ($i = 1, \dots, N_{EqSG}$)), and thus, the real power outputs of equivalent SGs obtained from the first OPF would be equal to at least the minimum real power output values of equivalent SGs. Given that the $4 \cdot P^{min}_{unit,EqSG^{j}_{i}}$ value is above the minimum real power output for an individual unit, at least one unit in the *i*-th SG plant would have to be in service, which means that none of the SG plants would be able to be disconnected from the network.

For equivalent SGs with the first OPF dispatch above the minimum real power limit for a single unit (i.e., equivalent SGs not disconnected from the network), the procedure

shown in Figure 6.6 is carried out to identify the minimum required number of units in service in the plant that can produce the power output corresponding to the first OPF dispatch of the equivalent SG ($P_{EqSG_i}^{4,OPF\ 1}$). Detailed description of each stage in the procedure (i.e., blocks in Figure 6.6) for the *i*-th equivalent SG is given below.

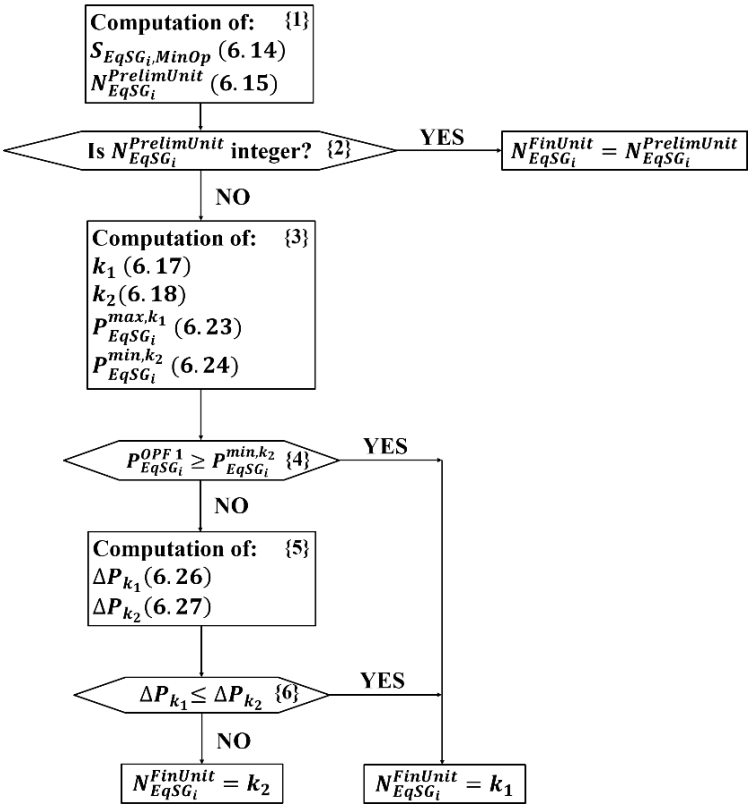

Figure 6.6 The procedure for identifying the optimal number of units in service for each SG plant based on the first OPF results

Block {1} in Figure 6.6: In the first stage of the procedure, the minimum operating capacity of the *i*-th equivalent SG that can produce the $P_{EqSG_i}^{4,OPF\ 1}$ power output is calculated assuming that the $P_{EqSG_i}^{4,OPF\ 1}$ value corresponds to the maximum real power limit for this capacity value. According to (6.11):

$$P_{EqSG_i}^{4,OPF\ 1} = p_{EqSG_i}^{max} \cdot S_{EqSG_i,MinOp} \rightarrow S_{EqSG_i,MinOp} = \frac{P_{EqSG_i}^{4,OPF\ 1}}{p_{EqSG_i}^{max}}, \quad (6.14)$$

where $S_{EqSG_i,MinOp}$ is the minimum operating capacity of the *i*-th equivalent SG that can produce the $P_{EqSG_i}^{4,OPF\ 1}$ output value.

The theoretical number of units represented by the *i*-th equivalent SG with the minimum operating capacity, so-called the preliminary number of units in service in the *i*-th SG plant for the $P_{EqSG_i}^{4,OPF\,1}$ power output, is computed as follows:

$$N_{EqSG_i}^{PrelimUnit}=\frac{S_{EqSG_i,MinOp}}{S_{unit,EqSG_i^j}}, \tag{6.15}$$

where $N_{EqSG_i}^{PrelimUnit}$ is the preliminary number of units in service in the *i*-th SG plant for the $P_{EqSG_i}^{4,OPF\,1}$ power output, i.e., the preliminary number of units in service in the *i*-th SG plant for the given hour.

Block {2} in Figure 6.6: At this stage of the procedure, it is assessed whether the $N_{EqSG_i}^{PrelimUnit}$ value is an integer. In case $N_{EqSG_i}^{PrelimUnit}$ is an integer value, then the preliminary number of units in service is actually the final number of units in service in the *i*-th SG plant ($N_{EqSG_i}^{FinUnit}$) for the $P_{EqSG_i}^{4,OPF\,1}$ power output, i.e., for the given hour, and the procedure terminates; otherwise the procedure continues with the computations in the following stage.

Block {3} in Figure 6.6: Let assume that the non-integer $N_{EqSG_i}^{PrelimUnit}$ value is a number between integer values k_1 and k_2 obtained by rounding down and up the $N_{EqSG_i}^{PrelimUnit}$ value to the nearest integer, respectively:

$$k_1 < N_{EqSG_i}^{PrelimUnit} < k_2, \tag{6.16}$$

$$k_1=\lfloor N_{EqSG_i}^{PrelimUnit} \rfloor, \tag{6.17}$$

$$k_2=\lceil N_{EqSG_i}^{PrelimUnit} \rceil, \tag{6.18}$$

where k_1 and k_2 are the nearest integers for the $N_{EqSG_i}^{PrelimUnit}$ value, $\lceil x \rceil$ and $\lfloor x \rfloor$ stands for rounding up and down number *x* to the nearest integer, respectively.

These two integer values, k_1 and k_2, represent potential candidates for the final number of units in service in the *i*-th SG plant for the given hour. Based on (6.3), (6.10), (6.15), and (6.16), the following relation between the $P_{EqSG_i}^{4,OPF\,1}$ value and the maximum real power limits of the equivalent SGs of the *i*-th SG plant with k_1 and k_2 number of units in

service (i.e., the *i*-th equivalent SGs representing k_1 and k_2 number of units) can be derived:

$$k_1 < \frac{S_{EqSG_i,MinOp}}{S_{unit,EqSG_i^j}} < k_2, \tag{6.19}$$

$$k_1 < \frac{P_{EqSG_i}^{4,OPF\,1}/p_{EqSG_i}^{max}}{S_{unit,EqSG_i^j}} < k_2, \tag{6.20}$$

$$k_1 \cdot S_{unit,EqSG_i^j} \cdot p_{EqSG_i}^{max} < P_{EqSG_i}^{4,OPF\,1} < k_2 \cdot S_{unit,EqSG_i^j} \cdot p_{EqSG_i}^{max}, \tag{6.21}$$

$$p_{EqSG_i}^{max} \cdot S_{EqSG_i}^{k_1} < P_{EqSG_i}^{4,OPF\,1} < p_{EqSG_i}^{max} \cdot S_{EqSG_i}^{k_2}, \tag{6.22}$$

$$P_{EqSG_i}^{max,k_1} < P_{EqSG_i}^{4,OPF\,1} < P_{EqSG_i}^{max,k_2}, \tag{6.23}$$

where $P_{EqSG_i}^{max,k_1}$ and $P_{EqSG_i}^{max,k_2}$ are the maximum real power limits in MW of the *i*-th equivalent SG representing k_1 and k_2 number of units, respectively, $S_{EqSG_i}^{k_1}$ and $S_{EqSG_i}^{k_2}$ is the rated capacity of the *i*-th equivalent SG representing k_1 and k_2 number of units, respectively. Therefore, the $P_{EqSG_i}^{4,OPF\,1}$ value is certainly between the values of the maximum real power limits in MW of the *i*-th equivalent SGs representing k_1 and k_2 number of units.

Depending on the $P_{EqSG_i}^{4,OPF\,1}$ value and the minimum real power limit in p.u. for the *i*-th equivalent SG, two scenarios are possible:

- *Scenario 1*: The $P_{EqSG_i}^{4,OPF\,1}$ value is equal to or larger than the minimum real power limit of the *i*-th equivalent SG representing k_2 number of units (see Figure 6.7 (a); blue bars denote the ranges of real power production for the *i*-th equivalent SGs representing k_1 and k_2 number of units, while the green dashed line indicates the $P_{EqSG_i}^{4,OPF\,1}$ value):

$$P_{EqSG_i}^{4,OPF\,1} \geq P_{EqSG_i}^{min,k_2} = p_{EqSG_i}^{min} \cdot S_{EqSG_i}^{k_2} = p_{EqSG_i}^{min} \cdot k_2 \cdot S_{unit,EqSG_i^j}\ , \tag{6.24}$$

where $P_{EqSG_i}^{min,k_2}$ is the minimum real power limit in MW of the *i*-th equivalent SG representing k_2 number of units.

- *Scenario 2*: This scenario can only occur if there is no overlap between the ranges of real power output for the *i*-th equivalent SGs representing k_1 and k_2 number of units (see Figure 6.7 (b)). (*Note*: In the case of Scenario 1, it is irrelevant whether there is an overlap between the ranges). In this scenario, the $P_{EqSG_i}^{4,OPF\,1}$ value is between the maximum real power limit in MW of the *i*-th equivalent SG representing k_1 number of units and the minimum real power limit in MW of the *i*-th equivalent SG representing k_2 number of units:

$$P_{EqSG_i}^{max,k_1} < P_{EqSG_i}^{4,OPF\,1} < P_{EqSG_i}^{min,k_2} . \tag{6.25}$$

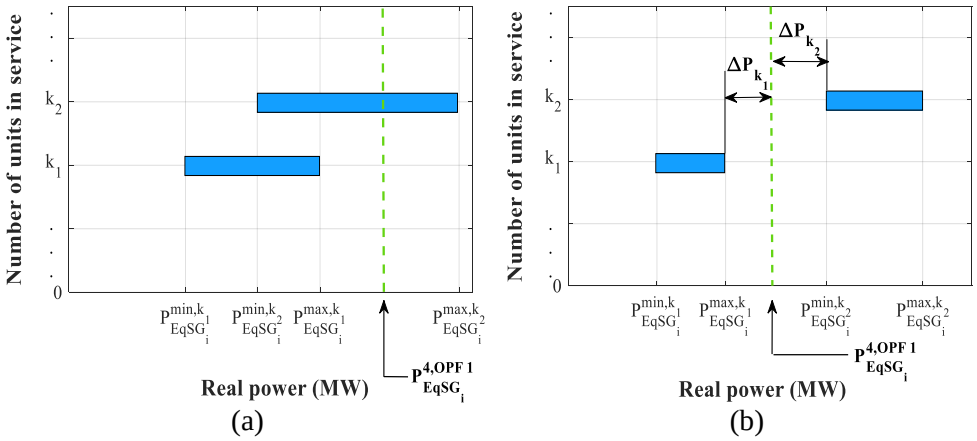

Figure 6.7 The illustration of Scenario 1 (a) and Scenario 2 (b)

Block {4} in Figure 6.6: The $P_{EqSG_i}^{4,OPF\,1}$ value is compared with the minimum real power limit in MW of the *i*-th equivalent SG representing k_2 number of units ($P_{EqSG_i}^{min,k_2}$), i.e., Scenario 1 is considered. If the $P_{EqSG_i}^{4,OPF\,1}$ value satisfies the Scenario 1 condition, then the $P_{EqSG_i}^{4,OPF\,1}$ value is within the allowed range of real power output of the *i*-th equivalent SG representing k_2 number of units (according to (6.23), the $P_{EqSG_i}^{4,OPF\,1}$ value is below the maximum real power limit in MW of the *i*-th equivalent SG representing k_2 number of units), and the final number of units in service in the *i*-th SG plant for the given hour is k_2; otherwise the following step of the procedure related to Scenario 2 is carried out.

Block {5} in Figure 6.6: Given that the $P_{EqSG_i}^{4,OPF\,1}$ value satisfies Scenario 2 condition, (i.e., expression (6.25)), it is necessary to calculate differences ΔP_{k_1} and ΔP_{k_2} shown in Figure 6.7 (b) as follows:

$$\Delta P_{k_1} = P_{EqSG_i}^{4,OPF\,1} - P_{EqSG_i}^{max,k_1}, \tag{6.26}$$

$$\Delta P_{k_2} = P_{EqSG_i}^{min,k_2} - P_{EqSG_i}^{4,OPF\,1}, \tag{6.27}$$

where ΔP_{k_1} and ΔP_{k_2} represent the deviations of the $P_{EqSG_i}^{4,OPF\,1}$ value from the the maximum real power limit in MW of the *i*-th equivalent SG representing k_1 number of units and the minimum real power limit in MW of the *i*-th equivalent SG representing k_2 number of units, respectively.

Block {6} in Figure 6.6: The final stage of the procedure involves the comparison of ΔP_{k_1} and ΔP_{k_2} values, and the determination of the final number of units in service in the *i*-th SG plant for the considered hour during the day as follows:

$$N_{EqSG_i}^{FinUnit} = \begin{cases} k_1, & \Delta P_{k_1} \leq \Delta P_{k_2} \\ k_2, & \Delta P_{k_1} > \Delta P_{k_2} \end{cases}. \tag{6.28}$$

Given that the $P_{EqSG_i}^{4,OPF\,1}$ output value is outside the ranges of real power production of the *i*-th equivalent SGs representing k_1 and k_2 units (as seen in Figure 6.7 (b)), adopting k_1 or k_2 number of units in service indicates that the *i*-th equivalent SG will not be able to produce the $P_{EqSG_i}^{4,OPF\,1}$ output value. The second OPF, which recalculates the power outputs of equivalent SGs according to the established capacity values, will force the power dispatch of the *i*-th equivalent SG to be within the real power limits for the chosen number of units in service, meaning the final dispatch of the *i*-th equivalent SG will be either reduced (in the case of the chosen k_1 number of units) or increased (in the case of the chosen k_2 number of units) compared to the $P_{EqSG_i}^{OPF\,1}$ value. The final SG dispatch deviates from the actual optimal economic SG dispatch by making a choice between the closest higher or smaller integer number of units in (6.28) (i.e., by choosing between the k_1 and k_2 number of units). It should be noted that the procedure does not seek to provide the dispatch resulting in the absolute minimum of the total SG production cost but it uses engineering judgment to identify a generation schedule that is close to the true optimal economic SG dispatch.

For clarity, a numerical example of selecting the number of units in service in the *i*-th SG plant is provided here. The parameters of individual units in the plant are:

$S_{unit,EqSG_i^j}$=120 MVA, $Reserve_{unit,EqSG_i^j}$=0.15 p.u., $PF_{nom,unit,EqSG_i^j}$=0.9, and $p^{min}_{unit,EqSG_i^j}$=0.55 p.u.. According to (6.6), the maximum real power limit in p.u. for individual units is:

$$p^{max}_{unit,EqSG_i^j}=(1-0.15)\cdot 0.9 = 0.76 \text{ p. u.}. \tag{6.29}$$

The ranges of real power production in MW of the *i*-th equivalent SG for (1-4) number of units in service are calculated according to (6.10) and (6.11):

$$P_{EqSG_i}^{min,N^{unit}_{EqSG_i}} = N^{unit}_{EqSG_i}\cdot p^{min}_{unit,EqSG_i^j}\cdot S_{unit,EqSG_i^j} = N^{unit}_{EqSG_i}\cdot 0.55\cdot 120 = N^{unit}_{EqSG_i}\cdot 66, \tag{6.30}$$

$$P_{EqSG_i}^{max,N^{unit}_{EqSG_i}} = N^{unit}_{EqSG_i}\cdot p^{max}_{unit,EqSG_i^j}\cdot S_{unit,EqSG_i^j} = N^{unit}_{EqSG_i}\cdot 0.76\cdot 120 = N^{unit}_{EqSG_i}\cdot 91.2, \tag{6.31}$$

where $N^{unit}_{EqSG_i}$ is varied from one to four, and the following values are obtained (blue bars in Figure 6.8 illustrate these ranges.):

$$\begin{aligned} N^{unit}_{EqSG_i} &= 1 \quad \rightarrow \quad (66-91.2)\text{ MW} \\ N^{unit}_{EqSG_i} &= 2 \quad \rightarrow \quad (132-182.4)\text{ MW} \\ N^{unit}_{EqSG_i} &= 3 \quad \rightarrow \quad (198-273.6)\text{ MW} \\ N^{unit}_{EqSG_i} &= 4 \quad \rightarrow \quad (264-364.8)\text{ MW} \end{aligned} \tag{6.32}$$

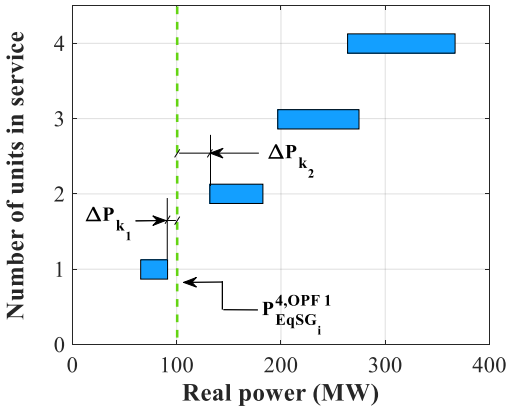

Figure 6.8 The illustration of the selection of the number of units in service in an SG plant

Let assume that the power dispatch of the *i*-th equivalent SG obtained in the first OPF (the $P^{4,OPF\ 1}_{EqSG_i}$ value) is 100 MW marked by green dashed line in Figure 6.8. According to (6.14) and (6.15), the minimum operational capacity of the *i*-th equivalent SG and the preliminary number of units in service in the *i*-th SG plant are:

$$S_{EqSG_i,MinOp} = \frac{P_{EqSG_i}^{4,OPF\,1}}{p_{EqSG_i}^{max}} = \frac{P_{EqSG_i}^{4,OPF\,1}}{p_{unit,EqSG_i^j}^{max}} = \frac{100}{0.76} = 131.58 \text{ MVA}, \quad (6.33)$$

$$N_{EqSG_i}^{PrelimUnit} = \frac{S_{EqSG_i,MinOp}}{S_{unit,EqSG_i^j}} = \frac{131.58}{120} = 1.1. \quad (6.34)$$

Given that the $N_{EqSG_i}^{PrelimUnit}$ is not an integer, k_1 and k_2 values have to be computed:

$$k_1 = \lfloor N_{EqSG_i}^{PrelimUnit} \rfloor = 1, \quad (6.35)$$

$$k_2 = \lceil N_{EqSG_i}^{PrelimUnit} \rceil = 2. \quad (6.36)$$

Following this, Scenario 1 is considered, i.e., the $P_{EqSG_i}^{4,OPF\,1}$ value, 100 MW, is compared with the minimum real power limit in MW of the *i*-th equivalent SG representing two (k_2) units ($P_{EqSG_i}^{min,k_2}$), which is equal to 132 MW (see (6.32)). Given that the $P_{EqSG_i}^{4,OPF\,1}$ value (100 MW) is smaller than the $P_{EqSG_i}^{min,k_2}$ value (132 MW), the $P_{EqSG_i}^{4,OPF\,1}$ value satisfies Scenario 2 condition (6.25), and the differences ΔP_{k_1} and ΔP_{k_2} have to be calculated using (6.26) and (6.27):

$$\Delta P_{k_1} = P_{EqSG_i}^{4,OPF\,1} - P_{EqSG_i}^{max,k_1} = 100 - 91.2 = 8.8 \text{ MW}, \quad (6.37)$$

$$\Delta P_{k_2} = P_{EqSG_i}^{min,k_2} - P_{EqSG_i}^{4,OPF\,1} = 132 - 100 = 32 \text{ MW}. \quad (6.38)$$

The $P_{EqSG_i}^{max,k_1}$ value is the maximum real power limit in MW of the *i*-th equivalent SG representing a single unit and is equal to 91.2 MW according to (6.32).

Given that $\Delta P_{k_1} < \Delta P_{k_2}$ holds, the final number of units in service in the *i*-th SG plant is one according to (6.28). This indicates that the final power output of the *i*-th equivalent SG defined by the second OPF will be limited to 91.2 MW (the maximum real power limit of the *i*-th equivalent SG representing a single unit), i.e., the *i*-th equivalent SG will not be able to provide the value of 100 MW obtained in the first OPF.

As described, the first OPF defines the minimum required number of units in operation for each SG plant, which in turn provides new rated capacities for all equivalent SGs

($N_{EqSG_i}^{FinUnit} \cdot S_{unit,EqSG_i}$) in the test network. The second OPF then recalculates the power outputs of the equivalent SGs remained in service after the first OPF calculation, and provides the final dispatch of all equivalent SGs in the network. The mathematical formulation of the second OPF problem is analogous to (6.13), with the rated capacities of equivalent SGs defined based on the first OPF results and actual minimum real power limits of equivalent SGs:

$$
\begin{gathered}
min \sum_{i=1}^{N_{EqSG}} Cost_{EqSG_i} = min \sum_{i=1}^{N_{EqSG}} \left(a_i \left(P_{EqSG_i}^{N_{EqSG_i}^{FinUnit},OPF\,2} \right)^2 + b_i P_{EqSG_i}^{N_{EqSG_i}^{FinUnit},OPF\,2} + c_i \right) \\
P_k - P_{gk} + P_{dk} = 0, k = 1, \dots, N_{bus}, \\
P_k = V_k \sum_{l=1}^{N_{bus}} V_l Y_{kl} \cos(\theta_k - \theta_l - \psi_{kl}), k = 1, \dots, N_{bus}, \\
Q_k - Q_{gk} + Q_{dk} = 0, k = 1, \dots, N_{bus}, \\
Q_k = V_k \sum_{l=1}^{N_{bus}} V_l Y_{kl} \sin(\theta_k - \theta_l - \psi_{kl}), k = 1, \dots, N_{bus}, \\
P_{EqSG_i}^{min,N_{EqSG_i}^{FinUnit}} \le P_{EqSG_i}^{N_{EqSG_i}^{FinUnit},OPF\,2} \le P_{EqSG_i}^{max,N_{EqSG_i}^{FinUnit}}, i = 1, \dots, N_{EqSG}, \\
Q_{EqSG_i}^{min,N_{EqSG_i}^{FinUnit}} \le Q_{EqSG_i}^{N_{EqSG_i}^{FinUnit},OPF\,2} \le Q_{EqSG_i}^{max,N_{EqSG_i}^{FinUnit}}, i = 1, \dots, N_{EqSG}, \\
\sqrt{\left(P_{EqSG_i}^{N_{EqSG_i}^{FinUnit},OPF\,2} \right)^2 + \left(Q_{EqSG_i}^{N_{EqSG_i}^{FinUnit},OPF\,2} \right)^2} \le S_{EqSG_i}^{N_{EqSG_i}^{FinUnit}}, i = 1, \dots, N_{EqSG}, \\
V_k^{min} \le V_k \le V_k^{max}, k = 1, \dots, N_{bus}, \\
Line_{loading,m} \le Line_{loading,m}^{max}, m = 1, \dots, N_{line}, \\
TR_{loading,n} \le TR_{loading,n}^{max}, n = 1, \dots, N_{TR},
\end{gathered}
\qquad ,(6.39)
$$

where: $P_{EqSG_i}^{N_{EqSG_i}^{FinUnit},OPF\,2}$ and $Q_{EqSG_i}^{N_{EqSG_i}^{FinUnit},OPF\,2}$ are the real and reactive power output values of the *i*-th equivalent SG representing $N_{EqSG_i}^{FinUnit}$ units that are obtained from the second OPF, respectively, $P_{EqSG_i}^{min,N_{EqSG_i}^{FinUnit}}$ and $P_{EqSG_i}^{max,N_{EqSG_i}^{FinUnit}}$ is the minimum and maximum real power limit in MW of the *i*-th equivalent SG representing $N_{EqSG_i}^{FinUnit}$ units, respectively, $Q_{EqSG_i}^{min,N_{EqSG_i}^{FinUnit}}$ and $Q_{EqSG_i}^{max,N_{EqSG_i}^{FinUnit}}$ is the minimum and maximum reactive power limit in Mvar of the *i*-th equivalent SG representing $N_{EqSG_i}^{FinUnit}$ units, respectively, $S_{EqSG_i}^{N_{EqSG_i}^{FinUnit}}$ is the rated capacity of the *i*-th equivalent SG representing $N_{EqSG_i}^{FinUnit}$ units. The values of real and reactive power limits are calculated using (6.5) – (6.11) for the $N_{EqSG_i}^{FinUnit}$ number of units ($N_{EqSG_i}^{unit} = N_{EqSG_i}^{FinUnit}$), while the $S_{EqSG_i}^{N_{EqSG_i}^{FinUnit}}$ is defined based on (6.3) for $N_{EqSG_i}^{FinUnit}$ units in service. As in the case of the first OPF, the constraints for all bus voltage magnitudes are 0.9 p.u. and 1.1 p.u., and the maximum allowed line and transformer loading is 100%.

Following the two-step OPF calculation, the pre-disturbance operating conditions of all elements in the network are defined. Then, system stability simulations are performed in DIgSILENT/PowerFactory software. Transient system stability is assessed through electromechanical simulations (block {6} in Figure 6.4). Three-phase self-clearing short-circuit faults at the middle of all transmission lines are simulated for each system operating point (i.e., each hour in the analysed TS). Three-phase faults are chosen as they usually result in the most severe system conditions [182]. A single type of short-circuit faults is considered as the objective of the study is to establish whether the variation in spatial HRES plant composition for the same total HRES plant power output affects transient stability performance of the system and the change in fault type should not have a significant influence on the results of the comparative analysis. The duration of all faults is 100 ms. For each transient system stability simulation, TSI value is calculated according to expression (4.3) given in Section 4.2.3, which is repeated below for clarity:

$$TSI = \frac{360° - \delta_{max}}{360° + \delta_{max}} \cdot 100\%, \tag{6.40}$$

where δ_{max} is the maximum difference between rotor angles of any two SGs in the network at the same time instance.

6.3.2.3 Part III

The third part of the procedure involves statistical analysis of the obtained TSI values (block {9} in Figure 6.4). For each hour in the TS, the non-parametric kernel PDF is estimated on the basis of the TSI values for the given hour:

$$\hat{f}_h(x) = \frac{1}{N_F \cdot h} \sum_{i=1}^{N_F} K\left(\frac{x - x_i}{h}\right), \tag{6.41}$$

where $\hat{f}_h(x)$ is the kernel density estimate of the unknown PDF *f*, *x* is a random variable (TSI), N_F is the number of faults simulated for the given hour, *K* is the non-negative kernel function with the integral equal to one, x_i is the TSI value for the *i*-th short-circuit fault, and *h* is a bandwidth.

The normal distribution with zero mean and standard variance of one is adopted as a kernel function in the study as it is the most widely used [140]. When it comes to the

bandwidth, the optimal value of the parameter *h* is defined using the solve-the-equation plug-in method as it demonstrated the best performance among a range of bandwidth estimation techniques [194]. Detailed description of the solve-the-equation plug-in method is provided in Section 4.2.3.1.

Given that a large number of three-phase short-circuit faults is simulated for each hour in the TS, the most probable TSI value (according to the estimated kernel PDF) is defined for each hour (block {10} in Figure 6.4), and then used as a representative TSI for the given hour in the further analysis. Defining the representative TSI for each hour in the TS results in a set of 24 representative TSIs that provides the information about hourly variation in the transient stability status of the system.

6.3.2.4 Part IV

The first three parts of the procedure are focused on generating system operating conditions and carrying out daily transient stability assessment of the system, while Part IV analyses the influence of RES power distribution across the network (i.e., spatial HRES plant composition) on the transient stability performance of the system. In order to investigate if, and under which conditions, the selection of spatial HRES plant composition for a particular total HRES plant power output becomes relevant for transient stability behaviour of the system, groups of system operating conditions characterized by similar total HRES plant production and total system demand are identified first (block {11} in Figure 6.4). Similarity in the total HRES plant power output and system load is necessary in order to decouple the impact of HRES plant production and system demand on TSI value from the influence of RES power distribution across the network. Following the identification of the relevant groups of operating points, representative TSI values for operating points in the same group are compared to assess the correlation between spatial HRES plant composition and transient stability status of the system (block {12} in Figure 6.4).

6.3.3 Test Scenarios

Three TSs involving different system loading levels and RES states are defined to reflect realistic system operation and shown in Table 6.1. The maximum and minimum system loading corresponds to a system operating condition in winter and summer of 2017, respectively, and the corresponding system loading curves are illustrated in Figure 6.9

[196]. Both RES states from Table 6.1 are designed according to the information about the location and rated capacity of existing and future RESs reported by the respective TSOs and their more detailed description is provided in Table 6.2.

Table 6.1 Test scenarios

Scenario number	System loading level	RES state
TS 1	Maximum loading	Current RES
TS 2	Maximum loading	Future RES
TS 3	Minimum loading	Future RES

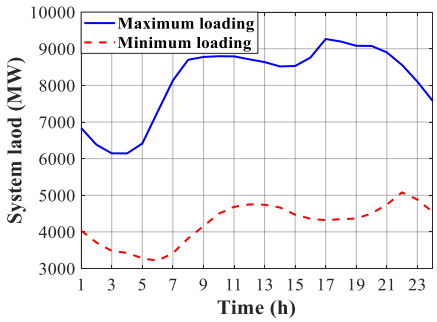

Figure 6.9 Maximum (blue solid) and minimum (red dashed) system loading curves

Table 6.2 Detailed description of RES states

RES state	Number of WFs	Total WF capacity (MW)	Number of PV plants	Total PV capacity (MW)
Current	17	1,190	0	0
Future	21	7,438	11	470

RES plants included in the Current RES state are marked by blue wind turbine symbols in Figure 6.2, while WFs and PV plants planned to be installed in the future are represented by orange wind turbine and orange PV panel symbols, respectively, in Figure 6.2. A less detailed diagram of the test system indicating spatial distribution of RES power plants over four areas in both Current and Future RES state is shown in Figure 6.10 (RES plants are marked as "*RESx*", where *x* is a number from 1 to 17 and from 1 to 32 in the case of the Current and Future RES state, respectively).

RES state at present, i.e., the Current RES state in Table 6.1 and Table 6.2, includes 17 WFs (no PV plants among the installed RESs). The total installed WF capacity at present is 1,190 MW (Area 1: 168 MW, Area 2: 86 MW, Area 3: 374 MW, Area 4: 562 MW), which is 9.4% of the installed SG capacity. Considering future network development, the installation capacity of the existing WFs will increase, WFs at new locations will be installed, and a number of PV plants will be connected to the system. Therefore, the

Future RES state, as referred to in this study, will include 21 WFs and 11 PV plants, with the total installed capacity of 7,908 MW (62.4% of the installed SG capacity). The WF installation capacity in the Future RES state per area is: Area 1: 1,112 MW, Area 2: 86 MW, Area 3: 5,192 MW, and Area 4: 1,048 MW. When it comes to PV plants, nine out of eleven PV plants are to be installed in Area 4 with the total capacity of 300 MW, while Area 1 and Area 3 are going to contain a 100 MW and a 70 MW PV plant, respectively.

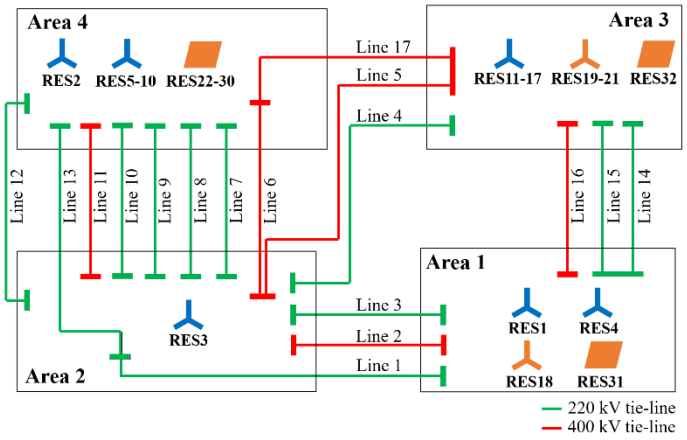

Figure 6.10 The less detailed schematic diagram of the test system indicating RESs per area (blue wind turbine symbols are RES plants at present; orange wind turbine and PV panel symbols are WFs and PV plants to be installed in the future, respectively)

6.4 Results and Discussion

At each hour of the three considered TSs, the power production of RES power plants was defined in a probabilistic manner as described in Section 6.3.2.1. RES penetration level at each hour of the TSs is calculated as follows:

$$RES_{Level,i}(\%) = 100 \cdot \frac{P_{HRES_i}}{P_{Load_i}}, \tag{6.42}$$

where $RES_{Level,i}$ is the RES penetration level at the *i*-th hour, P_{HRES_i} and P_{Load_i} is the total HRES plant production and the total system load at the *i*-th hour, respectively. RES penetration level per hour for the analysed TSs is presented in Figure 6.11. As can be seen, the average RES penetration level for TS 1-3 is about 10%, 30%, and 60%, respectively.

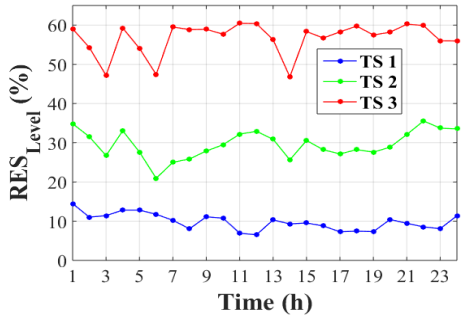

Figure 6.11 RES penetration level per hour in TS 1 (blue), TS 2 (green) and TS 3 (red)

The two-step OPF procedure described in Section 6.3.2.2.1 is conducted at each hour during the day for all three TSs. Table D.1 – Table D.3 given in Appendix D provide the information about the number of SG units in service per hour in all three TSs (assuming that each of 42 SG plants in the test system contains four identical units). Table 6.3 gives an overview of these data in terms of the range of the number of SG units in operation during the day for the whole test system and each of the four individual areas. As expected, the number of units in service in TS 3 is the smallest over all TSs. For most of the hours during the day, the number of units in service in the whole system in TS 3 is around a half of the corresponding value in TS 1. When it comes to the individual areas in the system, the ratio of the number of units in operation in TS 3 and TS 1 is about 25%, 50%, 50%, and 35% for Area 1, Area 2, Area 3, and Area 4, respectively.

Table 6.3 The range of the number of units in service during the day for all three TSs

Scenario	The whole system	Area 1	Area 2	Area 3	Area 4
TS 1	(106 - 144)	(13 - 16)	(27 - 43)	(37 - 51)	(29 - 34)
TS 2	(95 - 126)	(10 - 14)	(25 -38)	(39 - 49)	(21 - 27)
TS 3	(48 - 66)	(3 - 5)	(13 - 19)	(21 - 31)	(4 - 11)

Following probabilistic determination of the power outputs of RES plants and equivalent SGs in the test network, 24-hour transient system stability assessment is performed for each of the three TSs. The kernel PDF is estimated using the obtained TSIs (200 TSI values per hour), and the most probable TSI value is defined for each hour in the TSs. Figure 6.12 shows the change of TSI during the day for three TSs in order to show the overall transient system behaviour. In order to simplify the representation of the results, TSI values presented in Figure 6.12 are the most probable (representative) TSI values for each hour in the TSs. All simulated cases were transiently stable, and no cases of slow-interaction converter-driven instability were identified. According to Figure 6.12, the TSI

calculated under TS 1 and TS 2 remains high and reasonable constant during the day (over 70 most of the time), while TSI exhibits greater variations in TS 3 with the largest drop in TSI value observed at hours 4:00, 19:00 and 21:00 (at these hours RES energy injected into the system from Area 3 is at least seven times larger than RES production in Area 1, and RES13 in Area 3 has the largest power output (see Figure 6.13 for the location of RES13 in the test system)).

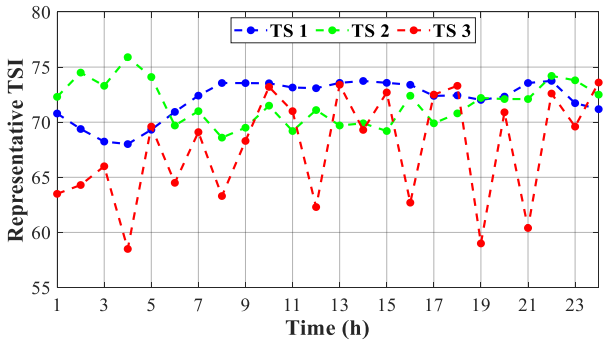

Figure 6.12 Representative TSI values for each hour in the TSs

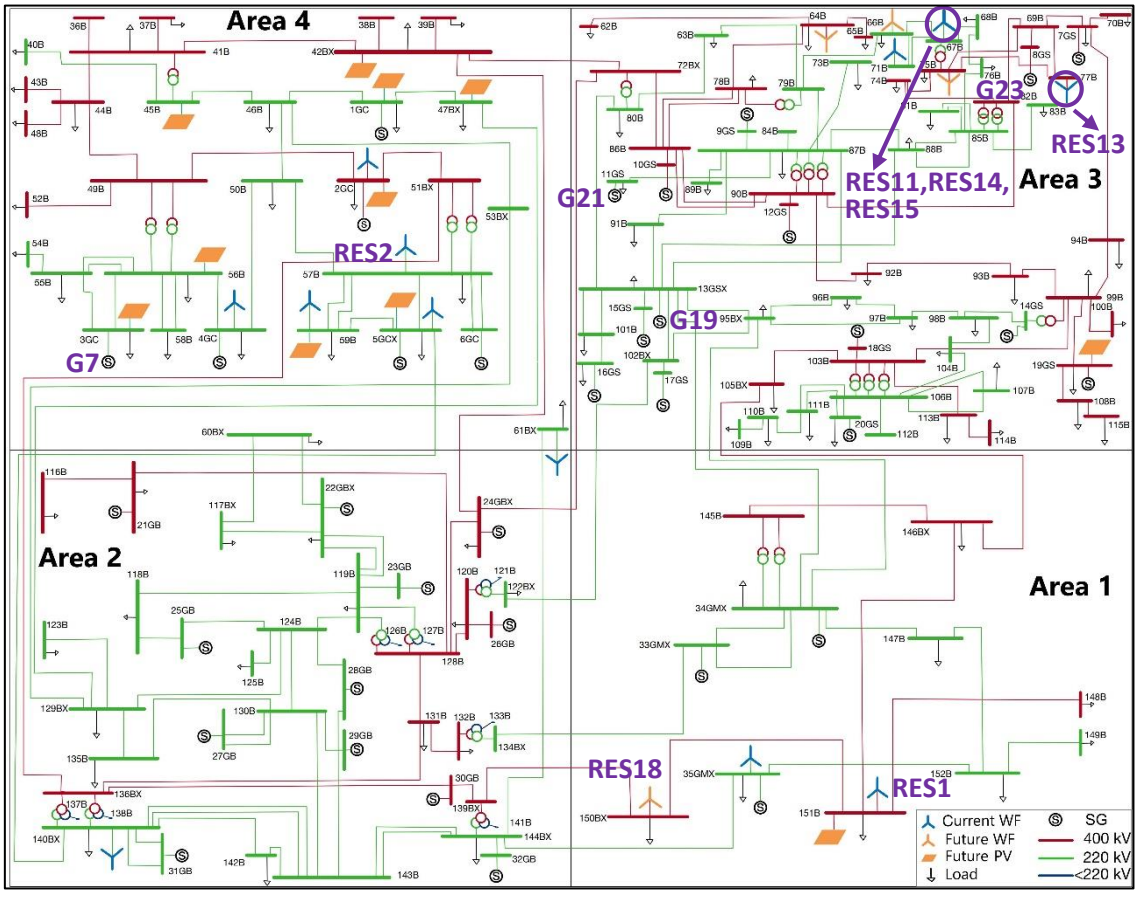

Figure 6.13 The schematic diagram of the test system with the specified locations of relevant SGs and RESs

In order to investigate the influence of spatial HRES plant composition on transient system stability performance, in each TS, hours with similar total HRES plant production and total system demand are identified using visual inspection and representative TSIs for hours in the same group are compared. Groups of operating points characterized by similar total HRES plant power output and system demand in TS 1, TS 2 and TS 3 are given in Table 6.4, Table 6.5 and Table 6.6, respectively. (*Note*: In Table 6.4 - Table 6.6, "*Share_x*" represents the participation of RES production in Area *x* in the total HRES plant power output ($\sum_{x=1}^{4} Share\_x = 100\%$), while the TSI values correspond to the most probable TSI values for the chosen hours). Given that there is a single RES plant in Area 2 in both RES states, the participation of Area 2 in the total HRES plant production is significantly smaller compared to the other three areas. The maximum Share_2 value for the selected operating points from TS 1 is 12.5%, whereas no more than 3.3% of the total HRES plant output is produced in Area 2 at the selected hours in TS 2 and TS 3. RES penetration level for all selected operating conditions in Table 6.4, Table 6.5 and Table 6.6 is around 10%, 30%, and 60%, respectively.

Table 6.4 Selected operating points from TS 1

Group	Hour	TSI	P_{HRES} (MW)	P_{LOAD} (MW)	Share_1 (%)	Share_2 (%)	Share_3 (%)	Share_4 (%)
1	9:00	73.5	976	8776	8.4	4.3	34.0	53.3
	10:00	73.5	948	8797	12.9	1	32.5	53.6
2	11:00	73.1	610	8792	19.0	2.7	36.7	41.6
	12:00	73.1	570	8712	19.6	9.2	31.9	39.3
3	14:00	73.7	792	8518	13.6	9.9	32.8	43.7
	15:00	73.6	814	8530	16.5	2	28.7	52.8
	22:00	73.7	832	8556	7.9	11.5	37.4	43.2
4	17:00	72.4	676	9266	21.9	12.4	24.3	41.4
	18:00	72.4	686	9197	9.6	12.6	26.8	51.0

Table 6.5 Selected operating points from TS 2

Group	Hour	TSI	P_{HRES} (MW)	P_{LOAD} (MW)	Share_1 (%)	Share_2 (%)	Share_3 (%)	Share_4 (%)
1	9:00	71	2448	8776	10.0	3	61.8	25.2
	16:00	72.7	2472	8759	14.6	1.6	69.2	14.6
2	11:00	69	2832	8792	34.1	3	40.3	22.6
	12:00	71	2868	8712	10.8	3	50.3	35.9
3	17:00	69.5	2516	9266	32.4	2	47.1	18.5
	18:00	70.5	2598	9197	13.8	2.9	60.4	22.9

As seen in Table 6.4 and Table 6.5, there is basically no difference between the representative TSI values for hours within the same group for TS 1 and TS 2. This is expected given that the maximum variation in representative TSI values over the whole day is only 6 in TS 1 (the difference between TSI values at 22:00 h and 4:00 h (Figure 6.12)) and 7 in TS 2 (the difference between TSI values at 4:00 h and 8:00 h (Figure 6.12)).

When it comes to RES distribution across the network, the operating points within Group 3 and 4 in TS 1, and Group 2 and 3 in TS 2 are characterized by more considerable differences in spatial HRES plant composition compared to the remaining groups from the relevant TS. Namely, in Group 3 in TS 1, the amount of RES power produced in Area 3 is around 5 times larger than the RES production in Area 1 at 22:00 h, whereas this ratio reduces to 2.4 and 1.7 at 14:00 h and 15:00 h, respectively. Similarly, in Group 4 in TS 1, the RES production in Area 4 is almost twice the production in Area 1 at 17:00 h, and the ratio increases to around five at 18:00 h, while the RES shares of Area 2 and 3 are almost identical at both hours in Group 4. Given that RES penetration level is around 10% for the selected hours from TS 1, change in RES power distribution across the network has negligible effect on the optimal economic dispatch of SGs. The maximum difference between SG power outputs for the hours within any group is below 1% of the total SG production.

When it comes to Groups 2 and 3 in TS 2, similar amount of RES power is produced in Areas 1 and 3 at 11:00 h and 17:00 h from Group 2 and Group 3, respectively, while RES power in Area 1 corresponds to about 20% of RES power in Area 3 at the other operating point form the relevant group. In addition, the ratio of the RES share of Area 4 and Area 1 at 11:00 h (Group 2) and 17:00 h (Group 3) is about 5 and 3 times smaller, respectively, than at the other hour from the same group.

Unlike in TS 1, larger differences in the SG dispatch at hours in the same group can be observed. The maximum difference in the rated capacity values of SGs in service for hours in the same group corresponds to around 3.5%, 2.6% and 8.5% of the total capacity of the committed SGs for Group 1, 2, and 3, respectively. When it comes to the real power production of individual SGs, the maximum difference for Group 1, 2 and 3 is about 3.3%, 1.9%, and 8.5%, respectively, of the total SG production in the network. Still, the maximum rotor angle difference occurs between the same SGs (G7 in Area 4

and G21 in Area 3 (see Figure 6.13 for the locations of G7 and G21 in the test system)) for all selected operating points in Table 6.5. The rated capacity values of G7 and G21 are the same for all hours given in Table 6.5.

Finally, three groups with three time samples can be used for analysing the impact of spatial HRES plant composition on the global transient system stability status in TS 3 (see Table 6.6).

Table 6.6 Selected operating points from TS 3

Group	Hour	TSI	P_{HRES} (MW)	P_{LOAD} (MW)	Share_1 (%)	Share_2 (%)	Share_3 (%)	Share_4 (%)
1	10:00	73.2	2594	4496	30.8	0.2	48.7	20.3
	15:00	72.7	2608	4469	25.9	1.3	46.0	26.8
	20:00	70.9	2620	4504	26.4	0.2	55.8	17.6
2	11:00	71	2832	4684	34.1	3	40.3	22.6
	12:00	62.3	2868	4750	10.8	3	50.3	35.9
	21:00	60.4	2858	4745	6.5	2.3	62.9	28.3
3	16:00	62.7	2472	4359	14.6	1.6	69.2	14.6
	17:00	72.5	2516	4319	32.4	2	47.1	18.5
	19:00	59	2508	4363	9.3	3.3	68.1	19.3

Hours from Group 1 (10:00, 15:00, and 20:00) result in similar representative TSI. As for RES distribution across the network at these hours, the maximum difference between the RES shares of Area 1, Area 3 and Area 4 is approximately 5%, 10%, and 9%, respectively. Furthermore, the RES power plant with the largest power production is in Area 1 at hours 10:00 and 20:00 (RES18 and RES1, respectively, which are geographically close to each other), while the "dominant" RES (RES2) is located in Area 4 at 15:00 h (see Figure 6.13 for the locations of RES18, RES1 and RES2 in the test system). However, the RES plant with the second largest power output at 15:00 h (RES18) is located in Area 1, and the difference between the top two RES outputs at this hour is only 38 MW (approximately 1.5% of the total HRES plant production at 15:00 h). The optimal economic dispatch of SGs at 10:00 h and 20:00 h is almost identical (the maximum difference between real power outputs of SGs is around 3 MW). The only difference in the sets of SGs in service at these two hours and at 15:00 h is in a single SG plant (G19) in Area 3 (see Figure 6.13 for the location of G19 in the test system) with the rated capacity of 40 MVA, which is not in operation at 15:00 h. Still, the real power

production for other SGs in service (i.e., all SGs except G19) is similar with the maximum difference of about 3.5 MW.

On the other hand, the impact of spatial HRES plant composition on the most probable TSI values can be observed for operating conditions from Groups 2 and 3. Hours 11:00 (Group 2) and 17:00 (Group 3) with the transient stability status different from other operating points in the relevant group are shaded in Table 6.6. These hours are associated with higher TSI value (71 and 72.5 at 11:00 h and 17:00 h, respectively) compared to other hours within their respective groups (the representative TSI value for these operating conditions is about 60). When it comes to HRES plant composition, the main differences are in RES distribution across Area 1 and Area 3. Namely, the ratio of RES power provided by Area 3 and Area 1 is 1.2 at 11:00 h (Group 2) and 1.4 at 17:00 h (Group 3), whereas the Share_3 value is at least 4.5 times larger than the Share_1 value in the case of other operating points from Groups 2 and 3. Spatial HRES plant compositions for characteristic hours (i.e., a pair of hours characterized by different representative TSI values) from Groups 2 and 3 are illustrated in Figure 6.14 using dots of different colours and sizes. Hours 11:00 and 21:00 from Group 2 are shown in Figure 6.14 (a), whereas Figure 6.14 (b) presents hours 17:00 and 19:00 from Group 3. The sizes of the dots in Figure 6.14 reflect the RES share of individual areas in the total HRES plant production. In addition, the RES plant with the highest power output (RES1) is located in Area 1 at 11:00 h (Group 2) and 17:00 h (Group 3), whereas the highest individual RES plant production comes from Area 3 in the case of the remaining hours in Group 2 and 3 (the relevant plants are RES11, RES13, RES14 and RES15, all of them located in a geographically small region). Figure 6.13 provides the locations of RES1, RES11, RES13-15 in the test system.

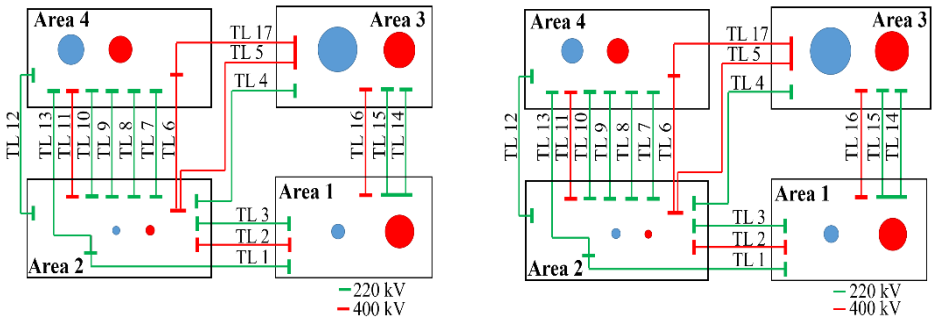

Figure 6.14 Illustration of spatial HRES plant compositions for characteristic hours from TS 3: (a): Group 2: 11:00 h (red) and 21:00 h (blue); (b): Group 3: 17:00 h (red) and 19:00 h (blue)

When it comes to the optimal economic dispatch of SGs at hours within Group 2, there is no significant difference in the SG commitment. The rated capacities of SGs in operation at 11:00 h and 12:00 h are the same, while the maximum difference between their real power outputs is below 5 MW. In addition, the maximum rotor angle difference occurs between the same generators: G7 in Area 4 and G23 in Area 3 (see Figure 6.13 for the locations of G7 and G23 in the test system). The main reason for better transient stability performance of the system at 11:00 h compared to the status at 12:00 h is highly underexcited operating mode of G7 at 12:00 h, which in turn results in high rotor angle value for this generator.

In the case of operating points in Group 3, the number of SGs with different rated capacity at 16:00 h and 17:00 h, 16:00 h and 19:00 h, 17:00 h and 19:00 h, is 7, 3, and 4, respectively. Even though the rated capacity of committed SGs at hours with similar representative TSI (i.e., 16:00 h and 19:00 h) is different for three generators, the difference in the real power output of these SGs is between 15 MW and 20 MW, that is, 0.8% and 1% of the total production of all SGs. The maximum difference between the real power production of the remaining SGs is below 7 MW. In addition, the maximum rotor angle difference at 16:00 h and 19:00 h occurs between the same pair of generators (G21 and G23, both in Area 3). On the other hand, the major difference between SG unit commitment at 17:00 h and the other two hours is in the capacity of G23 in Area 3. At 17:00 h G23 with two units in service (the total capacity of 410 MVA) is the largest SG in the network, whereas only one unit in G23 is in operation at 16:00 h and 19:00 h.

Therefore, the previous analysis demonstrated that the spatial HRES plant composition does not influence system transient stability in the case of low RES penetration levels (below 30% in analysed cases), however, in the case of higher penetration level of about 60% this impact becomes much more prominent. It can be concluded that the location and number of SGs in operation, as well as their power outputs, influenced by the location and output of RESs (i.e., spatial HRES plant composition) and total system demand, affect the transient stability of the power system with a high RES penetration level. The extent of this effect will depend on network and generation characteristics, generation location (both SGs and RESs), and most certainly on the level of penetration of RESs.

6.5 Summary

This chapter presented the analysis of the contribution of the geographically distributed HRES plant to the transient stability of a large interconnected TN. Three representative operation scenarios involving different combinations of the system loading and RES states were simulated over a 24-hour time period.

The RES distribution across the network (i.e., spatial HRES plant composition) does not influence the optimal economic SG dispatch, and consequently system transient stability in the case of low RES penetration levels. However, in the case of higher RES penetration level of about 60%, the transient stability status of the system becomes affected by the chosen HRES plant composition. Thus, it can be concluded that for any network there is a critical RES penetration level above which different spatial HRES plant compositions with the same total power output can result in different transient stability performance of the system, and in the cases of RES penetration above the critical value, the deployment of individual RES plants within the spatially distributed HRES plant should be decided after assessing overall system transient (and other) stability performance. The analysis on the impact of the selection of the spatially distributed HRES plant composition on the transient stability status of the system represents the fifth original contribution of the thesis.

Therefore, offering a service of controllable and stable power production to TSO may be very complicated if aggregator's portfolio includes RES plants that are widely geographically distributed. This may not be a problem from the perspective of transient stability of the system, as demonstrated, in case of low RES penetration, however, beyond certain "critical" level transient stability of the system might become a limiting factor and the conventional economic dispatch in these cases might lead to inadequate system dynamic performance. This implies that in cases of higher RES penetration the scheduling of individual HRES plant components would have to be carried out in a coordinated manner with the TSO as the information about the influence of HRES plant composition on the overall system stability would have to be considered. Given that is not likely that all RESs integrated into the TN belong to a single aggregator (as it was the case in the CS presented in this chapter), one would assume that several HRES plant aggregators at TN level would be present in the future. All aggregators will then be offering a VPP type of service to the TSO, and thus, will have to coordinate their

scheduling with the TSO. The required level of coordination between the system operator and aggregators will depend on the capacities of individual plants within HRES plants as well as their location in the system (i.e., whether they are located in a part of the network that is critical from the perspective of system dynamic performance). Including system stability limits in everyday management of a single spatially distributed HRES plant in the TN is already a considerable departure from the current economy-driven dispatch of generation units, and the increase in the number of HRES plants at TN level will only introduce additional complexities in the coordinated operation of the TSO and geographically widely distributed aggregators.

7 Conclusions and Further Work

7.1 Major Conclusions

The thesis has presented the results of the research carried out in the area of dynamic equivalent modelling of HRES plants and the area of geographically distributed HRES plant operation. The research aims involved the development of DEMs of HRES plant for annual transient stability studies from the perspective of the global transient stability status and the shape of plant power responses in time domain, as well as the exploratory analysis on the impact of geographically distributed HRES plant on the transient stability of the TN.

The following sections provide the main conclusions of the research presented in each of the chapters of this thesis.

7.1.1 Chapter 1 Introduction

The chapter presented the main research areas of the thesis, together with the critical overview of the relevant past work. The need for dynamic equivalent modelling of HRES plants, which represent a promising option for overcoming the issue of variability in power production of RESs, was discussed. The typical principles of HRES plant design and operation were presented. Different approaches for dynamic equivalent modelling of power plants and networks were analysed. Furthermore, the need for taking into account system dynamic performance when deciding on the dispatch of individual plants within a geographically widely distributed HRES plant was introduced. Finally, the main aims

and objectives as well as the contributions of the research presented in the thesis were specified.

7.1.2 Chapter 2 Techniques for Dynamic Equivalent Modelling of Power Plants and Networks

This chapter provided a comprehensive overview of the techniques for developing DEMs of power systems. Modal analysis-, coherency- and system identification-based methods represent the main approaches for dynamic equivalent modelling of power plants and networks. System identification-based methods were found to be the most adequate for equivalent modelling of modern plants/networks as they rely on the measured or simulated system responses, and thus, are not technology-dependent.

Due to ever growing proliferation of measurement devices in power systems, the need for the application of data analytics techniques in power system operation and control has arisen. The chapter presented a review of clustering algorithms, which represent one of the most widely used unsupervised data mining methods. The main stages in the clustering process, together with the main characteristics of five major categories of clustering algorithms, were described. The suitability of each type of clustering methods for clustering static and time series data as well as large datasets was discussed. In addition, the chapter addressed common challenges in performing data clustering (the choice of the number of clusters and distance metric, high dimensionality of time series data).

7.1.3 Chapter 3 Probabilistic Analysis and Modelling of HRES Plant for System Stability Studies

The third chapter of the thesis introduced the computationally efficient procedure for determining the most probable impact of HRES plant on power system stability throughout the year. The procedure relies on the identification of typical annual HRES plant compositions on the basis of historical plant production dataset and the clustering algorithm. System stability results, produced by probabilistic MC approach based on characteristic annual plant compositions, are divided into groups according to similarity, and these groups represent the outputs of the procedure. The groups of system stability results provide the information about the most probable influence of the HRES plant on

power system stability during the year, and enable the identification of HRES plant compositions characterized by similar performance in system stability studies. The methodology was tested on the HRES plant with six generation and storage technologies and connected to the external grid represented by an infinite bus (small-disturbance, transient and long-term voltage stability) or a single SG (frequency stability). *Development of the methodology for identifying typical annual impact of HRES plant on power system stability performance represents the first original contribution of the thesis.*

The chapter also provided procedures for developing preliminary EMs of HRES plant for small-disturbance, transient, frequency and long-term voltage stability studies. EM development relies on the information about the typical annual performance of the HRES plant in the given system stability studies. EM for small-disturbance stability is in the form of a TF (a black-box model), whereas EMs for the remaining three stability studies are in the form of an equivalent SG or WF (a grey-box model). The results obtained in the CS (the same CS as the one used for demonstrating the procedure for identifying typical annual HRES plant performance in system stability simulations) are promising in terms of the model order and number of equivalents required for representing the HRES plant behaviour in system stability analysis throughout the year. *The procedures for developing preliminary EMs of HRES plant for small-disturbance, transient, frequency and long-term voltage stability studies represent the second original contribution of the thesis.*

7.1.4 Chapter 4 Data-driven Equivalent Modelling of HRES Plant for Power System Transient Stability Studies

In this chapter the methodology for dynamic equivalent modelling of HRES plants for transient stability studies from the perspective of the overall transient stability status was developed. The TSI value was chosen for describing the global transient stability performance of the system, and consequently for assessing model accuracy. The DEM structure corresponds to a low-order TF with voltage magnitude and power at the PCC as input and output, respectively (separate TFs were developed for real and reactive power responses). *The methodology for developing DEMs of HRES plants for transient stability studies from the perspective of the overall transient stability assessment represents the third original contribution of the thesis.*

The proposed methodology is based on characteristic annual HRES plant compositions and TN short-circuit fault statistical data, which in turn provides a set of models capable of representing the most probable dynamic HRES plant behaviour in annual transient stability simulations. In addition, these key features of the proposed methodology are the reason for the low computational burden of transient stability analysis when applying developed DEM. HRES plant power responses resulting in similar TSI were simulated by a common model regardless of dissimilarities in their shape in time domain. The presented DEMs are attractive for practical application as the choice of the model from the previously defined set of equivalents at any time of the year is determined only by HRES plant operating scenario. It was found that the duration of historical data recording period, the sampling rate of the historical production dataset and missing production data of individual plants within the HRES plant do not have a significant effect on DEM performance. The chapter also proposed the technique for overcoming the unavailability of historical data of individual technologies.

In both CSs presented in the chapter, small number of equivalents were required for modelling the whole HRES plant in annual transient stability studies, and they resulted in low TSI error when tested on a wide range of system operating conditions and TN short-circuit faults. A comparative analysis showed that the developed DEMs are characterized by higher TSI accuracy than the "negative" constant power load model commonly used for representing RESs in dynamic simulations. Furthermore, the DEMs demonstrated satisfactory performance in terms of the accuracy of the shape of real and reactive power responses at the PCC in time domain, even though the focus of model development was not on obtaining accurate HRES plant power responses.

7.1.5 Chapter 5 Deep Learning-based Equivalent Modelling of HRES Plant for Power System Transient Stability Studies

This chapter represents a further evaluation of the models described in Chapter 4. It presented the methodology for dynamic equivalent modelling of HRES plants for transient stability studies with the focus on the shape of time domain HRES plant power responses. The proposed DEM is in the form of LSTM network (a deep ANN) with real and imaginary part of the positive sequence voltage at the PCC, and real and reactive power at the PCC as inputs and outputs, respectively. As in the case of the methodology

described in Chapter 4, the historical HRES plant production dataset, TN short-circuit fault statistics, and the clustering algorithms are the main characteristics of the modelling procedure.

The most probable HRES plant power responses in annual transient stability simulations were clustered according to their similarity in time, and an LSTM network was designed for each cluster. Automatic identification of the optimal LSTM network structure and efficient training of LSTM network on a large cluster of responses ensure a computationally efficient modelling procedure. The presented methodology results in few models suitable for representing the whole HRES plant in transient stability studies throughout the year. The methodology also incorporates the procedure that enables the selection of the most adequate DEM at any time of the year using the information about HRES plant operating scenario only, which makes the proposed methodology suitable for practical applications.

The methodology was tested on the HRES plant consisting of three non-dispatchable RESs, and the developed DEMs demonstrated satisfactory performance in both the shape of power responses at the PCC and TSI value (used for describing the global transient stability status of the system). The LSTM-based models were also compared with the TF-based models developed in Chapter 4 for a number of system operating points and TN short-circuit faults, which can be seen as a further assessment of TF-based model accuracy. The obtained results demonstrated that focusing on reproducing time domain power responses at the PCC is not needed for reliable assessment of the overall transient stability of the system, meaning TF-based DEMs from Chapter 4 can be confidently used for representing the HRES plant in transient stability simulations. *Deep learning-based methodology for dynamic equivalent modelling of HRES plant for transient stability studies from the perspective of the shape of time domain HRES plant power responses represents the fourth original contribution of the thesis.*

In this and previous two chapters of the thesis, three different clustering algorithms were used: the fuzzy c-means clustering method, the KDE method and the agglomerative HC method, as these three methods were found to be the most suitable for tasks in hand. The fuzzy c-means clustering algorithm was used for clustering historical HRES plant production data, i.e., determining typical annual HRES plant compositions. Each clustering object in the historical production dataset consists of real power outputs of

individual technologies within the HRES plant at a specific time interval in the considered historical period, whereas the number of clustering objects corresponds to the total number of time intervals in the historical period. The main attributes of the fuzzy c-means clustering algorithm that make it suitable for clustering large historical plant production dataset are: low computational complexity ((*O*(*N*), where *N* is the number of clustering objects)), the ability to perform "soft" clustering, which is especially useful in case of clusters not being well separated [132], and the proven efficiency in application in similar clustering tasks in the past [70, 161, 162]. Given that the number of clusters has to be specified in advance, the combination of three widely applied clustering indicators, MSE, CDI, and MIA, was used to estimate the optimal number of clusters in the investigated dataset.

When it comes to the clustering of TSI values in the data-driven methodology, the KDE method was chosen over the fuzzy c-means clustering algorithm in order to avoid defining the optimal number of clusters *a priori*. Furthermore, the KDE method can identify arbitrary shaped clusters and has strong mathematical background. The drawback of the KDE approach is its computational complexity (due to the need for computing the density estimate and local maximum for each clustering object, and estimating the optimal bandwidth value [191]), and difficulty in obtaining a "reasonable nonparametric density estimation" in the multivariate settings ("the curse of dimensionality") [157]. This, however, was not the case in this study nor it will be in the case of development of DEM of any practical HRES plant as the clustering dataset is one-dimensional and its size is determined by the number of typical HRES plant compositions that cannot be unreasonably large.

Finally, in deep learning-based methodology, time domain HRES plant power responses were divided into groups according to similarity in time using the agglomerative HC algorithm with the unweighted average linkage. As mentioned in Chapter 2, partitioning, hierarchical and model-based clustering algorithms have been typically used for time series clustering. Unlike the partitioning algorithms, the HC is a deterministic algorithm (the dendrogram is always the same as it does not depend on the initial cluster centres) and does not require the number of clusters to be specified in advance [140]. Furthermore, the HC algorithm with the unweighted average linkage is not sensitive to

noise and outliers, and takes into consideration the number of elements in clusters when deciding on their merging [140]. As for the model-based clustering, the structure of models and a criterion for assessing their similarity have to be defined in advance, and then another clustering algorithm (e.g., the partitioning or HC) has to be applied to the previously computed similarity measures. Even though the HC algorithm has quadratic computational complexity, computational time is not an issue when developing DEMs for any HRES plant as the clustering dataset size is defined by the number of typical plant compositions and MC CSs per composition, and these numbers cannot be unreasonably high.

7.1.6 Chapter 6 Limitations of the Reliance on Assessment of the Contribution of Spatially Distributed HRES Plant to Real System Operation

The chapter discussed the principle of the operation of VPPs at DN level, which can be adopted for the concept of geographically widely distributed HRES plant at TN level, and presented the preliminary analysis on the influence of the selection of distributed HRES plant composition on transient system stability performance. The location and output of individual RESs in the HRES plant affect the location and number of SGs (in the rest of the system) in operation, and consequently their rotor angle responses to system disturbances, meaning different spatial HRES plant compositions producing the same total power production may result in significantly different transient stability behaviour of the system. The CS involving simplified representations of four real TNs, and the HRES plant consisting of PV plants and WFs spatially distributed across the system was used in the analysis performed in a probabilistic manner. Three representative 24-hour TSs involving different TN loading and RES production levels were considered. TSI index was chosen for describing the transient stability status of the system. It was found that the impact of the spatial HRES plant composition on transient stability of the TN depends on RES penetration level. Its influence was more prominent when RES penetration reached a relatively high value of around 60%. The results obtained with the test system showed that the deployment of individual RES plants within geographically distributed HRES plant in cases of higher penetration of RESs in the system should be decided after assessing overall system transient stability performance, as the conventional economic dispatch of generation units may lead to inadequate system dynamic behaviour. *Exploratory study on the impact of*

geographically distributed HRES plant on transient stability of the TN represents the fifth original contribution of the thesis.

7.2 Further Work

The work presented in the thesis has achieved all the aims of the research specified in Chapter 1. Still, there are a number of potential extensions and improvements of the research that are described below.

- All presented equivalent modelling procedures should be further evaluated on a more realistic TN model as the largest TN model used in the part of the research on equivalent modelling of HRES plants consists of 3 SGs (the IEEE 9-bus network). Though not significantly different, or different at all, results are expected, this would be worthwhile further testing of developed models and methodologies. Furthermore, in order to assess the maximum possible reduction in the computational time required for performing power system stability simulations due to the use of the DEM instead of the detailed HRES plant dynamic model, individual units in the WF and PV plant should be represented separately in the detailed HRES plant dynamic model (aggregate models of the WF and PV plant were used in the test systems in this thesis).
- Apart from larger TN model, further extensions of preliminary methodologies for developing EMs of HRES plants for small-disturbance, frequency and long-term voltage stability simulations include the following:
    - The modelling procedures for all three aforementioned system stability studies should take into consideration the variation of TN operating conditions during the year (a single TN operating point was analysed in Chapter 3) and introduce a parameter optimization procedure more efficient than the used iterative search (e.g., an evolutionary algorithm). The clusters of system stability results were identified by visual inspection, which was possible due to clear separation of clusters. However, this cannot be guaranteed for any HRES plant and TN model, and adequate unsupervised data mining methods (clustering algorithms) should be applied.

- Modes produced by converter controllers that are within the frequency range characteristic for electromechanical modes could be included in small-disturbance stability analysis. These modes could then be used for developing EM structure for HRES plant compositions without SGs in service.
- In the case of frequency stability study, more representative system disturbances defined using statistical or historical data (following the approach for short-circuit fault statistics in the data-driven and deep learning-based methodologies) should be included in frequency stability simulations. When it comes to EM for HRES plant compositions comprising converter-connected technologies only, more strict assessment of the influential parameters estimated in the optimization procedure is needed. Sensitivity analysis techniques (e.g., the Morris screening method) could be used for that purpose.
- In the case of long-term voltage stability study, the preliminary equivalent is characterized by a single maximum reactive power limit, which is then used for all HRES plant operating points allocated to the given EM. Defining the maximum reactive power capability as a function of the total HRES plant real power output and voltage at the PCC should be investigated. Furthermore, the location of the critical bus could be introduced as additional factor for differentiating the impact of HRES plant compositions on long-term voltage stability, and consequently assessing EM accuracy. Also, replacing the infinite bus in the test system used in Chapter 3 with a Thevenin equivalent could potentially result in a system with long-term voltage stability issues.

- In this thesis, all methodologies for developing EMs of HRES plant rely on a certain level of uncertainty in HRES plant operating scenario (±5% around the typical annual plant composition) and location of individual plants within the HRES plant ((0-5) km) when performing system stability simulations with the detailed plant model. Future studies should explore the influence of the adopted uncertainty level on HRES plant behaviour in system stability simulations, and consequently on the number, structure and parameter values of EMs. Similarly, as mentioned above, sensitivity analysis could be used for this purpose to determine the most influential parameters/uncertainties affecting the results.

- All performed transient stability simulations assumed self-clearing faults and the same fault duration for all short-circuit faults. Future work should investigate the influence of the change in the network topology due to fault clearing by opening a transmission line and different fault durations on the TSI values of the system as well as the shape of time domain HRES plant power responses. Thus, the MC approach for defining cases used in DEM development should include the probabilistic variations in fault duration and the way of fault clearing (i.e., choosing between the self-clearing and opening of the faulted line). Another extension of the work on dynamic equivalent modelling of HRES plant for system transient stability studies should involve the simulation of different network topologies for the same pre-disturbance HRES plant operating condition, and analysing how this affects the power flows in the network and the transient stability performance of the system. Taking into consideration the pre-disturbance network configuration state might result in a need to have different DEMs for different combinations of a single typical annual HRES plant composition and pre-disturbance network topologies.
- Both data-driven and deep learning-based methodologies for dynamic equivalent modelling of HRES plant for transient system stability studies are based on the most probable HRES plant responses in annual transient stability simulations. The research presented in the thesis, thus, has not considered the tripping of individual converter-based technologies in the HRES plant (as it is assumed that these plants are equipped with fault-through-ride capability and do not trip after a fault), as well as the loss of synchronism of individual SG-based plants in the HRES plant. Future work should include the analysis on DEM performance in the case of these extreme events. The reduction in TF-based DEM accuracy for these disturbances compared to the accuracy for the most probable disturbances will depend on the significance of these disturbances for the global transient stability behaviour described by TSI value. When it comes to LSTM-based models, these extreme disturbances will result in HRES plant power responses considerably different from the ones simulated in the thesis (in terms of the shape in time domain), which implies that a single LSTM network will not be able to reproduce both types of the plant responses with the same, high accuracy.

- The data-driven equivalent modelling methodology relies on TSI for describing the global transient stability status, and evaluating model accuracy. Even though the TSI represents a widely used index for assessing transient stability of the system, the use of a combination of several transient stability indices instead of a single one (TSI) should be investigated. Potential additional indices include the transient rotor angle severity index, the critical fault clearing time, the maximum rotor angle deviation, speed deviation and acceleration of individual generators in the system, etc. Using multiple indices for describing the overall transient stability performance of the system should result in more comprehensive transient stability assessment, and DEM validation on the basis of several indices would provide a higher confidence in the ability of the developed model to reliably represent the HRES plant in transient stability simulations throughout the year. Given that voltage magnitude is the only input signal, TF-based models cannot take into account the change in the phase angle of the voltage at the PCC. In order to make TF-based models suitable for representing HRES plant responses to phase jumps, their inputs signals should be the same as for LSTM-based DEMs - the real and imaginary parts of the positive sequence voltage at the PCC. Thus, TF-based model would need to have a multiple-input-single-output model structure as opposed to the single-input-single-output structure used in the thesis.
- When it comes to LSTM-based models, potential increase in the accuracy of model power responses in time domain by using a variant of the standard LSTM network (a comprehensive list is given in [125]) and/or different network training algorithm as it influences network generalization ability (metaheuristic algorithms have shown to have a potential to outperform the backpropagation-based learning [124]) should be analysed. Another area for potential improvement is the process of selecting LSTM network training data. In this thesis, the set of training responses from a cluster was created by uniformly sampling the values of cluster responses at the time of the first swing peak. However, given that clusters are usually not perfectly compact, it might be the case that cluster responses are grouped in few narrow distinctive ranges. The selection process of the training data that takes into account the distribution of responses within the cluster should result in a more representative training dataset compared to the uniform sampling.

- In order to comprehensively investigate the influence of geographically distributed HRES plant on transient stability of the system, the analysis should be carried out for larger number of scenarios. Performing transient stability assessment for larger number of TN loading and total HRES plant production levels as well as higher number of spatial HRES plant compositions associated with the same total HRES plant production and TN loading level is needed. More extensive simulations will provide more reliable conclusions on conditions under which the choice of the dispatch of the distributed HRES plant becomes relevant for transient stability performance of the system as well as on the level of the contribution of HRES plant to system stability. At this stage, the minimum run time and downtime of SGs were not taken into account when performing hourly OPF calculations per day. As these times can influence the set of SGs that can be disconnected from the network at consecutive hours during the day, these constraints should be included in future analysis. Finally, performing this type of study for other types of system stability should be a part of the further work in this area as well.

References

[1] A. Lebedys, D. Akande, N. Coënt, N. Elhassan, G. Escamilla, I. Arkhipova, and A. Whiteman, "Renewable capacity statistics 2022," The International Renewable Energy Agency (IRENA), Abu Dhabi, 2022.

[2] "Renewables 2021: Analysis and forecast to 2026," International Energy Agency (IEA), 2021.

[3] K. Dykes, J. King, N. DiOrio, R. King, V. Gevorgian, D. Corbus, N. Blair, K. Anderson, G. Stark, C. Turchi, P. Moriarity, "Opportunities for Research and Development of Hybrid Power Plants," Golden, CO: National Renewable Energy Laboratory, 2020.

[4] "Status review of renewable support schemes in Europe for 2018 and 2019," Renewables Work Stream of Electricity Working Group, Council of European Enegy Regulators (CEER), 2021.

[5] "Key support elements of RES in Europe: moving towards market integration," Council of European Energy Regulators (CEER), 2016.

[6] M. Ahlstrom, J. Mays, E. Gimon, A. Gelston, C. Murphy, P. Denholm, and G. Nemet, "Hybrid resources: challenges, implications, opportunities, and innovation," *IEEE Power and Energy Magazine*, vol. 19, no. 6, pp. 37 - 44, 2021.

[7] A. Hina Fathima, K. Palanisamy, "Optimization in microgrids with hybrid energy systems - a review," *Renewable and Sustainable Energy Reviews*, vol. 45, pp. 431-446, 2015.

[8] S. Panda, S. Mohanty, P. K. Rout, and B. K. Sahu, "A conceptual review on transformation of micro-grid to virtual power plant: issues, modeling, solutions, and future prospects," *International Journal of Energy Research*, vol. 46, no. 6, pp. 7021-7054, 2022.

[9] "Renewable hybrid power plants: exploring the benefits and market opportunities," Wind Europe, 2019.

[10] M. Bolinger, W. Gorman, J. Rand, R. Wiser, S. Jeong, J. Seel, C. Warner, and B. Paulos, "Hybrid power plants: status of installed and proposed projects," Lawrence Berkeley National Laboratory, 2021.

[11] *Bulgana Green Power Hub* [Online]. Available: https://bulganagreenpowerhub.com.au/.

[12] *Coober Pedy Hybrid Renewable Power Station* [Online]. Available: https://edlenergy.com/project/coober-pedy/.

[13] *The Port Augusta Renewable Energy Park* [Online]. Available: https://www.iberdrola.com/about-us/what-we-do/onshore-wind-energy/port-augusta-project.

[14] *The Stillwater Triple Hybrid Plant* [Online]. Available: https://www.enelgreenpower.com/our-projects/operating/stillwater-hybrid-plant.

[15] *Adani Green Energy* [Online]. Available: https://www.adanigreenenergy.com/newsroom/media-releases/adani-green-switches-on-indias-first-hybrid-power-plant.

[16] P. Johnson. "The first utility scale renewable energy plant combining solar and wind generation with battery storage opens in the US" [Online]. Available: https://electrek.co/2022/10/06/first-clean-energy-plant-opens-using-solar-wind-battery-storage/.

[17] G. Parkinson. "World "first" wind, solar, and battery project finally starts production after 3-year wait" [Online]. Available: https://reneweconomy.com.au/world-first-wind-solar-and-battery-project-finally-starts-production-after-3-year-wait/.

[18] S. Ross. "China's first solar-tidal photovoltaic power plant fully operational" [Online]. Available: https://marketbusinessnews.com/chinas-first-solar-tidal-photovoltaic-power-plant-fully-operational/308537/.

[19] J. V. Milanović, and S. M. Zali, "Validation of equivalent dynamic model of active distribution network cell," *IEEE Transactions on Power Systems*, vol. 28, no. 3, pp. 2101-2110, 2013.

[20] S. M. Zali, and J. V. Milanović, "Generic model of active distribution network for large power system stability studies," *IEEE Transactions on Power Systems*, vol. 28, no. 3, pp. 3126-3133, 2013.

[21] G. Chaspierre, G. Denis, P. Panciatici, and T. Van Cutsem, "An active distribution network equivalent derived from large-disturbance simulations with uncertainty," *IEEE Transactions on Smart Grid*, vol. 11, no. 6, pp. 4749-4759, 2020.

[22] "WECC Wind Power Plant Dynamic Modeling Guide," WECC Renewable Energy Modeling task Force, 2014.

[23] "WECC PV Power Plant Dynamic Modeling Guide," WECC Renewable Energy Modeling task Force, 2014.

[24] California ISO, "Dynamic model review guideline for inverter based interconnection requests," 2021.

[25] CIGRE Report Task Force C4.C6.35, "Modelling of inverter-based generation for power system dynamic studies," 2018.

[26] CIGRE Report Working Group C4.605, "Modelling and aggregation of loads in flexible power networks," 2014.

[27] IEEE PES General Systems Subcommittee – Task Force on Dynamic System Equivalents, "Dynamic system equivalents: a survey of available techniques," *IEEE Transactions on Power Delivery*, vol. 27, no. 1, pp. 411-420, 2012.

[28] A. Gonzales, J.R., Riba, and A. Ruis, "Optimal sizing of a hybrid grid-connected photovoltaic–wind–biomass power system," *Sustainability*, vol. 7, pp. 12787-12806, 2015.

[29] A. R. Silva, and A. Estanqueiro, "From wind to hybrid: A contribution to the optimal design of utility-scale hybrid power plants," *Energies*, vol. 15, no. 7, pp. 1-19, 2022.

[30] J. L. Duchaud, G. Notton, C. Darras, and C. Voyant, "Multi-objective particle swarm optimal sizing of a renewable hybrid power plant with storage," *Renewable Energy*, vol. 131, pp. 1156-1167, 2019.

[31] A. P. J. Stanley, and J. King, "Optimizing the physical design and layout of a resilient wind, solar, and storage hybrid power plant," *Applied Energy*, vol. 317, pp. 1-14, 2022.

[32] R. de Azevedo, and O. Mohammed, "Profit-maximizing utility-scale hybrid wind-PV farm modeling and optimization," in *Procedings of the IEEE Southeast Conference 2015*, Fort Lauderdale, Florida, USA, 2015, pp. 1-8.

[33] M. K. Mehta, G. J. van Holthoon, D. A. von Terzi, and M. B. Zaaijer, "Technical and economic value of utility-scale wind-storage hybrid power plants," in *Proceedings of Hybrid Power Systems Workshop, 2021 (online)*, 2021.

[34] T. Ochoa, E. Gil, A. Angulo, and C. Valle, "Multi-agent deep reinforcement learning for efficient multi-timescale bidding of a hybrid power plant in day-ahead and real-time markets," *Applied Energy*, vol. 317, pp. 1-13, 2022.

[35] A. Sanchez de la Nieta, J. Contreras, and J. I. Munoz, "Optimal coordinated wind-hydro bidding strategies in day-ahead markets," *IEEE Transactions on Power Systems*, vol. 28, no. 2, pp. 798-809, 2013.

[36] A. Sanchez de la Nieta, J. Contreras, and J. P. S. Catalao, "Optimal single wind hydro-pump storage bidding in day-ahead markets including bilateral contracts," *IEEE Transactions on Sustainable Energy*, vol. 7, no. 3, pp. 1284-1294, 2016.

[37] Y. Wang, S. Luo, Y. Wu, M. Miao, and S. Wang, "Operation strategy of a hybrid solar and biomass power plant in the electricity markets," *Electric Power System Research*, vol. 167, pp. 183-191, 2019.

[38] R. Rockafellar, and S. Uryasev, "Optimization of conditional value-atrisk," *Journal of Risk*, vol. 2, no. 3, pp. 21-41, 2000.

[39] P. K. Olulope, K. A. Folly, and G. K. Venayagamoorthy, "Modelling and simulation of hybrid distributed generation and its impact on transient stability of power system," in *Proceedings of the 2013 IEEE International Conference on Industrial Technology (ICIT)*, Cape Town, South Africa, 2013, pp. 1757-1762.

[40] D. V. Pombo, "Coordinated frequency and active power control of hybrid power plants: an approach to fast frequency response," MSc thesis, Energy Technology, Aalborg University, 2018.

[41] A. B. Attya, and A. Vickers, "Operation and control of a hybrid power plant with the capability of grid services provision," *Energies*, vol. 14, pp. 1-15, 2021.

[42] S. M. Zali, "Equivalent dynamic model of distribution network with distributed generation," PhD thesis, School of Electrical and Electronic Engineering, The University of Manchester, 2012.

[43] J. M. Undrill, A.E. Turner, "Construction of power system electromechanical equivalents by modal analysis," *IEEE Transactions on Power Apparatus and Systems*, vol. PAS-90, no. 5, pp. 2049-2059, 1971.

[44] W. W. Price, and B. A. Roth "Large-scale implementation of modal dynamic equivalents," *IEEE Transactions on Power Apparatus and Systems*, vol. PAS-100, no. 8, pp. 3811-3817, 1981.

[45] D. Chaniotis, and M. A. Pai, "Model reduction in power systems using Krylov subspace methods," *IEEE Transactions on Power Systems*, vol. 20, no. 2, pp. 888-894, 2005.

[46] J. Qi, J. Wang, H. Liu, and A. D. Dimitrovski, "Nonlinear model reduction in power systems by balancing of empirical controllability and observability covariances," *IEEE Transactions on Power Systems*, vol. 32, no. 1, pp. 114-126, 2017.

[47] S. E. M. de Oliveira, and A. G. Massaud, "Modal dynamic equivalent for electric power systems - Part I: Theory," *IEEE Transactions on Power Systems*, vol. 3, no. 4, pp. 1723-1730, 1988.

[48] A. J. Germond, and R. Podmore, "Dynamic aggregation of generating unit models," *IEEE Transactions on Power Apparatus and Systems*, vol. PAS-97, no. 4, pp. 1060-1069, 1978.

[49] M. L. Ourari, L. A. Dessaint, and V. Q. Do, "Dynamic Equivalent Modeling of Large Power Systems Using Structure Preservation Technique," *IEEE Transactions on Power Systems*, vol. 21, no. 3, pp. 1284-1295, 2006.

[50] J. P. Yang, G. H. Cheng, and Z. Xu, "Dynamic reduction of large power system in PSS/E," in *IEEE/PES Transmission and Distribution Conference & Exhibition: Asia and Pacific*, Dalian, China, 2005, pp. 1-4.

[51] A. Chang, and M. M. Adibi, "Power system dynamic equivalents," *IEEE Transactions on Power Apparatus and Systems,* vol. PAS-89, no. 8, pp. 1737-1744, 1970.

[52] R. Podmore, "Identification of coherent generators for dynamic equivalents," *IEEE Transactions on Power Apparatus and Systems,* vol. PAS-97, no. 4, pp. 1344-1354, 1978.

[53] J. Chow, *Power system coherency and model reduction*. New York, USA: Springer, 2013.

[54] R. Nath, S.S. Lamba, K.S. Prakasa Rao, "Coherency based system decomposition into study and external areas using weak coupling," *IEEE Transactions on Power Apparatus and Systems,* vol. PAS-104, no. 6, pp. 1443-1449, 1985.

[55] S. Geeves, "A modal-coherency technique for deriving dynamic equivalents," *IEEE Transactions on Power Systems,* vol. 3, no. 1, pp. 44-51, 1988.

[56] J. S. Lawler, and R. A. Schlueter, "Computational algorithms for constructing modal-coherent dynamic equivalents," *IEEE Transactions on Power Apparatus and Systems,* vol. PAS-101, no. 5, pp. 1070-1080, 1982.

[57] P. M. van Oirsaw, "A dynamic equivalent using modal coherency and frequency response," *IEEE Transactions on Power Systems,* vol. 5, no. 1, pp. 289-295, 1990.

[58] M. Shiroei, B. Mohammadi-Ivatloo, and M. Parniani, "Low-order dynamic equivalent estimation of power systems using data of phasor measurement units," *Electrical Power and Energy Systems,* vol. 74, pp. 134-141, 2016.

[59] A. T. Saric, M. T. Transtrum, and A. M. Stankovic, "Data-driven dynamic equivalents for power system areas from boundary measurements," *IEEE Transactions on Power Systems,* vol. 34, no. 1, pp. 360-370, 2019.

[60] A. M. Stankovic, A. T. Saric, and M. Milosevic, "Identification of nonparametric dynamic power system equivalents with artificial neural networks," *IEEE Transactions on Power Systems,* vol. 18, no. 4, pp. 1478-1486, 2004.

[61] F. Ma, and V. Vittal, "A hybrid dynamic equivalent using ANN-based boundary matching technique," *IEEE Transactions on Power Systems,* vol. 27, no. 3, pp. 1494-1502, 2012.

[62] P. Li, W. Gu, L. Wang, B. Xu, M. Wu, and W. Shen, "Dynamic equivalent modeling of two-staged photovoltaic power station clusters based on dynamic affinity propagation clustering algorithm," *International Journal of Electrical Power and Energy Systems,* vol. 95, pp. 463-475, 2018.

[63] J. Zou, C. Peng, Y. Yan, H. Zheng, and Y. Li, "A survey of dynamic equivalent modeling for wind farm," *Renewable and Sustainable Energy Reviews,* vol. 40, pp. 956-963, 2014.

[64] P. Wang, Z. Zhang, Q. Huang, N. Wang, X. Zhang, and W.-J. Lee, "Improved wind farm aggregated modeling method for large-scale power system stability studies," *IEEE Transactions Power Systems,* vol. 33, no. 6, pp. 6332-6342, 2018.

[65] M. Ali, "Probabilistic modelling techniques and a robust design methodology for offshore wind farms," PhD thesis, School of Electrical and Electronical Engineering, The University of Manchester, Manchester, 2012.

[66] H. Wu, Z. Liu, Y. Chen, B. Xu, and X. Qi, "Equivalent Modeling Method for Regional Decentralized Photovoltaic Clusters Based on Cluster Analysis," *CPSS Transactions on Power Electronics and Applications,* vol. 3, no. 2, pp. 146-153, 2018.

[67] E. Muljadi, C.P. Butterfield, A. Ellis, J. Mechenbier, J. Hochheimer, R. Young, N. Miller, R. Delmerico, R. Zavadil, J.C. Smith, "Equivalencing the collector system of a large wind power plant," in *2006 IEEE Power Engineering Society General Meeting*, Montreal, Canada, 2006, pp. 1-9.

[68] M. A. Chowdhury, W. X. Shen, N. Hosseinzadeh, and H. R. Pota, "A novel aggregated DFIG wind farm model using mechanical torque compensating factor," *Energy Conversion and Management*, vol. 67, pp. 265-274, 2013.

[69] L. M. Fernández, F. Jurado, and J. R. Saenz, "Aggregated dynamic model for wind farms with doubly fed induction generator wind turbines," *Renewable Energy*, vol. 33, no. 1, pp. 129-140, 2008.

[70] J. Zou, C. Peng, H. Xu, and Y. Yan, "A fuzzy clustering algorithm-based dynamic equivalent modeling method for wind farm with DFIG," *IEEE Transactions on Energy Conversion*, vol. 30, no. 4, pp. 1329-1337, 2015.

[71] H. Zhou, P. Ju, Y. Xue, and J. Zhu, "Probabilistic equivalent model of DFIG-based wind farms and its application in stability analysis," *Journal of Modern Power Systems and Clean Energy* vol. 4, no. 2, pp. 248-255, 2016.

[72] M. Ali, I. S. Ilie, J. V. Milanović, G. Chicco, "Wind farm model aggregation using probabilistic clustering," *IEEE Transations on Power Systems*, vol. 28, no. 1, pp. 309-316, 2013.

[73] P. Chao, W. Li, X. Liang, Y. Shuai, F. Sun, and Y. Ge, "A comprehensive review on dynamic equivalent modeling of large photovoltaic power plants," *Solar Energy*, vol. 210, pp. 87-100, 2020.

[74] Z. Ma, J. Zheng, S. Zhu, X. Shen, L. Wei, X. Wang, K. Men, "Online clustering modeling of large-scale photovoltaic power plants," in *Proceedings of the 2015 IEEE Power & Energy Society General Meeting*, Denver, USA, 2015, pp. 1-5.

[75] D. Remon, A. M. Cantarellas, and P. Rodriguez, "Equivalent model of large-scale synchronous photovoltaic power plants," *IEEE Transactions on Industry Applications*, vol. 52, no. 6, pp. 5029-5040, 2016.

[76] W. Liu, W. Liu, J. Pan, X. Du, and B. Xu, "Equivalent modeling of distributed photovoltaic power station clusters based on deep belief network," in *2018 International Conference on Power System Technology*, Guangzhou, China, 2018, pp. 4333-4339.

[77] M. Rasheduzzaman, J. A. Mueller, and J. W. Kimball, "Reduced-order small-signal model of microgrid systems," *IEEE Transactions on Sustainable Energy*, vol. 6, no. 4, pp. 1292-1305, 2015.

[78] A. Ishchenko, J. M. A. Myrzik, and W. L. Kling, "Dynamic equivalencing of distribution networks with dispersed generation using Hankel norm approximation," *IET Generation, Transmission and Distribution*, vol. 1, no. 5, pp. 818-825, 2007.

[79] A. V. Jayawardena, L.G. Meegahapola, D.A. Robinson, S. Perera, "An Aggregated Linearised Model of a Grid-tied Microgrid forstability studies," in *2015 Australasian Universities Power Engineering Conference (AUPEC)*, Wollongong, NSW, Australia, 2015, pp. 1-6.

[80] X. Wu, "New approaches to dynamic equivalent of active distribution network for transient analysis," PhD thesis, E.ON Energy Research Center RWTH Aachen University, Aachen, Germany, 2016.

[81] J. C. Boemer, "On stability of sustainable power systems: network fault response of transmission system and very high penetration of distributed generation," PhD thesis, Delft University of Technology, 2016.

[82] D. Gussain, J. L. Rueda, J. C. Boemer, and P. Palensky, "Identification of dynamic equivalents of active distribution networks through MVMO," *IFAC-PapersOnLine*, vol. 49, no. 27, pp. 262-267, 2016.

[83] F. de Oliveira Resende, "Contributions for microgrids dynamic modelling and operation," PhD thesis, Engineering Faculty, Porto University, 2007.

[84] F. O. Resende, and J. A. Pecas Lopes, "Development of dynamic equivalents for microgrids using system identification theory," in *2007 IEEE Lausanne PowerTech conference*, Lausanne, Switzerland, 2007, pp. 1-6.

[85] B. Zaker, G. B. Gharehpetian, and M. Karrari, "Small signal equivalent model of synchronous generator-based gridconnected microgrid using improved Heffron-Phillips model," *Electrical Power and Energy Systems*, vol. 108, pp. 263-270, 2019.

[86] B. Zaker, G. B. Gharehpetian, and M. Karrari, "A novel measurement-based dynamic equivalent model of grid-connected microgrids," *IEEE Transactions on Industrial Informatics*, vol. 15, no. 4, pp. 2032-2043, 2019.

[87] G. Chaspierre, G. Denis, P. Panciatici, and T. Van Cutsem, "A dynamic equivalent of active distribution network: Derivation, update, validation and use cases," *IEEE Open Access Journal of Power and Energy*, vol. 8, pp. 497-509, 2021.

[88] G. Chaspierre, P. Panciatici, and T. Van Cutsem, "Control of a battery energy storage system to compensate for ADN equivalents inaccuracies," in *Proceedings of the 22nd Power Systems Computation Conference (PSCC)*, Porto, Portugal, 2022, pp. 1-7.

[89] E. O. Kontis, T. A. Papadopoulos, M. H. Syed, E. Guillo-Sansano, G. M. Burt, and G. K. Papagiannis, "Artificial-intelligence method for the derivation of generic aggregated dynamic equivalent models," *IEEE Transactions on Power Systems*, vol. 34, no. 4, pp. 2947 - 2956, 2019.

[90] G. Mitrentsis, H. Lens, "Data-driven dynamic models of active distribution networks using unsupervised learning techniques on field measurements," *IEEE Transactions on Smart Grid*, vol. 12, no. 4, pp. 2952-2965, 2021.

[91] X. S. Feng, "Dynamic equivalencing of distribution network with embedded generation," PhD thesis, School of Engineering, University of Edinburgh, 2012.

[92] P. N. Papadopoulos, T. A. Papadopoulos, A. J. Roscoe, G. M. Burt, G. K. Papagiannis, and P. Crolla, "Black-box dynamic equivalent model for microgrids using measurement data," *IET Generation, Transmission & Distribution*, vol. 8, no. 5, pp. 851-861, 2014.

[93] P. N. Papadopoulos, G. K. Papagiannis, A. J. Roscoe, P. Crolla, T. A. Papadopoulos, and G. M. Burt, "Measurement-based analysis of the dynamic performance of microgrids using system identification techniques," *IET Generation, Transmission & Distribution*, vol. 9, no. 1, pp. 90-103, 2015.

[94] S. M. Zali, and J. V. Milanović, "Dynamic equivalent model of distribution network cell using Prony analysis and nonlinear least square optimization," in *2009 IEEE Bucharest PowerTech*, Bucharest, Romania, 2009, pp. 1-6.

[95] A. M. Azmy, and I. Erlich, "Identification of dynamic equivalents for distribution power networks using recurrent ANNs," in *Proceedings of IEEE PES Power Systems Conference and Exposition*, New York, NY, USA, 2004, pp. 1-6.

[96] A. M. Azmy, I. Erlich, and P. Sowa, "Artificial neural network-based dynamic equivalents for distribution systems containing active sources," *IEE Proceedings - Generation, Transmission and Distribution*, vol. 151, no. 6, pp. 681-688, 2004.

[97] J. Matevosyan, et al., "Aggregated models of wind-based generation and active distribution network cells for power system studies – literature overview," in *2011 IEEE Trondheim PowerTech conference*, Trondheim, Norway, 2011, pp. 1-8.

[98] J. Denecke, I. Erlich, "Dynamic equivalents of active distribution networks," in *Proceedings of 2017 IEEE Power & Energy Society General Meeting*, Chicago, IL, USA, 2017, pp. 1-5.

[99] C. Zheng, S. Wang, Y. Liu et al., "A novel equivalent model of active distribution networks based on LSTM," *IEEE Transactions on Neural Network Learning*, vol. 30, no. 9, pp. 2611-2624, 2019.

[100] F. Calero, "Impact of distributed battery energy storage on electric power transmission and distribution systems," PhD thesis, Department of Electrical and Computer Engineering, the University of Waterloo, 2020.

[101] L. D. P. Ospina, V. U. Salazar, and D. P. Ospina, "Dynamic equivalents of nonlinear active distribution networks based on Hammerstein-Wiener models: an application for long-term power system phenomena," *IEEE Transactions on Power Systems (Early Access)*, 2022.

[102] P. Kundur, *Power system stability and control*. New York, NY, USA: McGraw-Hill, 1994.

[103] P. V. Kokotovic, J. J. Allemong, J. R. Winkelman, and J. H. Chow, "Singular perturbation and iterative separation of time scales," *Automatica*, vol. 16, no. 1, pp. 23-33, 1980.

[104] U. D. Annakkage, N. K. C Nair, Y. Liang, A. M. Gole, V. Dinavahi, B. Gustavsen, et al., "Dynamic system equivalents: A survey of available techniques," *IEEE Transactions on Power Delivery*, vol. 27, no. 1, pp. 411-420, 2012.

[105] J. Machowski, J.W. Bialek, and J.R. Bumby, *Power system dyanmics: stability and control*. John Wiley & Sons, Ltd, 2008.

[106] C. Li, J. Xu, and C. Zhao, "A coherency-based equivalence method for MMC inverters using virtual synchronous generator control," *IEEE Transactions on Power Delivery*, vol. 31, no. 3, pp. 1369-1378, 2016.

[107] K. K. Anaparthi, B. Chaudhuri, and B. C. Pal, "Coherency identification in power systems through principal component analysis," *IEEE Transactions on Power Systems*, vol. 20, no. 3, pp. 1658-1660, 2005.

[108] J. R. Winkelman, J. H. Chow, B. C. Bowler, B. Avramovic, and P. V. Kokotovic, "An analysis of interarea dynamics of multi-machine systems," *IEEE Transactions on Power Apparatus and Systems*, vol. PAS-100, no. 2, pp. 754-763, 1981.

[109] R. J. Galarza, J. H. Chow, W. W. Price, A. W. Hargrave, and P. M. Hirsch, "Aggregation of exciter models for constructing power system dynamic eqauivalents," *IEEE Transactions on Power Systems*, vol. 13, no. 3, pp. 782-788, 1998.

[110] J. Sjoberg, Q. Zhang, L. Ljung, A. Benveniste, B. Delyon, P. Glorennec, et al., "Nonlinear black-box modeling in system identification: A unified overview," *Automatica*, vol. 31, no. 12, pp. 1691-1724, 1995.

[111] J. Ponoćko, "Data Analytics Based Demand Profiling and Advanced Demand Side Management for Flexible Operation of Sustainable Power Networks," PhD thesis, School of Electrical and Electronic Engineering, The University of Manchester, 2019.

[112] F. M. Bianchi, E. Maiorino, M. C. Kampffmeyer, A. Rizzi, and R. Jenssen. An overview and comparative analysis of recurrent neural networks for short term load forecasting [Online] Available: https://arxiv.org/pdf/1705.04378.pdf

[113] S. Haykin, *Neural networks and learning machines*, 3rd ed. Prentice Hall, 2009.

[114] R. DiPetro, C. Rupprecht, N. Navab, and G. D. Hager. Analyzing and exploiting NARX recurrent neural networks for long-term dependencies [Online] Available: https://arxiv.org/pdf/1702.07805.pdf

[115] T. Lin, B. G. Horne, P. Tino, and C. L. Giles, "Learning long-term dependencies in NARX recurrent neural networks," *IEEE Transactions on Neural Networks*, vol. 7, no. 6, pp. 1329-1996, 1996.

[116] R. Pascanu, T. Mikolov, and Y. Bengio, "On the difficulty of training recurrent neural networks," in *Proceedings of 30th International Conference on Machine Learning*, Atlanta, Georgia, USA, 2013, pp. 1310-1318.

[117] A. Graves, "Supervised sequence labelling with recurrent neural networks," PhD thesis, Faculty of Computer Science, Technical University of Munich, 2008.

[118] Z. C. Lipton, J. Berkowitz, and C. Elkan. A critical review of recurrent neural networks for sequence learning [Online] Available: https://arxiv.org/pdf/1506.00019.pdf

[119] Y. Bengio, P. Simard, and P. Frasconi, "Learning long-term dependencies with gradient descent is difficult," *IEEE Transactions on Neural Networks*, vol. 5, no. 2, pp. 157-166, 1994.

[120] G. Chen. A gentle tutorial of recurrent neural network with error backpropagation [Online] Available: https://arxiv.org/pdf/1610.02583.pdf

[121] Z. Cui, K. Ruimin, and Y. Wang, "Deep stacked bidirectional and unidirectional LSTM recurrent neural network for network-wide traffic speed prediction," in *Proceedings of 6th International Workshop Urban Computing (UrbComp)*, Halifax, Canada, 2017, pp. 1-11.

[122] S. Hochreiter, J. Schmidhuber "Long Short-Term Memory," *Neural Computation*, vol. 9, no. 8, pp. 1735-1780, 1997.

[123] X. Ma, Z. Tao, Y. Wang, H. Yu, and Y. Wang, "Long short-term memory neural network for traffic speed prediction using remote microwave sensor data," *Transportation Research Part C: Emerging Technologies*, vol. 54, pp. 187-197, 2015.

[124] A. Shrestha, and A. Mahmood, "Review of deep learning algorithms and architectures," *IEEE Access*, vol. 7, pp. 53040-53065, 2019.

[125] Y. Yu, C. Hu, and J. Zhang, "A review of recurrent neural networks: LSTM cells and network architectures," *Neural Computation*, vol. 31, pp. 1235-1270, 2019.

[126] K. Greff, R. K. Srivastava, J. Koutnik, B. R. Steunebrink, and J. Schmidhuber, "LSTM: A search space odyssey," *IEEE Transactions on Neural Networks and Learning Systems*, vol. 28, no. 10, pp. 2222-2232, 2017.

[127] L. Han, H. Jing, R. Zhang, and Z. Gao, "Wind power forecast based on improved long short term memory network," *Energy*, vol. 189, pp. 1-9, 2019.

[128] J. Lei, C. Liu, and D. Jiang, "Fault diagnosis of wind turbine based on long short-term memory networks," *Renewable Energy*, vol. 133, no. 422-432, 2019.

[129] F. A. Gers, J. Schmidhuber, and F. Cummins, "Learning to forget: continual prediction with LSTM," in *1999 Ninth International Conference on Artificial Neural Networks ICANN 99*, Edinburgh, UK, 1999, pp. 850-855.

[130] R. DiPetro, and G. D. Hager, "Deep learning: RNNs and LSTM," in *Handbook of Medical Image Computing and Computer Assisted Intervention*: The Elsevier and MICCAI Society Book Series, 2020, pp. 503-519.

[131] A. K. Jain, M.N. Murty, and P.J. Flynn, "Data clustering: a review," *ACM Computing Surveys*, vol. 31, no. 3, pp. 264-323, 1999.

[132] R. Xu, and D. Wunsch, "Survey of clustering algorithms," *IEEE Transactions on Neural Networks*, vol. 16, no. 3, pp. 645-678, 2005.

[133] S. Aghabozorgi, A. Seyed Shirkhorshidi, and T. Ying Wah, "Time-series clustering – A decade review," *Information Systems*, vol. 53, pp. 16-38, 2015.

[134] T. Warren Liao, "Clustering of time series data—a survey," *Pattern Recognition*, vol. 38, no. 11, pp. 1857-1874, 2005.

[135] T. Fu, "A review on time series data mining," *Engineering Applications of Artificial Intelligence*, vol. 24, no. 1, pp. 164-181, 2011.

[136] M. Vlachos, G. Kollios, and D. Gunopulos, "Discovering Similar Multidimensional Trajectories," in *Porceedings of 18th International Conference on Data Engineering*, San Jose, CA, USA, 2002, pp. 1-12.

[137] E. Keogh and C. A. Ratanamahatana, "Exact indexing of dynamic time warping," *Knowledge and Information Systems*, vol. 7, no. 3, pp. 358-386, 2005.

[138] Z. Geler, V. Kurbalija, M. Ivanović, M. Radovanović, and W. Dai, "Dynamic time warping: Itakura vs Sakoe-Chiba," in *2019 IEEE International Symposium on INnovations in Intelligent SysTems and Applications (INISTA)*, Sofia, Bulgaria, 2019, pp. 1-6.

[139] C. C. Aggarwal, and C. K. Reddy, *Data clustering: Algorithms and applications*. Florida, USA: CRC Press, 2013.

[140] J. Han, M. Kamber, and J. Pei, *Data Mining Concepts and Techniques*, 3rd ed. Waltam, USA: Elsevier Inc., 2012.

[141] D. Arthur, and S. Vassilvitskii, "k-means++: the advantages of careful seeding," in *Proceedings of the Eighteents Annual ACM-SIAM Symposium on Discrete Algorithms*, New Orleans, Lousiana, USA, 2007, pp. 1023-1035.

[142] R. T. Ng, and J. Han, "CLARANS: A method for clustering objects for spatial data mining," *IEEE Transactions on Knowledge and Data Engineering*, vol. 14, no. 5, pp. 1003-1016, 2002.

[143] D. Gerbec, S. Gasperic, and F. Gubina, "Determination and allocation of typical load profiles to the eligible consumers," in *2003 IEEE Bologna PowerTech*, Bologna, Italy, 2003, pp. 1-5.

[144] B. S. Everitt, S. Landau, M. Leese and D. Stahl, *Cluster analysis*, 5th ed. John Wiley & Sons, Ltd., 2011.

[145] G. Chicco, R. Napoli, and F. Piglione, "Comparisons among clustering techniques for electricity customer classification," *IEEE Transactions on Power Systems*, vol. 21, no. 2, pp. 933-940, 2006.

[146] S. Guha, R. Rastogi, and K. Shim, "CURE: an efficient clustering algorithm for large databases," in *Proceedings of the 1998 ACM SIGMOD international conference on Management of data*, Seattle, Washington, USA, 1998, pp. 73-84.

[147] M. Bicego, V. Murino, and M. A. T. Figueiredo, "Similarity-based clustering of sequences using hidden Markov models," in *Proceedings of the 3rd international conference on Machine learning and data mining in pattern recognition*, Leipzig, Germany, 2003, pp. 86-95.

[148] T. Oates, L. Firoiu, and P. R. Cohen, "Clustering time series with hidden markov models and dynamic time warping," in *Proceedings of IJCAI-99 Workshop Neural, Symbolic, and Reinforcement Learning Methods for Sequence Learning*, Stockholm, Sweden, 1999, pp. 17-21.

[149] K. Kalpakis, D. Gada, V. Puttagunta, "Distance measures for effective clustering of ARIMA time-series," in *Proceedings of 2001 IEEE International Conference on Data Mining*, San Jose, CA, USA, 2001, pp. 273-280.

[150] W. W. S. Wei, *Time series analysis: univariate and multivariate methods*, 2nd ed. Pearson Education, Inc., 2006.

[151] E. A. Maharaj, "A significance test for classifying ARMA models," *Journal of Statistical Computation and Simulation*, vol. 54, no. 4, pp. 305-331, 1996.

[152] P. Smyth, "Clustering sequences with hidden Markov models," *Advances in Neural Information Processing*, vol. 9, pp. 648-654, 1997.

[153] T. Kohonen, "The self-organizing map," *Proceedings of the IEEE*, vol. 78, no. 9, pp. 1464-1480, 1990.

[154] M. Ester, H. P. Kriegel, J. Sander, and X. Xu, "A density-based algorithm for discovering clusters in large spatial databases with noise," in *Proceedings of 1996 International Conference on Knowledge Discovery and Data Mining (KDD'96)*, Portland, Oregon, USA, 1996, pp. 226-231.

[155] M. Ankerst, M. M. Breunig, H. P. Kriegel, and J. Sander, "OPTICS: ordering points to identify the clustering structure," in *Proceedings of ACM SIGMOD'99 International Conference on Management Data*, Philadelphia, USA, 1999, pp. 49-60.

[156] A. Hinneburg, and D. A. Keim, "An efficient approach to clustering in large multimedia databases with noise," in *Proceedings of the Fourth International Conference on Knowledge Discovery and Data Mining (KDD'98)*, New York, USA, 1998, pp. 58-65.

[157] M. P. Wand, and M. C. Jones, *Kernel smoothing*. Boca Raton, FL, USA: Chapman & Hall/CRC, 1995.

[158] M. Chiș, S. Banerjee, and A. E. Hassanien, "Clustering time series data: An evolutionary approach," in *Foundations of Computational Intelligence*, vol. 6, 2009, pp. 193-207.

[159] G. Chicco, R. Napoli, P. Postolache, M. Scutariu and C. Toader, "Customer characterization for improving the tariff offer," *IEEE Transactions on Power Systems*, vol. 18, no. 1, pp. 381-387, 2003.

[160] G. J. Tsekouras, P. B. Kotoulas, C. D. Tsirekis, E. N. Dialynas, and N. D. Hatziargyriou, "A pattern recognition methodology for evaluation of load profiles and typical days of large electricity customers," *Electric Power System Research*, vol. 78, no. 9, pp. 1494-1510, 2008.

[161] M. Begovic, A. Pregelj, A.Rohatgi, D. Novosel, "Impact of renewable distributed generation on power systems," in *Proceedings of the 34th Hawaii International Conference on System Science*, Maui, Hawaii, USA, 2001, pp. 654-663.

[162] T. C. Havens, J .C. Bezdek, C. Leckie, L. O. Hall, M. Palaniswami, "Fuzzy c-means algorithms for very large data," *IEEE Transactions on Fuzzy Systems*, vol. 20, no. 6, pp. 1130-1146, 2012.

[163] Y. Zhu, "Ranking of power system loads based on their influence on power system stability," PhD thesis, School of Electrical and Electronic Engineering, The University of Manchester, 2019.

[164] *DIgSILENT PowerFactory 2020 User Manual*. DIgSILENT GmbH, 2020. [Online]. Available: https://www.digsilent.de/en/powerfactory-download.html.

[165] M. J. Gibbard, N. Martins, J. J. Sanchez-Gasca, N. Uchida, V. Vittal, and L. Wang, "Recent applications of linear analysis techniques," *IEEE Transactions on Power Systems*, vol. 16, no. 1, pp. 154-162, 2001.

[166] P. Gupta, R. S. Bhatia, and D. K. Jain, "Active ROCOF relay for islanding detection," *IEEE Transactions on Power Systems*, vol. 32, no. 1, pp. 420-429, 2017.

[167] "Frequency Measurement: Requirements and Usage," ENTSO-E, RG-CE System Protection & Dynamics Sub Group, 2018, [Online]. Available: https://docstore.entsoe.eu/Documents/SOC%20documents/Regional_Groups_Continental_Europe/2018/TF_Freq_Meas_v7.pdf.

[168] W. Hu, Z. Wu, and V. Dinavahi, "Dynamic analysis and model order reduction of virtual synchronous machine based microgrid," *IEEE Access*, vol. 8, pp. 106585-106600, 2020.

[169] "Stability definitions and characterization of dynamic behavior in systems with high penetration of power electronic interfaced technologies," IEEE Power & Energy Society Technical Report, April 2020, [Online]. Available: https://resourcecenter.ieee-pes.org/technical-publications/technical-reports/PES_TP_TR77_PSDP_stability_051320.html.

[170] *MATLAB and Statistics Toolbox Release 2018*. The Mathworks, Inc., Natick, Massachusetts, United States.

[171] D. Pudjianto, C. Ramsay, and G. Strbac, "Virtual power plant and system integration of distirbuted energy resources," *IET Renewable Power Generation*, vol. 1, no. 1, pp. 10-16, 2017.

[172] "D5.2 - Assessment of the combination of RES and storage alternatives under the Manager Energy for Hybrid Plants (ME4HP) and REDOX flow battery characterization," CROSSBOW Project, [Online]. Available: http://crossbowproject.eu/deliverables/, 2019.

[173] P. M. Anderson, and A. A. Fouad, *Power system control and stability*. Iowa: Iowa State University Press, 1977.

[174] J. Schlabbach, and K. H. Rofalski, *Power system engineering: Planning, design, and operation of power systems and equipment*. Weinheim, Germany: WILEY-VCH Verlag GmbH & Co, 2008.

[175] J. Y. Jackson, "Interpretation and use of generator reactive capability diagrams," *IEEE Transactions on Industry and General Applications*, vol. IGA-7, no. 6, pp. 729-732, 1971.

[176] Energinet. Technical regulation 3.2.2 for PV power plants above 11 kW [Online] Available: https://en.energinet.dk/media/C4ED8450A81243EE83ED795040D5DADD.PDF?la=en&hash=56CE2D05FBB235E28A01D454022FE26744C074EF

[177] Energinet. Technical regulation 3.2.5 for wind power plants above 11 kW [Online] Available: https://en.energinet.dk/-/media/BD322E7805694462AB125E5B5D0D79BC.PDF?la=en&hash=DB619E3EAD98AD2F2691CEA0B68BE8B438F4B3FD

[178] Energinet. Technical regulation 3.3.1 for battery plants [Online] Available: https://en.energinet.dk/-/media/304060D165A9447FBA3D6ED8B73CCC9E.pdf?la=en&hash=037064A5AA7E9396EB9C946A7857CA7D0A7A688C

[179] "Turbine-governor models: Standard dynamic turbine-governor systems in NEPLAN power system analysis tool," NEPLAN AG, 2017, [Online]. Available: https://www.neplan.ch/wp-content/uploads/2015/08/Nep_TURBINES_GOV.pdf.

[180] "Exciter models: Standard dynamic excitation systems in NEPLAN power system analysis tool," NEPLAN AG, 2013, [Online]. Available: https://www.neplan.ch/wp-content/uploads/2015/08/Nep_EXCITERS1.pdf.

[181] *Wind turbines – Part 27 – 1: Electrical simulation models – Wind turbines*, 2015.

[182] P. N. Papadopoulos, and J. V. Milanović, "Probabilistic framework for transient stability assessment of power systems with high penetration of renewable generation," *IEEE Transactions on Power Systems*, vol. 32, no. 4, pp. 3078-3088, 2017.

[183] F. Gonzalez-Longatt, and J. L. Rueda Torres, *Modelling and simulation of power electronic converter dominated power systems in PowerFactory*. Springer Nature Switzerland AG, 2021.

[184] A. Adrees, and J. V. Milanović, "Study of frequency response in power system with renewable generation and energy storage," in *Proceedings of the 19th Power Systems Computation Conference (PSCC)*, Genoa, Italy, 2016, pp. 1-7.

[185] A. Adrees, and J.V. Milanović, "Impact of energy storage systems on the stability of low inertia power systems," in *Proceedings of the 2017 IEEE PES Innovative Smart Grid Technologies Conference Europe (ISGT-Europe)*, Torino, Italy, 2017, pp. 1-6.

[186] "Technical background for the low frequency demand disconnection requirements," European Network of Transmission System Operators (ENTSO-E), 2014, [Online]. Available: https://eepublicdownloads.entsoe.eu/clean-documents/Network%20codes%20documents/NC%20ER/141215_Technical_background_for_LFDD.pdf.

[187] G. Rietveld, P. S. Wright, and A. J. Roscoe, "Reliable rate-of-change-of-frequency measurements: Use cases and test conditions," *IEEE Transactions on Instrumentation and Measurement*, vol. 69, no. 9, pp. 6657-6666, 2020.

[188] M. T. Hagh, and T. Khalili, "A review of fault ride through of PV and wind renewable energies in grid codes," *International Journal of Energy Research*, vol. 43, no. 4, pp. 1342-1356, 2019.

[189] W. Li, *Risk assessment of power systems: models, methods, and applications*, 2nd ed. Hoboken, New Jersey: John Wiley & Sons, Inc., 2014.

[190] K. C. Cebrian, L. Camilo, N. Kagan, N. M. Matsuo, and H. Arango, "Consideration of voltage sags disruption risks in distribution planning studies," in *Proceedings of the CIRED 18th International Conference on Electricity Distribution*, Turin, Italy, 2005, pp. 1-4.

[191] V. C. Raykar, and R. Duraiswami, "Fast optimal bandwidth selection for kernel density estimation," in *Proceedings of the 6th SIAM International Conference on Data Mining*, Washington, DC, USA, 2006, pp. 524-528.

[192] I. Iacopini, "Spatio-temporal analysis of car crash occurrences," MSc thesis, Department of Physics, University of Turin, 2015.

[193] D. W. Scott, *Multivariate density estimation: theory, practice, and visualization*. New York, USA: John Wiley, 1992.

[194] M. C. Jones, J. S. Marron, and S. J. Sheather, "A brief survey of bandwidth selection for density estimation," *Journal of the American Statistcal Association*, vol. 91, no. 433, pp. 401-407, 1996.

[195] I. B. Mohamad, and D. Usman, "Standardization and its effects on k-means clustering algorithm," *Research Journal of Applied Sciences, Engineering and Technology*, vol. 6, no. 17, pp. 3299-3303, 2013.

[196] ENTSO-E Transparency Platform. [Online] Available: https://transparency.entsoe.eu

[197] R. D. Zimmerman, and C. E. Murillo-Sanchez, *Matpower User's Manual, Version 7.1*. 2020. [Online]. Available: https://matpower.org/docs/MATPOWER-manual.pdf.

[198] R. Preece, and J .V. Milanović, "Efficient estimation of the probability of small-disturbance instability of large uncertain power systems," *IEEE Transactions on Power Systems*, vol. 31, no. 2, pp. 1063-1072, 2016.

[199] R. C. Leborgne, G. Olguin, J. M. Carvalho Filho, and M. H. J. Bollen, "Differences in voltage dip exposure depending upon phase-to-phase and phase-to-neutral monitoring connections," *IEEE Transactions on Power Delivery*, vol. 22, no. 2, pp. 1153-1159, 2007.

[200] Y. Zhang, "Techno-economic assessment of voltage sag performance and mitigation," PhD thesis, School of Electrical and Electronic Engineering, The University of Manchester, Manchester, U.K., 2008.

[201] T. N. Sainath, O. Vinyals, A. Senior, and H. Sak, "Convolutional, Long Short-Term Memory, fully connected deep neural networks," in *Proceedings of the 2015 IEEE International Conference on Acoustics, Speech and Signal Processing (ICASSP)*, South Brisbane, QLD, Australia, 2015, pp. 4580-4584.

[202] L. Yang, and A. Shami, "On hyperparameter optimization of machine learning algorithms: Theory and practice," *Neurocomputing*, vol. 415, pp. 295-316, 2020.

[203] M. Clerc, *Particle Swarm Optimization*. ISTE Ltd, 2006.

[204] Y. Shi, and R. C. Eberhart, "Empirical study of particle swarm optimization," in *Proceedings of the 1999 Congress on Evolutionary Computation-CEC99*, Washington, DC, USA, 1999, pp. 1945-1950.

[205] R. C. Eberhart, and Y. Shi, "Particle swarm optimization: developments, applications and resources," in *Proceedings of the 2001 Congress on Evolutionary Computation*, Seoul, South Korea, 2001, pp. 81-86.

[206] D. W. Boeringer, and D. H. Werner, "Particle swarm optimization versus genetic algorithms for phased array synthesis," *IEEE Transactions on Antennas and Propagation*, vol. 52, no. 3, pp. 771-779, 2004.

[207] R. Poli, J. Kennedy, and T. Blackwell, "Particle swarm optimization: An overview," *Swarm Intelligence*, vol. 1, no. 1, pp. 33-57, 2007.

[208] D. P. Kingma, and J. L. Ba, "Adam: A method for stochastic optimization," in *Proceedings of the 3rd International Conference for Learning Representations*, San Diego, USA, 2015, pp. 1-15.

[209] W. Zhong, M. A. A. Murad, M. Liu, and F. Milano, "Impact of virtual power plants on power system short-term transient response," *Electric Power Systems Research*, vol. 189, p. 106609, 2020.

[210] T. Guo, and J. V. Milanović, "Probabilistic framework for assessing the accuracy of data mining tool for online prediction of transient stability," *IEEE Transactions on Power Systems*, vol. 29, no. 1, pp. 377-385, 2014.

[211] J. D. M. Alvarado, "Probabilistic transient stability assessment and corrective control of power systems with increasing penetration of non-synchronous generation," PhD thesis, Department of electrical and electronic engineering, The University of Manchester, 2021.

[212] R. Preece, and J .V. Milanović, "Tuning of a damping controller for multiterminal VSC-HVDC grids using the probabilistic collocation method," *IEEE Transactions on Power Delivery*, vol. 29, no. 1, pp. 318–326, 2014.

[213] Vestas Americas Inc. V80-2.0 MW: Unsurpassed reliability and performance at high-wind sites in North America [Online] Available: http://www.vestas.com

[214] M. Fan, V. Vittal, G. T. Heydt, and R. Ayyanar, "Probabilistic power flow studies for transmission systems with photovoltaic generation using cumulants," *IEEE Transactions on Power Systems*, vol. 27, no. 4, pp. 2251–2261, 2012.

[215] G. L. Torres, and V. H. Quintana, "An interior-point method for nonlinear optimal power flow using voltage rectangular coordinat," *IEEE Transactions on Power Systems*, vol. 13, no. 4, pp. 1211-1218, 1998.

Appendix A: Kernel Density Estimation Approach

A.1: Derivation of the Expression for the AMISE Criterion

Bias and variance of the kernel density estimate can be computed as follows [157]:

$$Bias\left(\hat{f}_h(x)\right) = E\left[\hat{f}_h(x)\right] - f(x) = E[K_h(x)] - f(x), \tag{A.1}$$

$$Var\left(\hat{f}_h(x)\right) = \frac{1}{N} Var\left(K_h(x)\right), \tag{A.2}$$

$$Var\left(K_h(x)\right) = E\left[\left(K_h(x)\right)^2\right] - (E[K_h(x)])^2. \tag{A.3}$$

The formula for $E[K_h(x)]$ is:

$$E[K_h(x)] = \int \frac{1}{h} K\left(\frac{x-t}{h}\right) f(t)dt. \tag{A.4}$$

Applying a change of variables $(x-t)/h = w$, (A.4) can be expressed as follows:

$$E[K_h(x)] = \int K(w) f(x-hw)dw. \tag{A.5}$$

Expanding $f(x-hw)$ in a Taylor series about *x* results in the following expression:

$$E[K_h(x)] = \int K(w)\left[f(x) - hwf'(x) + \frac{1}{2}h^2w^2f''(x) + \cdots\right]dw. \tag{A.6}$$

Given that the following holds:

$$\int K(w)dw = 1, \int wK(w)dw = 0, \mu_2(K) = \int w^2K(w)dw < \infty, \tag{A.7}$$

(A.6) can be presented in the following simplified form:

$$E[K_h(x)] = f(x) + \frac{1}{2}h^2f''(x)\mu_2(K) + o(h^2). \tag{A.8}$$

The expression for $E\left[\left(K_h(x)\right)^2\right]$, required for the computation of the variance of the kernel density estimate, can be derived similarly to $E[K_h(x)]$:

$$E\left[\left(K_h(x)\right)^2\right] = \int \left(\frac{1}{h}K\left(\frac{x-t}{h}\right)\right)^2 f(t)dt = \frac{1}{h}\int (K(w))^2 f(x-hw)dw, \quad \text{(A.9)}$$

$$E\left[\left(K_h(x)\right)^2\right] = \frac{1}{h}f(x)\int \left(K(w)\right)^2 dw + o(\frac{1}{h}), \quad \text{(A.10)}$$

$$E\left[\left(K_h(x)\right)^2\right] = \frac{1}{h}f(x)R(K) + o(\frac{1}{h}). \quad \text{(A.11)}$$

Finally, the expressions for the bias, variance and MSE of the kernel density estimate are as follows:

$$Bias\left(\hat{f}_h(x)\right) = \frac{1}{2}h^2 f''(x)\mu_2(K) + o(h^2), \quad \text{(A.12)}$$

$$Var\left(\hat{f}_h(x)\right) = \frac{1}{N}\left[\frac{1}{h}f(x)R(K) + o\left(\frac{1}{h}\right) - (f(x) + o(1))^2\right] = \frac{f(x)R(K)}{Nh} + o\left(\frac{1}{Nh}\right), \quad \text{(A.13)}$$

$$MSE\left(\hat{f}_h(x)\right) = Var\left(\hat{f}_h(x)\right) + \left(Bias\left(\hat{f}_h(x)\right)\right)^2, \quad \text{(A.14)}$$

$$MSE\left(\hat{f}_h(x)\right) = \frac{f(x)R(K)}{Nh} + \frac{1}{4}h^4\left(\mu_2(K)\right)^2\left(f''(x)\right)^2 + o\left(\frac{1}{Nh} + h^4\right). \quad \text{(A.15)}$$

Integrating (A.15), the expression for the MISE criterion can be obtained:

$$MISE\left(\hat{f}_h(x)\right) = \frac{R(K)}{Nh} + \frac{1}{4}h^4\left(\mu_2(K)\right)^2 R\left(f''(x)\right) + o\left(\frac{1}{Nh} + h^4\right). \quad \text{(A.16)}$$

Finally, the AMISE criterion can be defined as follows:

$$AMISE\left(\hat{f}_h(x)\right) = \frac{R(K)}{Nh} + \frac{1}{4}(\mu_2(K))^2 h^4 R(f''(x)). \quad \text{(A.17)}$$

A.2: The Optimal Bandwidth for the Estimator of the Integrated Squared Density Functionals

The $\widehat{\Psi}_r$ estimator can be expressed as follows [157]:

$$\widehat{\Psi}_r = \frac{1}{N}\sum_{i=1}^{N} \hat{f}_h^{(r)}(x_i) = \frac{1}{N^2 g_r^{r+1}}\sum_{i=1}^{N}\sum_{j=1}^{N} K^{(r)}(\frac{x_i - x_j}{g_r}), \quad \text{(A.18)}$$

$$\widehat{\Psi}_r = \frac{1}{N g_r^{r+1}}K^{(r)}(0) + \frac{1}{N^2 g_r^{r+1}}\sum_{i=1}^{N}\sum_{\substack{j=1 \\ j\neq i}}^{N} K^{(r)}(\frac{x_i - x_j}{g_r}). \quad \text{(A.19)}$$

The bias of the estimate of the Ψ_r functional is:

$$Bias\left(\widehat{\Psi}_r\right) = E\left(\widehat{\Psi}_r\right) - \Psi_r. \tag{A.20}$$

The expected value of the $\widehat{\Psi}_r$ estimator can be computed as follows:

$$E\left(\widehat{\Psi}_r\right) = \frac{1}{Ng_r^{r+1}} K^{(r)}(0) + \frac{N(N-1)}{N^2} E\left(\frac{1}{g_r^{r+1}} K^{(r)}\left(\frac{x_1 - x_2}{g_r}\right)\right), \tag{A.21}$$

$$E\left(\frac{1}{g_r^{r+1}} K^{(r)}\left(\frac{x_1 - x_2}{g_r}\right)\right) = \iint \frac{1}{g_r^{r+1}} K^{(r)}\left(\frac{x-y}{g_r}\right) f(x) f(y) dx dy. \tag{A.22}$$

Using the integration by parts and the change of variables ($\frac{x-y}{g_r} = w$), (A.22) can be expressed as follows:

$$E\left(\frac{1}{g_r^{r+1}} K^{(r)}\left(\frac{x_1 - x_2}{g_r}\right)\right) = \iint K(w)\, f(y + g_r w) f^{(r)}(y) dw dy, \tag{A.23}$$

and expanding $f(y + g_r w)$ in a Taylor series about *y* results in the following expression:

$$E\left(\frac{1}{g_r^{r+1}} K^{(r)}\left(\frac{x_1 - x_2}{g_r}\right)\right) = \Psi_r + \frac{1}{2} g_r^2 \mu_2(K) \Psi_{r+2} + o(g_r^2). \tag{A.24}$$

The expression for the bias then equals:

$$Bias\left(\widehat{\Psi}_r\right) = \frac{1}{Ng_r^{r+1}} K^{(r)}(0) + \frac{1}{2} g_r^2 \mu_2(K) \Psi_{r+2} + o(g_r^2). \tag{A.25}$$

Finally, the optimal bandwidth value for the $\widehat{\Psi}_r$ estimate is:

$$g_r = \left[-\frac{2K^{(r)}(0)}{\mu_2(K) \Psi_{r+2} N}\right]^{1/(r+3)}. \tag{A.26}$$

A.3: The Normal Scale Rule

The standard density function of zero mean and unit variance is [157]:

$$\Phi(x) = \frac{1}{\sqrt{2\pi}} e^{-x^2/2}. \tag{A.27}$$

Assuming that the underlying PDF is a normal density with zero mean and variance σ^2, the underlying PDF can be expressed as follows [157]:

$$\Phi_\sigma(x) = \frac{1}{\sigma\sqrt{2\pi}} e^{-x^2/2\sigma^2} = \frac{1}{\sigma}\Phi(\frac{x}{\sigma}). \tag{A.28}$$

The *r*-th derivative of the underlying PDF is [157]:

$$\Phi_\sigma{}^{(r)}(x) = \frac{\partial^r}{\partial x^r}\Phi_\sigma(x) = \frac{\partial^r}{\partial x^r}\left(\frac{1}{\sigma}\Phi(\frac{x}{\sigma})\right) = \frac{1}{\sigma^{r+1}}\Phi^{(r)}(\frac{x}{\sigma}), \tag{A.29}$$

$$\Phi^{(r)}(x) = (-1)^r H_r(x)\Phi(x), \tag{A.30}$$

$$H_r(x) = \sum_{j=0}^{r/2}(-1)^j OF(2j)\binom{r}{2j}x^{r-2j}, \tag{A.31}$$

$$OF(2j) = (2j-1)(2j-3)\ldots 1 = \frac{(2j)!}{2^j j!}, \tag{A.32}$$

where H_r is the *r*-th Hermite polynomial and *OF* is the "Odd Factorial".

Given that the underlying PDF is known (A.28), density functionals can be computed exactly:

$$\Psi_r = \int \Phi_\sigma{}^{(r)}(x)\Phi_\sigma(x)dx = \int \frac{1}{\sigma^{r+1}}\Phi^{(r)}\left(\frac{x}{\sigma}\right)\frac{1}{\sigma}\Phi(\frac{x}{\sigma})dx, \tag{A.33}$$

$$\Psi_r = \frac{(-1)^r}{\sigma^{r+2}}\int H_r\left(\frac{x}{\sigma}\right)\left(\Phi(\frac{x}{\sigma})\right)^2 dx = \frac{(-1)^r}{\sigma^{r+2}}\int H_r\left(\frac{x}{\sigma}\right)\frac{1}{2\pi}e^{-x^2/\sigma^2}dx, \tag{A.34}$$

$$\Psi_r = \frac{(-1)^r}{2\pi\sigma^{r+2}}\sum_{j=0}^{r/2}(-1)^j OF(2j)\binom{r}{2j}\int\left(\frac{x}{\sigma}\right)^{r-2j} e^{-x^2/\sigma^2}dx. \tag{A.35}$$

Knowing that $\int e^{-x^2}dx = \sqrt{\pi}$, and $\int x^j e^{-x^2}dx = 0$ for odd *j*, the following expression for the Ψ_r functional can be obtained:

$$\Psi_r = \frac{(-1)^r}{2\pi\sigma^{r+2}} \cdot \frac{(-1)^{r/2}\sqrt{\pi}\sigma r!}{2^r\left(\frac{r}{2}\right)!}. \tag{A.36}$$

Given that *r* is even, the final expression for the Ψ_r functional is:

$$\Psi_r = \frac{(-1)^{r/2} r!}{(2\sigma)^{r+1}\left(\frac{r}{2}\right)!\sqrt{\pi}}. \tag{A.37}$$

Appendix B: The Parameters and Accuracy of Transfer Function-Based Dynamic Equivalent Models

B.1: Case Study - I

B.1.1: Dynamic Equivalent Model 2

The mathematical model of DEM 2 is:

$$z_{Fault,P}(t) = -8.51;\ z_{Fault,Q}(t) = 9.66, \tag{B.1}$$

$$z_{TF,P}(t) = \mathcal{L}^{-1}\left[\frac{-5.2s^6-311s^5+602.2s^4-7339s^3+1.1\cdot10^4s^2+6031s+2760}{s^6+158.4s^5+1226s^4+2.5\cdot10^4s^3+9.6\cdot10^4s^2+2.7\cdot10^4s+2.9\cdot10^4}\right]u_{PCC}(t), \tag{B.2}$$

$$z_{TF,Q}(t) = \mathcal{L}^{-1}\left[\frac{3.9s^4+135.5s^3+418.4s^2+2125s-301.5}{s^4+12.4s^3+156.2s^2+402.5s+1727}\right]u_{PCC}(t), \tag{B.3}$$

$$P_{EQ}(t) = P_{Ss} + 2.19z_{EQ,P}(t);\ Q_{EQ}(t) = Q_{Ss} + 3.9z_{EQ,Q}(t), \tag{B.4}$$

The accuracy of DEM 2 in terms of the shape of HRES plant power responses in time domain is presented in Figure B.1 for the DEM 2 training dataset and in Figure B.2 for the test 2019 year.

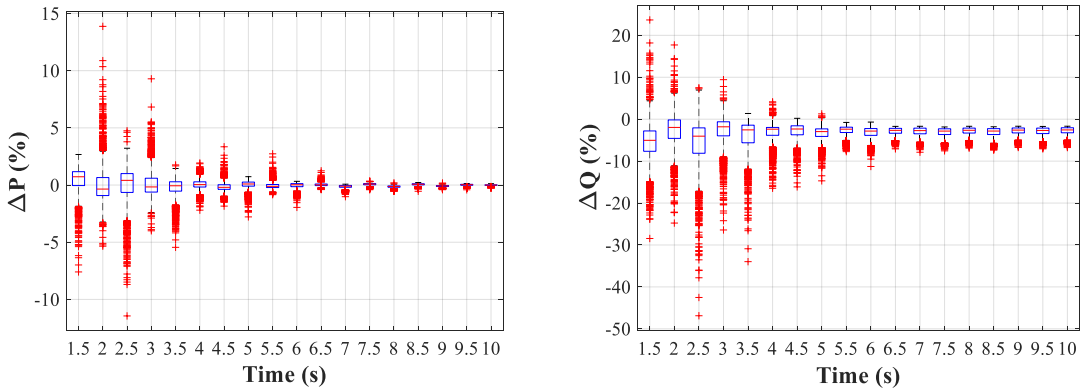

(a) (b)

Figure B.1 CS-I: Training DEM 2 dataset: Comparison between the power responses of the detailed model and DEM 2 ((a): real power, (b): reactive power)

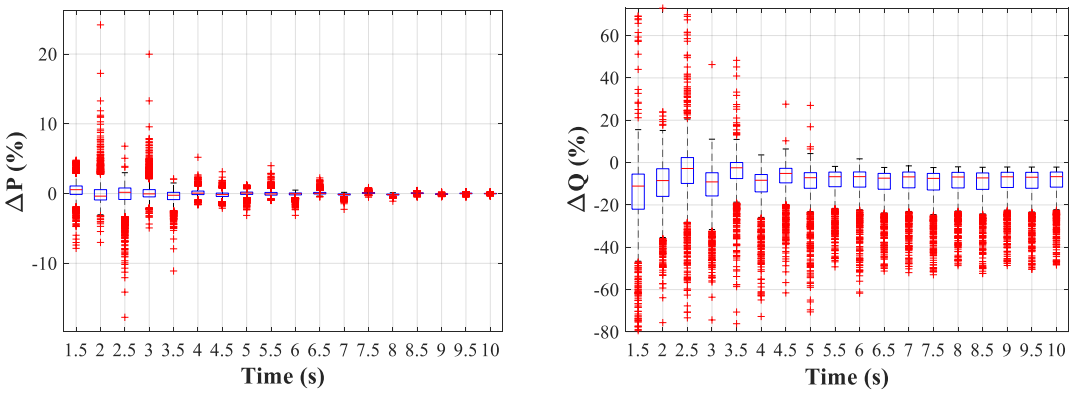

Figure B.2 CS-I: Test 2019 year: Comparison between the power responses of the detailed model and DEM 2 ((a): real power, (b): reactive power)

B.2: Case Study - II

B.2.1: Clusters of historical plant production and system demand data

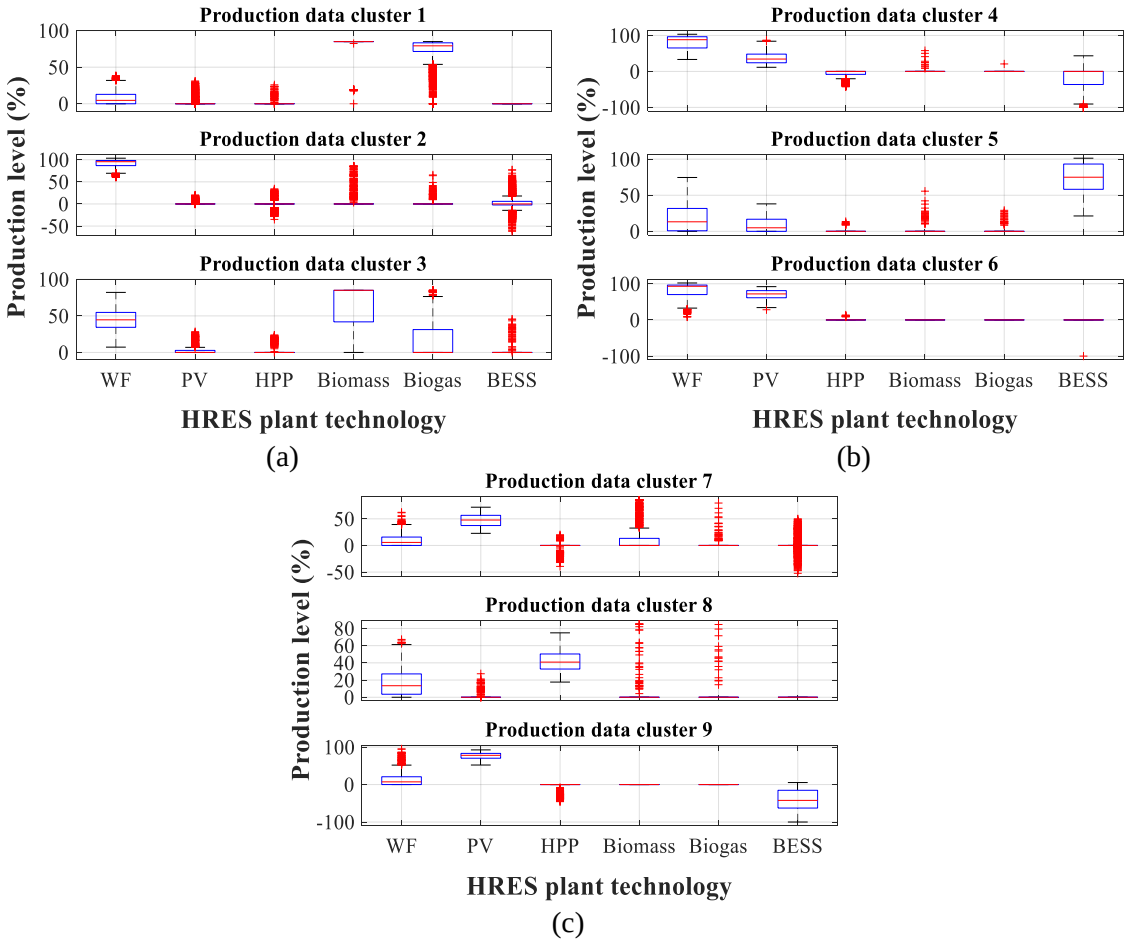

Figure B.3 CS-II: Clusters of HRES plant compositions (base power of the production levels is the rated power of the individual plant)

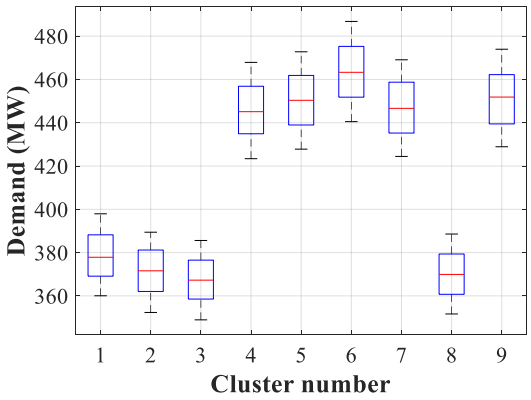

Figure B.4 CS-II: Clusters of historical total demand levels

B.2.2: Dynamic Equivalent Model 1

The mathematical model of DEM 1 is:

$$z_{Fault,P}(t) = -9.51;\ z_{Fault,Q}(t) = 3.87, \tag{B.5}$$

$$z_{TF,P}(t) = \mathcal{L}^{-1}\left[\frac{-3.8s^5-140.2-918.2s^3-9031s^2+5145s+828.4}{s^5+25s^4+282.1s^3+1630s^2+1\cdot10^4s+1\cdot10^4}\right]u_{PCC}(t), \tag{B.6}$$

$$z_{TF,Q}(t) = \mathcal{L}^{-1}\left[\frac{1.4s^6+410.6s^5+2.5\cdot10^4s^4+1.6\cdot10^4s^3+3.9\cdot10^5s^2-1.5\cdot10^5s-2.4\cdot10^4}{s^6+170.2s^5+1.2\cdot10^4s^4+5.3\cdot10^4s^3+3.8\cdot10^5s^2+4.4\cdot10^5s+3.7\cdot10^5}\right]u_{PCC}(t), \tag{B.7}$$

$$P_{EQ}(t) = P_{Ss} + 2.15z_{EQ,P}(t);\ Q_{EQ}(t) = Q_{Ss} + 10.34z_{EQ,Q}(t). \tag{B.8}$$

The accuracy of DEM 1 in terms of the shape of HRES plant real and power responses in time domain is presented in Figure B.5 (a) and Figure B.5 (b) for the DEM 1 training dataset, respectively.

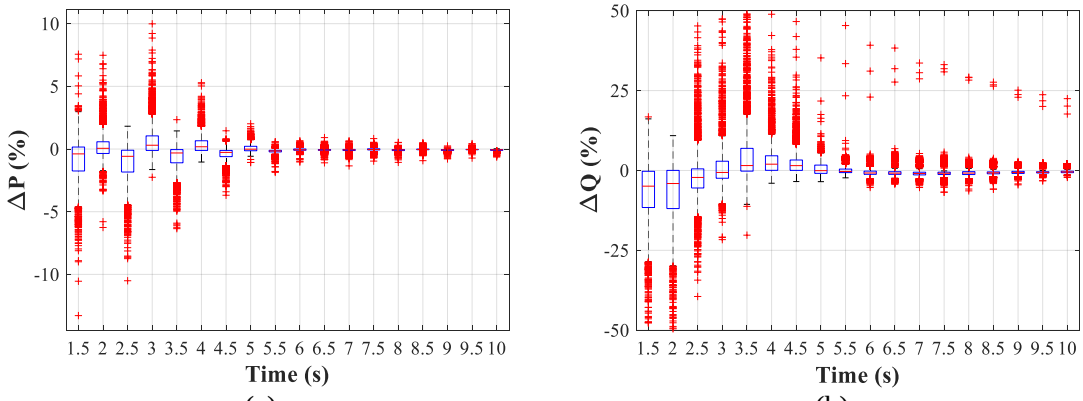

Figure B.5 CS-II: Training DEM 1 dataset: Comparison between the power responses of the detailed model and DEM 1 ((a): real power, (b): reactive power)

B.2.3: Dynamic Equivalent Model 3

The mathematical model of DEM 3 is:

$$z_{Fault,P}(t) = -8.87;\ z_{Fault,Q}(t) = 1.51, \tag{B.9}$$

$$z_{TF,P}(t) = \mathcal{L}^{-1}\left[\frac{-1.7s^6+365s^5-1488s^4+6.8\cdot10^4s^3-5.6\cdot10^5s^2+1.2\cdot10^6s-5\cdot10^4}{s^6+423s^5+8214s^4+1.3\cdot10^5s^3+1.3\cdot10^6s^2+6.8\cdot10^6s+2.6\cdot10^5}\right]u_{PCC}(t), \tag{B.10}$$

$$z_{TF,Q}(t) = \mathcal{L}^{-1}\left[\frac{5.4s^3+2170s^2+5\cdot10^4s-5816}{s^3+323.7s^2+3735s+5.1\cdot10^4}\right]u_{PCC}(t), \tag{B.11}$$

$$P_{EQ}(t) = P_{Ss} + 4.52z_{EQ,P}(t);\ Q_{EQ}(t) = Q_{Ss} + 4.96z_{EQ,Q}(t). \tag{B.12}$$

The accuracy of DEM 3 in terms of the shape of HRES plant real and power responses in time domain is presented in Figure B.6 (a) and Figure B.6 (b) for the DEM 3 training dataset, respectively.

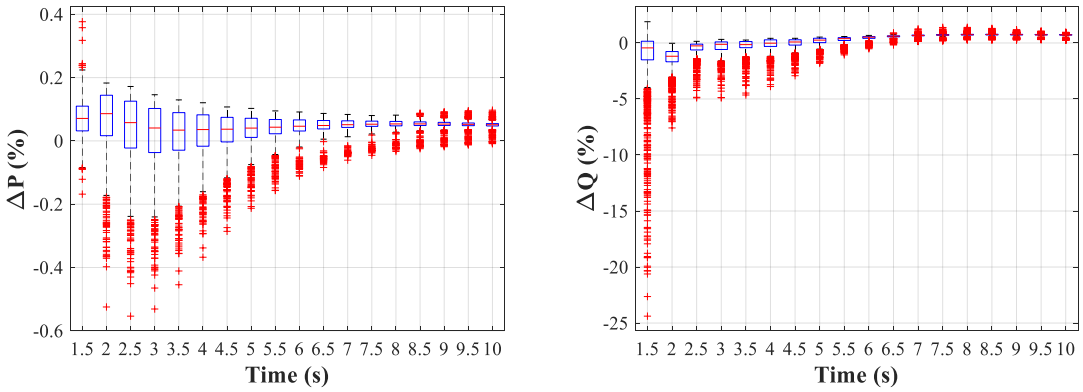

Figure B.6 CS-II: Training DEM 3 dataset: Comparison between the power responses of the detailed model and DEM 3 ((a): real power, (b): reactive power)

Appendix C: CS-I: Clusters of HRES Plant Power Responses and Optimal LSTM Network Topologies

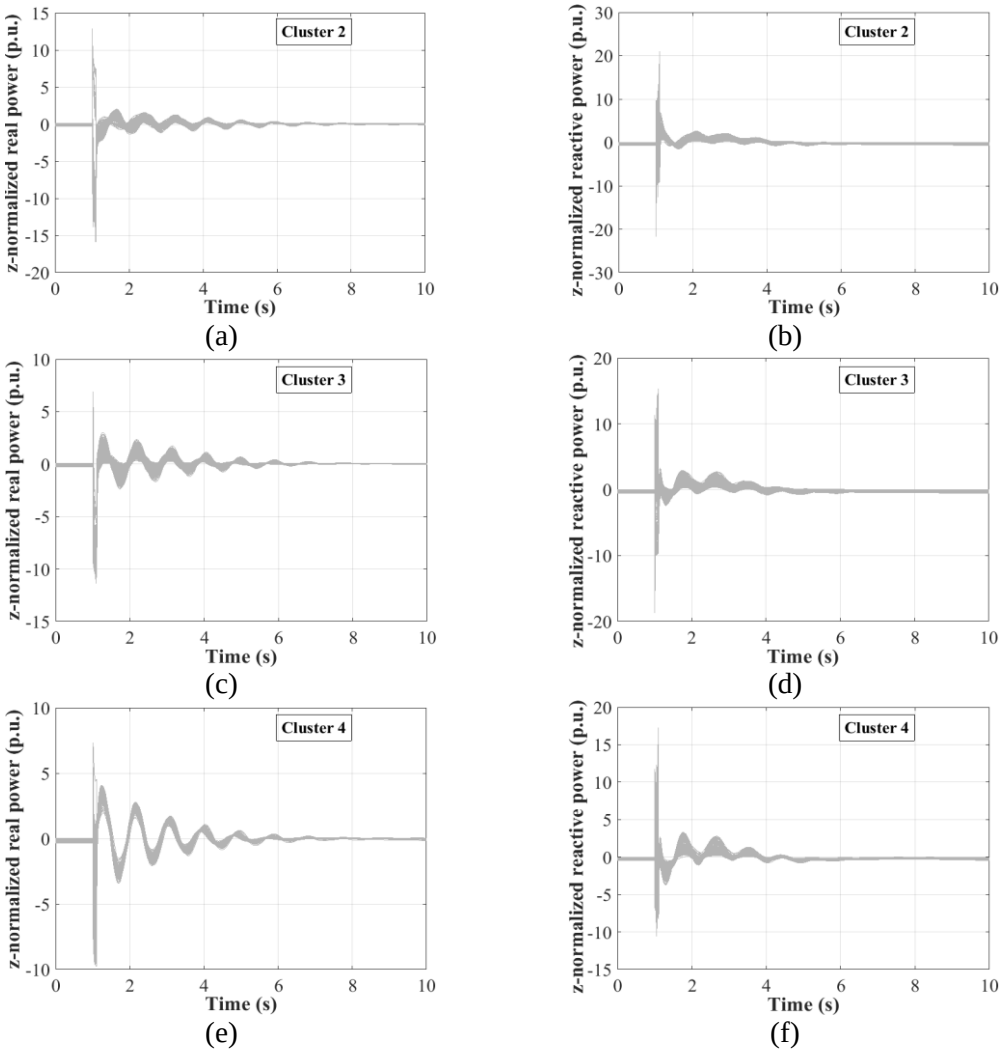

Figure C.1 Clusters of z-normalized power responses ((a): Cluster 2 - real power; (b): Cluster 2 - reactive power; (c): Cluster 3 - real power; (d): Cluster 3 - reactive power; (e): Cluster 4 - real power; (f): Cluster 4 - reactive power)

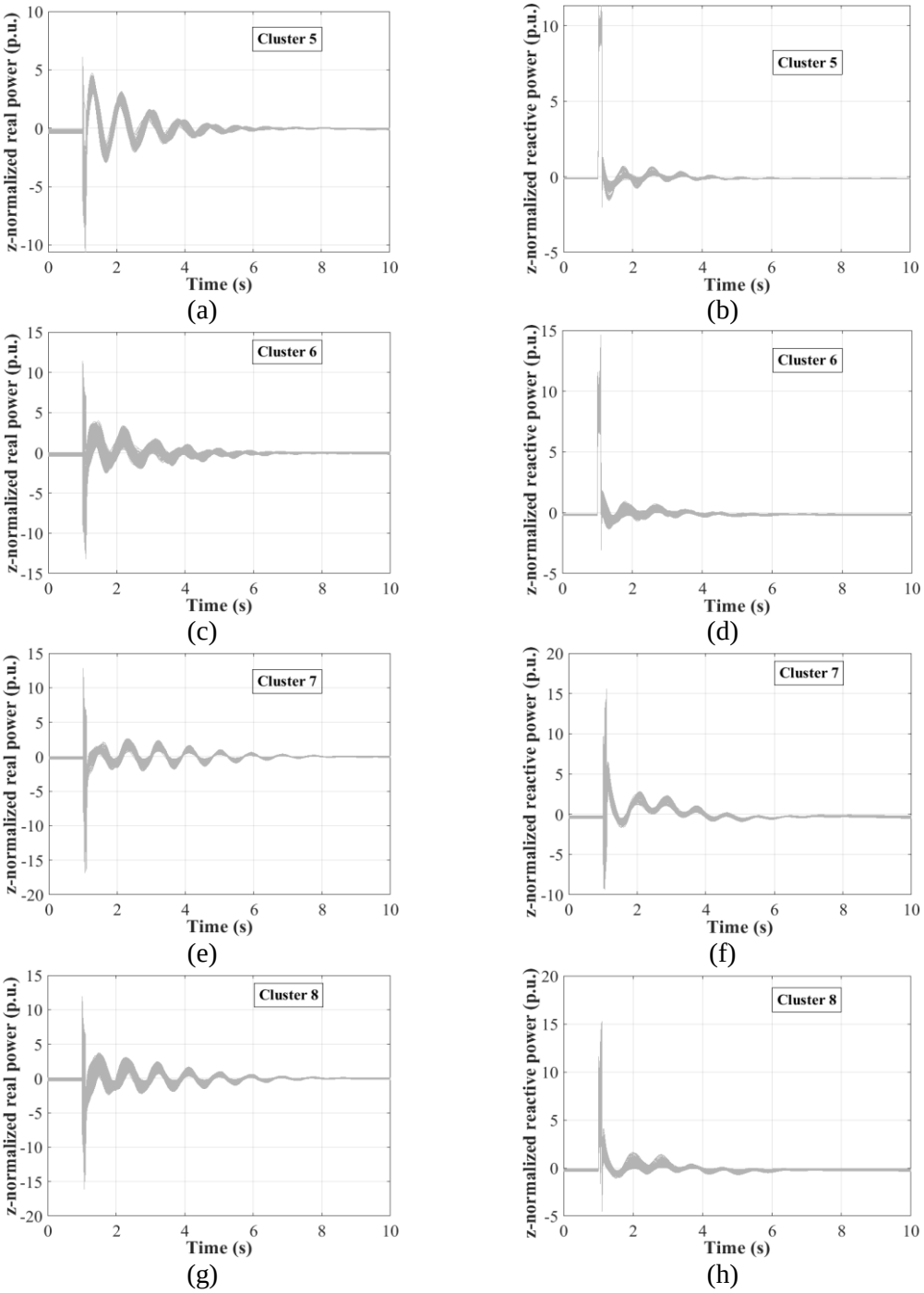

Figure C.2 Clusters of z-normalized power responses ((a): Cluster 5 - real power; (b): Cluster 5 - reactive power; (c): Cluster 6 - real power; (d): Cluster 6 - reactive power; (e): Cluster 7 - real power; (f): Cluster 7 - reactive power; (g): Cluster 8 - real power; (h): Cluster 8 - reactive power)

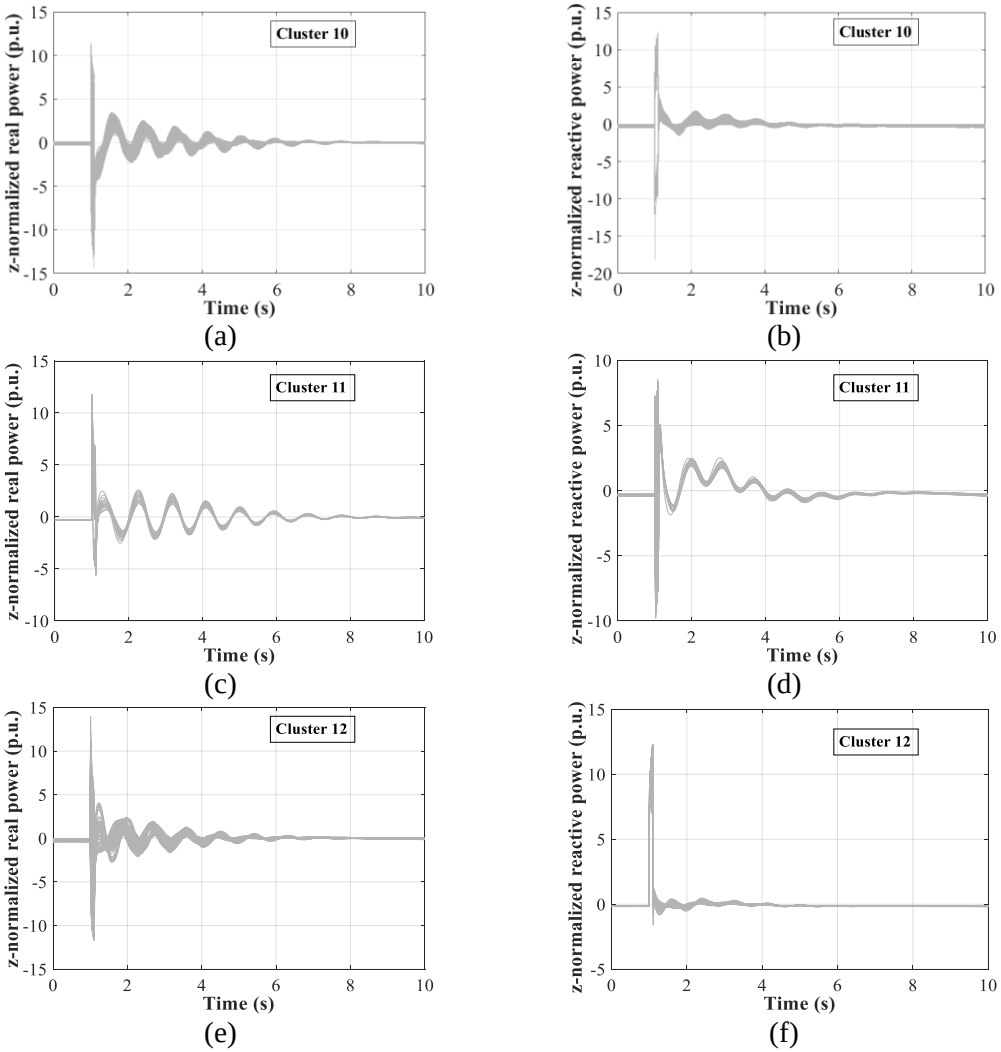

Figure C.3 Clusters of z-normalized power responses ((a): Cluster 10 - real power; (b): Cluster 10 - reactive power; (c): Cluster 11 - real power; (d): Cluster 11 - reactive power; (e): Cluster 12 - real power; (f): Cluster 12 - reactive power

Table C.1 The LSTM network structure and the number of LSTM network estimable parameters for clusters 2-5, 7, 9, 11, 12

Cluster	LSTM layers	FC layers	No. parameters per LSTM layer	No. parameters per FC layer	Total no. parameters
C 2	(189)	(301; 2)	(151,200)	(57,190; 604)	208,994
C 3	(138; 67; 72)	(1000; 2)	(82,248; 55,208; 165,120)	(173,000; 2,002)	477,578
C 4	(300; 10)	(1000; 2)	(373,200; 12,440)	(11,000; 2,002)	398,462
C 5	(200)	(73; 2)	(168,800)	(14,673; 148)	183,621
C 7	(76)	(759; 2)	(26,448)	(58,443; 1,520)	86,411
C 9	(231; 300)	(188; 2)	(223,608; 638,400)	(56,588; 378)	918,974
C 11	(155; 143)	(470; 2)	(102,920; 171,028)	(67,680; 942)	342,570
C 12	(185)	(1000; 2)	(145,040)	(186,000; 2,002)	333,042

Appendix D: The Number of SG Units in Service for All Three TSs

Table D.1 TS 1: The number of SG units in service per hour in each SG plant, each area and the whole test system

Plant\Hour	1	2	3	4	5	6	7	8	9	10	11	12	13	14	15	16	17	18	19	20	21	22	23	24
G1	3	3	3	3	3	3	3	3	4	4	4	4	4	4	4	4	4	4	4	4	4	4	3	3
G2	2	2	2	2	2	2	2	3	3	3	3	3	3	3	3	3	4	4	3	3	3	3	2	2
G3	3	3	3	3	3	3	3	4	4	4	4	4	4	4	4	4	4	4	4	4	4	4	4	4
G4	0	0	0	0	0	0	0	0	0	0	1	1	0	0	0	0	2	1	1	1	0	0	0	0
G5	0	0	0	0	0	0	0	0	0	0	1	1	0	0	0	0	1	1	1	1	0	0	0	0
G6	4	4	4	4	4	4	4	4	4	4	4	4	4	4	4	4	4	4	4	4	4	4	4	4
G7	4	4	4	4	4	4	4	4	4	4	4	4	4	4	4	4	4	4	4	4	4	4	4	4
G8	2	2	2	2	2	2	2	3	3	3	3	3	3	3	3	3	3	3	3	3	3	3	2	2
G9	4	4	4	4	4	4	4	4	4	4	4	4	4	4	4	4	4	4	4	4	4	4	4	4
G10	4	4	4	4	4	4	4	4	4	4	4	4	4	4	4	4	4	4	4	4	4	4	4	4
G11	4	4	4	4	4	4	4	4	4	4	4	4	4	4	4	4	4	4	4	4	4	4	4	4
G12	4	4	4	4	4	4	4	4	4	4	4	4	4	4	4	4	4	4	4	4	4	4	4	4
G13	2	2	1	1	2	2	2	3	3	3	3	3	3	3	3	3	3	3	3	3	3	3	3	2
G14	1	1	1	1	1	1	2	2	2	2	3	2	2	2	2	2	3	3	3	3	2	2	2	1
G15	0	0	0	0	0	0	0	0	0	0	0	0	0	0	0	0	1	1	0	0	0	0	0	0
G16	4	4	4	4	4	4	4	4	4	4	4	4	4	4	4	4	4	4	4	4	4	4	4	4
G17	4	4	4	4	4	4	4	4	4	4	4	4	4	4	4	4	4	4	4	4	4	4	4	4
G18	4	4	4	4	4	4	4	4	4	4	4	4	4	4	4	4	4	4	4	4	4	4	4	4
G19	4	4	4	4	4	4	4	4	4	4	4	4	4	4	4	4	4	4	4	4	4	4	4	4
G20	4	4	4	4	4	4	4	4	4	4	4	4	4	4	4	4	4	4	4	4	4	4	4	4
G21	4	4	4	4	4	4	4	4	4	4	4	4	4	4	4	4	4	4	4	4	4	4	4	4
G22	2	2	2	2	2	3	4	4	4	4	4	4	4	4	4	4	4	4	4	4	4	4	4	4
G23	4	4	4	4	4	4	4	4	4	4	4	4	4	4	4	4	4	4	4	4	4	4	4	4
G24	0	0	0	0	0	0	2	4	4	4	4	4	4	4	4	4	4	4	4	4	4	4	3	0
G25	0	0	0	0	0	0	0	0	0	0	0	0	0	0	0	0	0	0	0	0	0	0	0	0
G26	0	0	0	0	0	0	0	0	0	0	0	0	0	0	0	0	0	0	0	0	0	0	0	0
G27	2	1	1	1	1	4	4	4	4	4	4	4	4	4	4	4	4	4	4	4	4	4	4	4
G28	4	4	4	4	4	4	4	4	4	4	4	4	4	4	4	4	4	4	4	4	4	4	4	4
G29	4	4	4	4	4	4	4	4	4	4	4	4	4	4	4	4	4	4	4	4	4	4	4	4
G30	4	4	4	4	4	4	4	4	4	4	4	4	4	4	4	4	4	4	4	4	4	4	4	4
G31	0	0	0	0	0	0	4	4	4	4	4	4	4	4	4	4	4	4	4	4	4	4	4	4
G32	3	3	1	0	3	4	4	4	4	4	4	4	4	4	4	4	4	4	4	4	4	4	4	4
G33	0	0	0	0	0	0	0	2	0	0	3	3	0	0	0	2	3	3	3	3	3	0	0	0
G34	0	0	0	0	0	1	3	4	4	4	4	4	4	3	3	4	4	4	4	4	4	4	3	3

Plant\Hour	1	2	3	4	5	6	7	8	9	10	11	12	13	14	15	16	17	18	19	20	21	22	23	24
G35	3	3	3	3	3	4	4	4	4	4	4	4	4	4	4	4	4	4	4	4	4	4	4	3
G36	4	4	4	4	4	4	4	4	4	4	4	4	4	4	4	4	4	4	4	4	4	4	4	4
G37	4	4	4	4	4	4	4	4	4	4	4	4	4	4	4	4	4	4	4	4	4	4	4	4
G38	4	4	4	4	4	4	4	4	4	4	4	4	4	4	4	4	4	4	4	4	4	4	4	4
G39	0	0	0	0	0	0	0	0	0	0	0	0	0	0	0	0	0	0	0	0	0	0	0	0
G40	4	4	4	4	4	4	4	4	4	4	4	4	4	4	4	4	4	4	4	4	4	4	4	4
G41	4	4	4	4	4	4	4	4	4	4	4	4	4	4	4	4	4	4	4	4	4	4	4	4
G42	4	4	4	4	4	4	4	4	4	4	4	4	4	4	4	4	4	4	4	4	4	4	4	4
Area 1	13	13	13	13	13	13	13	14	15	15	15	15	15	15	15	15	16	16	15	15	15	15	13	13
Area 2	30	30	28	27	30	33	39	42	40	40	43	43	40	39	39	42	43	43	43	43	43	40	39	38
Area 3	39	38	37	37	38	42	46	49	49	49	50	49	49	49	49	49	51	51	50	50	49	49	48	43
Area 4	29	29	29	29	29	29	29	31	31	31	33	33	31	31	31	31	34	33	33	33	31	31	30	30
System	111	110	107	106	110	117	127	136	135	135	141	140	135	134	134	137	144	143	141	141	138	135	130	124

Table D.2 TS 2: The number of SG units in service per hour in each SG plant, each area and the whole test system

Plant\Hour	1	2	3	4	5	6	7	8	9	10	11	12	13	14	15	16	17	18	19	20	21	22	23	24
G1	2	2	2	2	2	3	3	3	3	3	3	3	3	3	3	0	3	3	3	3	3	3	3	3
G2	0	0	0	0	0	2	2	2	2	2	2	2	2	2	2	2	0	2	3	2	2	2	2	2
G3	3	3	3	3	3	4	4	4	4	4	3	3	4	4	3	4	4	4	4	4	4	3	3	3
G4	3	3	3	3	3	4	4	4	4	4	4	4	4	4	4	4	4	4	4	4	4	4	3	3
G5	2	2	2	2	2	2	2	2	2	2	2	2	2	2	2	2	3	2	3	2	2	2	2	2
G6	4	4	4	4	4	4	4	4	4	4	4	4	4	0	0	4	4	4	4	4	4	4	4	4
G7	3	3	3	3	3	4	4	4	4	4	4	4	4	4	4	4	4	4	4	4	4	4	4	3
G8	2	1	2	1	2	2	2	2	2	2	2	2	2	2	2	2	2	2	2	2	2	2	2	2
G9	0	0	0	0	0	0	0	0	0	0	0	0	0	0	0	0	0	0	0	0	0	0	0	0
G10	0	0	0	0	0	0	0	0	0	0	0	0	0	0	0	0	0	0	0	0	0	0	0	0
G11	4	4	4	4	4	4	4	4	4	4	4	4	4	4	4	4	4	4	4	4	4	4	4	4
G12	1	1	1	1	1	2	2	2	2	2	2	2	2	2	2	2	2	2	2	2	2	2	2	2
G13	2	2	2	2	2	2	3	3	0	3	3	3	3	3	3	3	3	3	3	3	3	2	2	2
G14	4	4	4	4	4	4	4	4	4	4	4	4	4	4	4	4	4	4	4	4	4	4	4	4
G15	1	1	1	1	1	2	2	2	2	2	2	2	2	2	2	2	2	2	1	2	2	1	1	1
G16	4	4	4	4	4	4	4	4	4	4	4	4	4	4	4	4	4	4	4	4	4	4	4	4
G17	4	4	4	4	4	4	4	4	4	4	4	4	4	4	4	4	4	4	4	4	4	4	4	4
G18	4	4	4	4	4	4	4	4	4	4	4	4	4	4	4	4	4	4	4	4	4	4	4	4
G19	4	4	4	4	4	4	4	4	0	4	4	4	4	4	4	4	4	4	4	4	4	4	4	4
G20	4	4	4	4	4	4	4	4	4	4	4	4	4	4	4	4	4	4	4	4	4	4	4	4
G21	4	4	4	4	4	4	4	4	4	4	4	4	4	4	4	4	4	4	4	4	4	4	4	4
G22	2	2	2	1	2	2	2	3	2	3	2	2	2	3	2	2	4	4	4	4	2	2	2	2
G23	4	4	4	4	4	4	4	4	4	4	4	4	4	4	4	4	4	0	3	4	4	4	4	4
G24	0	0	0	0	0	0	0	0	0	0	0	0	0	0	0	0	0	3	0	0	0	0	0	0
G25	0	0	0	0	0	0	0	0	0	0	0	0	0	0	0	0	0	0	0	0	0	0	0	0
G26	0	0	0	0	0	0	0	0	0	0	0	0	0	0	0	0	0	0	0	0	0	0	0	0
G27	0	0	0	0	0	1	3	4	4	4	2	3	2	4	2	4	4	4	4	4	3	1	1	0
G28	3	3	4	3	4	4	4	4	4	4	4	4	4	4	4	4	4	4	4	4	4	4	4	4
G29	4	4	4	4	4	4	4	4	4	4	4	4	4	4	4	4	4	4	4	4	4	4	4	4
G30	4	4	4	4	4	4	4	4	4	4	4	4	4	4	4	4	4	4	4	4	4	4	4	4

Plant\Hour	1	2	3	4	5	6	7	8	9	10	11	12	13	14	15	16	17	18	19	20	21	22	23	24
G31	4	4	4	3	4	4	4	4	4	4	4	4	4	4	4	4	4	4	4	4	4	4	4	4
G32	2	2	3	2	2	3	3	3	3	3	3	3	3	3	3	3	3	4	4	3	3	3	3	3
G33	0	0	0	0	0	0	0	0	0	0	0	0	0	0	0	0	0	0	0	0	0	0	0	0
G34	0	0	0	0	0	0	0	2	0	0	0	0	0	0	0	0	3	3	3	0	0	0	0	0
G35	0	0	0	0	2	3	4	4	4	4	4	3	4	4	3	4	4	4	4	4	4	3	3	3
G36	4	4	4	4	4	4	4	4	4	4	4	4	4	4	4	4	4	4	4	4	4	4	4	4
G37	3	3	3	3	3	4	4	4	4	4	4	4	4	4	4	4	4	4	4	4	4	4	4	4
G38	4	4	4	4	4	4	4	4	4	4	4	4	4	4	4	4	4	4	4	4	4	4	4	4
G39	0	0	0	0	0	0	0	0	0	0	0	0	0	0	0	0	0	0	0	0	0	0	0	0
G40	4	4	4	4	4	4	4	4	4	4	4	4	4	4	4	4	4	4	4	4	4	4	4	4
G41	2	2	2	2	2	2	2	2	2	2	2	2	2	2	2	2	0	2	3	2	2	2	2	2
G42	4	4	4	3	4	4	4	4	4	4	4	4	4	4	4	4	4	4	4	4	4	4	4	4
Area 1	10	10	10	10	10	13	13	13	13	13	13	13	13	13	13	10	11	13	14	13	13	13	13	13
Area 2	27	27	28	25	29	32	33	35	33	33	33	32	33	33	32	33	34	37	38	33	33	32	32	32
Area 3	40	40	41	39	41	43	46	48	40	48	45	46	45	48	45	47	49	48	47	49	46	42	42	41
Area 4	22	21	22	21	22	26	26	26	26	26	25	25	26	22	21	26	27	26	27	26	26	25	24	23
System	99	98	101	95	102	114	118	122	112	120	116	116	117	116	111	116	121	124	126	121	118	112	111	109

Table D.3 TS 3: The number of SG units in service per hour in each SG plant, each area and the whole test system

Plant\Hour	1	2	3	4	5	6	7	8	9	10	11	12	13	14	15	16	17	18	19	20	21	22	23	24
G1	1	1	1	1	1	1	1	1	1	1	1	1	1	1	1	1	1	2	1	1	1	1	1	1
G2	0	0	0	0	0	0	0	0	0	0	0	0	0	0	0	0	0	0	0	0	0	0	0	0
G3	1	1	1	1	1	1	1	1	1	1	1	1	2	2	1	2	1	1	2	1	1	2	2	2
G4	2	2	2	2	2	2	2	1	2	2	2	2	2	2	2	2	2	1	2	2	2	2	2	2
G5	1	1	1	1	1	1	1	1	1	1	1	1	1	1	1	1	1	1	1	1	1	1	1	1
G6	0	0	0	1	1	0	1	0	0	0	1	1	2	2	0	2	2	0	2	0	2	2	2	0
G7	0	0	0	1	1	0	1	0	0	0	1	1	1	1	0	1	1	0	1	0	1	1	1	0
G8	1	1	1	1	1	1	1	1	1	1	1	1	1	1	1	1	1	0	1	1	1	1	1	1
G9	0	0	0	0	0	0	0	0	0	0	0	0	0	0	0	0	0	0	0	0	0	0	0	0
G10	0	0	0	0	0	0	0	0	0	0	0	0	0	0	0	0	0	0	0	0	0	0	0	0
G11	1	1	1	1	1	1	1	1	1	1	1	1	1	1	1	1	1	0	1	1	1	1	1	1
G12	1	1	1	1	1	1	1	1	1	1	1	1	1	1	1	1	1	1	1	1	1	1	1	1
G13	1	1	1	1	1	1	1	1	1	1	1	1	1	1	1	1	1	3	1	1	1	1	1	1
G14	3	3	3	3	3	3	3	3	3	3	3	3	3	4	3	3	3	4	3	3	3	3	3	3
G15	0	0	0	0	0	0	0	0	0	0	0	0	0	0	0	0	0	0	0	0	0	0	0	0
G16	4	4	4	4	4	4	4	4	4	4	4	4	4	4	4	4	4	4	4	4	4	4	4	4
G17	2	2	2	2	3	2	3	2	3	3	3	3	3	4	3	3	2	0	3	3	3	3	3	3
G18	3	4	4	3	4	4	4	3	4	4	4	4	4	4	4	4	3	4	4	4	4	4	4	4
G19	4	4	4	4	4	4	4	4	4	4	4	4	4	4	0	4	4	4	4	4	4	4	4	4
G20	2	2	2	2	2	2	2	2	2	2	2	2	2	3	2	2	2	0	2	2	2	2	2	2
G21	2	2	2	2	2	2	2	2	2	2	2	2	2	3	2	3	2	4	2	2	2	2	3	2
G22	0	0	0	0	0	0	0	0	0	0	0	0	0	0	0	0	0	4	0	0	0	0	0	0
G23	2	2	3	0	0	2	0	2	2	3	3	3	4	4	3	1	2	0	1	3	3	3	4	4

Plant\Hour	1	2	3	4	5	6	7	8	9	10	11	12	13	14	15	16	17	18	19	20	21	22	23	24
G24	0	0	0	0	0	0	0	0	0	0	0	0	0	0	0	0	0	0	0	0	0	0	0	0
G25	0	0	0	0	0	0	0	0	0	0	0	0	0	0	0	0	0	0	0	0	0	0	0	0
G26	0	0	0	0	0	0	0	0	0	0	0	0	0	0	0	0	0	0	0	0	0	0	0	0
G27	0	0	0	0	0	0	0	0	0	0	0	0	0	0	0	0	0	0	0	0	0	0	0	0
G28	0	0	0	0	0	0	0	0	0	0	0	0	0	0	0	0	0	0	0	0	0	0	0	0
G29	1	1	1	1	1	1	1	1	1	1	1	1	1	2	1	2	1	1	1	1	1	1	1	1
G30	1	1	1	1	1	1	1	1	1	1	1	1	1	2	1	2	1	1	1	1	1	1	2	1
G31	2	2	2	2	2	2	2	2	2	2	2	2	2	2	2	2	2	2	2	2	2	2	2	2
G32	1	1	1	1	1	1	1	1	1	1	1	1	1	1	1	1	1	1	1	1	1	1	1	1
G33	0	0	0	0	0	0	0	0	0	0	0	0	0	0	0	0	0	0	0	0	0	0	0	0
G34	0	0	0	0	0	0	0	0	0	0	0	0	0	0	0	0	0	0	0	0	0	0	0	0
G35	0	0	0	0	0	0	0	0	0	0	0	0	0	0	0	0	0	0	0	0	0	0	0	0
G36	3	2	2	3	3	2	2	2	2	3	3	3	3	3	3	3	3	2	3	3	3	3	3	3
G37	2	2	2	2	2	2	2	2	2	2	2	2	2	2	2	2	2	1	2	2	2	2	2	2
G38	4	4	4	4	4	4	4	4	4	4	4	4	4	4	4	4	4	4	4	4	4	4	4	4
G39	0	0	0	0	0	0	0	0	0	0	0	0	0	0	0	0	0	0	0	0	0	0	0	0
G40	4	4	4	4	4	4	4	4	4	4	4	4	4	4	4	4	4	0	4	4	4	4	4	4
G41	1	1	1	1	0	1	1	1	1	1	1	1	1	1	1	1	1	1	1	1	1	1	1	1
G42	2	2	2	2	0	2	2	2	2	2	2	2	2	2	2	2	2	2	2	2	2	2	2	2
Area 1	3	3	3	3	3	3	3	3	3	3	3	3	3	5	3	5	3	4	3	3	3	3	4	3
Area 2	19	18	18	19	16	18	18	18	18	19	19	19	19	19	19	19	19	13	19	19	19	19	19	19
Area 3	23	24	25	21	23	24	23	23	25	26	26	26	27	31	22	25	23	27	24	26	26	26	28	27
Area 4	7	7	7	9	9	7	9	6	7	7	9	9	11	11	7	11	10	4	11	7	10	11	11	8
System	52	52	53	52	51	52	53	50	53	55	57	57	60	66	51	60	55	48	57	55	58	59	62	57

Appendix E: List of author's thesis based publications

E 1. Journal papers

Published journal papers:

E1. A. Radovanović and J. V. Milanović, "Equivalent modelling of hybrid RES plant for power system transient stability studies," *IEEE Transactions on Power Systems,* vol. 37, no. 2, pp. 847-859, 2022 (DOI: 10.1109/TPWRS.2021.3104625)

E2. M. Krpan, I. Kuzle, A. Radovanović, and J. V. Milanović, "Modelling of supercapacitor banks for power system dynamics studies", *IEEE Transactions on Power Systems,* vol. 36, 5, pp. 3987-3996, 2021 (DOI: 10.1109/TPWRS.2021.3059954)

Submitted journal papers:

E3. A. Radovanović and J. V. Milanović, "Deep learning-based equivalent modelling of hybrid RES plant for efficient, repetitive power system transient stability studies," submitted to *IEEE Transactions on Power Systems,* 2022

E 2.Conference papers

Published conference papers:

E4. A. Radovanović, and J. V. Milanović, "Exploratory study towards equivalent dynamic modelling of hybrid renewable energy source plant based on historical production data", *2019 IEEE Milan PowerTech conference*, Milan, 2019, pp. 1-6.

E5. A. Radovanović, J. N. Plaza, X. Li and J. V. Milanović, "The influence of hybrid renewable energy source plant composition on transmission system stability", *2020 IEEE PES Innovative Smart Grid Technologies Conference Europe (ISGT-Europe),* the Hague, 2020, pp. 1-5.

E6. A. Radovanović, J. Li, J. V. Milanović, N. Milosavljević, R. Storchi, "Application of agglomerative hierarchical clustering for clustering of time series data", *2020*

IEEE PES Innovative Smart Grid Technologies Conference Europe (ISGT-Europe), the Hague, 2020, pp. 1-5.

E7. A. Radovanović, X. Ye, J. V. Milanović, N. Milosavljević, R. Storchi, "Application of k-medoids partitioning algorithm for clustering of time series data", *2020 IEEE PES Innovative Smart Grid Technologies Conference Europe (ISGT-Europe),* the Hague, 2020, pp. 1-5.

E8. A. Radovanović, A. Siafaras, J. V. Milanović, "Towards development of equivalent model of hybrid renewable energy source plant for voltage stability studies", *2021 IEEE Madrid PowerTech conference,* Madrid, 2021, pp. 1-6.

E9. A. Radovanović, Y. Wang, J. V. Milanović, "Towards development of equivalent model of hybrid renewable energy source plant for small disturbance stability studies", *2021 IEEE Madrid PowerTech conference,* Madrid, 2021, pp. 1-6.

E10. A. Radovanović, and J. V. Milanović, "Limitations of the applicability of the concept of HRES plant in practical implementation", *CIRED 2021 conference*, Geneva, 2021, pp. 1-5.

E11. A. Radovanović, H. Huang, and J. V. Milanović, "Probabilistic assessment of the effect of a spatially distributed hybrid renewable energy source plant on system transient stability", *17th International Conference on Probabilistic Methods Applied to Power Systems (PMAPS 2022),* Manchester, 2022.

E 3. Technical reports

E12. A. Radovanović, J. V. Milanović, D. Rayo Garcia et al., "Modelling of non-dispatchable RES and analysis on storage alternatives to support Hybrid RES", Deliverable 5.1, EU H2020 Project "CROSS BOrder management of variable renewable energies and storage units enabling a transnational Wholesale market (CROSSBOW)", (H2020-773430), July 2019.

E13. D. Rayo Garcia, R. de Arriba, A. Radovanović, J. V. Milanović, et al., "Assessment of the combination of RES and storage alternatives under the Manager Energy for Hybrid Plants (ME4HP) and REDOX flow battery characterization", Deliverable 5.2, EU H2020 Project "CROSS BOrder management of variable renewable energies and storage units enabling a transnational Wholesale market (CROSSBOW)", (H2020-773430), November 2019.

E14. D. Rayo Garcia, R. de Arriba, A. Radovanović, J. V. Milanović, et al., "CROSSBOW Hybrid RES Dispatchable Unit – Intermediate Version", Deliverable 5.3, EU H2020 Project "CROSS BOrder management of variable renewable energies and storage units enabling a transnational Wholesale market (CROSSBOW)", (H2020-773430), December 2019.

E15. D. Rayo Garcia, R. de Arriba, A. Radovanović, J. V. Milanović, et al., "CROSSBOW Hybrid RES Dispatchable Unit", Deliverable 5.3, EU H2020 Project "CROSS BOrder management of variable renewable energies and storage

units enabling a transnational Wholesale market (CROSSBOW)", (H2020-773430), May 2020.

Appendix F: List of non-thesis based author's publications

F 1. Journal papers

Published journal papers:

F1. D. Đorđević, A. Radovanović, J. Dragosavac, Ž. Janda, "The analysis of step-up transformer tap change on the quantities at the point of connection to transmission grid", *Proceedings of Electrical Engineering Institute Nikola Tesla*, vol. 27, no. 27, pp. 91-103, 2017.

F 2.Conference papers

Published conference papers:

F2. A. Radovanović, and D. Grujić, "Islanding of grid connected photovoltaic system – causes, consequences and protection", *14th International Symposium INFOTEH-JAHORINA 2015*, Jahorina, Bosnia and Herzegovina, 2015, pp. 1-4.

F3. A. Radovanović, and Ž. Đurišić, "Smart photovoltaic systems", *32nd CIGRE Serbia Counseling*, Zlatibor, Serbia, 2015, pp. 1-5.

F4. A. Radovanović, and Ž. Đurišić, "The estimation of extreme wind speeds in the South Banat region", *32nd International Conference ENERGETIKA*, Zlatibor, Serbia, 2016, pp. 1-6.

F5. N. Georgijević, A. Radovanović, M. Dilparić, D. Đorđević, and D. Milošević, "Voltage control - analysis of transmission system operator requirements and directions for the new units choice", *17th Symposium on Control and Telecommunications in the Electric Power System*, CIGRE Serbia, Vršac, Serbia, 2016, pp. 1-9.

F6. N. Georgijević, S. Lukić, M. Dilparić, D. Đorđević, A. Radovanović, B. Filipović, "Influence of excitation system structure and parameters on modal analysis of serbian power system", *33rd CIGRE Serbia Counseling*, Zlatibor, Serbia, 2017, pp. 1-10.

F7. N. Georgijević, A. Radovanović, M. Milinković, D. Đorđević, "Fact approximation of the power plant reactive power capability at the plant of common

coupling", *17th International Symposium INFOTEH-JAHORINA 2018*, Jahorina, Bosnia and Herzegovina, 2018, pp. 1-4.